UNIVERSITY OF SOUTHAMPTON

Electro-Optic Polymer Based Mid-Index Phase Modulator in Silicon Nitride Waveguide Technology

by

Teerapat Rutirawut

ORCiD ID: 0000-0003-0159-152X

A thesis submitted for

the degree of Doctor of Philosophy

in the

Faculty of Engineering and Physical Sciences

Optoelectronics Research Centre

March 2021

University of Southampton

ABSTRACT

FACULTY OF ENGINEERING AND PHYSICAL SCIENCES

OPTOELECTRONICS RESRACH CENTRE

Doctor of Philosophy

by Teerapat Rutirawut

ORCiD ID: 0000-0003-0159-152X

Among the demand for higher bandwidth driven by media and cloud computing applications grows, the need for cost and power efficient, short reach and long-haul optical transceivers becomes more eminent. Silicon photonics is emerging as a technology of choice for realising photonic integrated circuits for intensity modulation-direct detection communication systems. Silicon Nitride (SiN) is a common material in the electronics industry and is now becoming a choice of materials for the photonics industry as it is a fully compatible platform for photonic integrated circuits. Advantage in using the SiN waveguide as the EO polymer modulator are the low number in fabrication step.

In this research, the electro-optic polymer modulations have been adapted to design high-speed phase modulator on low temperature silicon nitride platforms. The side-chain EO polymer with Phenyl vinylene thiophene vinylene (FTC) based chromophore that can provides the outstanding EO coefficient will be used as a modulating medium. In order to achieve a high modulation performance and also keep a fabrication still simple and low-cost, the SiN strip and slot structure has been investigated to provide an enlarge overlap between optical and electrical modulating field. All designs of modulators in this research can be fabricated using only two lithography steps and a low-cost CMOS compatible BEOL process decreasing substantially fabrication time and design/test turnaround.

Photonic and electrical RF models were cooperatively simulated to optimise dimension parameters of the phase modulator with in-plane CPW electrode integrated to three different SiN waveguide platforms. The modulator devices were then fabricated in line with the simulated designs and coated with three different types of EO polymer cladding. The high voltage poling technique for activating an EO activity in polymer was presented with in-house developed setup. For the modulator measurements, the devices were characterised for the modulation performance mainly in DC mode, and the decent modulator was tested with the high-speed modulation experiment.

The remarkable modulator in this research has exhibited the outstanding modulation performance among the reported MZI based modulators with EO polymer integration. The modulator with lowest half-wave voltage is presented with 10 V while the modulator with lowest voltage-length product is revealed with 3.4 V·cm. The transmission data rate in high-speed is demonstrated up to 40Gb/s with the extinction ration of ~2.6dB.

CONTENTS

List of Figures

Declaration of Authorship

I, Teerapat Rutirawut, declare that the thesis entitled *Electro-Optic Polymer Based Mid-Index Phase Modulator in Silicon Nitride Waveguide Technology* and the work presented in the thesis are my own, and have been generated by me as the result of my own original research.

I confirm that:

- This work was done wholly or mainly while in candidature for a research degree at the University;
- Where any part of this thesis has previously been submitted for a degree or any other qualification at this University or any other institution, this has been clearly stated;
- Where I have consulted the published work of others, this is always clearly attributed;
- Where I have quoted from the work of others, the source is always given. With the exception of such quotations, this thesis is entirely my own work;
- I have acknowledged all main source of help;
- Where the thesis is based on work done by myself jointly with others, I have made clear exactly what was done by others and what I have contributed myself;
- Parts of this work have been published in conference proceedings and journal articles as listed in List of Publications.

Signed: ……..

Date: ……17/06/2021…….

Acknowledgments

This work could not be done without the guidance and support I have received from many people throughout my PhD study. Firstly, I would like to express my sincerest gratitude to my supervisor Professor Frederic Y. Gardes for invaluable advice and endless support. He has always pulled me out of downcast feeling from uncountable experiment failures and filled up my mind again with motivations and inspirations until the completion of this work.

I would like to thank all members in Silicon Photonics group for their help and support, particularly Professor Graham Reed, Professor Goran Mashonovich, and Professor David Thomson for their brilliant leadership to the group, Dr Nannicha Hattasan who has introduced me to join this amazing Silicon Photonics community, Dr Thalia Dominguez Bucio for tirelessly working to develop the SiN waveguide technology and always being available for any question from me, Dr Lorenzo Mastronardi for nicely organising to keep the measurement tools and software in our laboratory working, Dr Scott A. Reynold for his professional skill to design my first high-voltage poling setup which has been very helpful to my research over these years.

Dr Mehdi Banakar, for being my best mentor on cleanroom processes throughout my PhD study, also being as my life coach who always suggest me how to live joyfully in the UK.

I would also like to express my gratitude to Professor Ramon Rios Torres, Dr Marta Meazza and Matthew O. Jenner in School of Chemistry who have worked very hard to produce EO polymer for enabling my very first workable modulator. I would also thank Professor Shiyoshi Yokoyama and Dr Alisa Bannaron from Kyushu University for providing the outstanding performance EO polymer to be tested on my devices.

I am also grateful to all the technicians in Zepler Institute Cleanroom Complex at the University of Southampton who have helped me along the research way. Many colleagues across the Optoelectronics Research Centre (ORC) and Electronics and Computer Science (ECS) have helped me at one time or another during these years of my study, thank you to Dr Martynas Beresna, Dr Timothy Lee, Dr Monika Glanc-Gostkiewicz, Dr Russel Torah, Glenn Topley, Paula Smith, Ilias Skandalos, Stefan Ilie, Greta De Paoli, Senta Jantzen and many more that I may have missed.

There are so many friends I would like to thank and hold a huge amount of gratitude for their friendship; particularly, Norberto, Fernando, Soonki, Kasia, Andrei, Krzysztof, Hao Li and Haoyan. They have spent all these study years with me and also listen to whatever troubles I had.

I would like to thank the Development and Promotion of Science and Technology Talents Project of Royal Thai Government for the financial support through my PhD study.

Apart from the supports on my research and study, I would like to thank my love Wanvisa Talataisong for her faultless love. Especially, I would not be able to finish my PhD journey without love and support from her during the most suffering time of COVID-19 situation. I know we will forever support to each other in anyway, anywhere and anytime without any argument. Everything is possible when I have got your back.

Last but not least, I am very thankful to my parents and my brother in Thailand for always remotely serving me with love, care and encouragement; my Mum Sunun and my Dad Teerachai who never doubt my abilities and let me create my lifestyle freely since I was a naughty boy, and my brother Teerapong who has tirelessly taken care of our family's wellbeing. This is an invaluable support which made me so proud of being myself. A special thanks to my brother's kids Thunthorn and Thunyarat for entertaining me with their shows in every time I had a video call to our family.

Nomenclature

Abbreviations

BOX	Buried oxide
BTO	Barium Titanate
CMOS	Complementary Metal Oxide Semiconductor
CPW	Coplanar waveguide
CVD	Chemical vapor deposition
EME	Eigenmode expansion
EO polymer	Electro-Optic Polymer
FDE	Finite difference eigenmode
FDTD	Finite difference time domain
FSR	Free spectral range
FTC	Phenyl vinylene thiophene vinylene
GC	Grating coupler
GSG	Ground-signal-ground
$LiNbO_3$	Lithium Niobate
MMA	Methyl methacrylate
MMI	Multimode interference structure
MZI	Mach–Zehnder interferometer
MZM	Mach-Zehnder modulator
PCP	Poling circuit layer
PECVD	Plasma-Enhanced Chemical Vapour Deposition
PIC	Photonics integrated circuits
PSW	Plasmonic slot waveguide
RF	Radio frequency
SiP	Silicon photonics
SiN	Silicon Nitride

SiO_2	Silicon Dioxide
SPPs	Surface plasmon-polaritons
TIR	Total internal reflection
TWM	Traveling wave modulator

Mathematical symbols

σ_{poling}	Poling coefficient
$\vec{D}$	Optical displacement field
$\vec{E}_{mod}$	Electric modulation field
$\vec{E}_{opt}$	Optical field
E_{sat}	A minimum electric field strength required for obtaining the saturated Pockels coefficient
E_{poling}	Electric field poling
$\varepsilon'_{r,ij}$	Modulating relative permittivity
$\varepsilon_{r,ij}$	Unperturbed relative permittivity
f_{3dB}	The 3dB modulation bandwidth
Γ	Overlap integral factor
$\gamma_{33,bulk}$	Pockels coefficient of bulk polymer
I_{out}	Intensity at the output waveguide
I_{in}	Intensity at the input of waveguide
$\chi^{(2)}$	Non-zero of 2nd- nonlinear susceptibility
L_p	Propagation length
$L_{slot\text{-}taper}$	Slot-taper length
L_{MMI}	Length of multi-mode interference cavity
$M(f)$	Modulation frequency
n_{ij}	Unperturbed refractive index
n_{high}	High-refractive index

n_{low}	Low-refractive index
n_{SiN}	Refractive index of SiN
$n_{polymer}$	Refractive index of polymer
$\vec{P}^{(2)}$	Second-order nonlinear polarisation
P	Net polarisation
Λ	Grating period
r_{33}	Electro optics coefficient
$r_{33,in-device}$	Electro optics coefficient in device
T_g	Glass transition temperature
V_{pol}	Poling voltage
V_{mod}	Modulation voltage
$V_\pi \cdot L$	Voltage-length product
W_{ridge}	Slot width of slot waveguide
W_{MMI}	Width of multi-mode Interference
$W_{strip\text{-}end}$	Width of strip-end in taper
W_{ridge}	Width of strip waveguide
Z_0	Characteristic impedance
$\Delta\phi$	Optical phase different
Δn_{eff}	Refractive index change
$\Delta n_{EO}(x,y)$	Local refractive index change

Chapter 1. INTRODUCTION

As there is an increasing demand in optical communication, optical switching and optical beam steering in applications such as Light Detection and Ranging (LIDAR), low loss on chip switching, or free space communications applications (LIFI), the development of optical phase modulator on a low-cost mid index platform is one of key factor to keep pace with the possible high demand of low-cost integrated devices in the future. Wideband operating wavelength is an essential for long distance or low-cost beam steering in LIDAR [1] as shown in Figure 1-1(b). High modulation frequencies are also required to perform scanning or switching at high speed. High transmission power within a small footprint design is another important criterion for improving density of a low index platform. Current silicon-based modulator used for beam steering are still using the thermo-optic modulation as shown in Figure 1-1(a) to obtain a sufficient device density. Nevertheless, the bandwidth is limited to the wavelength above 1.1µm with a low modulation speed. To enhance the above performances, silicon nitride (SiN) is used instead of silicon for its capability to handle high optical power and wideband transmission wavelength below 1.1µm. The electro-optic polymer is also utilized to feature large bandwidth at high modulating frequencies. Furthermore, the photonics slot structure is intended to provide a means to obtain the small footprint necessary for phase array devices.

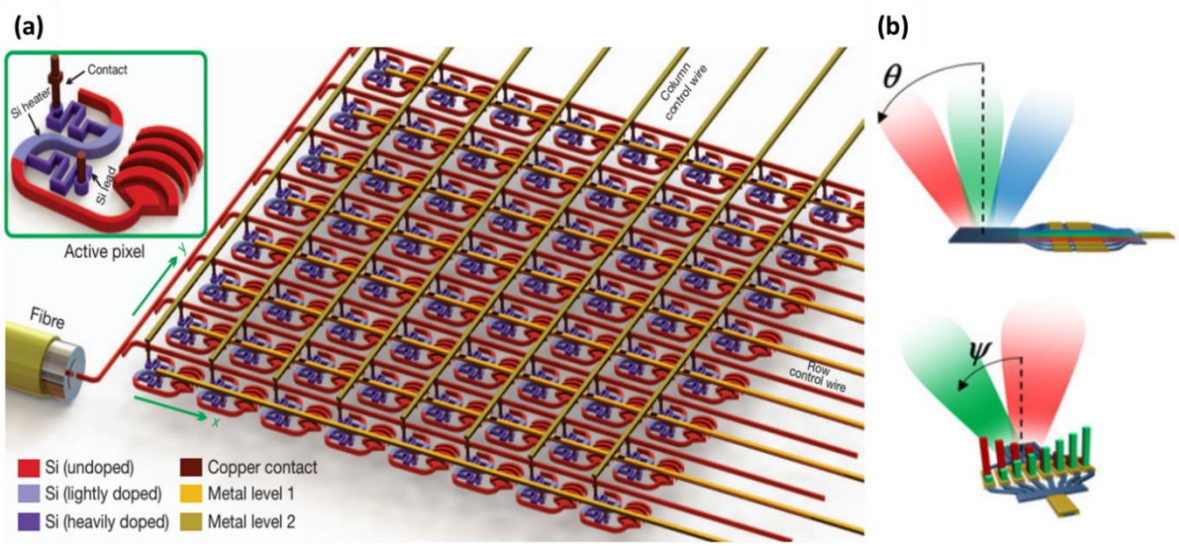

Figure 1-1 (a)Tuneable phase array for beam steering application[1] and (b) schematic diagrams illustrating a beam steering with wavelength dependent beam orientation[1].

1.1 Modulators in Silicon Photonics

Silicon photonics (SiP) has become an attracted technology platform for complex integrated photonics circuits over the past few years. The innovation and development in previously silicon electronics fabrication infrastructure leading to the high precision in optical components fabrication such as optical waveguides and grating by using SiP technology. Therefore, silicon photonics is the photonics platform that allows the integration of thousands of photonics components on a single chip [2, 3]. Active silicon photonics gained widespread attention after Soref and Bennett proposed the effects of the carrier concentration on the refractive index of silicon and successfully demonstrated that the refractive index of doped silicon can be varied with the variation of applied electric field [4]. This electrooptic effect in silicon is generally reported as a plasma dispersion effect. In consequence of the discovery of the variation of silicon RI with electric field, optical modulators and photodetectors are became more interested in SiP platform. High speed modulators are key building blocks in SiP for many applications. Thus, modulators based on several different architectures, such as Mach-Zehnder Interferometer, Michelson Interferometer and micro ring resonators based modulators have been demonstrated in SiP platform [5-8]. High speed modulators based on resonator have gained enormous interest recently, due to its ultra-low modulation power consumption. However, these modulators are suffering from the limited optical bandwidth, strict wavelength dependence and a thermal instability [9]. SiP modulators based on Mach-Zehnder interferometer became the candidate devices for achieving + 40 Gb/s data rates due to their large bandwidths. Travelling wave Mach-Zehnder modulators (TW-MZM) are also used in many commercial systems because of their thermal stability and high fabrication tolerance.

The fast growing in the cloud services offered by data centres and the increasing demand for higher bandwidth driven by web-based applications leading to the requirement for faster and inexpensive short reach optic solutions [10]. SiP is a promising technology because of the compatibility with the proven complementary metal oxide semiconductor (CMOS) manufacturing process and capable of supporting 100 Gb/s, and later 400 Gb/s, intra-data centre connectivity requirements ranging from 0.5 to 10 km. SiP modulators based on Mach-Zehnder are candidate devices for achieving these data rates due to their large bandwidths.

The performance of electro-optic modulators is evaluated based on their 3dB electro optic bandwidth, power consumption, driving voltage and required voltage to achieve a π phase shift. Higher bandwidth modulators can achieve higher bitrates. Lower driving voltage is a key factor in the performance of a modulator. As the operating voltage of the CMOS technology is getting smaller, SiP modulators with lower driving voltage are more desirable. The drive voltage performance of a modulator is usually presented in literature using the $V_\pi L$ figure of merit. This value presents the required drive voltage to achieve a π phase shift per unit length. Therefore, a lower $V_\pi L$ value is more

desirable. In interferometer-based modulators, there is a trade-off between drive voltage and bandwidth. This trade-off is fully analysed in the next chapters and an optimized design is presented.

1.2 Active Devices on Silicon Nitride Platform

There is a growing demand for low-cost devices targeted at enabling high speed data traffic of optical interconnects. A high speed, compact, cost-effective optical modulator is essential to support this increasing demand. Most of modulators are commonly fabricated on the integrated silicon (Si) or silicon nitride (SiN) photonic circuits due to the compatibility with existing CMOS technology as well as the electronic device fabrication.

State-of-the-art Si based modulators are mostly depended on the concepts of carrier charge movement in Si such as pn-junction [11-14] and pin-junction [15]. Electric field modulators based on the Franz–Keldysh effect [4-6] have also been demonstrated and rely on a pin junction. Apart from efficiency and fast speed, these modulators suffer from increase insertion losses due to carriers or bandgap absorption and require a complex fabrication process with high temperature required for doping activation or germanium epitaxy. Alternative concepts of optical modulator which are simpler in terms of fabrication and are compatible with Back End of the Line (BEOL) multi-layer processing are based on the integrations of other active material such as, lithium niobate ($LiNbO_3$)[16, 17], barium titanate (BTO)[18, 19], electro-optic PZT[20], or electro-optic polymer (EO-polymer)[21, 22].

To modulate the optical signals in the photonic integrated circuit, phase modulators, have been used to adjust the optical phase delay in interferometers or ring resonators for modulating output amplitude. A modulator based on the SiN platform feasibly provides several advantages beyond that on Si platform such as lower propagation loss[23, 24], fabrication flexibility[25-27], selectable refractive index[28], broader transparency range[29-31], tunable operating wavelength[32], and a high tolerance to temperature variation[33, 34]. SiN enables a broader field of applications, however, it has a centrosymmetric behaviour which does not allow intrinsic electrooptic properties and therefore it is not generally possible to obtain optical modulation through an electric field [35]. Moreover, doping of semi-conductive materials cannot be applied to the SiN because of its dielectric property. The integration of $LiNbO_3$ or BTO with SiN is a potential route but does require complex fabrication schemes such as epitaxy, planarization and bonding resulting in potential yield issues.

In the telecommunication industry, lithium niobate ($LiNbO_3$) is already the standard EO material to function in phase modulators, however, EO polymers are recently becoming the new promising material of choice due to 10-times higher EO efficiency compare to $LiNbO_3$, low operation voltage [36], and low power consumption [37]. The integration of EO-polymers with SiN

waveguides to form optical modulators provides flexibility and simplicity for BEOL fabrication methods. Using EO-polymer, several modulators have achieved high-speed, energy-efficient modulation, whilst using few fabrication steps. The EO-polymer based modulators have been demonstrated at a very low voltage-length product of 0.345 V·mm [38] or a modulation frequency beyond 100 GHz [22]. The mechanism of electro-optic effect in the EO polymer is a shuttling of the electrons within the chromophore molecules which is a very fast electronic motion below a femtosecond in time scale [39, 40], and high-speed EO modulators have been demonstrated with a bandwidth above 100 GHz [41-43]. Moreover, EO polymer-based modulators can be prepared at low temperature (<350 degree Celsius) by a simple process composed of three steps, which comprise waveguide etch, metal lift-off and polymer spin-coating. This can be compared to more than 60 steps process and ~10 lithography masks for a standard silicon or an EAM SiGe modulator [22, 44, 45].

Nevertheless, very few EO-polymer modulator based on SiN [46, 47] have been demonstrated. Owing to its lower index contrast compared to Silicon, the challenge on the SiN platform is to obtain the best modulation efficiency whilst retaining a low absorption loss. Few waveguide structures have been introduced to demonstrate modulation capabilities, however, their efficiency is still far from the Si modulator with efficiency such as 900 V·cm in a SiN ridge design[46], or 17.6 V·cm in a thin SiN design[47]. Slot waveguides coupled to a pn junction have been adopted in high confinement materials [48-51] such as Si to enable a high overlap between the optical mode, the E-field and the EO material, nevertheless due to the insulator nature of SiN this was only used in silicon.

Due to the random alignment of chromophores in the initial state of EO-polymer, its EO coefficient is zero as deposited and requires activation process described as poling. The poling of EO-polymer is taking the form of a strong electric field applied through the polymer in the region surrounding the modulating waveguide whilst the temperature of the polymer is raised close to the glass transition temperature. To simplify the process, the poling is typically performed by using the device modulation electrodes[52, 53]. An in-plane electrode where the electrodes are located on the same plane as waveguide is an alternative structure to reduce the complexity of fabrication as it requires only a single step of metal lift-off process[54]. The modulation performance of modulators has been proposed by only calculating an overlapping factor of the optical power in the polymer or overlapping factor of the optical field and modulation electric fields within the polymer [55-57]. The realistic spatial distribution of poling efficiency in EO-polymer has not been extensively considered, and the influence of carrier charge in the Si-substrate to both poling and modulation electric fields is still undeveloped.

1.3 Scope and Objectives

The current state of the art in EO polymer phase modulators in silicon photonics technology has plenty of scopes for development, particularly for improving modulation performance. Whilst

most of the modulators still rely on relatively complicated fabrication processes using silicon, only a few papers have demonstrated EO polymer modulators on silicon nitride waveguide [58-60]. The aim of this research project is to design, fabricate and characterise the first prototype of optically wideband EO polymer phase modulator with a SiN slot waveguide structure using a low temperature process and a simple fabrication process. The target specifications are detailed below.

- Demonstration of very first high-speed MZI-based EO polymer modulator on SiN technology operating in C-band at data rate exceeding the standard rates of 28 or 56 Gb/s.
- Low-cost fabrication process relied on only 2 steps of lithography layer and simple material integration method with spin-coating process and one time polymer activation.
- SiN waveguide based modulator possibly to operate on wideband optical wavelength e.g. C-band, O-band, visible, mid-IR (benefit for LIDAR applications [61], optical switching and LIFI)
- No requirement of expensive SOI wafer. The initial substrate requires only a low-cost bulk Si-wafer with few μm-thick thermal oxide layers.
- No need of very high resolution and long-time consumption with e-beam lithography process.
- Low thermal sensitive device based on MZI structure.
- Up-scalable system for the applications without requirement of intensive compactness of the modulator device (e.g. LIDAR, LIFI etc.)
- Compatible to the CMOS fabrication technology and Back End of the Line (BEOL) processing (≤350°C).

1.4 Report Overview

The aim of this introduction chapter was to provide an overview of the silicon photonics device based on SiN platform and highlight their potential applications, especially the optical modulator device. The remainder of this thesis is organised as follows:

Chapter 2 will focus on the background of silicon nitride waveguide and electro-optic polymer for fabricating optical phase modulator. Different structures and the guiding mechanisms waveguides for EO polymer phase modulator will be presented, followed by the structure of modulator important parameters for the modulator characterisation. The design and structure of electrode for signal modulation will be reviewed and discussed. The review of the current state-of-art will also be presented in this chapter.

Chapter 3 will present the design and simulation of photonic component on SiN platform, starting from the introduction of important tools used to design and simulate all components in the EO-polymer modulator in this research. Follow by the explanation of important parameters and

optimisation of passive components including grating coupler, waveguide, MMI splitters, and Mach-Zehnder interferometer structure. Then, the design and optimisation parameters of two designs of waveguide including strip waveguide and slot waveguide will be presented. The drawing procedure of mask layout for fabricating all components in the device will also be explained in this chapter. Finally, the optimal design for all components used in the fabrication process will be summarised in this chapter.

Chapter 4 will provide details of the fabrication processes starting from the preparation of EO- polymer. Then, the fabrication of the components in the device including the deposition and patterning of SiN, the deposition and patterning of metal electrode, the development of polymer coating process, and the activation of EO-polymer will be detailed.

Chapter 5 will report the characterisation results of the devices fabricated by following the procedure in chapter 4. All fabricated passive components will be optically tested. The result from the DC modulation and high-frequency modulations including electro-optic efficiency of polymer, $V_{\pi} \cdot L$ modulation, and modulation bandwidth will also be summarised in this chapter. Finally, the comparison between the simulation and experimental results will be discussed.

Chapter 6 will provide an overall summary of this thesis and present the conclusions. The outlook for the future fabrication of the EO polymer modulation based on SiN platform using the higher efficiency and novel EO polymer will be also outlined.

Chapter 2.
BACKGROUND & LITERATURE REVIEW

2.1 Silicon Nitride Waveguide

Silicon Nitride (SiN) is a common material in the electronics industry and is now becoming a choice of materials for the photonics industry as it is a fully CMOS (Complementary Metal Oxide Semiconductor) compatible platform for photonic integrated circuits. Therefore, SiN on silicon photonics technology allow an integration of electronic and optical system on the same chip by using the same fabrication techniques. Moreover, SiN is a material with a broadband transparent window, with low nonlinear losses, and a relatively low thermo-optic coefficient. These key properties of SiN are leading to a vast variety of applications covering from mid-infrared to ultra-violet regime.

SiN is a promising material for fabricating waveguides and resonators, owing to its low optical loss at visible and near-infrared wavelengths and compatibility with CMOS processing. Therefore, SiN waveguide provides a transparency in both visible[61-63] and infrared regime[64, 65]. Due to the low nonlinearity of SiN, it also allows for propagation of high optical power density [66, 67]. Both visible-IR transparency and low nonlinearity enable potential applications of phase modulator in optical communication and LIDAR[68]. Moreover, SiN waveguides have more robustness to fabrication imperfections (e.g. etching roughness or dimension deviation) than silicon waveguide due to the lower index contrast that is about 2:1.45 at 1,550nm (SiN : SiO_2)[69].

Fabrication of thin film slab waveguides for visible guiding (λ = 632 nm) has been reported in 1976 when the Si_3N_4 cores with a silicon dioxide (SiO_2) lower cladding (buffer layer) have been created on top of a silicon substrate[62]. The structures were generated by thermally oxidising silicon to form a buffer layer on top of the silicon substrate, then following by depositing the Si_3N_4 on the SiO_2 to form a waveguide. As is the case today, the oxidisation of SiO_2 based on thermal techniques remains one of the lowest loss oxide-based buffering materials due to a low surface roughness from the original high-quality silicon substrate and the absence hydrogen in the material and growth process. The waveguide with higher index can be fabricated by using deposition techniques such as chemical vapor deposition (CVD), then the waveguide patterns are generated, followed by etching to form the waveguides. Early SiN waveguides have been fabricated with an air upper cladding design resulting in a high loss dominated by surface roughness and lithography induced waveguide scattering and material optical absorption. So, the advancements in upper cladding oxide deposition has been applied to reduce losses. In 1984, planar and channel optical waveguides based Si_3N_4/SiO_2 have been fabricated to form various techniques including thermal oxidation, sputtering, and CVD to compare the loss of SiN waveguides with variations in core, upper cladding material density,

lithography and etching induced waveguide roughness. Losses in thermally annealed slab waveguides were reported to be 0.5 dB/cm at the wavelength of 514.5 nm while losses for the ridge channel waveguides were found to be~ 1-2 dB/cm [70]. Annealing at elevated temperatures led to densification of the deposited films and reduced optical scattering by unwanted material clusters formed during CVD process. The Si_3N_4 waveguide with SiO_2 cladding layer for near-IR guidance have been firstly reported in 1987 [71]. Optical losses of <0.3 dB/cm at wavelengths in the 1.3 – 1.6 μm range has been reported for this waveguide. Losses in this telecommunications waveband due to hydrogen (H)-based absorption peaks at 1.52 μm (in the Si_3N_4 core) and 1.40 μm (in the SiO_2 cladding) were reported to be of 1.2 and 2.2 dB/cm, respectively. These peaks of loses can be largely removed when the device has been annealed at high temperature (1100-1200 °C). In 1993, the first photonics integrated circuits (PIC) based Si_3N_4 waveguide has been fabricated for immunosensors [72]. Mach-Zehnder interferometer structures were used as a sensing region when the detection of proteins occurred by etching the waveguide cladding to allow the interaction between the guided mode in the exposed waveguide core with the sensing analytes. This reported visible sensing interferometer on-chip demonstrated the capabilities of the emerging Si_3N_4 with the PIC process. By the late 1990s, the process and device development in a related nitride-based material, silicon oxynitride (SiO_xN_y) have been reported with further advanced device design and process capabilities of the nitrides [73, 74]. Despite a fully integrated interferometer based on SiN waveguides for sensing applications, reported from many research groups in late 1990s, this material platform came back to the spotlight again in 2005. Technique to fabricate low loss SiN waveguide for near-IR guiding has been developed and demonstrated by Sandia Labs (USA) in 2005 [75]. Sidewall roughness has been a point of focus for improvement, as it is one of the main causes for inducing high propagation losses. Therefore, sidewall roughness measurements were taken during the fabrication of waveguide devices for various processing conditions in this work. By smoothing the sidewall roughness, the lowest linear waveguide loss of 0.1 dB/cm was achieved at a wavelength of 1550 nm for buried channel Si_3N_4 waveguides. From 2008 – 2011, the silicon oxynitride ($SiON_x$) waveguides [76] and Si_3N_4 waveguides [77-79] have been developed and reported for applications in near-IR. In 2011, the development of SiN platforms for near-IR region was mostly focused on telecom (NIR C-Band at 1550 nm), and the waveguide cross-sections were for moderate confinement (SiN-film heights > 100 nm), despite some research groups reporting low confinement waveguides (SiN-film height < 100 nm). After 2011, there is a growing interest on high confinement SiN waveguide and resonators with a thickness h > 400 nm for applications in mid-IR guiding (wavelength > 2000 nm), which are reported by several groups [80-83]. In 2015–2016, moderate confinement for SiN technologies were proposed and developed for various applications including the biosensing application [84-86]. Since 1977, a wide range of SiN based waveguides for visible, near-IR, and mid-IR devices including filters, polarization splitters, fibre to waveguide mode transformers, tunable optical add/drop

multiplexers, thermally controlled optical switches, and bus-coupled ring resonators were developed and demonstrated.

Due to many beneficial properties as mentioned above, the state of the art of SiN waveguide has been demonstrated through low guiding loss across visible-IR range by a number of research groups as shown in Table 2-1.

Table 2-1 The state of the art of silicon nitride waveguide platform[87]

Research Group	**λ (nm)**	**Substrate**	**Core**	**Cladding**	**Width (nm)**	**Height (nm)**	**Straight (dB/cm)**
Gent/Baets	532	SiO_2 HDP-CVD	SiN PECVD	SiO_2	300 400 50	180	7.00 @ 532 3.25 @ 532 2.25 @ 532
Aachen/Witzens	660	SiO_2/1.45	SiN/1.87 PECVD	SiO_2 (Water)	700	100	0.51 @ 600
Gent/Baets	780	SiO_2 (h = 2.4μm) HDP-CVD	SiN PECVD 1.89@780	SiO_2	500 600 700	220	2.25 @ 780 1.50 @ 780 1.30 @ 780
Gent/Baets	900	SiO_2 (h = 2.4μm) HDP-CVD	SiN PECVD	SiO_2	600 700 800	220	1.30 @ 900 0.90 @ 900 0.62 @ 900
IME/Lo	1270–1580	SiO_2 (h = 2.2μm)	Si_3N_4 LPCVD	SiO_2	1000	400	0.32 @ 1270 1.30 @ 1550 0.40 @ 1580
IME/Lo	1270–1580	SiO_2 (h = 3.32μm)	Si_3N_4 PECVD	SiO_2	1000	400	0.45 @ 1270 3.75 @ 1550 1.10 @ 1580
IME/Lo	1270–1580	SiO_2 (h = 3.32μm)	Si_3N_4 PECVD	SiO_2	1000	600	0.24 @ 1270 3.50 @ 1550 0.80 @ 1580
Trento/Pavesi	1550	SiO_2 (h = 2. μm)	Multilayer	Air/SiO_2			1.50 @ 1550
Sandia/Sullivan	1550	SiO_2 (h = 5.0μm)	Si_3N_4 LPCVD	SiO_2	800	150	0.11–1.45 @ 1550
Twente/Driesen	1550	SiO_2/1.45	SiON PECVD	-	2000-2500	140-190	0.20 @ 633 0.20 @ 1550
IME/Lo	1550	SiO_2 (h = 5.0μm)	SiN/2.03 PECVD	SiO_2	700	400	2.1 @ 1550
LioniX-UCSB	1550	SiO_2/1.45 (h = 8.0μm)	Si_3N_4 LPCVD	SiO_2	2800	100	0.09 @ 1550
LioniX-UCSB	1550	SiO_2/1.45 (h = 8.0μm)	Si_3N_4 LPCVD	SiO_2	2800	80	0.02 @ 1550
Cornell/Lipson	1550	SiO_2	Si_3N_4 LPCVD	SiO_2	1800	910	0.04 @ 1550
LioniX	1550	SiO_2 (h = 8.0μm)	Si_3N_4 LPCVD	SiO_2	700-900	800 1000 1200	0.37 @ 1550 0.45 @ 1550 1.37 @ 1550
Toronto-IME/Poon	1270–1580	SiO_2 (h = 2.2μm)	Si_3N_4 LPCVD	SiO_2	900	400	0.34 @ 1270 1.30 @ 1550 0.40 @ 1580
Toronto-IME/Poon	1270–1580	SiO_2 (h = 3.32μm)	Si_xN_y PECVD	SiO_2	1000	600	0.24 @ 1270 3.50 @ 1550 0.80 @ 1580

CNM-VLC	1550	SiO_2 (h = 2.5μm)	Si_3N_4 LPCVD	SiO_2	1000	300	1.41 @ 1550
UCD/Yoo	1550	SiO_2	Si_3N_4 LPCVD	SiO_2	2000	200	0.30 @ 1550
LigenTec	1550	SiO_2 (h = 0.13-0.35μm) Thermal	Si_3N_4 LPCVD	SiO_2	2000	800	No reported loss for this device
Chalmers/Torres	1550	SiO_2 (h = 2.0μm)	Si rich SiN_x LPCVD	SiO_2	1650	700	1.00 @ 1550
Ghuagzhou/Shao	1550-1600	SiO_2 (h = 2.0μm)	Si_xN_y ICP-CVD		1400	600	0.79 @ 1575
Columbia/Lipson	2300-3500	SiO_2 (h = 4.5μm)	Si_3N_4 LPCVD	SiO_2	2700	950	0.60 @ 2600
MIT/Agarwal	2400-3700	SiO_2/1.45 (h = 4.0μm)	Si rich SiN_x LPCVD	SiO_2	4000	2500	0.16 @ 2650 2.10 @ 3700

2.2 Electro-Optic Polymer

The Electro-Optic (EO) properties in polymer systems is originated from non-centrosymmetric alignment of chromophore molecules. A chromophore molecule consists of a donor-acceptor that distribute π-conjugated electron system as shown in Figure 2-1. This π-conjugated system allows the electron transferred from the donor side to the acceptor side through a π-bridge in the middle. The donor, acceptor and π-bridge can be substituted by various chemical structures.

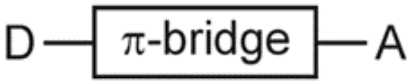

Figure 2-1 Donor-acceptor in the π-conjugated electron system [88]

To realise the nonlinearity of these chromophore molecules into a device layer, they must be doped into matrix materials. Polymers are a suitable choice of material for this purpose because the chromophore molecules can be well packed into the chain structure of a polymer, and the fabrication process of polymer layer onto a device is simple as compared to other forms of material [89-91]. Polymer systems are categorised by the point of view of the bonding and distribution types of chromophores [92]. Once they are turned into an EO device, each type of polymer will provide different level of molecular relaxation and glass transition temperature (T_g). These properties imply to a limitation of EO efficiency and long-term stability of that product. The polymer with high T_g and low relaxation effect is able to provide higher EO efficiency and longer temporal stability for the device. However, the long-term stability of EO polymer will be linked to the difficulty of molecular alignment (also called poling process) that will be explained later in this chapter.

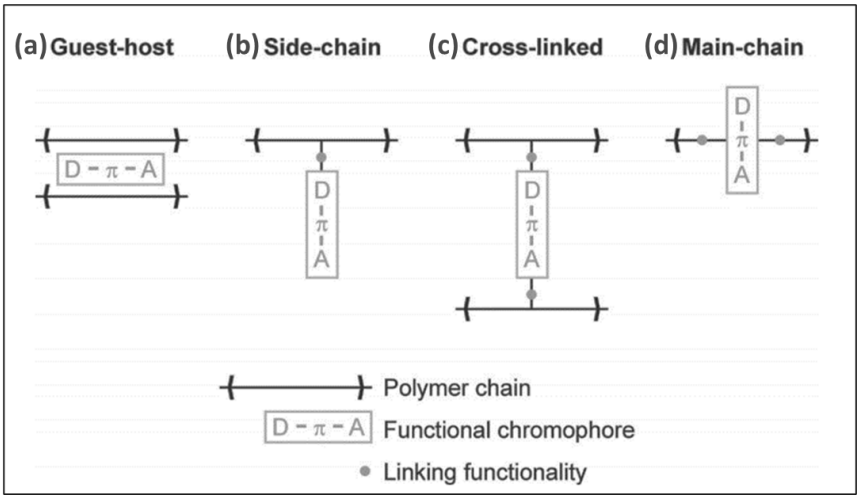

Figure 2-2 Schematics of the different packing types of EO polymer (a) guest-host, (b) side-chain, (c) cross-linked and (d) main-chain [89].

- **Guest-host:** The unattached chromophores (as guest) are physically mixed with a polymer host as shown in Figure 2-2(a). It has the advantages of simple polymer preparation and high relaxation of guest molecules in polymer host. On the other hand, due to unbinding between guest and host, the EO efficiency of this system is not guaranteed for a long-term stability by the relaxation effects. Another disadvantage is a light scattering led by high concentration of guest which causes dipole-dipole interaction and phase-separation.
- **Side-chain:** The chromophores are chemically attached to the backbone polymer as shown in Figure 2-2(b). This type of polymer is called side-chain. With the lower molecular relaxation as compared to the guest host system, a high concentration of chromophores can be incorporated into the backbone without phase-separation and aggregation. The motion of chromophores is obstructed by side-chain attachment, and its T_g is mostly higher than guest host system. Hence, its stability is higher than that of guest-host system with the same chromophore concentration.
- **Cross-linked:** The chromophores are linked to more than one polymer chain with covalent bonds as shown in Figure 2-2(c). This crosslinking makes the most long-term stable, but re-alignment of chromophore is not allowed in this polymer system. Whilst the polymer is not crosslinked, the chromophore molecules still be relaxed for easy alignment liked the side-chain. Its EO efficiency is similar to that of side-chain and main-chain and T_g is lower. However, the preparation must rely on a complicated process of chemical engineering.
- **Main-chain:** For the main-chain system, the chromophores become part of main polymer chain as shown in Figure 2-2(d). This system has improved the mechanical stability but low solubility because its molecular relaxation is more restricted. At the same time, it also has more difficult alignment of chromophores as compared to the side-chain. Additionally, its T_g is low compared to the side-chain because the main polymer chain has owned the low T_g

in chromophores. The EO efficiency of this system is not significantly different from side-chain, but the long-term stability is slightly lower than that of side-chain.

In summary, the advantages and disadvantages are rearranged to compare the important properties of these polymer systems as following:

Limited level of EO efficiency: Guest-host < Side-chain, Main-chain < Cross-linked

Long-term stability: Guest-host < Side-chain < Main-chain < Cross-linked

Difficulty of molecular alignment (poling): Guest-host < Side-chain, Cross-linked < Main-chain

Complexity of polymer preparation: Guest-host < Side-chain < Cross-linked < Main-chain

Therefore, the proper type of polymer system for this project which provide a relatively high EO effect and whilst retaining a relatively simple preparation process is the side-chain EO polymer.

2.2.1 Pockels Effect

EO effect refers to an optical phenomenon that presents changing optical properties of material, especially the refractive index, caused by an electric modulation field. If the refractive index is linearly changed proportional to the electric modulation field, this effect will be called the linear electro-optic effect or the "Pockels effect". On the other hand, the EO effect will be classified as another type, called the "Kerr effect" where it presents a nonlinear relation to the applied field. However, the non-centrosymmetric molecules in EO polymer can cause the domination of Pockels effect, so this report will focus on details of the Pockels effect observed in EO polymer.

The Pockels effect is a result of the second-order nonlinear optical phenomena due to the interaction between the electric modulation field $(\vec{E}_{mod})$ and the optical field $(\vec{E}_{opt})$in a material with non-zero of 2nd- nonlinear susceptibility $(\chi^{(2)})$. In case of EO polymer with this effect, the vector components of second-order nonlinear polarisation $(\vec{P}^{(2)})$ and net polarisation $(\vec{P})$ can be written by [89, 93]

$$P_i^{(2)}(\omega_l, \omega_h) = 2\varepsilon_0 \sum_{jk} \chi_{ijk}^{(2)} E_{opt,j} E_{mod,k} \quad (1)$$

and

$$P_i = P_i^{(L)} + P_i^{(2)}$$

$$= \varepsilon_0 \sum_j \chi_{ij}^{(1)} E_{opt,j} + 2\varepsilon_0 \sum_{jk} \chi_{ijk}^{(2)} E_{opt,j} E_{mod,k}$$

$$= \varepsilon_0 \sum_j \left(\chi_{ij}^{(1)} + 2\sum_k \chi_{ijk}^{(2)} E_{mod,k}\right) E_{opt,j} \quad (2)$$

where ε_0, $\vec{P}^{(L)}$and $\chi^{(1)}$ are the vacuum permittivity, the linear term of polarisation and the first-order optical susceptibility, respectively, and the indices $i, j, k \in \{\hat{x}, \hat{y}, \hat{z}\}$ denotes the three orthogonal coordinate system. By using Eq.(2), the component of optical displacement field $\vec{D} = \varepsilon_0 E_{opt,j} + \vec{P}$ can be expressed by

$$D_i = \varepsilon_0 E_{opt,j} + \varepsilon_0 \sum_j \left(\chi_{ij}^{(1)} + 2\sum_k \chi_{ijk}^{(2)} E_{mod,k}\right) E_{opt,j}$$

$$= \varepsilon_0 \sum_j \left(\delta_{ij} + \chi_{ij}^{(1)} + 2\sum_k \chi_{ijk}^{(2)} E_{mod,k}\right) E_{opt,j} \quad (3)$$

where δ_{ij} is the Einstein notation. By comparing to the definition of permittivity $\left(\vec{D} = \varepsilon_0 \varepsilon_r \vec{E}\right)$, the modulating relative permittivity ($\varepsilon'_{r,ij}$) can be defined by

$$\boldsymbol{\varepsilon'_{r,ij}} = \boldsymbol{\delta_{ij}} + \boldsymbol{\chi_{ij}^{(1)}} + \mathbf{2}\sum_k \boldsymbol{\chi_{ijk}^{(2)}} \boldsymbol{E_{mod,k}}$$

$$= \varepsilon_{r,ij} + \Delta\varepsilon_{r,ij} \quad (4)$$

where $\varepsilon_{r,ij} = \delta_{ij} + \chi_{ij}^{(1)}$ means an unperturbed relative permittivity, and the perturbation term is $\Delta\varepsilon_{r,ij} = 2\sum_k \chi_{ijk}^{(2)} E_{mod,k}$. To understand the definition of electro-optic coefficient, the electric impermeability ($\eta = \frac{1}{\varepsilon}$) must be introduced. The corresponding change of the impermeability is given by

$$\boldsymbol{\Delta\eta_{ij}} = \boldsymbol{\eta'_{ij}} - \boldsymbol{\eta_{ij}} = \frac{\mathbf{1}}{\boldsymbol{\varepsilon'_{r,ij}}} - \frac{\mathbf{1}}{\boldsymbol{\varepsilon_{r,ij}}} = \frac{-\boldsymbol{\Delta\varepsilon_{r,ij}}}{\boldsymbol{\varepsilon_{r,ij}}(\boldsymbol{\varepsilon_{r,ij}} + \boldsymbol{\Delta\varepsilon_{r,ij}})} \approx \frac{-\boldsymbol{\Delta\varepsilon_{r,ij}}}{(\boldsymbol{\varepsilon_{r,ij}})^2} \quad (5)$$

$$= -\sum_k \frac{2}{n_{ij}^4} \chi_{ijk}^{(2)} E_{mod,k} \equiv \sum_k r_{ijk} E_{mod,k} \quad (6)$$

where $r_{ijk} = -\frac{2}{n_{ij}^4}\chi_{ijk}^{(2)}$, $\varepsilon_{r,ij} = n_{ij}^2$, and n_{ij} is an unperturbed refractive index. The coefficient r_{ijk} are known as the linear electro-optic (Pockel) coefficient and can be written in a form of third-rank tensor. As a result of a symmetry in the impermeability tensor [94], η_{ij} are invariant to permutation of i and j. Thus $\Delta\eta_{ij}$ can have only six instead of nine (3^2) independent elements. It is conventional to rename this pair of indices (i, j) as a single index (l) by using the following definition:

$$\boldsymbol{ij}: \quad \boldsymbol{\hat{x}\hat{x}} \quad \boldsymbol{\hat{y}\hat{y}} \quad \boldsymbol{\hat{z}\hat{z}} \quad \boldsymbol{\hat{y}\hat{z} = \hat{z}\hat{y}} \quad \boldsymbol{\hat{x}\hat{z} = \hat{z}\hat{x}} \quad \boldsymbol{\hat{x}\hat{y} = \hat{y}\hat{x}} \quad (7)$$

l:	1	2	3	4	5	6

Therefore, the coefficient r_{ijk} can be replaced by r_{lk}, where $k = 1$ corresponds to $\hat{x}$, $k = 2$ to $\hat{y}$, $k = 3$ to $\hat{z}$. The Eq.(6) can be written in form of a matrix equation:

$$\begin{bmatrix} \Delta\eta_1 \\ \Delta\eta_2 \\ \Delta\eta_3 \\ \Delta\eta_4 \\ \Delta\eta_5 \\ \Delta\eta_6 \end{bmatrix} = \begin{bmatrix} r_{11} & r_{12} & r_{13} \\ r_{21} & r_{22} & r_{23} \\ r_{31} & r_{32} & r_{33} \\ r_{41} & r_{42} & r_{43} \\ r_{51} & r_{52} & r_{53} \\ r_{61} & r_{62} & r_{63} \end{bmatrix} \begin{bmatrix} E_{mod,\hat{x}} \\ E_{mod,\hat{y}} \\ E_{mod,\hat{z}} \end{bmatrix} \tag{8}$$

In case of EO polymers, it is typically assumed to be activated by the application of $\hat{z}$-direction electric field in the poling process. The electro-optic tensor can be formed with only two independent coefficients [95]:

$$r_{lk} = \begin{bmatrix} 0 & 0 & r_{13} \\ 0 & 0 & r_{13} \\ 0 & 0 & r_{33} \\ 0 & r_{13} & 0 \\ r_{13} & 0 & 0 \\ 0 & 0 & 0 \end{bmatrix} \tag{9}$$

Usually, the coefficient r_{33} is considerably larger than r_{13} by several times according to the direction of poling field [96-98]. To benefit from this advantage for modulator applications, the direction of applied e-field and optical field must be mainly aligned in the $\hat{z}$-axis and similar to the direction of r_{33}. For this specific case, the dominant impermeability change is $\Delta\eta_3$, and the rest of the terms can be ignored.

$$\Delta\eta_3 = r_{33}E_{mod,\hat{z}} \tag{10}$$

From Eq.(5) and (6) $$\frac{-\Delta\varepsilon_{r,\hat{z}\hat{z}}}{n_{\hat{z}\hat{z}}^4} = r_{33}E_{mod,\hat{z}} \tag{11}$$

Considering $\varepsilon_r + \Delta\varepsilon_r = (n_r + \Delta n_r)^2$ and using the approximation $\Delta\varepsilon_r \approx 2n\Delta n$ when $|\Delta n|$ is small, to obtain

$$\Delta n_{\hat{z}\hat{z}} = -\frac{1}{2}n_{\hat{z}\hat{z}}^3 r_{33}E_{mod,\hat{z}} \tag{12}$$

With the given condition having only the $\hat{z}$-component fields, the subscription index $\hat{z}$ can be abandoned.

$$\Delta n = -\frac{1}{2}n^3 r_{33}E_{mod} \tag{13}$$

In practice, this formula can be applied to calculate a modulated index change (Δn) in the EO polymer with the following conditions:

- The EO polymer is a homogeneous material (has a uniform distribution of chromophore molecules).
- The polymer is fully poled with a uniform electrical poling field that dictates a perfect uniformity of electro-optic coefficient r_{33}.
- The electrical modulation field and the optical field are entirely overlapped to each other within the polymer, and all the fields have only the component in the same direction to the poling field (the poling field dictates the orientation of chromophore dipole).

If we assume that the electrical modulation field is generated by an application of voltage (V) onto a pair of paralleled electrodes with gap distance d, the modulating field can be defined as $E_{mod} = \frac{V}{d}$. Thus, the modulated index change can be written as:

$$\Delta n = -\frac{1}{2} n^3 r_{33} \frac{V}{d} \tag{14}$$

2.2.2 Polymer Activation Process

In a EO polymer, a chromophore molecule act as a microscopic electric dipole moment leading to polarisation in a material and then presenting the Pockel's effect as described in previous sub-section. By taking a microscopic view as presented in Figure 2-3, an EO polymer containing a lot of chromophore molecules. Naturally, these molecules are randomly oriented by thermal energy as shown in Figure 2-3(a), also called an isotropic ordering. The molecular dipoles are cancelled out with each other, and thus a macroscopic electro-optic activity does not exist. Hence, the creation of a non-zero dipolar alignment is essential to produce an electro-optic effect in the EO polymer.

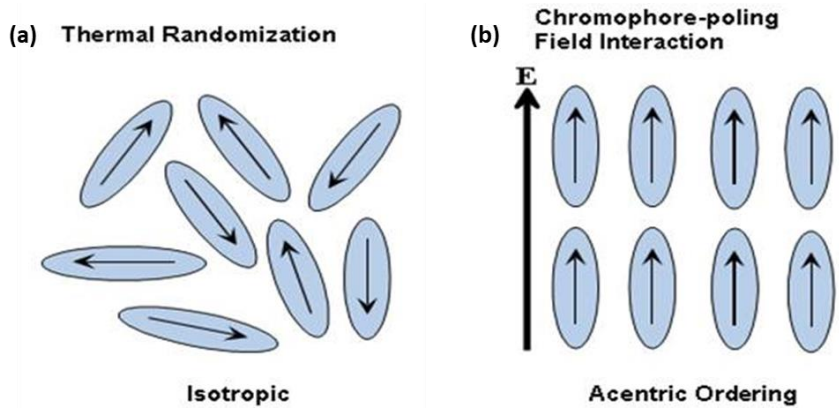

Figure 2-3 Dipole molecular ordering: (a) Acentric ordering, (b) Isotropic ordering. Figure adapted from [99].

To induce acentric ordering of dipolar chromophores as shown in Figure 2-3(b), the EO material must be heated up to the glass transition temperature (T_g) and exposed to a strong static

electric field. This process of molecular alignment is called a "Poling process". Although there are various techniques for poling an EO polymer[100], electrode contact poling and corona poling are the two most common techniques of chromophore poling process.

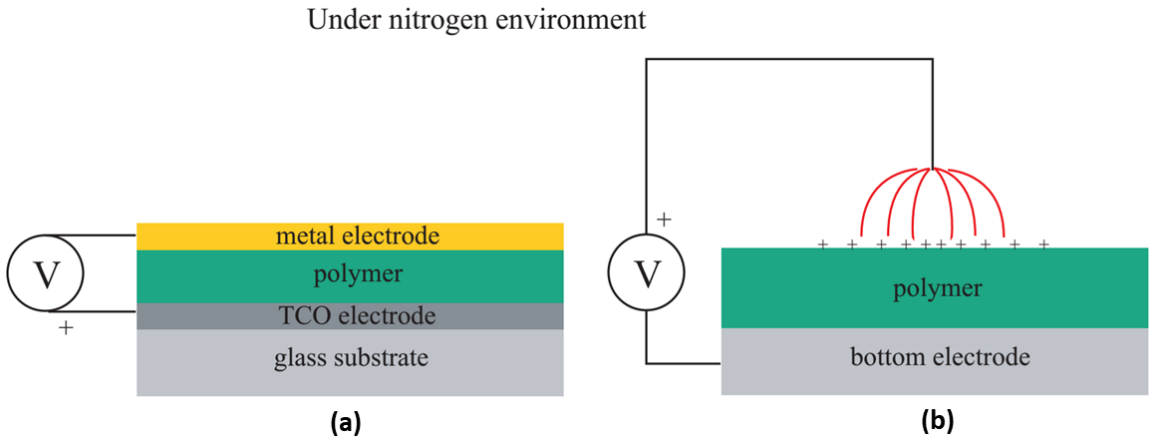

Figure 2-4 Schematics of polymer poling technique: (a) Electrode contact poling. [90] (b) Corona poling.

- **Electrode contact poling**: The setup of this technique consists of the polymer layer in the middle of sandwich-electrode as shown in Figure 2-4(a). The sandwich-electrode is applied by a high voltage and thus the polymer layer is placed in the region of strong electric field. The advantage of this technique is the uniformity of applied field, and the electrode can be expanded for a large area or patterned for a local field application. Due to the direct contact of electrode to the polymer, the breakdown voltage of polymer limits the maximum applied voltage. Moreover, the polymer layer can be damaged by a leakage current due to defects in polymer layer [101].
- **Corona poling**: The setup of this technique is illustrated in Figure 2-4(b). An electrode is attached to the bottom of the polymer layer. There is a top electrode in the form of needle or wire which is placed above the layer to be poled. Once the air breakdown voltage is applied between the top and bottom electrodes, the ions are formed around the tip of top electrode and induce the accumulated charge on surface of polymer layer. The poling field is generated across the layer. By using this technique, the leakage current is very low as compared to the electrode contact poling. On the other hand, the strength of poling field is complex for calculation.

To simplify the fabrication process, the poling electrodes were designed to be in line with the polymer layer. Therefore, the design of device in this project relies on the electrode contact poling technique. The details of sample design are discussed in chapter 3.

2.2.3 Reviews of Well-known Polymer

As discussed previously, EO polymers with side-chain structure are the preferred choice for this project owing to its large EO efficiency, good stability, and relatively simple synthesis and poling process. In this subsection, side-chain EO polymers are reviewed with various chemical formulae of chromophore and polymer backbone.

2.2.3.1 Disperse Red 1 Based EO Polymer

Dispersed Red 1 (DR1) is one simple type of chromophores that was widely used in the early stage of development on the EO polymer modulator. Several synthesis processes of DR1 based EO polymer has been reported with the EO coefficient (r_{33}) up to 12 pm/V [102-108]. Moreover, the DR1 based polymer with side-chain structure is well known and can display a much better long-term stability than another with a guest-host structure [109]. The two kinds of polymer that are mostly used as a polymer backbone for this side-chain structure are polymethyl methacrylate (PMMA) and amorphous polycarbonate (APC).

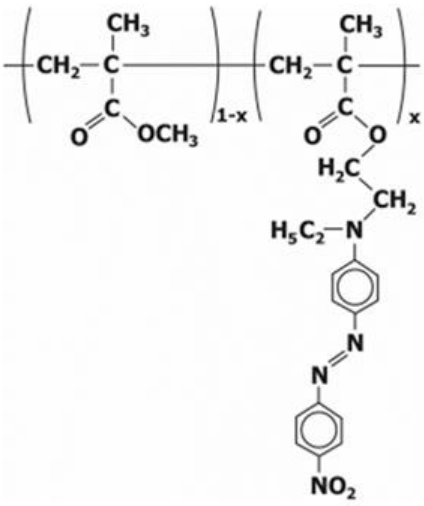

Figure 2-5 Chemical structure of side-chain PMMA-co-DR1 polymer.

PMMA based EO polymers are some of the most promising material for the application of EO modulators. The main reason is that PMMA is widely applied into a lot of applications for thin films and waveguides, so the fabrication processes and recipe are already well developed. The optical transparency of PMMA is also compatible with telecommunication wavelengths. The chemical structure of the side-chain PMMA-co-DR1 polymer is shown in Figure 2-5. this structure has been reported to have a refractive index of ~ 1.6 and a glass transition temperature around 132°C [110]. The major advantage of PMMA-co-DR1 is few steps of synthesis and a low price, as DR1 has been widely used in dyeing and printing industry.

2.2.3.2 FTC Chromophore Based EO Polymer

Phenyl vinylene thiophene vinylene (FTC) is another kind of chromophore which is vastly used in the preparation of EO polymer. FTC molecule consists of three parts of common chromophore structure (as described in section 2.2) liked DR1, but they have been improved in regard to their polarising ability. Due to the long π-bridge and the large electron withdrawing ability of acceptor, the EO polymer based FTC can display a strong temporal stability and high r_{33} of 36 pm/V [105]. To increase the EO effect, a large number of chromophores-based FTC have been developed by modifying an electron acceptor structure. AJL8 is well known as an improved FTC with very high EO coefficient with an r_{33} of 94 pm/V [111]. Furthermore, FTC based chromophores have also been modified in their electron donor structure and have been synthesised with an improved EO property. They exhibit a r_{33}value up to 150 pm/V and showed a high T_g that imply a further increment of device stability. There are also a number of FTC chromophore with modification for improving a specific property of EO polymer. The chemical structures of standard and enhanced FTC based chromophore are shown in Figure 2-6.

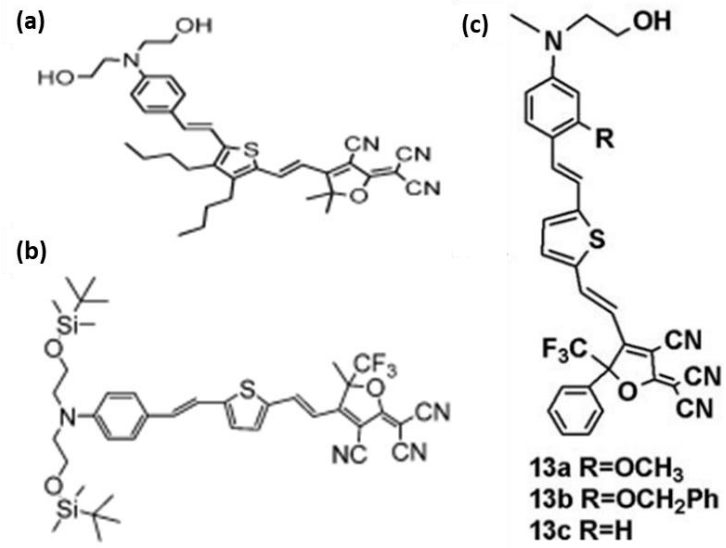

Figure 2-6 Chemical structures of FTC based chromophore: a) standard FTC chromophore b) AJL8 chromophore and c) modified electron donor in FTC chromophore.

2.2.3.3 EO Polymers with Dendrimer Chromophores

The molecular structures of chromophore that are reviewed above have been defined as dipolar molecules. When the dipolar molecules are highly polarised by the poling electric field, the dipole-dipole interaction obstructs the poling process to perfectly align chromophores in EO polymer [112]. The dendritic structure has been introduced into the development of chromophore because the presence of void in this structure can help to reduce the interaction between chromophores. Therefore, the poling process can be more efficient in the dendrimer than traditional structures. On the other hand, the dendrimer-based chromophores reported a relatively low r_{33} of only about 80

pm/V. However, remarkable efficiency has been reported when the EO polymer with a mixture of dendrimer and dipolar chromophores was synthesised. Novel chromophore exhibits a r_{33} value of almost 200 pm/V [113]. The dendrimers show a large EO efficiency and can still be improved, nevertheless, the preparation process is substantially more complex and require a number of chemical precursors.

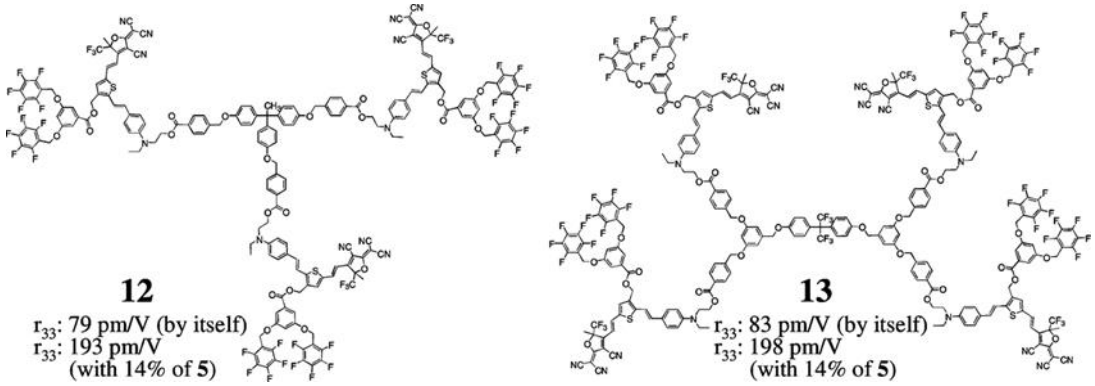

Figure 2-7 Chemical structures of dendrimer chromophore and their EO coeffient [114].

2.2.4 Summary

The simple DR1 chromophore is a commercial chemical that help to ease the preparation process. However, the EO coefficient is relatively low comparing to the other types. This can be an obstacle in future applications as the size of modulator is required to be scaled down. On the other hand, the dendrimer chromophore is difficult to synthesise and prepare. They might require a substantial development time to obtain a suitable chemical process; on the other hand, they can provide a very large EO efficiency. FTC based chromophore is therefore a suitable research choice in this project and provide further flexibility for further molecular modification linked to stability and EO increase.

2.3 Waveguide Designs in Phase Modulator

The major advantages of EO polymer-based modulators are a high modulation performance and simple fabrication process. These properties are directly derived from the type of polymer and the architecture that are used to design and fabricate the waveguide in the modulator. To modulate the signal by using the EO polymer-based modulators, interaction between guided optical signal and modulated signal is the important factor to be considered. In the optical modulator, the optical signal can be modulated by changing their optical properties such as the effective index. Therefore, in this work, an EO polymer will be introduced into the modulator to act as the index changing due to an applied electric field. The different in the design of optical waveguide in the modulator leading to the different in the interaction between optical mode in the waveguide and EO polymer resulting in

the different in modulating performance. Thus, in this section, the design of waveguide with different structure for EO polymer-based modulators will be reported.

2.3.1 Reviews of Existing Design

2.3.1.1 EO polymer in strip and rib waveguide

Usually, an EO polymer can be introduced to be a modulating medium with two simple approaches. Firstly, the EO polymer can be used as a core material as depicted in Figure 2-8(a-b). In 2005, a three layers of polymer slab waveguide have been demonstrated for the metal-defined EO polymer phase modulators [115]. In this work, a metal film has been deposited on top of the upper cladding. A non-perfect bonding of metal film on a polymer substrate subject to an induce tensile strain in polymer waveguide. The signal modulation will be achieved by varying the induced strain in the EO polymer waveguide resulting in the changing of refractive index due to the photoelastic effect of polymer. The second is the modulator designed with EO polymer cladding as shown in Figure 2-8(c-e). The rib [116, 117] or strip [118] waveguides are normally use as an optical guiding medium with the EO polymer cladding. With these structures, the signal can be modulated by changing the refractive index of polymer cladding.

These designs have different advantage and drawback. The design with EO polymer as core provides a large interaction region between optical signal and electric modulating field, but it can also exhibit a high propagation loss. On the other hand, the design with EO polymer as cladding provides low loss but result in a low EO effect as well.

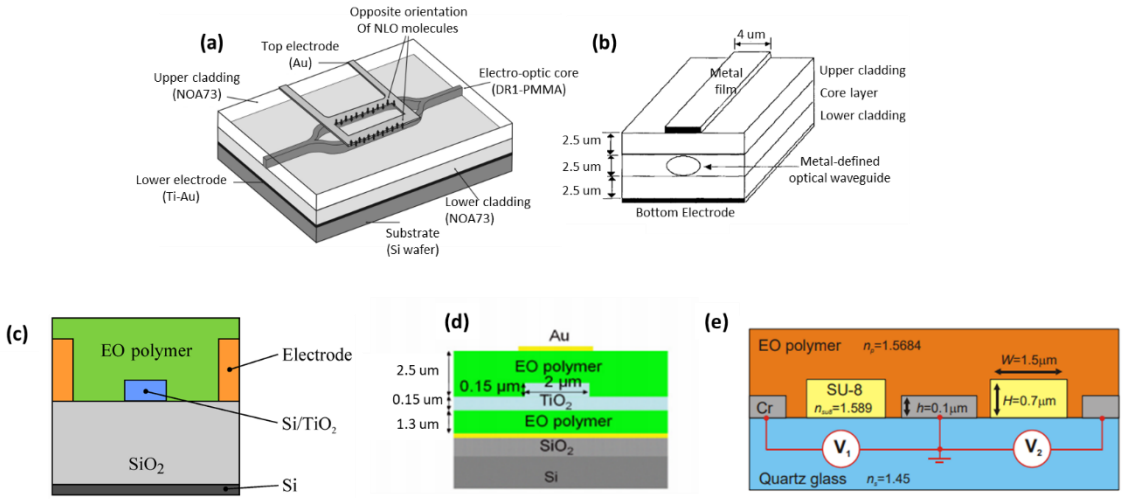

Figure 2-8 Schematics of MZI modulator with difference in design of core and cladding material: (a) The EO polmer is used as core [37, 115]. (b-d) The EO polymer is used as cladding of waveguide [110, 117, 118].

2.3.1.2 EO polymer in slot waveguide and strip-loaded slot waveguide

To increase the performance of this modulator type, an improved design of the modulating waveguide is to introduce a large interaction area between an optical mode with the modulated signal with a low loss waveguide. The slot waveguide and strip-loaded slot waveguide were chosen for this purpose. For this waveguide design, the optical field is confined mostly in the slot filled with EO polymer as shown in Figure 2-9(a). So, the EO polymer modulator using these waveguides require a low electric field strength to induce a change of polymer index. The use of polymer phase modulator based on silicon slot waveguide with ring resonator structure has been reported in 2005 [119]. In 2008, silicon slot waveguide with nonlinear polymer cladding was proposed and a $V_\pi \cdot L$ of 0.5 V·cm has been reported [120]. Double slotted waveguide for EO polymer modulators have been proposed in 2015 by using TiO_2 waveguide as presented Figure 2-9(b) [56]. By comparing the result from TiO_2 waveguide with single-slot, it becomes clear that the EO effect is significantly enhanced in the double-slot configuration than the single-slot and a V_π of 1.6 V was achieved. For this device, a $V_\pi \cdot L$ below 1 V·cm was demonstrated but an optical insertion loss above 35 dB was measured. The performance of EO polymer modulators based on an Si slot waveguide has been reported with V_π = 1.2 V, $V_\pi \cdot L$ = 2.1 V·mm when the modulation frequency up to 100 GHz at the operating optical bandwidth over C-band (1520-1580 nm) was used[121]. The drawback of this structure is the low voltage dropped across the slot if the resistance of waveguide material is relatively high compared to EO polymer. This problem can be solved by using a vertical electrode design as presented in Figure 2-9(c-d). For this design, the waveguide will be placed parallelly in vertical direction instead of horizontal direction as the general slot waveguide. EO polymer layer will be deposited in between two waveguides to act as the guiding medium for guided modal in the waveguide. By using the vertical slot waveguide for EO polymer modulator, the low $V_\pi \cdot L$ of 0.66 V·cm was achieved in 2018 [122]. Although the EO polymer modulator based vertical slot waveguide showing the lower $V_\pi \cdot L$ when comparing with horizontal slot waveguide, the complexity in fabrication of vertical slot waveguide cannot be avoided.

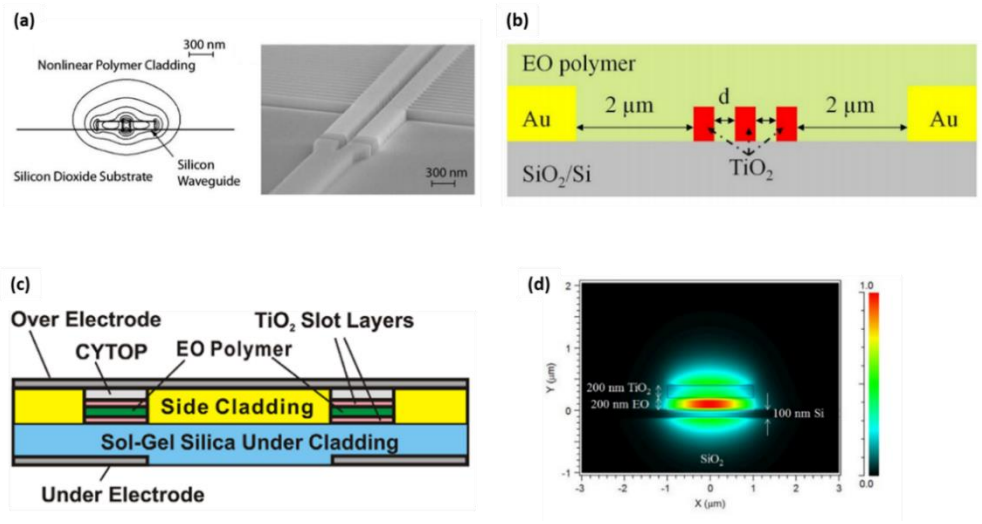

Figure 2-9 (a) Structure of EO polymer modulating waveguide with a slot waveguide structure [120]. (b)) Schematic the EO polymer filled TiO_2 double-slot modulator when d =150 nm [56]. (c) Schematic and (d) Modal simulation profile of vertical slot waveguide modulators [122, 123].

As presented in sub-section 2.2.2, poling process can be done by applying a strong static electric field through the EO polymer in the direction of desired electric field of optical mode in the waveguide. In general, the electrode contact poling technique has been used for the slot waveguide by placing the waveguide in between two electrodes. The applied voltage use for poling process is depend directly on the distance between two electrodes. Thus, the shorter distance resulting in the lower voltage needed for chromophore alignment. So, another type of slot waveguide, strip-loaded slot waveguide, has been developed for this propose. It is the slot waveguide where the waveguides have the strip which will be connected with the metal contact as presented in Figure 2-10(a-b). Therefore, the waveguide itself can act as the metal electrode for poling process. So, the distance for poling the polymer filled in the slot waveguide will be the distance of slot gap which is very small compare with the conventional slot waveguide structure. Although the strip-loaded slot waveguide has the advantage over the conventional slot waveguide in terms of the small poling distance, the dielectric material such as SiN cannot be used to fabricate the waveguide which is limited the number of materials for waveguide fabrication.

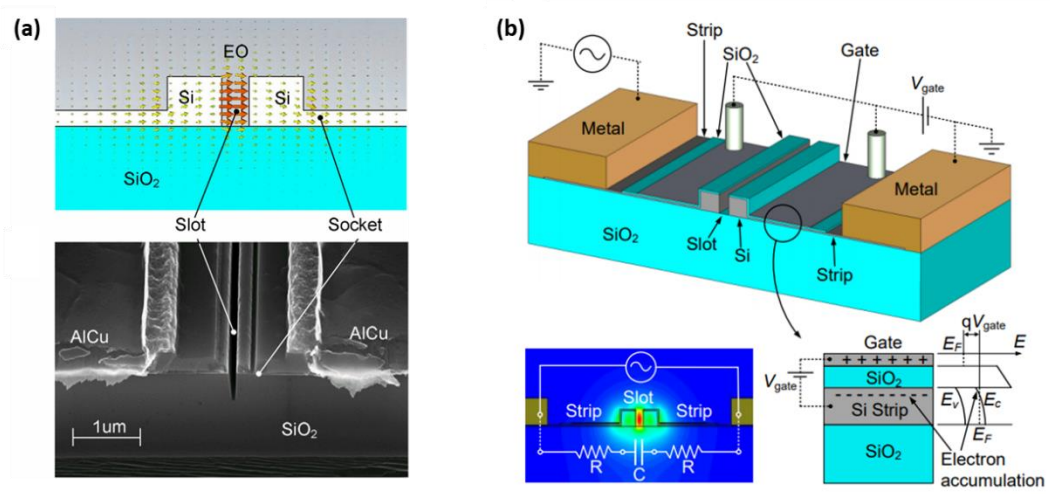

Figure 2-10 (a) The schematic and scanning electron microscope image of silicon strip-load slot waveguide [22]. (b) The connection of the optical active region with metal electrodes by means of thin silicon strips. On top of the silicon strips an SiO2 film is deposited and covered with the gate electrode [124].

Due to the different structure of slot waveguides compared to normal waveguides, their optical mode profiles are also different. Hence, the optical mode converter is required to take this account for reducing an insertion loss [125].

2.3.1.3 EO polymer in photonic crystal waveguide

The photonic crystal structure has been proposed to improve the performance of EO modulator. By using the property of low group velocity in photonic crystals, the modulating length and the operating voltage can be reduced. Figure 2-11 shows the structure of slot integrated photonic crystal waveguide in Mach–Zehnder interferometer (MZI) modulator. The highest performances of modulators with this design have been reported for a very low V_π 0.97 V and $V_\pi \cdot L$ 0.29 V·mm at modulation frequency of 100 kHz across wavelength 1544 -1560 nm [21, 121, 126]. The reported results also reflect to the disadvantage of photonic crystal structure. The modulation speed is limited to the index dispersion of photonic crystals, and the narrow optical bandwidth is also their unique property.

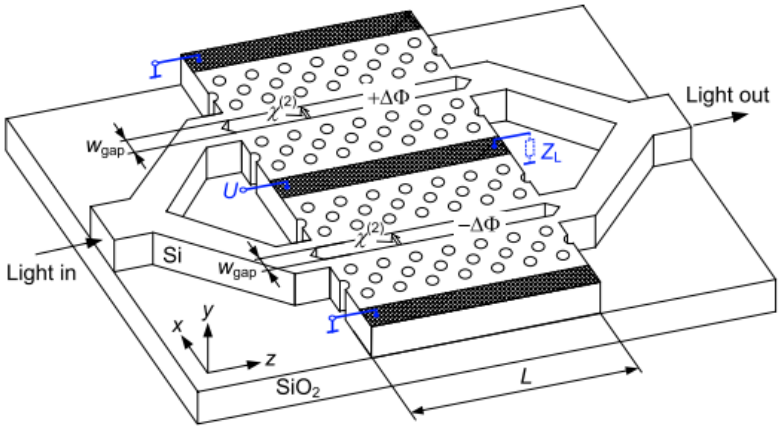

Figure 2-11 Schematic of MZI modulator with structure of slot integrated photonic crystal waveguide [127].

2.3.1.4 EO polymer in plasmonic slot waveguide

The term of "plasmonics" states the study of interaction between electromagnetic wave and conduction electron in a metal. The original study of this phenomena was focused on the excitation and oscillation of free electrons by coupling photons onto the interface between metal and dielectric. The coupled electromagnetic waves are localised near the surface and propagate along the interface, it is called a surface plasmon-polaritons (SPPs). SPPs or plasmonic modes has been known for decades [114], however, there has been renewed interest and a rapid development of research in silicon photonics area because of the localisation of guiding the light in subwavelength structure beyond the diffraction limit. Several types of metallic structures have been proposed for guiding light in plasmonic modes, including a thin metal film, an array of metal nanoparticle or nanowire[128-131], a metal groove[132], a metal nanostrip[133] and a metallic slot structure[134, 135]. However, it needs to be realised that such geometries of overlayer metallic structures can be used to confine a guided mode within a subwavelength area. To achieve a subwavelength localisation for a modulator design, the metal slot waveguide is the only structure that has been used to play roles of both highly confined waveguide and modulating electrode at the same time.

Due to the high field intensity at the metal surface, the propagation loss of plasmonic mode is a trade-off for high confinement of plasmonic slot waveguide (PSW) as shown in Figure 2-12(a). Consequently, the propagation length (L_p) of plasmonic mode is an essential characteristic of plasmonic slot waveguides which indicates the propagation distance that the plasmonic mode will decrease its power to $1/e$ times of the original power. This length is proportional to a gap size and a metal slot height as shown in Figure 2-12(b).

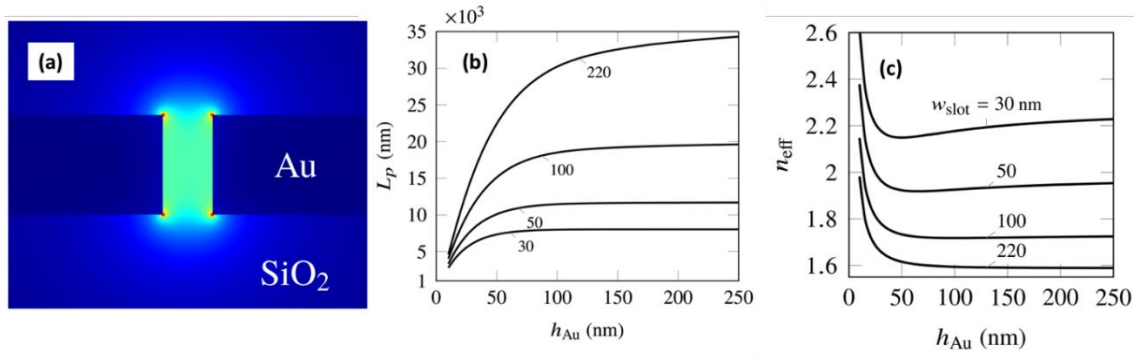

Figure 2-12 (a) Plasmonic mode in a metal slot waveguide, (b-c) Propagation length (L_P) and effective index at 1,550nm as a function of slot height (h_{Au}) for plasmonic gold slot at variation of slot width (w_{slot}) = 30, 50, 100 and 220nm and [136].

The propagation loss can be reduced by increasing a slot width, but the confinement is also decreased as shown in term of effective index in Figure 2-12(c). At a certain slot width, there is a threshold of thickness for achieving a maximum propagation length. Even though the slot height keeps increasing above the threshold, the propagation length would not have much enhancement. Hence, these factors require the optimisation depending on a requirement of target design.

Apart from the photonic-plasmonic coupling efficiency, the major advantage of PSW is happened from the high optical confinement inside the slot. Moreover, the metal slot can play a role of electrical electrode at the same time and that also allows the high frequency modulating signal to occupy in the region perfectly overlapping with the optical field as shown in Figure 2-13. This is the key factor of PSW structure to enhance the modulating efficiency with the low applied voltage and power because the small width of electrode gap directly affects to reduce the RC-time constant which is inversely proportional to the modulation bandwidth [137]. The simulation of modal confinement in PSW showing that this structure is a promising device for EO polymer phase modulator due to the high confinement of optical modes in polymer and small width of electrode gap. But the fabrication process of PSW requires a high accuracy in terms of structure dimensions and alignment leading to complication with the deposition of a very thin photoresist with a long length to generate the plasmonic slot.

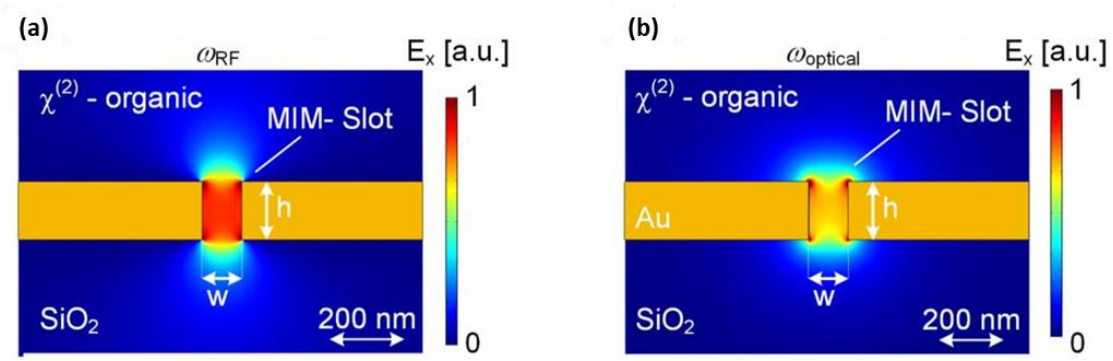

Figure 2-13 (a) The cross section with high frequency modulating field and (b) the optical field in the plasmonic slot waveguide.

2.3.2 Slot Waveguide

Various design of the optical waveguides for the fabrication of EO polymer phase modulator as presented in section 2.3.1 showing that each design has different advantage and disadvantage. By considering the large interaction between guided optical modes with the EO polymer, the complexity of fabrication steps, and the possibility to use high frequency modulation, horizontal slot waveguide is the best candidate among the others. In this sub-section, the physical background of slot waveguides will be discussed. The design of possible cross sections is presented with strong considerations of the feasibility of fabricating such structures.

Guiding mechanism for the conventional waveguide is based on total internal reflection (TIR) in a high index material (core) which is surrounded by a low index material (cladding). In this case, the guided modes of light are strongly confined in the high index region. A slot waveguide is an optical waveguide where the guided modes of light is strongly confined in a subwavelength-scale low refractive index region by TIR of external reflection. A slot waveguide consists of two strip or slab waveguides of high refractive index (n_{high}) materials separated by a subwavelength-scale low refractive index (n_{low}) slot region, surrounded by cladding materials with a lower refractive index (n_{clad}), as shown in Figure 2-14(a-b).

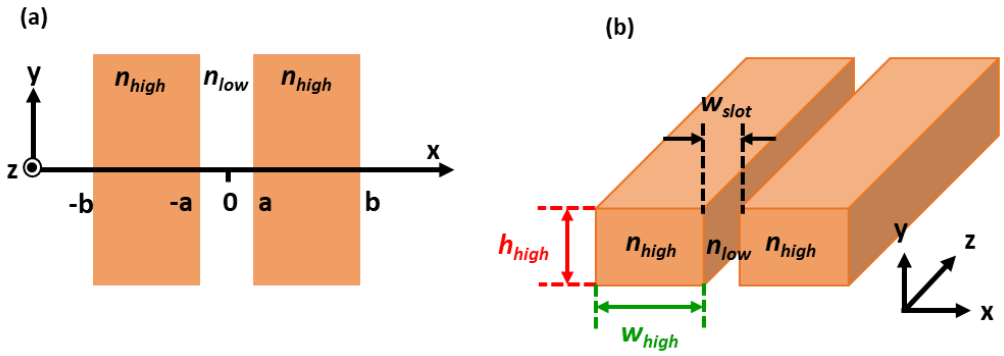

Figure 2-14 Schematic of the slot waveguide structure (a) with infinite height and (b) with finite height.

The principle of light guiding in void nanostructure has been proposed in 2004 by Almeida *et al.*[138]. Before this year, several waveguide structures have been proposed to guide or enhance light in low index materials, depending on external reflections provided by interference effects. Unlike TIR, the TIR based external reflection cannot be perfectly unity; therefore, the modes in these structures are inherently leaky modes. In addition, since interference is involved, these structures are strongly wavelength dependent.

Maxwell's equations state that, to satisfy the continuity of the normal component of electric flux density $D_{\perp}$, the corresponding electric field (E-field) must undergo a large discontinuity with much higher amplitude in the low index side for the high index contrast interface (Figure 2-15(a)). The strong field confinement in slot waveguides is a result of the continuity of the $D_{\perp}$ component of the electric displacement field perpendicular to an (uncharged) interface between gap (low index) and strip waveguides (high index) as shown in Figure 2-15(b). For materials with different permittivity (ε), a discontinuity of the normal component of the electric field $E_{\perp}$, can be express below:

$$D_{\perp,low} = D_{\perp,high} \tag{15}$$

$$\varepsilon_{low} E_{\perp,low} = \varepsilon_{high} E_{\perp,high}$$

$$E_{\perp,low} = \frac{\varepsilon_{high}}{\varepsilon_{low}} E_{\perp,high}$$

$$E_{\perp,low} = \frac{n_{high}^2}{n_{low}^2} E_{\perp,high} \tag{16}$$

where the indices "low" and "high" refers to the refractive index of gap and strip waveguides, respectively. The Eq. (16) can be achieved when the relationship $\varepsilon = n^2$ is employed. For the SiN slot waveguide, the electric field at the SiN/EO polymer interface is thus enhanced by $\frac{n_{SiN}^2}{n_{polymer}^2}$ within the polymer gap. This enhancement however decays exponentially with the distance from the interface. In a slot waveguide, two symmetric interfaces are separated closer than the decay length, which results in a nearly constant high field over the full slot region. The key parameter in designing a slot waveguide is to optimise the distance between two waveguides (gap width) and the dimension of waveguides (width and height) to achieve maximum power confinement in low index material (polymer).

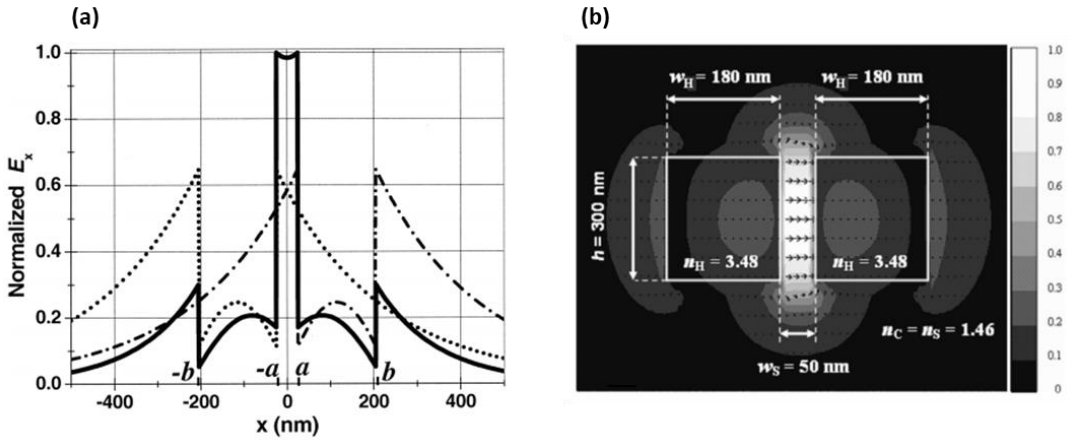

Figure 2-15 (a) Normalized transverse E-field (Ex) distribution of the fundamental TM eigenmode (solid curve) for the slab-based slot waveguide at λ = 1.55 μm [138]. (b) Contour of the E-field amplitude and the E-field lines in the slot waveguide [138].

2.3.3 State of The Art

In Table 2-2, the comparison of phase modulator characteristic shows pros and cons of each design. The simplest design with EO polymer cladding on conventional waveguide has been demonstrated very high figure of merit because of a small overlapping area between an optical mode and an applied electric field. The design with EO polymer in the core can provide a much lower figure of merit while the ring resonator design can give a large bandwidth of 10 GHz but operates in a narrow range of wavelength. With the design of doped silicon slot waveguide, the modulation frequency can be risen to the limit about 100 GHz due to the limitation by RC-time delay. The photonic crystal structure has been used to reduce a voltage-length factor ($V_\pi \cdot L$) by employing the slow light effect, moreover, its operating spectrum range is also limited by the RC time delay as well. Finally, the plasmonic slot provides the enhancement in both high modulation frequency and low figure of merit.

Table 2-2 The characteristic comparison of phase modulator based on EO-polymer modulator SiN waveguide with different designs.

Structure of phase modulator	**Waveguide material**	**EO efficiency of polymer r_{33} (pm/V)**	**Modulation frequency**	**Modulation figure of merit $V_\pi \cdot L$ (V·cm)**	**Insertion loss (dB)**
Waveguide with EO polymer core [139]	Side-chain polymer (DR1-PMMA)	12.6	4 GHz	5.2	-
Waveguide with EO polymer cladding [110]	Silicon nitride	1.7	1 KHz	900	-

Ring resonator with EO polymer cladding [60]	Silicon nitride	30	10 GHz	-	-
Slot waveguide [22]	Silicon doped with arsenic (10^{17} cm^{-3})	18	100 GHz	11	11
Photonic crystal slot [22, 140]	Silicon doped with phosphorus (10^{17} cm^{-3})	74	100 KHz	0.345	7
Plasmonic slot [21]	150 nm-thick gold	180	75 MHz - 170 GHZ	0.008	8

2.4 Mach-Zehnder Modulator

2.4.1 Mach-Zehnder Interferometer

Mach-Zehnder interferometer (MZI) is one of common waveguide structures which is used as an infrastructure of several EO polymer phase modulators [21, 42, 125, 141-143]. In general, The MZI consists of one input waveguide that is split into two phase modulating arms and then recombined again to an output waveguide as shown in Figure 2-16 [140]. Once the optical signal is launched into the input waveguide and split, they start with the same phase at the beginning of the two waveguides. If one of modulating arms has a different characteristic of optical path to the other, the recombination of them at the output waveguide is not a completely constructive interference. For example, the output will be destructive interference if there is a different optical path of half-wavelength (as be equal to a phase difference of π and also called an out-of-phase signal) as depicted in Figure 2-16(bottom). This is a basic concept for modulating optical signal with MZI structure.

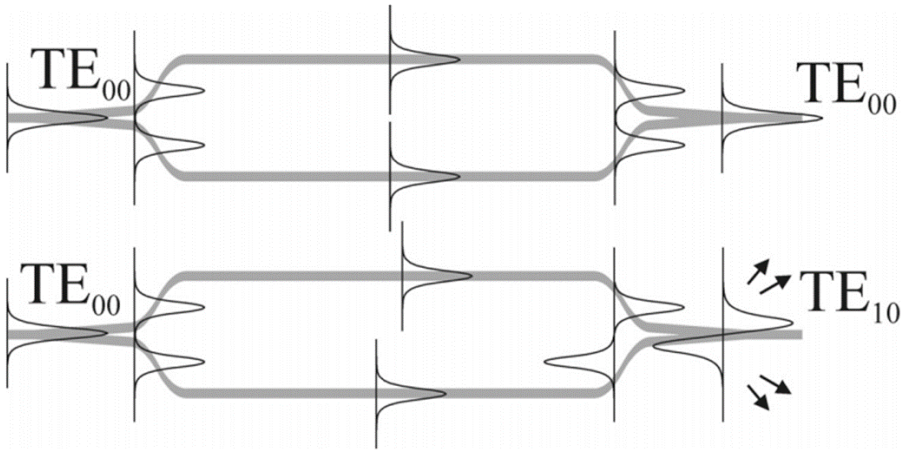

Figure 2-16 Schematic of modulator based on Mach-Zehnder interferometer [144].

The difference in optical phase ($\Delta\phi$) between the lights propagating in modulating arm can be calculated by

$$\Delta\phi = \frac{2\pi}{\lambda}\left(n_{eff,1}L_1 - n_{eff,2}L_2\right) \tag{17}$$

where $n_{eff,1}$, $n_{eff,2}$, L_1 , and L_2 are the effective index and length of each modulating arm, and λ is the wavelength of optical signal. The recombined intensity at the output waveguide (I_{out}) can be written in term of the input intensity (I_{in}) and phase difference ($\Delta\phi$) as

$$I_{out} = 2I_{in}\left(1 - cos(\Delta\phi)\right)$$

$$I_{out} = I_{in}cos^2\left(\frac{\Delta\phi}{2}\right) \tag{18}$$

However, the beam splitter in practical MZI device always has some certain level of splitting imbalance which is represented by γ factor. The γ factor is a ratio of split powers between MZI arms and must be less than 1. As a result of imbalance in splitter, the MZI will never give a perfect zero output at the wavelength with destructive interference condition. This results in the appearance of the extinction ratio (ER) which is related to γ factor via the equation $ER = \left(\frac{1+\gamma}{1-\gamma}\right)^2$. The function to represent the MZI output with splitting imbalance can be derived by starting from a basic formula of MZI output optical field (E_{out}):

$$\begin{aligned} E_{out} &= E_{arm1} + E_{arm2} \\ &= E_{in}\left(\frac{1}{1+\gamma}\right)e^{-i\phi_1} + E_{in}\left(\frac{\gamma}{1+\gamma}\right)e^{-i\phi_2} \end{aligned} \tag{19}$$

where $E_{arm1}$and E_{arm2} are the optical field propagating through each MZI-arm, E_{in} is MZI input field, and ϕ_1 and ϕ_2 are the optical phase of $E_{arm1}$and E_{arm2}, respectively. The MZI output transmittance (T_{MZI}) can be given by:

$$\begin{aligned} T_{MZI} &= \left|\frac{E_{out}}{E_{in}}\right|^2 \\ &= \left|\left(\frac{1}{1+\gamma}\right)e^{-i\phi_1} + \left(\frac{\gamma}{1+\gamma}\right)e^{-i\phi_2}\right|^2 \\ &= \left(\left(\frac{1}{1+\gamma}\right)e^{-i\phi_1} + \left(\frac{\gamma}{1+\gamma}\right)e^{-i\phi_2}\right)\cdot\left(\left(\frac{1}{1+\gamma}\right)e^{i\phi_1} + \left(\frac{\gamma}{1+\gamma}\right)e^{i\phi_2}\right) \end{aligned}$$

$$= \left(\frac{1}{1+\gamma}\right)^2 + \left(\frac{\gamma}{1+\gamma}\right)^2 + 2 \cdot \left(\frac{1}{1+\gamma}\right) \cdot \left(\frac{\gamma}{1+\gamma}\right) \cdot \cos(\Delta\phi)$$

$$= \frac{1^2+\gamma^2}{(1+\gamma)^2} + \frac{2\gamma}{(1+\gamma)^2}\cos(\Delta\phi)$$

$$\therefore \quad T_{MZI} = \left(\frac{1-\gamma}{1+\gamma}\right)^2 + \frac{4\gamma}{(1+\gamma)^2}\cos^2\left(\frac{\Delta\phi}{2}\right) \quad \text{or} \quad = \left(\frac{1}{ER}\right)^2 + \frac{4\gamma}{(1+\gamma)^2}\cos^2\left(\frac{\Delta\phi}{2}\right) \tag{20}$$

where $\Delta\phi$ represents the total phase difference between the MZI arms.

To consider the Eq. (17), we can do the modulation on either effective index (n_{eff}) or waveguide length (L) in order to change the phase difference. However, the modulation on waveguide length is almost impossible for a waveguide in practical devices because it is already fixed by the design and fabrication. Hence, the phase modulation by changing an effective index is therefore a common method for MZI based modulators.

The designs of modulator in this project will be based on the MZI structure, but the phase difference in this modulator will be generated by using the different length of modulating arms and the change in effective index. Initially, the phase offset is setup by the different length of modulating waveguides. This design is usually called an asymmetric MZI, and the output spectrum presents an interference pattern. Additionally, the pattern in spectrum can be shifted by changing the effective index of modulating arm. Figure 2-17 shows the shifting spectra of asymmetric MZI modulator by changing in effective index of modulating waveguide.

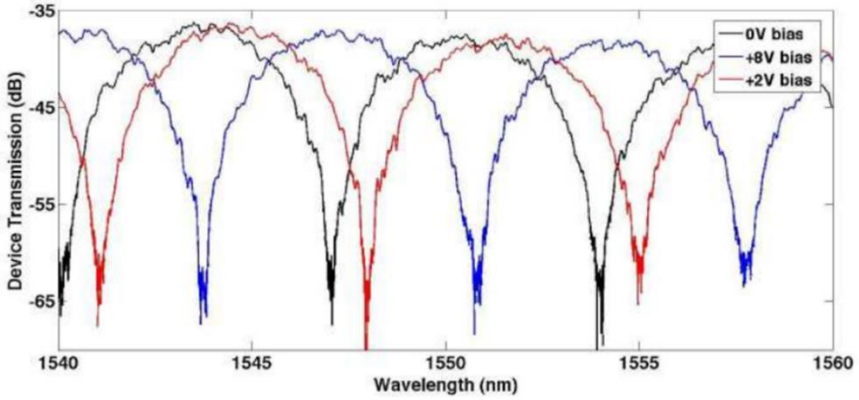

Figure 2-17 The shifting of output spectrum in asymmetric MZI due to the change in effective index of modulating waveguide by application of bias voltage across the waveguide [144].

2.4.2 Coplanar Waveguide Electrode

Transmission line for the electrical signal is one of the fundamental passive components at high frequency modulator. For optical modulator, the electrical signal should co-propagate with the optical signal. To minimise the transmission loss of the electrical line, these two signals should have

velocity minimal mismatch. Therefore, the design and structure of transmission line is the important parameters to be considered for the optical phase modulator.

Optical phase modulator based on Mach-Zehnder interferometer is a promising component for high speed and broadband optical communication system. A coplanar waveguide (CPW) is a transmission line structure that has often been used as a travelling-wave electrode for the MZI phase modulator owing to its advantage over a microstrip line structure. The microstrip line structure is the electrical electrode where the ground plane and the signal conductor are on the opposite side of the substrate. Since the ground plane lied on one side of the substrate while the signal conductor is applied on the other side, the electric field penetrate completely into the substrate resulting in a high loss in substrate. The CPW was firstly introduced in 1969 by C.P. Wen [145]. Since then, the transmission line with CPW has become a mainstream structure as the substrate loss is not dominating due to the ground plane and signal conductor being on the same side of the substrate and being separated by a gap. The electric field in CPW is concentrated in the gap (between signal and ground plane) and thus the field does not completely penetrate into the substrate resulting in less interaction between the field and substrate. Therefore, the characteristic impedance and phase velocity mostly depend on the CPW dimensions (thickness, width and gap) rather than the substrate thickness. Moreover, the simplification in the fabrication of the CPW as the ground and signal conductor are on the same side leading to the compatibility of this structure of transmission line with the CMOS fabrication process. The CPW is also flexible by enabling different characteristic impedance through the variation of gap and electrodes widths.

The schematic of CPW with three metal electrodes is presented in Figure 2-18. For optical signal modulation, the two arms of the MZI (waveguides) will be positioned in between the electrode gap.

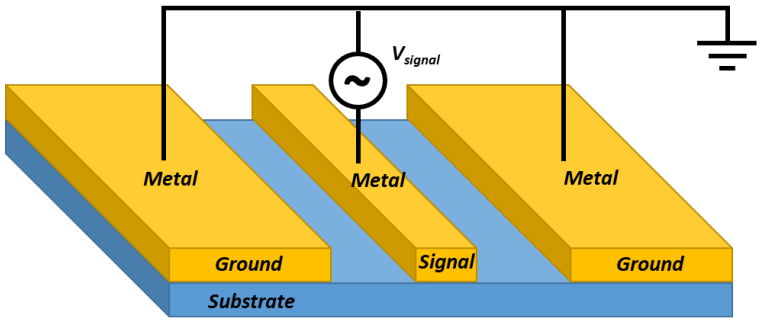

Figure 2-18 Schematic of transmission line with the coplanar waveguide structure showing that the ground plane and signal conductor are on the same side of the substrate.

Losses associated with the CPW at high frequency have to be considered to optimise the design of the CPW in optical phase modulator. The impedance of the transmission line can be characterised by understanding the equivalent circuit of transmission line as presented in Figure 2-19. Four elementary components in the equivalent circuit including resistance (R), inductance (L), shunt

capacitance (C) and shunt conductance (G) are linked with the characteristic impedance (Z_0) of the transmission line. To optimise the design of the CPW, the effect of electrode dimension with these elementary components will be discussed.

The resistance (R) per unit length (Ω/m) will be affected to the conductor losses and radiation loss. By varying the dimension of electrode (width and length), the resistance per unit length can be adjusted resulting in the loss changing. The relationship between the electrode dimension and R showing that the wider width of cross-section of electrode cause the decreasing of resistance leading to the lowering of loss. While the longer length of electrode resulting in the increasing of losses.

For the inductance (L) per unit length (H/m), the effect of geometry of the electrode with the inductance showing that the inductance can be decreased with the increasing of the electrode cross-section. Length of electrode is also affected to the inductance where the increasing of the electrode length can cause the increasing of inductance. Current travelling with different length in the conductor will have slightly different phase delays where the net effect will be inductive.

The shunt capacity (C) per unit length (F/m) is mainly corresponding with the permittivity of substrate and the dimension of signal conductor. When the width of signal conductor has been increased, the capacitance per unit length will also increase due to the increasing of the area between the signal conductor and the substrate. For the CPW, the dimension of gap between the signal conductor and ground plate is also affected to the capacitance as the varying in the gap size resulting in the change of electric field strength between these two electrodes.

The shunt conductor (G) per unit length (S/m) will be mainly affected by the conductance of the dielectric surround electrodes and loss tangent. The loss tangent presents the absorption of electromagnetic energy in the dielectric material which is showing that the higher the loss tangent, the higher dielectric loss [146]. The dielectric properties are usually defined in terms of real permittivity and loss tangent at certain frequency where the loss tangent defines how lossy the dielectric is.

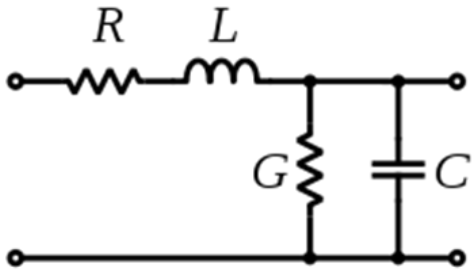

Figure 2-19 Schematic representation of the elementary component of a transmission line.

As frequency increases, more current will travel on the outer most surface of the conductor owing to an effect known as the skin effect [147]. The conductor loss is the total loss associated with

the conductor. Since this, both resistance (R) and inductance (L) will be affected by the skin effect. As the variation of frequency, the line inductance and resistance will change with changes in skin depth. Skin depth (δ) is a function of frequency, resistivity and permeability and they relationship can be defined as:

$$\delta = \frac{1}{\sqrt{\pi f \mu \sigma}} \tag{21}$$

where δ is a skin depth (m), f is a applied frequency (Hz), μ is a permeability and σ is a conductivity of the conductor. As shown in Eq.(21) that the increasing of frequency leading to the decreasing of skin dept which means that the current density will be increased. This increasing of current density on the surface of electrode will convert more energy into heat, which translates into more loss at higher frequencies.

For a propagating wave to be completely transmitted through the transmission line, the characteristic impedance (Z_0) will be considered ensures the less signal is reflection at the end of transmission line. Not only the termination should take the optimal value of the characteristic impedance but also the transmission line should have the same impedance otherwise, some of the signal will be reflected during the propagation in the transmission line resulting in a transmission loss. By applying the Kirchhoff's laws of voltage and current to the lumped element equivalent circuit presented in Figure 2-19 and solving the equations, the equation for characteristic impedance (Z_0) and the propagation constant (γ) can be expressed in Eq.(22) and Eq.(23), respectively.

$$Z_0 = \sqrt{\frac{R + j\omega L}{G + j\omega C}} \tag{22}$$

$$\gamma = \alpha + j\beta = \sqrt{(R + j\omega L)(G + j\omega C)} \tag{23}$$

To minimise the reflection of the signal at the end of the transmission line, the characteristic impedance (Z_0) of the transmission line must be the same as characteristic impedance (Z_0) of all devices used together with it. In the field of radio frequency (RF) and microwave engineering, by far and away, the most common transmission line standard is 50 Ω coaxial cable (coax), which is an unbalanced line. The 50 Ω first introduced as a nominal impedance during World War II work on radar and it is the first required Z_0 for minimum loss[148]. Therefore, the Z_0 of the transmission line (CPW) used in this research will be adjusted to 50 Ω by adjusting the dimension (width and height) of conductor to achieve the lowest transmission loss and effective index match between RF wave and optical signal.

2.4.3 Key Metrics of Performance

To determine the EO polymer coefficient and the performance of optical modulator, several characteristics are involved and must be declared.

2.4.3.1 In-device Electro-optic Coefficient ($r_{33,in-device}$)

The electro-optic coefficient represents the efficiency of EO polymer to the change refractive index of polymer in a presence of electric field. Thus, the unit of r_{33} is given by the inverse of electric field, for example, commonly in pm/V. The EO polymer with higher r_{33} will present stronger changing rate of refractive index. For the ideally poled EO polymer, the definition of r_{33} is mathematically derived in section 2.2.1 which is applicable under only a certain assumption including the uniform r_{33} in polymer.

For the integration of EO polymer into a waveguide modulator, the formation of uniform r_{33} is challenging due to the lack of uniformity and homogeneity in a poling field. Usually, the EO polymer is poled by applying the poling voltage onto the same electrode using for modulation purpose. The modulation electrode is normally designed with the finite conductors instead of a pair of large parallel conductors as used in a thin-film device. Additionally, the dielectric contrast between core and cladding materials also induces an inhomogeneous poling field. The local orientation of chromophore dipole in polymer is defined by a local direction of poling field. Thus, the formation of r_{33} in polymer is generated with non-uniformity and inhomogeneity as same as the distribution of the poling field. The mean value of the electro-optic coefficient ($r_{33,in-device}$) is usually lower than that of the ideal case and can be given by

$$r_{33,in-device} = \sigma_{poling} r_{33} \quad ; \ 0 \leq \sigma_{poling} \leq 1 \qquad (24)$$

where σ_{poling} is defined as a poling coefficient that dictates an efficiency of the poling process. This coefficient presents a quality of poled EO polymer comparing to that made by the ideal poling situation.

2.4.3.2 Overlap Integral Factor (Γ)

In term of a waveguide modulator with EO polymer presenting in core or cladding region, the optical guiding mode is partially overlap to the polymer region. The effective index change of optical mode (Δn_{eff}) is related to the EO polymer index change; however, they are not directly changed with the same magnitude. The effective index change is associated to an overlap between the electric modulation field $\left(\vec{E}_{mod}(x,y)\right)$ and the optical intensity $\left(\frac{c\varepsilon_0 n}{2}\left|\vec{E}_{opt}(x,y)\right|^2\right)$.

The effective index change can be defined by the average of local refractive index change $(\Delta n_{EO}(x,y))$. Due to the non-uniformity of $\vec{E}_{opt}(x,y)$ in the optical mode, $\Delta n_{EO}(x,y)$ is individually weighed by a local optical intensity $\left(\frac{c\varepsilon_0 n}{2}\left|\vec{E}_{opt}(x,y)\right|^2\right)$.

$$\Delta n_{eff} = \frac{\iint_{-\infty}^{\infty} \Delta n_{EO}(x,y)\left|\frac{c\varepsilon_0 n}{2}\vec{E}_{opt}(x,y)\right|^2 dxdy}{\iint_{-\infty}^{\infty}\left|\frac{c\varepsilon_0 n}{2}E_{opt}(x,y)\right|^2 dxdy} \tag{25}$$

The local refractive index change exists only in the EO polymer region, therefore the integration of $\Delta n(x,y)$ can be neglected elsewhere.

$$\Delta n_{eff} = \frac{\iint_{EO} \Delta n_{EO}(x,y)\left|\vec{E}_{opt}(x,y)\right|^2 dxdy}{\iint_{-\infty}^{\infty}\left|E_{opt}(x,y)\right|^2 dxdy} \tag{26}$$

Using the definition of Δn_{EO} in the Pockels effect Eq.(13) and considering the overlap between fields in term of dot product.

$$\Delta n_{eff} = -\frac{1}{2}n^3 \frac{\iint_{EO} r_{33}(x,y)\vec{E}_{mod}(x,y)\cdot\left|\vec{E}_{opt}(x,y)\cdot\hat{e}_{EO}(x,y)\right|^2 dxdy}{\iint_{-\infty}^{\infty}\left|E_{opt}(x,y)\right|^2 dxdy} \tag{27}$$

Due to the non-uniformity of $r_{33}(x,y)$, the mean value from Eq.(24) is considered here (also called $r_{33,in-device}$).

$$\Delta n_{eff} = -\frac{1}{2}n^3 r_{33,in-device} \frac{\iint_{EO} E_{mod}(x,y)\cdot\left|E_{opt}(x,y)\right|^2 dxdy}{\iint_{-\infty}^{\infty}\left|E_{opt}(x,y)\right|^2 dxdy} \tag{28}$$

Comparing to Eq.(14) and (24), the effective index change can be rewrite as [149]

$$\Delta n_{eff} = -\frac{1}{2}n^3 r_{33,in-device}\frac{V}{d}\Gamma \quad \text{or} \quad \Delta n_{eff} = -\frac{1}{2}n^3\sigma_{poling}r_{33}\frac{V}{d}\Gamma \tag{29}$$

where Γ is the overlap integral factor and defined by [150]

$$\Gamma = \frac{d}{V}\frac{\iint_{EO} E_{mod}(x,y)\cdot\left|E_{opt}(x,y)\right|^2 dxdy}{\iint_{-\infty}^{\infty}\left|E_{opt}(x,y)\right|^2 dxdy} \tag{30}$$

2.4.3.3 Half-wave Voltage (V_π) *and Voltage-length Product* ($V_\pi \cdot L$)

The half-wave voltage is an important characteristic of the electro-optic modulator that represents the level of the modulation voltage required for shifting an optical phase of π. Since this

parameter was originally associated to the phase change between the input and the output signal of a single phase-shifter, the π value means they are out-of-phase. The phase change (ϕ) of the optical signal in a phase-shifter can be written as

$$\phi = \frac{2\pi}{\lambda}\Delta n_{eff} L \tag{31}$$

where λ is a wavelength of the optical signal, Δn_{eff} is an effective index change of the optical mode in phase-shifter, and L is a length of the phase-shifter. By using Eq.(29), the phase change can be re written as

$$\phi = \frac{n^3 \pi \Gamma r_{33,in-device}}{\lambda d} V \cdot L \tag{32}$$

Then the half-wave voltage can be obtained by substituting $\phi = \pi$

$$V_\pi = \frac{\lambda d}{n^3 \Gamma L r_{33,in-device}} \tag{33}$$

For the Mach-Zehnder modulator (MZM), the phase difference is calculated from a comparison of output phases between the interferometer arms. The phase-shifter can be incorporated into either one of or both interferometer arms. When the MZM has a phase-shifter on both arms, the optical signal on each arm can be individually modulated, especially in the opposite direction so called "push-pull configuration". If both phase-shifters are identical in term of a modulation efficiency and equally driven, each phase-shifter is required to modulate by only $\pm\pi/2$ in order to provide a total phase difference of π between both arms [123]. Therefore, the half-wave voltage of push-pull driven MZM can be given by [150]

$$V_\pi = \frac{\lambda d}{2n^3 \Gamma L r_{33,in-device}} \tag{34}$$

By mean of comparing the overall performance of modulator, V_π is one of the figures of merit for evaluating the performance. However, the well-defined figure of merit should not be variant of the length of the phase-shifter. Therefore, the figure of merit can be given by $V_\pi \cdot L$ and

$$V_\pi \cdot L = \frac{\lambda d}{2n^3 \Gamma r_{33,in-device}} \tag{35}$$

where the "voltage-length product" is introduced. For example, one of the MZMs has a $V_\pi \cdot L$ of 2.5 V·cm. Therefore, if the MZM has a phase-shifter with the length of 1 cm, it can modulate an out-of-phase signal by applying ±2.5 V to the phase-shifters. The use of a low half-wave voltage and

a short phase-shifter can result in low optical propagation loss, low RF modulation wave loss, thus, low power consumption. Therefore, the improvement of the modulator performance mainly aims to reduce $V_\pi \cdot L$.

2.4.3.4 Modulation Speed or Bandwidth

High modulation speed or large bandwidth is demanded for the interconnect application. The modulation bandwidth is one of the most important metrics of performance for an optical modulator that dictates the ability to carry the data signal at a certain rate. The bandwidth is generally defined by the frequency at which the modulation efficiency is decreased to one certain level comparing its maximum value. The cut-off level depends on the application of the modulator; however, the most common level is -3dB drop of efficiency. Figure 2-20 shows the examples of experimental modulation efficiency plotted against the RF modulation frequency [151]. the 3dB-bandwidth of the blue line is found at 7GHz while the magenta line shows a three times larger bandwidth at 21GHz.

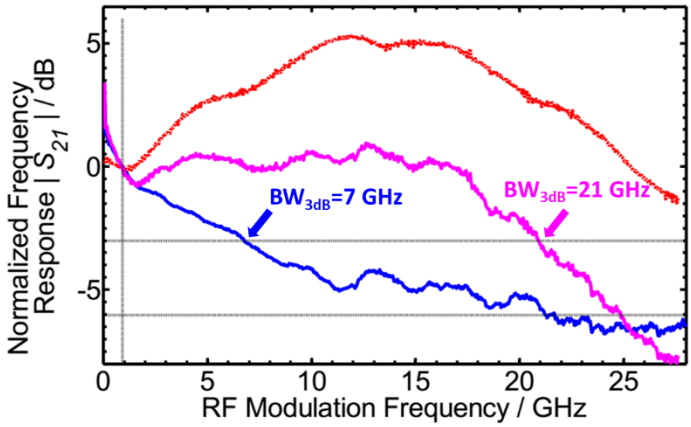

Figure 2-20 Modulation efficiency of MZM versus RF modulation frequency[151]

The limit of modulation bandwidth is directly related to the electrical behaviour of RF modulation wave in the modulator. To study the limit of bandwidth, the electrode structure of modulator must be considered as an equivalent RLC circuit (section 2.4.2), and the frequency response of this circuit needs to be reviewed. According to the RF wavelength comparing to the length of electrode, the modulator (in RF modulation measurement) can be basically categorised to two types: *lumped modulator* and *traveling-wave modulator (TWM)*. As a result, the different type accommodates the different RLC circuit as shown in Figure 2-21.

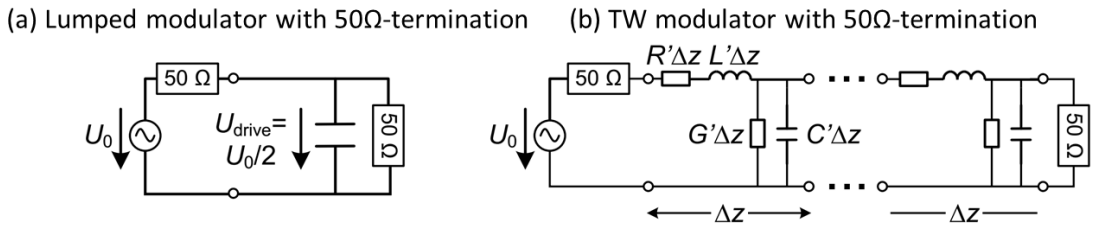

Figure 2-21 Equivalent circuit for (a) Lumped modulator. The drive voltage across the modulator is equal to half of the source voltage. The RF power is dissipated upon the loading capacitance and the 50Ω terminator. (b) Traveling-wave modulator. It is consisted of a series of lumped segments of Δz impedance and terminated by a 50Ω resistor. U_0 is the source voltage. [152]

For this work a MZM is incorporated with a CPW electrode. The electrode is designed to have an intrinsic 50Ω-impedance in order to match the internal impedance of the RF source. At the end of electrode, it also needs to be terminated with a 50Ω matched resistor to prevent the reflection of the RF wave which would interfere the incoming RF wave of the next modulation bit. Thus, there is a 50Ω resistor connecting to the right-end of both equivalent circuits as presented in Figure 2-21.

For the lumped modulator, the electrode is much shorter than the RF wavelength so that the modulation voltage can be considered uniform and instantaneous along the electrode and MZI arms. By considering the equivalent circuit in Figure 2-21(a), the effect of the capacitor could have a significant impact on modulation bandwidth. Due to the charging/dis-charging phenomena in the capacitor, the amplitude of the RF voltage across the phase-shifter is decreased by the effect of RC-time constant when increasing the RF frequency. The modulation efficiency will be reduced by factor of $\sim\frac{1}{2}$ (or -3dB) when the RF frequency approach to [125]

$$f_{3dB} = \frac{1}{4\pi RC} \tag{36}$$

where the 3dB modulation bandwidth (f_{3dB}) for lump modulator is defined, R and C are an internal resistance and capacitance of phase-shifter. In order to increase the bandwidth, the R and C need to be decreased. The capacitance can be decreased by enlarging the electrode gap, but that will result a larger half-wave voltage (V_π). the resistance can be decreased by increasing the electrode thickness, but that will increase the complexity of the fabrication process as hard to lift-off a metal layer.

For the TWM, the length of CPW electrodes is arbitrarily longer than the RF wavelength. The assumption of uniform modulation voltage along the electrode as used in a lumped model is no longer applicable. The RF and Optical signal are considered as two waves traveling together along the phase-shifter with separated velocities. Thus, the equivalent circuit of CPW electrodes is represented by a series of small lumped segments of Δz impedance as shown in Figure 2-21(b). As a result of electrode division, the capacitance in each segment can be assumed to be very small and neglectable. The modulation bandwidth is no longer limited by the charging/discharging effect (RC-time

constant) while other three main phenomena come to play role on this limitation: RF reflections (impedance mismatch), electrode attenuation loss and velocity mismatch between RF modulation wave and traveling optical signal. Ideally, TWM would be only limited by the last two factors if the Δz impedance is appropriately set equally to the impedance of RF source and termination. The electrode attenuation loss dictates a reduction of RF voltage amplitude along the electrode while the velocity mismatch decreases the interaction between RF electric field and optical field. Overall, those phenomena influent to the modulation bandwidth via a reduction of net modulation efficiency in term of frequency increment.

To evaluate the modulation bandwidth of TWM, the traveling RF voltage is taken into a consideration. The main limitations to the bandwidth are represented by the RF propagation loss and the walk-off between the optical and RF signal. We start to consider the effect if these limitations from the equation of RF voltage $V(z,t)$ along the electrode as a function of a longitudinal position (z) and time (t) [153, 154]

$$V(z,t) = V_0 \cdot e^{-\alpha z} \cdot \sin 2\pi f \left(\frac{z n_{RF}}{c} - t\right) \tag{37}$$

where V_0 is the amplitude of the RF voltage, f is the frequency, α is the attenuation coefficient, and n_{RF} is the effective index of RF signal. The voltage is presented in term of a travelling sinewave with its own travelling speed and attenuated along the propagating distance. If we consider the perception to this voltage in aspect of optical signal, the voltage seen by the frame of optical speed can be written as

$$V(z,t_0) = V_0 \cdot e^{-\alpha z} \cdot \sin 2\pi f \left(\frac{z(n_{RF}-n_{opt})}{c} + t_0\right)$$

$$V(z,t_0) = V_0 \cdot e^{-\alpha z} \cdot \sin 2\pi f \left(\frac{z\Delta n}{c} + t_0\right) \tag{38}$$

where n_{opt} is the group index of the optical signal, and t_0 is the time difference between the optical and RF signal. If we suppose to track the optical signal starting at the peak of RF voltage ($2\pi f t_0 = \pi/2$) at $z = 0$, the equation (38) can be re-written in form of cosine wave.

$$V(z,t_0) = V_0 \cdot e^{-\alpha z} \cdot \cos\left(\frac{2\pi f z \Delta n}{c}\right)$$

$$V(z) = V_0 \cdot e^{-\alpha z} \cdot \cos(\Delta k \cdot z) \qquad ; \Delta k = \frac{2\pi f \Delta n}{c} \tag{39}$$

where Δk is the difference of propagation constants. With the aim of calculating the total optical phase change modulated by this cosine RF voltage, the TWM must be considered as a series of small

phase-shifter elements with the length dz which is corresponding to the equivalent circuit of CPW electrode in Figure 2-21(b). Using the Eq. (32), the phase change ($d\phi$) generated by each element is

$$d\phi = \frac{n^3\pi\Gamma r_{33,in-device}}{\lambda d} V(z) \cdot dz \tag{40}$$

The total phase change (ϕ_{total}) can be calculated by integrating $d\phi$ from $z = 0$ to $z = L$ where TWM has a modulating length of L.

$$\phi_{total} = \frac{n^3\pi\Gamma r_{33,in-device}}{\lambda d} V_0 \int_{z=0}^{L} e^{-\alpha z} \cdot \cos(\Delta k \cdot z) \cdot dz \tag{41}$$

Using the "Integration by Parts" technique for twice,

$$\int_{z=0}^{L} e^{-\alpha z} \cdot \cos(\Delta k \cdot z) \cdot dz = \frac{\Delta k \cdot e^{-\alpha z}}{(\Delta k)^2+\alpha^2}\left(\sin(\Delta k \cdot z) - \frac{\alpha}{\Delta k}\cos(\Delta k \cdot z)\right)$$

So $$\phi_{total} = \frac{n^3\pi\Gamma r_{33,in-device}}{\lambda d} V_0 \left[\frac{\Delta k \cdot e^{-\alpha z}}{(\Delta k)^2+\alpha^2}\left(\sin(\Delta k \cdot z) - \frac{\alpha}{\Delta k}\cos(\Delta k \cdot z)\right)\right]_{z=0}^{L}$$

$$= \frac{n^3\pi\Gamma r_{33,in-device}}{\lambda d} V_0 \left[\frac{1}{(\Delta k)^2+\alpha^2}(\Delta k \cdot e^{-\alpha L}\sin(\Delta k \cdot L) - \alpha \cdot e^{-\alpha L}\cos(\Delta k \cdot L) + \alpha)\right] \tag{42}$$

To study the frequency response of TWM, the figure of merit representing the modulation efficiency should be defined appropriately. In this case, the half-wave voltage is used as the figure of merit for studying its frequency response. Based on the general definition of half-wave voltage, the required amplitude of RF voltage in order to generate the half-wave phase change $\phi_{total} = \pi$ can be given by

$$V_{0,\pi}(RF) = \frac{\lambda d}{n^3\Gamma r_{33,in-device}}\left[\frac{1}{(\Delta k)^2+\alpha^2}(\Delta k \cdot e^{-\alpha L}\sin(\Delta k \cdot L) - \alpha \cdot e^{-\alpha L}\cos(\Delta k \cdot L) + \alpha)\right]^{-1} \tag{43}$$

Considering the push-pull driving configuration in TWM, the half-wave voltage is divided by 2.

$$V_{0,\pi}(RF) = \frac{\lambda d}{2n^3\Gamma r_{33,in-device}}\left[\frac{1}{(\Delta k)^2+\alpha^2}(\Delta k \cdot e^{-\alpha L}\sin(\Delta k \cdot L) - \alpha \cdot e^{-\alpha L}\cos(\Delta k \cdot L) + \alpha)\right]^{-1} \tag{44}$$

The modulation frequency response is defined by the ratio of the half-wave voltage at DC ($f \to 0$) to the half-wave voltage at RF. For the DC modulation on TWM, the half-wave voltage $V_{0,\pi}(DC)$

can be derived by taking the limit ($f, \Delta k \to 0$) into Eq. (44), also substituting $\alpha = 0$ due to no loss in non-travelling voltage.

$$V_{0,\pi}(DC) = \frac{\lambda d}{2n^3 \Gamma r_{33,in-device}} \cdot \lim_{\Delta k \to 0} \frac{\Delta k}{\sin(\Delta k \cdot L)}$$

Using L'Hôpital's rule , $\lim_{x \to c} \frac{f(x)}{g(x)} = \lim_{x \to c} \frac{f\prime(x)}{g\prime(x)}$

$$V_{0,\pi}(DC) = \frac{\lambda d}{2n^3 \Gamma r_{33,in-device}} \cdot \lim_{\Delta k \to 0} \frac{(d\Delta k / d\Delta k)}{(d \sin(\Delta k \cdot L)/d\Delta k)}$$

$$\therefore \quad V_{0,\pi}(DC) = \frac{\lambda d}{2n^3 \Gamma r_{33,in-device}} \cdot \frac{1}{L} \tag{45}$$

which is demonstrating the same equation to Eq. (34). Next, the modulation frequency response in general case can be written by $M(f) = \frac{V_{0,\pi}(DC)}{V_{0,\pi}(RF)}$

$$M(f) = \left(\frac{\Gamma_{RF}}{\Gamma_{DC}} \cdot \frac{1}{L} \cdot \frac{1}{(\Delta k)^2 + \alpha^2}\right)(\Delta k \cdot e^{-\alpha L} \sin(\Delta k \cdot L) - \alpha \cdot e^{-\alpha L} \cos(\Delta k \cdot L) + \alpha) \tag{46}$$

where the parameters Γ_{RF}, Δk, and α can be implied as a function of RF frequency(f). Therefore, in order to calculate the modulation bandwidth, the $\Gamma_{RF}(f)$, $\Delta k(f)$, and $\alpha(f)$ must be known of can be plotted as a function of frequency.

For the ideal case of TWM with RF lossless electrode ($\alpha = 0$), the modulation frequency response can be written in a simplified form as

$$M(f) = \frac{\Gamma_{RF}(f)}{\Gamma_{DC}} \cdot \frac{\sin(\Delta k \cdot L)}{\Delta k \cdot L} \tag{47}$$

If we can assume that the overlap integral factor Γ_{RF} is equal to Γ_{DC} and constant, the modulation frequency response can be plotted as Figure 2-22.

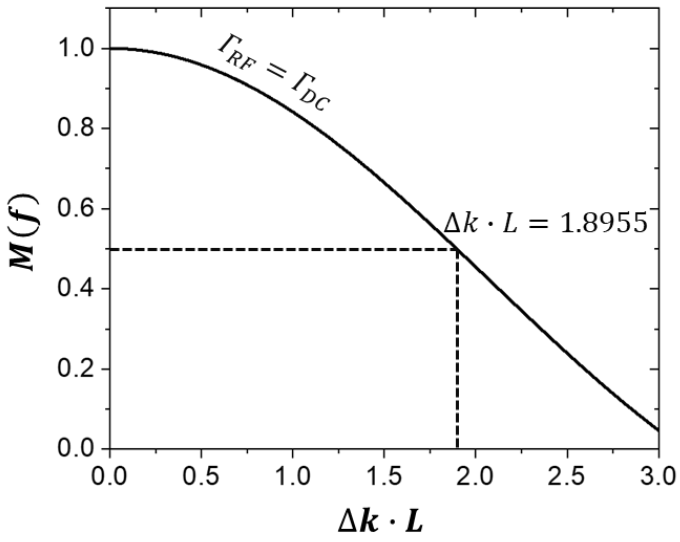

Figure 2-22 Modulation frequency response as a function of $\Delta k \cdot L$ under the assumption of $\Gamma_{RF} = \Gamma_{DC}$.

The modulation frequency response is decreased to 0.5 or 3dB-reduction level when $\Delta k \cdot L = 1.8955$. Therefore, 3dB cut-off frequency (f_{3dB}) can be estimated by

$$\Delta k \cdot L = \frac{2\pi f_{3dB}\Delta n}{c} L = 1.8955$$

$$f_{3dB} = \frac{1.8955}{2\pi L \Delta n} c \quad \text{or} \quad f_{3dB} = \frac{1.8955}{2\pi L (n_{RF} - n_{opt})} c \tag{48}$$

This obviously implies the bandwidth limitation by the walk-off between the optical and RF signal. Consequently, the CPW electrode should be appropriately optimised with the aim of minimising the difference of the RF effective index to the optical group index in order to enlarge the modulation bandwidth.

2.5 Chapter conclusion

In this research project, the design of modulator will be based on MZI structure with asymmetric arms design. The transmission line with CPW structure will be design and use for both EO polymer poling and the signal modulation. The structure of modulating waveguide will be initiated with a simple structure of EO polymer cladding, and all of waveguide components will be based on silicon nitride platform. PMMA-co-DR1 is chosen for developing a sample preparation process in the first stage. Then, the performance of modulator will be improved with reviewed material and design. The slot waveguide design will be adapted to develop the structure of modulating waveguide, and PMMA-co-DR1 is replaced by the high-efficient EO polymer based on FTC-chromophore.

Chapter 3.
DEVICE DESIGNS

In this chapter, the design of all components to fabricate Mach-Zehnder modulator (MZM) devices on SiN photonic circuit will be presented. Section 3.1 will introduce the optical and electrical simulator software use to optimise the design of MZM and also the software use to design a mask for lithography process. The design and optimisation parameters for the passive components in MZM devices such as grating coupler, taper, and MMI splitter will be presented in section 3.2. The design of MZM modulators based on a strip-waveguide, a slot waveguide, and enhanced design slot waveguide and their optimisation parameters to achieve the high efficiency modulator will be reported in section 3.3, 3.4, and 3.5, respectively. Then, section 3.6 will demonstrate the layout of mask design which include all the optimised components for MZM modulator. Finally, the design and important parameters for fabricating MZM modulator on SiN photonic circuit will be summarised in section 3.7.

3.1 Design Tools

To design and fabricate the optical based modulator, both optical and electrical parameters have to be considered as they are affected to efficiency of modulator. In this work, the designs of MZM components were optically and/or electrically simulated to optimise their performance. The optical simulations were mainly performed by using *Lumerical MODE* and *FDTD solutions*, while the simulators used for electrical simulations are *TX-Line 2003*, *Pathwave ADS* and *Silvaco* TCAD. According to the optimal results from simulation, the layout of devices will be finally generated with *Mentor Graphics Tanner L-Edit* in order to create a lithography mask for the fabrication process. Thus, this section provides the overview of these design tools and also clarifies the role of each solvers within certain simulator which were utilised within the scope of this research.

3.1.1 Optical Simulators

3.1.1.1 Lumerical MODE Solution

MODE Solution from *Lumerical* is a complete optical waveguide design environment for analysing and optimising the design of optical waveguides as well as other passive structures [100]. It consists of three different solvers: finite difference eigenmode (FDE) solver, 2.5D varFDTD and eigenmode expansion (EME) solver. Each solver is established for handling different and some specific structures of photonic component. In this thesis, only FDE and EME solvers were utilised for the design optimisation.

Finite difference eigenmode (FDE) solver is based on the 2D finite difference method in which to calculate the eigenmode profile on a cross-section of arbitrary waveguide by solving Maxwell's equations [121]. The effective index, group index, polarisation and propagation loss are also calculated along with the modal profile of optical mode as shown in Figure 3-1. The information of modal profile from this solver is a necessary parameter for studying characteristics of a waveguide. The frequency analysis tool is also available which can be used to study the dispersion effect in the waveguide. Other two useful features existing in this solver are bend radius settings and an overlap analysis tool which are capable for simulating the bent waveguides in the MZM.

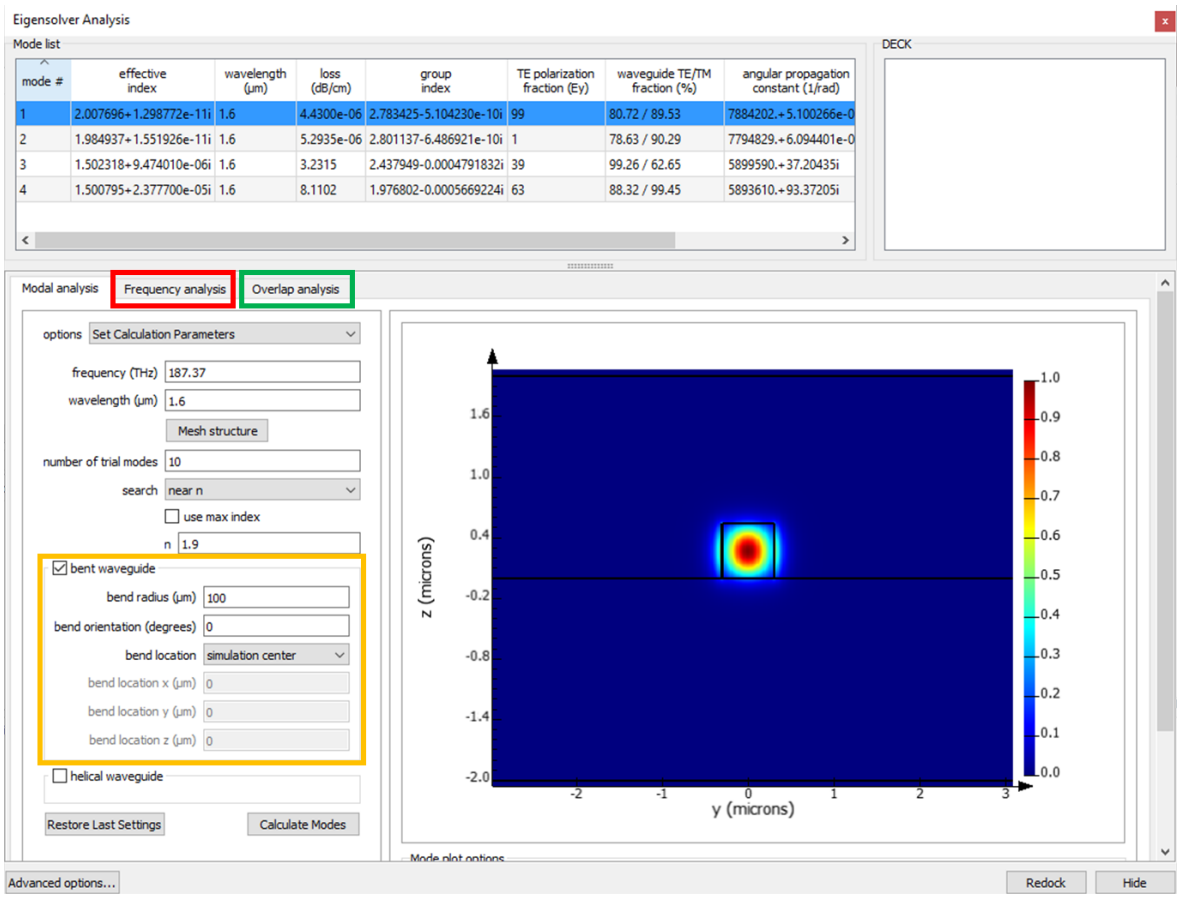

Figure 3-1 Finite difference eigenmode solver in *Lumerical MODE solution* with a frequency analysis tool (red frame), bend radius settings (orange frame) and an overlap analysis tool (green frame).

Moreover, the *MODE solution* of *Lumerical* provides another solver called eigenmode expansion (EME). This solver is suitable for simulating a photonic structure with long propagation length, for example, waveguide tapers and multimode interferences. The calculation of mode propagation based on EME will be performed by using the scattering matrix (S-matrix) of every cross-sectional division of the entire structure [22]. The simulation of modal propagation by using EME solver can be divided into three steps. In the first step, the photonic structure will be laterally divided into multiple cells as shown in Figure 3-2 (a), and the eigenmodes are computed over a cross-section of each cell by using FDE solver. Secondary, the modes overlap between adjacent cells are

calculated in which to obtain the S-matrices of every cells. Finally, the bi-directional transmittance and reflectance of the entire structure will be calculated from those S-matrices, and the mode propagation profile can be generated as shown in Figure 3-2 (b).

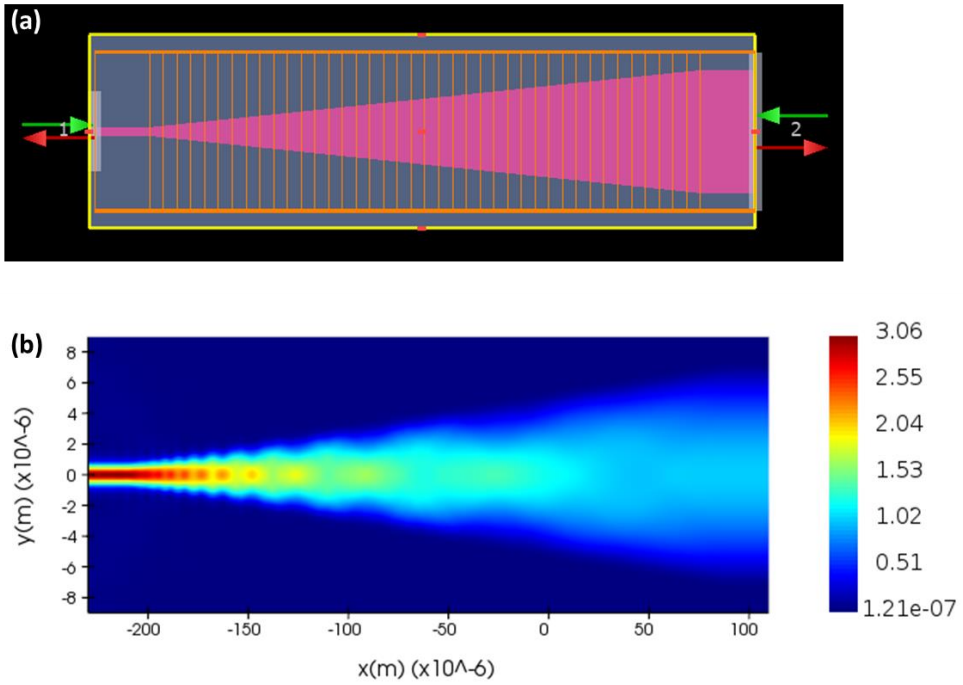

Figure 3-2 (a)Waveguide taper with the multiple cells boundary defined by eigenmode expansion (EME) solver and (b) top-view profile of the mode propagation simulated with EME solver.

As the EME solver simulated the modal profile by using the modes overlap between adjacent cells, thus the EME solver makes an optimisation much more time-efficient over a long-distance structure compared to FDTD-based simulator which requires higher computation resources and longer simulation time. Although the EME solver is working faster than the FDTD, it works accurately only for a simulation with straight light propagation or at small angle. The EME solver is not recommended for simulating the modal propagation within bend or ring structures. Therefore, in this work, this solver was applied for the optimisation of waveguide tapers and MMIs. However, the EME solver principally relies on an approximation of constant mode propagation throughout each cell division. The optimised results from EME solver are mostly suggested to be proven with a FDTD-based simulator at the end.

3.1.1.2 Lumerical FDTD Solution

The *FDTD solution* is another photonics design environment from *Lumerical* which is generally used to simulate the waveguide, MMI and taper. A single solver working in this simulator is based on the finite-difference time-domain (FDTD) method which is applicable for solving Maxwell's equations in all kinds of 2D/3D geometries [155]. There are plenty of special features in

this simulator for supporting a variety of photonic applications [60]. In this work, two special features including the symmetric/anti-symmetric boundary conditions and the far-field projection were applied to carry out the optimisation of grating coupler design. Moreover, the FDTD solution was also used to validate the final design of MMIs and tapers which were primarily optimised with the EME solver.

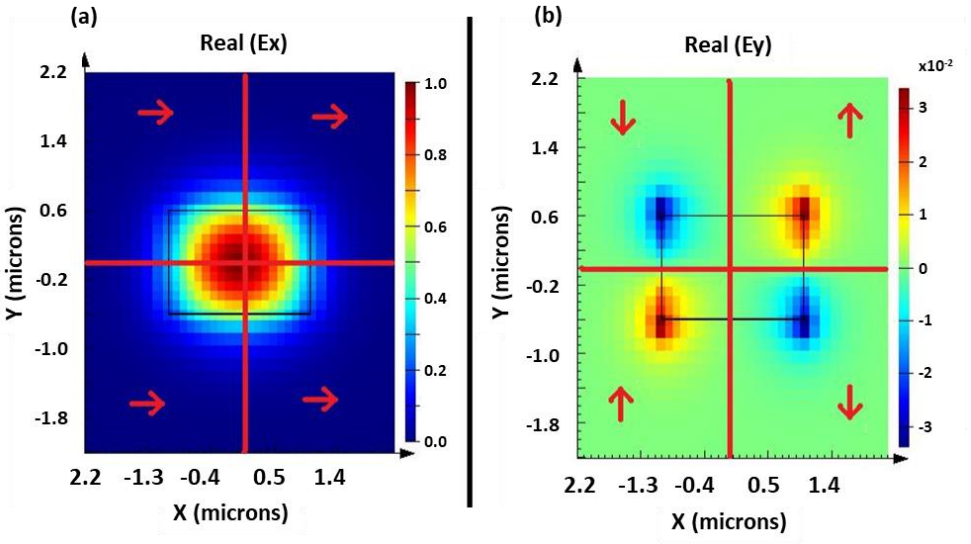

Figure 3-3 The figures show (a) x- and (b) y-component of electric field of mode in a rectangular cross-sectional waveguide. A plane of anti-symmetry is at x=0 while a plane of symmetry is at y=0 [90].

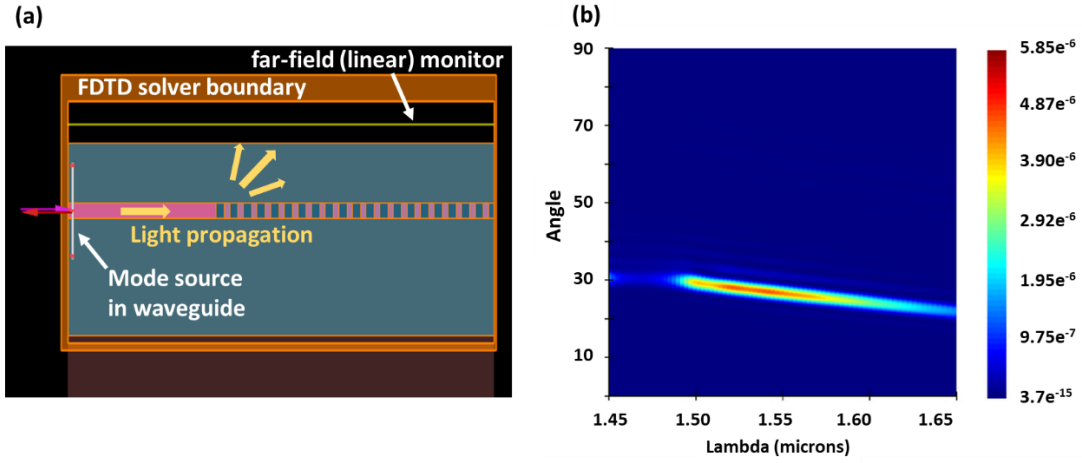

Figure 3-4 (a) Simulation setup of grating coupler in 2D-FDTD solution with a far-field monitor along the top cladding surface and (b) the projection profile of far-field intensity showing the coupling angle and peak wavelength around 28° and 1540nm, respectively.

The symmetric/anti-symmetric boundary conditions work out by taking an advantage of foldable electric/magnetic field data over the symmetry of optical mode profile [90]. This feature can assist to reduce the simulation time by factors of 2 to 8 depending on number of symmetric/anti-symmetric plane. In this work, the propagation of TE-mode in the waveguide along Z-axis has one

plane of symmetry (y=0) and one plane of anti-symmetry (x=0) as shown in Figure 3-3, its simulation time can be reduced by factor of 4 by using this feature.

The far-field projection is another helpful feature which was used in this work for speeding up the optimisation of grating coupler design. It is a hybrid technique between numerical and analytical method. To run the far-field projection, the near-field data will be simulated and recorded in a numerical approach Then, this data is decomposed to be a set of point-sources and analytically re-combined to be a set of plane waves at different angles and different wavelengths [156]. As shown in Figure 3-4(a), the structure of grating coupler is created within a 2D-FDTD solver with a mode source toward the grating teeth. The linear far-field monitor is placed in parallel to the top cladding layer (blue) in which to monitor all near-field diffracting upward from the grating and calculate the far-field profile in terms of angle and wavelength as presented in Figure 3-4(b). By considering the diffraction peak in this far-field profile, the coupling angle and peak wavelength can be obtained all at once. Therefore, the scanning of coupling angle of grating by rotating the monitor is no longer required, and the optimisation time can be explicitly shortened.

3.1.2 Electrical Simulators

3.1.2.1 TX-Line 2003

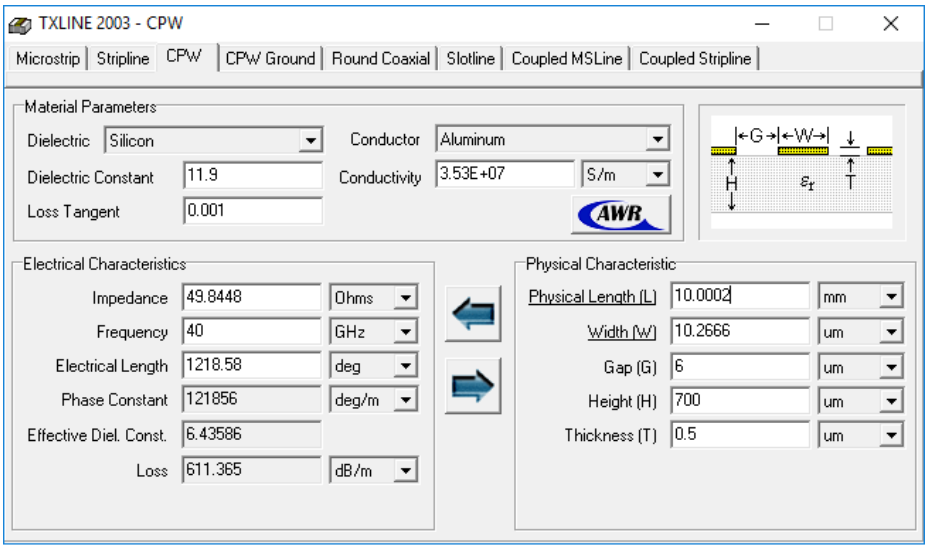

Figure 3-5 The graphic interface of *TX-Line 2003* displaying, for example, a calculated result for the coplanar waveguide (CPW) electrode.

TX-Line 2003 from *AWR*® is a free calculator for analysing the electrical characteristics of 2D transmission-line structures at radio frequency such as microstrip, stripline, and coplanar waveguide [43]. The coplanar waveguide (CPW) is one of the transmission-line structures which is commonly applied for working as electrodes in the optical modulators. Due to an analytical basis, *TX-Line 2003* provides an instant calculation result without any delay of simulation process. Therefore, in this work, this calculator was chosen to initially estimate the dimensions of CPW electrode design for a

desired radio frequency. For example, to design a 50Ω impedance CPW at 40 GHz with a fixed aluminium thickness of 0.5 µm and gap of 6 µm, the width of signal conductor is obtained about 10 µm as shown in Figure 3-5. However, this calculator can be used for only a basic electrical analysis in 2D. The additional elements such as top and bottom cladding layers, are not taken into account into the model. The commercial full 3D simulator *Pathwave ADS* is consequently required to validate the CPW electrode design accurately.

3.1.2.2 Pathwave ADS

Pathwave Advanced Design System or *Pathwave ADS* is a commercial electronic design automation (EDA) software from *Keysight Technologies*. The EDA is a set of software tools for designing, analysing, and verifying electronic system such as an integrated circuit (IC) and printed circuit board (PCB). *Pathwave ADS* consists of several related tools which support many electronic design functions including schematic wiring tool, PCB/IC design tool, DC/AC/EM simulators etc. In this work, the CPW electrode design was drawn as a PCB/IC layout in the design tool (Figure 3-6(a)) and imported to the electromagnetic (EM) simulator. In the simulator setup, the layer stack of our device was fully defined in 3D including the Si-substrate, top/bottom cladding, and conductor for CPW electrode as shown in Figure 3-6(b). Finally, the simulation output in Figure 3-6(c) will present the S-parameters, impedance, and attenuation over a simulated frequency range. This information can be used for analysing a frequency dependence of modulation efficiency in the optical modulator.

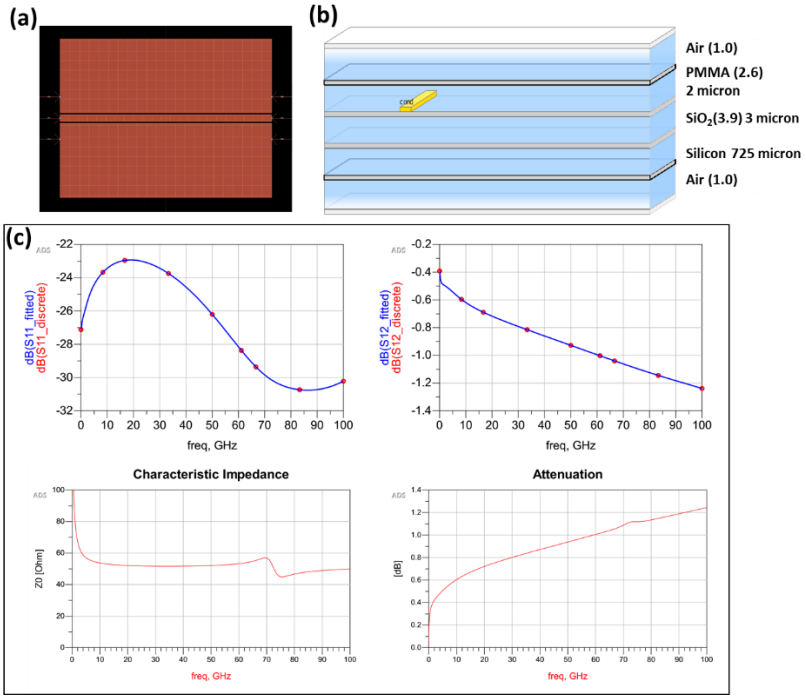

Figure 3-6 Images from Pathwave ADS software: (a) the design of coplanar waveguide (CPW) electrode drawn in PCB/IC layout tool, (b) the definition of layer stack defined in the EM simulator, and (c) the simulation results presenting S-parameters, impedance, and attenuation.

3.1.2.3 Silvaco TCAD

Technology Computer-Aided Design or TCAD is another type of EDA software especially aimed to model the semiconductor devices (diode and transistor) with alternatively inputting steps of their fabrication process, such as diffusion and ion implantation. It is also capable to simulate the electrical behaviour of those modelled devices based on physical models of semiconducting materials. In this work, the TCAD software from *Silvaco* was adopted to simulate the electric field distribution in our EO-polymer modulator device during the polymer poling process and the DC/AC modulation [157]. The key advantage of this TCAD is to support a floating metal contact which is essential to the modelled device for polymer poling process. Another advantage is a capability to simulate the device with a transient waveform such as sinusoidal modulation signal.

The main tools in the TCAD which were employed for the simulations of EO-polymer modulator are *DeckBuild*, *DevEdi*t and *ATLAS* [158-160]. The *DeckBuild* was used to create and run the command script for co-operating the other tools step by step. For example, our command script is arranged to call *DevEdit* for drawing/meshing a modulator structure with CPW electrode (Figure 3-7(a)) and transferred to be simulated by *ATLAS* with 5V DC-bias on the centre conductor. Figure 3-7(b) presents an example of electric field in the simulated device when applying the DC-bias.

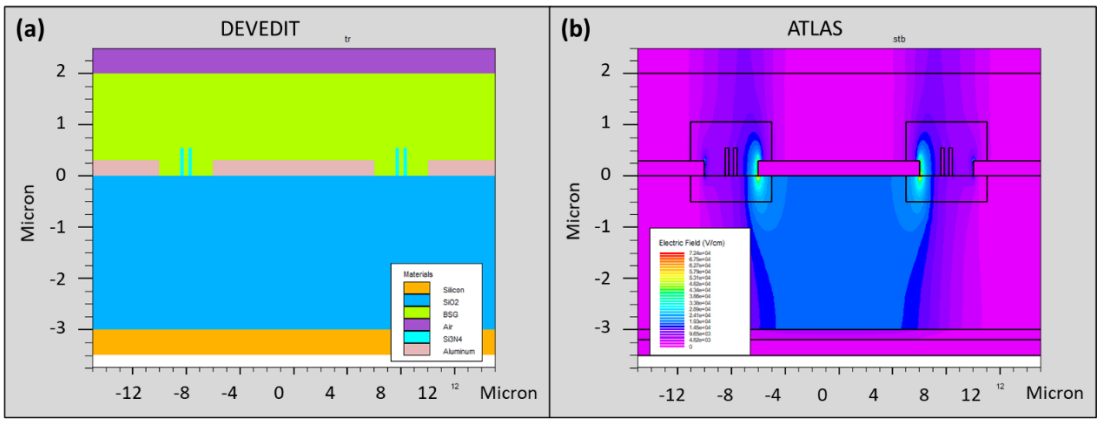

Figure 3-7 Examples of result using *Silvaco* TCAD software: (a) a device structure created by using *DevEdit* and (b) an electric field distribution of 5V DC-bias in device simulated with *ATLAS*.

3.1.3 Mask Designer

The mask designer in this context refers to the software developed for designing a mask used in lithography process. *Tanner L-Edit* is one of the commercial mask designer software which is developed by *Mentor Graphics Corporation.* This software supports an alternative mask drawing with programming code in *C++* language. In this work, *Tanner L-Edit* was chosen for preparing all the masks either in fabrication with photolithography or electron-beam (e-beam) lithography. By taking an advantage of programming ability, the variation of device design (such as sweeping width/length of waveguide) were systematically drawn and arranged into a layer in the mask by

implementing sets of device parameters and looping commands. Finally, the mask will be exported in standard GDSII file format which is support by most of the mask design software.

3.2 Passive Components

The passive components for building the Mach-Zehnder modulator (MZM) mainly consist of grating coupler (GC), waveguide, taper, bend, multimode interference structure (MMI), and Mach-Zehnder interferometer (MZI). In this session, the simulation model of these components is presented, and the optimization results are shown and discussed. Based on the different types and thicknesses of silicon nitride (SiN) using as a waveguide core material in this work, we have classified them into three waveguide platforms, and their layer stack are shown in Table 3-1. All materials in the simulation are defined as an optical lossless material.

Table 3-1 Dimension of the Mach-Zehnder modulator for three different designs.

Waveguide Core		**Lower Cladding**		**Top Cladding**	**Substrate**
Material	**Thickness (nm)**	**Material**	**Thickness (µm)**		
Stoichiometric SiN (n=2.0)	300	Buried Oxide (BOX, n=1.444)	2	2um-thick PMMA (n=1.48)	Bulk Si
Stoichiometric SiN (n=2.0)	600		3		
Si-rich SiN (n=2.5)	550		3		

3.2.1 Grating Couplers

In this work, the fully etched grating structures are designed to couple a TE-polarised beam incident from the optical fibre at the different coupling angle depending on the waveguide platform. The simulation procedure to optimise the grating coupler design was implemented by using 2D-FDTD solver in the software *Lumerical FDTD solution* for a centre wavelength of 1.550µm. Figure 3-8 shows the model using in the simulation and the definition of optimising parameters including a coupling angle, a grating period, a grating tooth width and a filling factor.

In the early phase of this work, a 300 nm Stoichiometric SiN was used for the simulation. The simulation procedure was performed to maximise the coupling efficiency. A TE-mode source is set above the waveguide while a mode monitor is set over the cross-section of fibre core inside the optical fibre. In this case, the coupling angle (θ) was fixed at 10°. The coupling efficiencies were calculated for every scanning step of grating period and filling factor. Figure 3-9(a) shows the coupling efficiency as a function of grating period (0.9 – 1.3 µm) at the filling factor of 57.8%. The coupling efficiency as a function of filling factor (10 – 90%) when the grating period is 1.06 is presented in Figure 3-9(b). The maximum coupling efficiency for this platform is equal to -11.3 dB when a grating period and a filling factor are 1.06 µm and 57.8%, respectively.

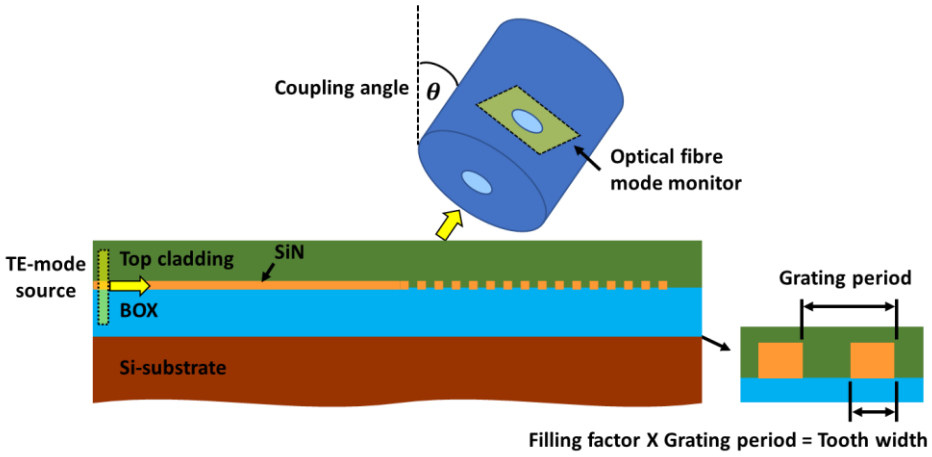

Figure 3-8 Schematice of the setup for the simulstion of grating coupler by using the optical fibre.

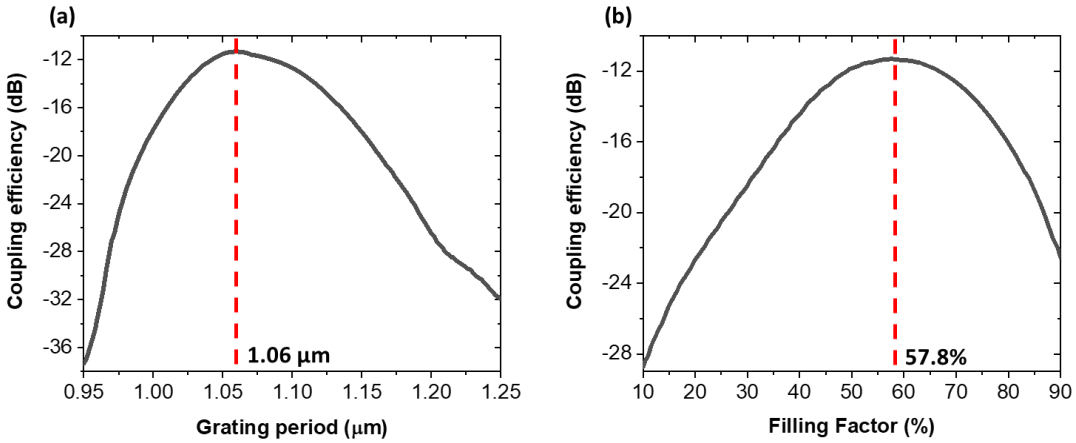

Figure 3-9 Coupling efficiency of grating coupler when the (a) grating period and (b) filling factor have been varied.

For the latter two platforms: 600 nm stoichiometric SiN and 550 nm Si-rich SiN, the simulation of grating coupler has been enhanced by using the far-field monitor as explained in Section 3.1.1.2. With a far-field monitor, the coupling angle can be directly obtained without scanning during the simulation. Therefore, only two design parameters including a grating period and a filling factor needed to be scanned to optimise three design parameters. The simulation model is set as shown in Figure 3-4(a). The TE-mode is assigned for the waveguide mode source, and the far-field monitor is set for monitoring all upward diffracted light from the grating.

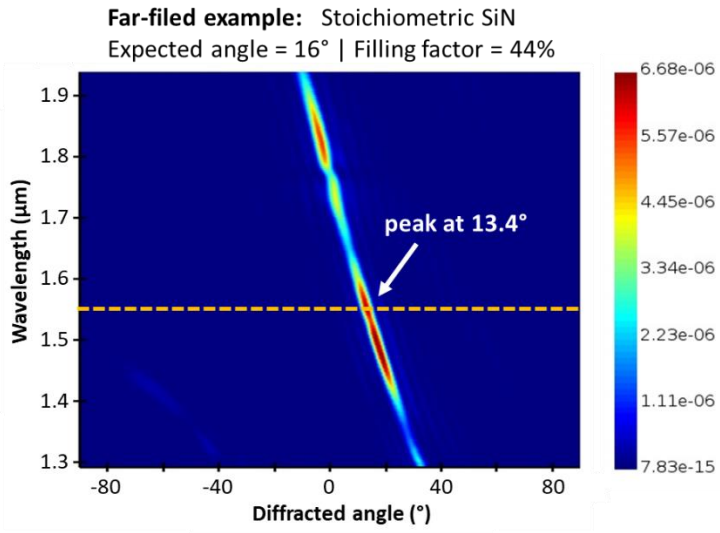

Figure 3-10 Intensity profile of the coupling signal when the wavelength is varied with diffracted angle of grating coupler for Stoichiometric SiN.

The monitor result is presented by an intensity profile in the wavelength domain and diffracted angle as shown in Figure 3-10. The profile is considered for a targeted centre wavelength of 1550 nm (dash line) where the diffracted angle at the peak intensity indicates the optimal coupling angle for this wavelength. To scan those design parameters, the filling factor is directly varied with an even step, however, the grating period is varied via another independent parameters which is the expected angle. Because the coupling angle of a grating is principally linked to this expected angle, the scanning range of expected angles can be implicitly used to define the approximated scope/limit of a target coupling angle. The relationship between the grating period and the expected angle is based on Bragg's equation as follows [161].

$$\Lambda = \frac{\lambda_0}{[ff \cdot n_{TE0} - (1-ff) \cdot n_{clad}] - \sin\theta_{exp}} \quad (49($$

where Λ is the grating period, λ_0 is the centre wavelength, ff is the filling factor, n_{TE0}, is the effective index of TE0-mode in waveguide, n_{clad} is the refractive index of cladding, and θ_{exp} is the expected angle. When all scanning simulations are implemented, the peak intensities from far-field profiles are integrated and plotted in Figure 3-11(a) for 600nm stoichiometric and Figure 3-11(b) for 550nm Si-rich SiN. Considering the peak intensities in these graphs (green arrows), their expected angle, diffracted angle (equivalent to a coupling angle) and filling factor at the peaks are taken to be re-simulated by using the model with optical fibre mode monitor as explained in Figure 3-8. With this model, the spectra of coupling efficiency are calculated. For the 600nm stoichiometric SiN, the spectra calculated with three sets of peak parameters from Figure 3-11(a) are presented in Figure 3-11(c). For the 550nm Si-rich SiN, Figure 3-11(d) shows the spectra calculated with two sets of peak parameters from Figure 3-11(b).

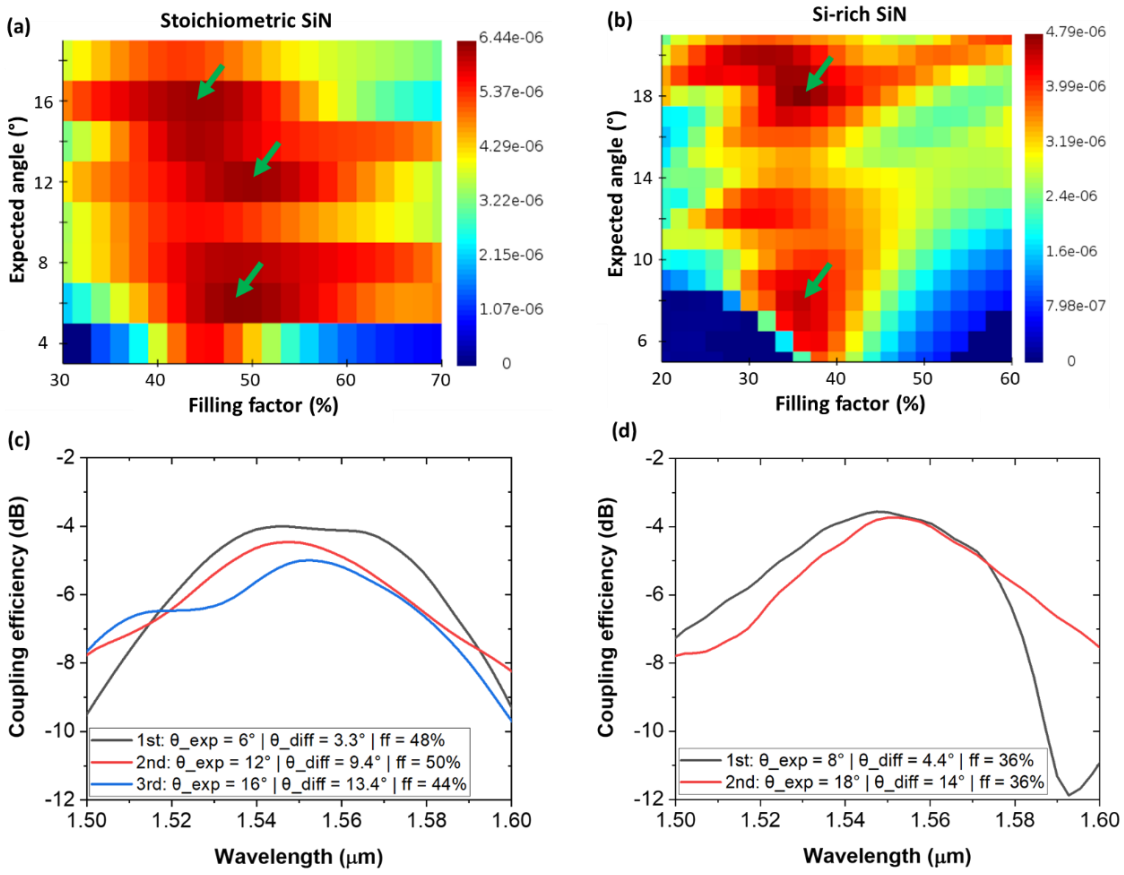

Figure 3-11 The peak intensities from far-field profiles when varying the expected angle and filling factor for (a) a 600nm stoichiometric and (b) a 550nm Si-rich SiN. The variation of coupling efficiency with wavelength for (c) a 600nm stoichiometric and (d) a 550nm Si-rich SiN.

To compare these spectra in term of grating performance, the grating parameters including the centre wavelengths(λ_{centre}), coupling efficiency, and coupling bandwidth are presented in Table 3-2. For the 600nm stoichiometric SiN, the first spectrum has the highest coupling efficiency and almost the same bandwidth as the largest one of the third design. Hence, its set of grating parameters is chosen to be the optimal design. For the 550nm Si-rich SiN, the parameter set in the first spectrum provides the best coupling efficiency while the bandwidth is only 2.6nm smaller than another, therefore, it is defined as the optimal grating design for this waveguide platform.

Table 3-2 Coupling efficiency and bandwidth of coupled signal from the grating to 600nm stoichiometric SiN and Si-rich SiN waveguides.

Core material	Spectrum order	Expected Angle (Coupling/Diff. angle)	Fill factor (%)	Period (μm)	λ_{centre} (μm)	Coupling eff. (dB)	2dB-bandwidth (nm)
600nm stoic. SiN	1st	6° (3.3°)	48	0.984	1.553	-4.07	63.7
	2nd	12° (9.4°)	50	1.049	1.547	-4.46	58.0
	3rd	16° (13.4°)	44	1.114	1.552	-5.01	64.3
550nm Si-rich SiN	1st	8° (4.4°)	36	0.928	1.546	-3.60	50.0
	2nd	18° (14.0°)	36	1.003	1.553	-3.75	52.6

In summary, the grating parameters and performance figures of all three waveguide platforms are concluded in Table 3-3 and will be applied for the fabrication.

Table 3-3 Summary of optimised parameters for the fabrication of grating coupler for different waveguide platforms.

Waveguide Core (nm)	Coupling angle	Fill factor (%)	Period (µm)	λ_{centre} (µm)	Coupling eff. (dB)	2dB-bandwidth (nm)
Stoic. SiN 300	10°	57.8	1.060	1.550	-11.3	-
Stoic. SiN 600	3.3°	48.0	0.984	1.553	-4.07	63.7
Si-rich SiN 550	4.4°	36.0	0.928	1.546	-3.60	50.0

3.2.2 Waveguides, Bends and Tapers

The waveguide-based components in this work are designed to be operated only on the fundamental TE-mode. The design of waveguides in this work are all based on a strip waveguide cross-section (without a slab layer). There are three types of those components that were optimised in this section as follows.

3.2.2.1 Waveguides

The FDE solver was used to search for the single-mode cut-off condition (width) of the waveguide. By varying the waveguide width, the simulation of waveguide cross-section provides the effective indices of all available modes. Another figure of the waveguide, which was also simultaneously calculated, is the group index. It will be utilised for estimating a free spectral range in MZI. These simulation results for all three waveguide platforms are presented in Figure 3-12 (a-f).

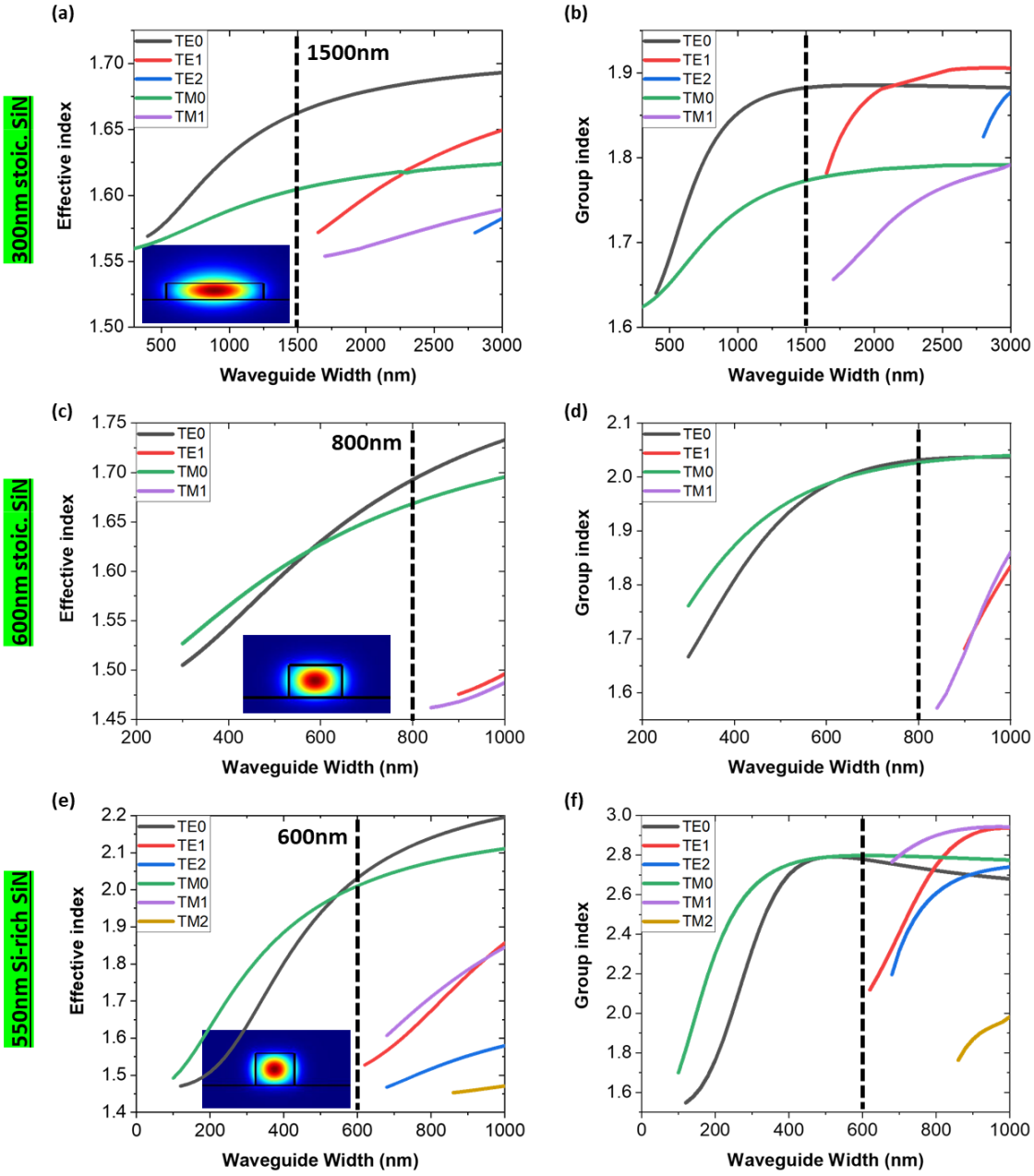

Figure 3-12 The effective index of TE and TM modes for (a) 300nm-thickness stoichiometric SiN, (c) 600nm-thickness stoichiometric SiN, and (e) 550nm-thickness Si-rich SiN with the variation of waveguide widths. The group index of TE and TM modes for (b) 300nm-thickness stoichiometric SiN, (d) 600nm-thickness stoichiometric SiN, and (f) 550nm-thickness Si-rich SiN with the variation of waveguide widths.

To nominate the waveguide widths corresponding to a single-mode cut-off condition, the widths were chosen with the dimension slightly smaller than the presence of a high order mode (e.g. TE1, TM1…). as indicated with the black dash-line in Figure 3-12. The optical intensity profiles of the single-mode cut-off width are presented in the inset images. These optimal widths for all waveguide platforms are concluded in Table 3-4 along with their TE0 mode properties.

Table 3-4 Optimised waveguide core and width for single-mode waveguide.

Waveguide Core (nm)	Width (nm)	Effective index	Group index
Stoic. SiN 300	1500	1.663	1.883
Stoic. SiN 600	800	1.693	2.032
Si-rich SiN 550	600	2.032	2.779

3.2.2.2 Bends

Once the optimal widths for single mode waveguides have been established, the FDE solver was applied again to simulate the optical profile of TE0-mode by enabling the bend radius settings as mentioned in section 3.1.1.1. Figure 3-13 shows the example of simulated optical mode profiles comparing between a straight waveguide (left) and in a bent waveguide (right) with a bend radius of 20µm for the 300nm stoichiometric SiN waveguide.

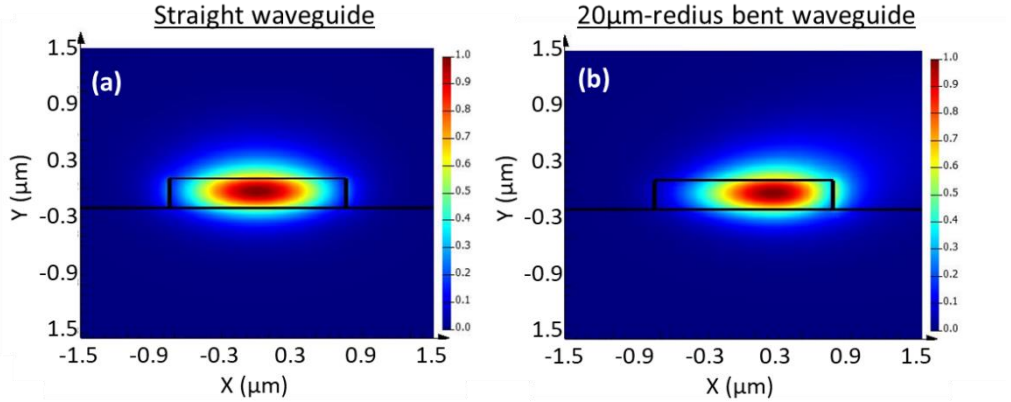

Figure 3-13 Modal profile the guided mode (TE0) in (a) a straight and (b) a 20µm bent stoichiometric SiN waveguide.

In principle, there are two major sources of the bend loss including a propagation loss in bent waveguide and mode mismatch losses between the straight and the bent waveguide. For the mode mismatch loss, it can be calculated by using the overlap analysis tool in FDE solver. This tool can be used by calculating the power overlap factor (Γ) between the modes, and the mode mismatch loss which is obtained by taking this overlap factor into the formula: $Loss_{mismatch} = -10log_{10}(\Gamma)$. If the propagation loss ($Loss_{prop}$) in bent waveguide is obtained, the total bend loss can be calculated by adding the mode mismatch losses at the two interfaces between the straight and bent waveguide with the known propagation loss for 90°-bend [162].

$$Loss_{total,\ 90°-bend} = -2_{interfaces} \times 10log_{10}(\Gamma) + \left(Bend\ radius \times \frac{\pi}{2} \times Loss_{prop}\right) \quad (50($$

By varying the bend radius in the simulation settings, Figure 3-14(a-c) show the 90°-bend loss as a function of bend radius for all three waveguide platforms. The added propagation losses are

assumed to be varied from 0 to 4 dB/cm. As shown in Figure 3-14, bend loss of all platforms are decreased with an increasing of bend radius until its reach the minimum point. The minimum point in each curve represents the minimum loss which indicates a transition between the influence of a mode mismatch loss and a propagation loss. With the increment of bend radius, the propagation loss is becoming more prominent because the total length of bent waveguide increases. The effect of propagation loss in the long propagation length due to an increasing of bend radius resulting in an increasing of bend loss after the minimum point. Therefore, the position of minimum loss is shifted to a smaller radius when assuming that the propagation loss is decreased. By comparing the curve in the same SiN waveguide with different added propagation loss, the result showing that the bend loss in the waveguide with added propagation loss of 4 dB/cm and 2 dB/cm are dramatically increased after the minimum point. While the bend loss of the waveguide with the added 1 dB/cm-propagation loss are more stable for all SiN platforms. The optimal bend radii can be defined by choosing the minimum point of these minima. Thus, in this work, the optimal bend radii are chosen by using the 1dB/cm curve to avoid the exponential loss of the mode mismatch effect. Thus, the optical radii of 300nm, 600nm stoichiometric SiN and 550 Si-rich SiN are 185, 50 and 25µm, respectively.

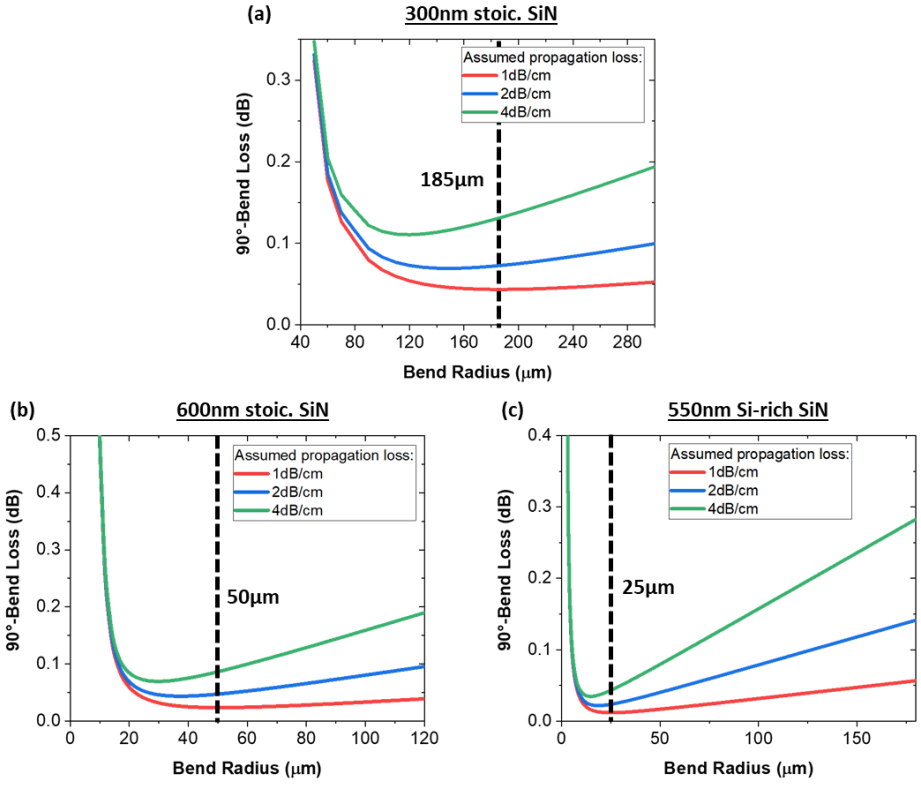

Figure 3-14 Variation of 90°-bend loss of the waveguide with different added propagation loss for (a) 300nm stoichiometric SiN, (b) 600nm stoichiometric SiN, and (c) 550 Si-rich SiN.

3.2.2.3 Tapers

In this section, the taper structures were designed intently for converting the TE0-mode from a grating coupler to the waveguide. To coupling the signal from grating to waveguide, the dimension

of the taper will be defined by the dimension of the grating width and waveguide width. One of taper width will be equal to width of grating coupler, which is 10µm, and another is equal to width of the single-mode waveguide depending on the waveguide platform. The EME solver as explained in section 3.1.1.1 was applied for optimising the taper length. By sweeping the taper length in the simulation model, the S-parameters of mode transfer from one to another end of taper are calculated. The square of S-parameter indicates the mode transmittance of the taper. The transmittances as a function of taper length are presented in Figure 3-15(a-c). The result showing that the longer taper length can provide a higher transmittance which indicates well completeness of mode conversion; however, it also decreases a compactness of the design. Therefore, the optimal taper lengths are defined by choosing a taper length at the beginning of curve saturation. The optical taper lengths are approximately report as 230, 220 and 230µm for 300nm, 600nm stoichiometric SiN and 550 Si-rich SiN, respectively.

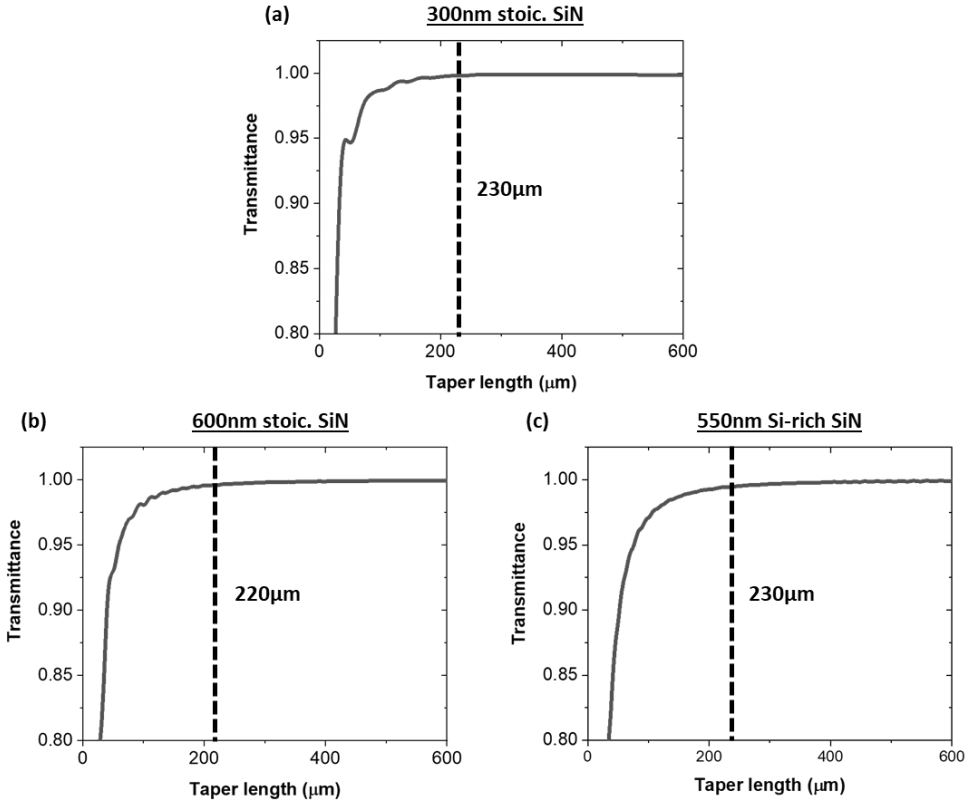

Figure 3-15 The graph between the transmittance from the coupling taper with the changing of taper length for (a) 300nm stoichiometric SiN, (b) 600nm stoichiometric SiN, and (c) 550 Si-rich SiN.

3.2.3 Multi-mode Interference (MMI) Coupler

The MMI had been designed to be used for splitting and combining the optical power in the SiN waveguides. In this work, two types of MMI such as 1x2 and 2x2 MMI were selected. A 2x2 MMI was selected for the early stage of the device fabrication with a (300nm stoichiometric SiN)

strip waveguide modulator design. A 1x2 MMI became a replacing component in the later-fabricated devices because its power splitting balance has more tolerance to the fabrication deviation. The top view of 1x2 and 2x2 MMI design are presented in Figure 3-16 (a) and (b). They consist of three sections including a section of one input waveguide for 1x2 or two input waveguides for 2x2, a section of multi-mode cavity of width (W_{MMI}) and length (L_{MMI}), and a section of two output waveguides. In the sections of input/output waveguide, the width of waveguide is equal to the optimal width of a single mode waveguide obtained in section 3.2.2. Between the sections, the taper of width (W_{taper}) and length (L_{taper}) is joined to support the mode transfer between taper and MMI. The distance between output waveguides is one of the important parameters. In this MMI design, the waveguide separation (S_{WG}) is which is sufficiently wide for negligible mode coupling between waveguides. These separations are specified by 9.8, 6.0 and 6.0µm for the MMI in the platforms: 300nm, 600nm stoichiometric SiN and 550nm Si-rich Sin, respectively.

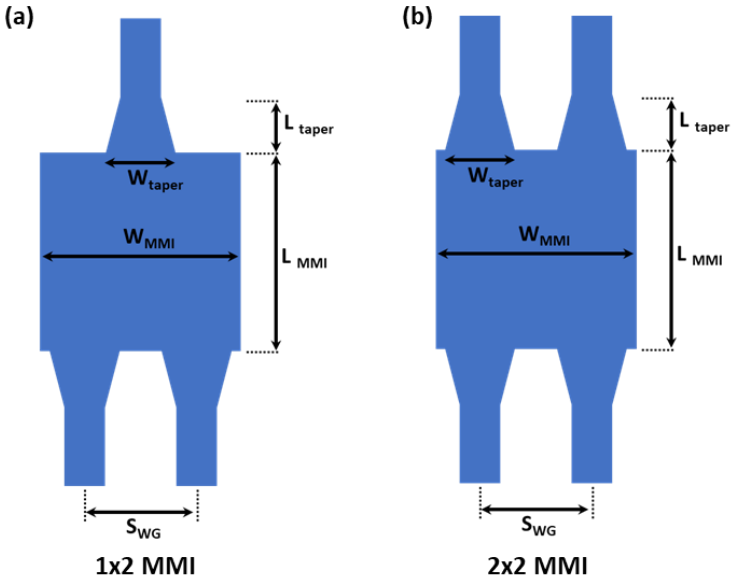

Figure 3-16 The top-view of MMI design with two designs of (a) 1x2 MMI and (b) 2x2 MMI.

Based on the predefined S_{WG}, a two-fold self-image in the MMI cavity is expected to match with this distance. By assuming a similarity of the two-fold self-image and TE1-mode profile in the cavity, FDE solver was used to simulate the optical mode profiles over the MMI cavity cross-section along to scanning W_{MMI}. The optimal W_{MMI} was found when its TE1-mode can provide a separation distance between two optical field peaks matching to S_{WG} value as presented in Figure 3-17. The optimal W_{MMI} obtained from the simulation are 8, 12 and 12µm for the 300nm, 600nm stoichiometric SiN and and 550nm Si-rich SiN, respectively. In addition, W_{taper} were defined by the approximated width of this optical field peak in TE1-mode which are 6.7, 4.0 and 4.0µm for the 300nm, 600nm stoichiometric SiN and and 550nm Si-rich SiN, respectively. By using the existing method of taper

optimisation (in section 3.2.2), the optimal taper lengths L_{taper} of for the 300nm, 600nm stoichiometric SiN and and 550nm Si-rich SiN were given as 120, 60 and 40 µm, respectively.

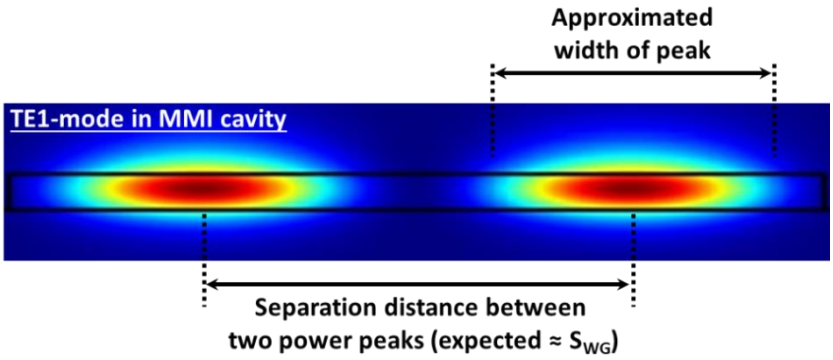

Figure 3-17 Example of TE1-mode profile in MMI cavity.

To finalise the MMI design, the MMI cavity length (L_{MMI}) was initially approximated by using the formulas $L_{MMI} = \frac{3L_\pi}{8}$ and $L_{MMI} = \frac{3L_\pi}{2}$ [163]. Here, (L_π) is the MMI beat length and can be expressed as $L_\pi = \frac{\lambda_0}{2(n_{eff,0} - n_{eff,1})}$ where λ_0 is the centre wavelength, and $n_{eff,0}$ and $n_{eff,1}$ are the effective index of TE0- and TE1-mode of MMI cavity. The sets of numbers for calculating the approximated L_{MMI} on every given platform are presented in Table 3-5, and the calculated results are also appended to the end of the table.

Table 3-5 Optimised MMI parameters for different waveguide platform.

Waveguide Core	W_{MMI} (µm)	$n_{eff,0}$	$n_{eff,1}$	L_π (µm)	Approx. L_{MMI} (µm)
300nm stoic. SiN [2x2 MMI]	18.0	1.71719	1.71565	503.25	754.87
600nm stoic. SiN [1x2 MMI]	12.0	1.83586	1.83258	236.06	88.52
550nm Si-rich SiN [1x2 MMI]	12.0	2.30572	2.30304	289.61	108.60

EME solver was applied to simulate a full MMI component by scanning L_{MMI} around the approximated value. The MMI transmittances of each output waveguide and in total are presented as a function of scanning cavity length in Figure 3-18 for (a) 300nm stoichiometric SiN, (c) 600nm stoichiometric SiN, and (e) 550nmSi-rich SiN. The optimal L_{MMI} are marked by a dash-line at the peak of transmittance curves. Along with those transmittance curves, the simulated light propagation in the MMI is presented in Figure 3-18 (b, d and f). In conclusion, all the optimal dimension parameters of MMIs are summarised into the Table 3-6.

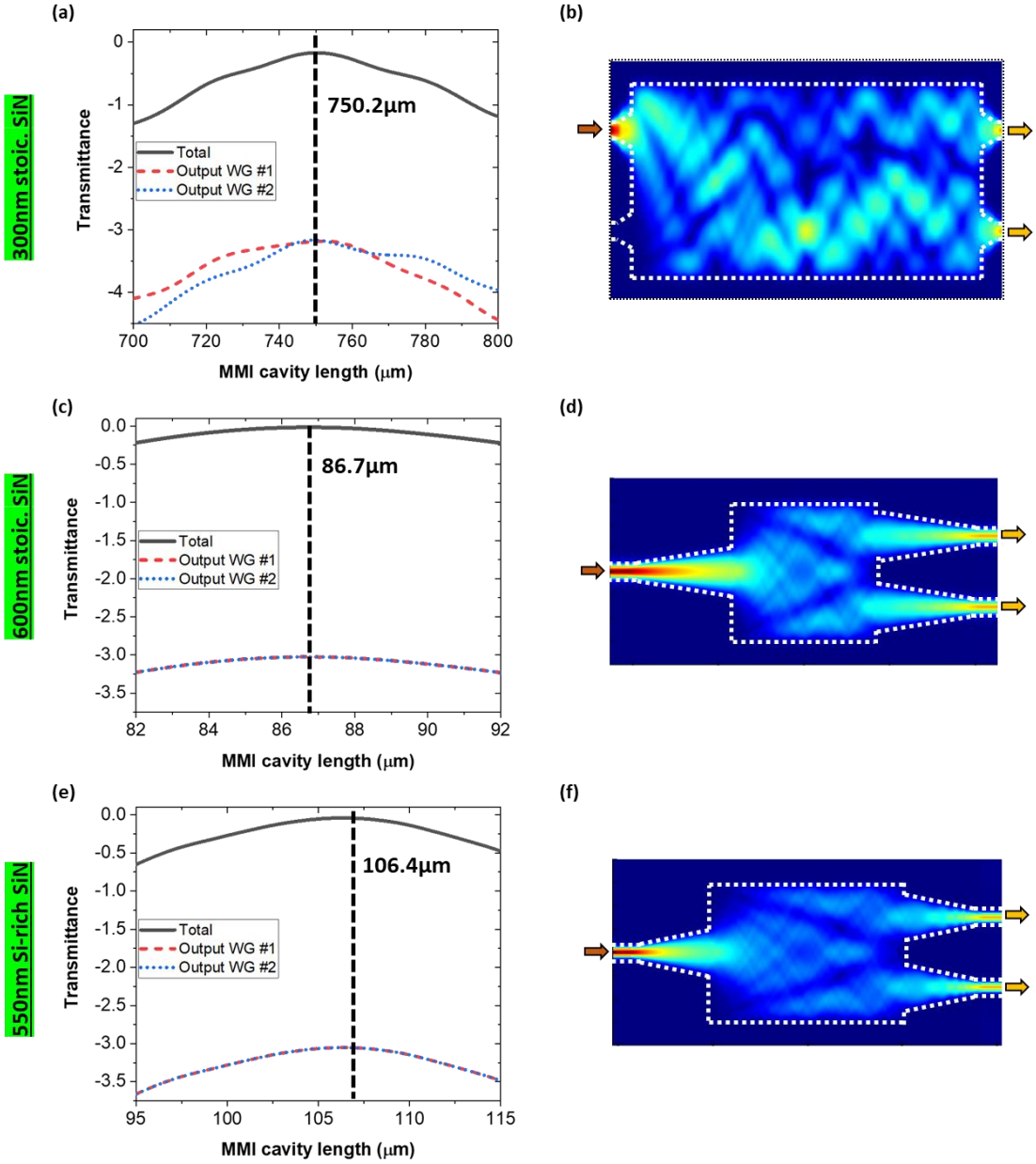

Figure 3-18 The transmittance of MMI for different waveguie platform of (a) 300nm stoichiometric SiN, (c) 600nm stoichiometric SiN, and (e) 550nm Si-rich SiN. The simulated modal propagation in the MMI for (b) 300nm stoichiometric SiN, (d) 600nm stoichiometric SiN, and (f) 550nm Si-rich SiN.

Table 3-6 The summary of the optimal dimension parameters of MMIs used in this work foe three waveguide platforms.

Waveguide Core	Waveguide width (nm)	W_{MMI} (μm)	L_{MMI} (μm)	S_{WG} (μm)	W_{taper} (μm)	L_{taper} (μm)
300nm stoic. SiN [2x2 MMI]	1500	18.0	750.2	9.8	6.7	120
600nm stoic. SiN [1x2 MMI]	800	12.0	86.7	6.0	4.0	60
550nm Si-rich SiN [1x2 MMI]	600	12.0	106.4	6.0	4.0	40

3.2.4 Mach-Zehnder Interferometer (MZI)

The Mach-Zehnder interferometer (MZI) in this work mainly consists of two MMIs that plays a role of a beam splitter on the input side (left) and a beam coupler on the output side (right). The schematic of MZI is exhibited in Figure 3-19. The MMIs in this structure can be either 1x2 MMI or 2x2 MMI. These MMIs are connected to each other by two single mode waveguides so called the MZI arms. Due to the aim of asymmetric MZI design, the MZI arms are designed to have different lengths, and this length difference is so called "Path Difference". The split light waves from the input MMI will travel over different path length and join up together again at the output MMI. As a result of difference in propagating distance, the interference is produced in the output signal as presented in section 2.4.1.

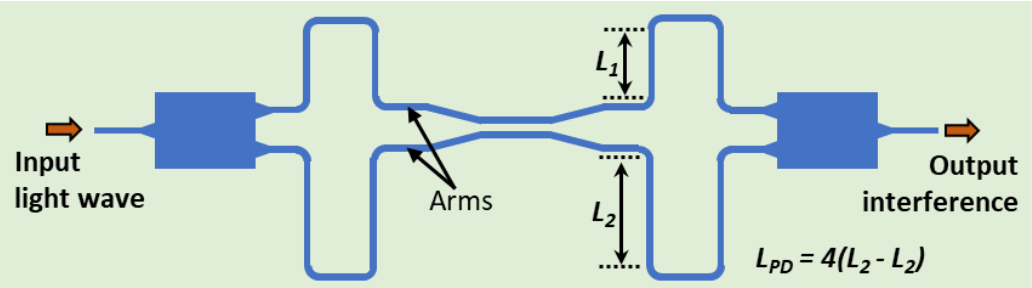

Figure 3-19 The schematic of Mach-Zehnder interferometer (MZI) used in this work.

A free spectral range (FSR) in the output interference of MZI is related to the length of MZI path difference (L_{PD}) and can be express as

$$FSR = \frac{\lambda^2}{n_g L_{PD}} \qquad (51($$

where λ is the operation wavelength, and n_g is the group index of TE0-mode in the MZI waveguide arms. In this work, we expected to produce the interference with FSR of ~10 nm in which periodic pattern is not too small for observing the modulation behaviour and not too large to observe in a spectral band (C-band). According to the simulated group indices from section 3.2.2, the corresponding path differences for all waveguide platforms are calculated and presented in Table 3-7.

Table 3-7 The summary of optical parameters for the MZI.

Waveguide Core	Wavelength (nm)	group index	Expected FSR (nm)	Path diffrence (µm)
300nm stoic. SiN [2x2 MMI]	1550	1.883	10	127.6
600nm stoic. SiN [1x2 MMI]		2.032		118.2
550nm Si-rich SiN [1x2 MMI]		2.779		86.5

3.3 Strip Waveguide Modulator

In the early phase of this work, the design method was focused only on a simple modulator structure and a basic optimisation strategy to demonstrate the possibility of sample fabrication and characterisation processes. Therefore, the design of optical modulator had been initiated from a combination of regular strip waveguides and in-plane electrode which does not require a complicated optimisation procedure prior to fabricate the devices.

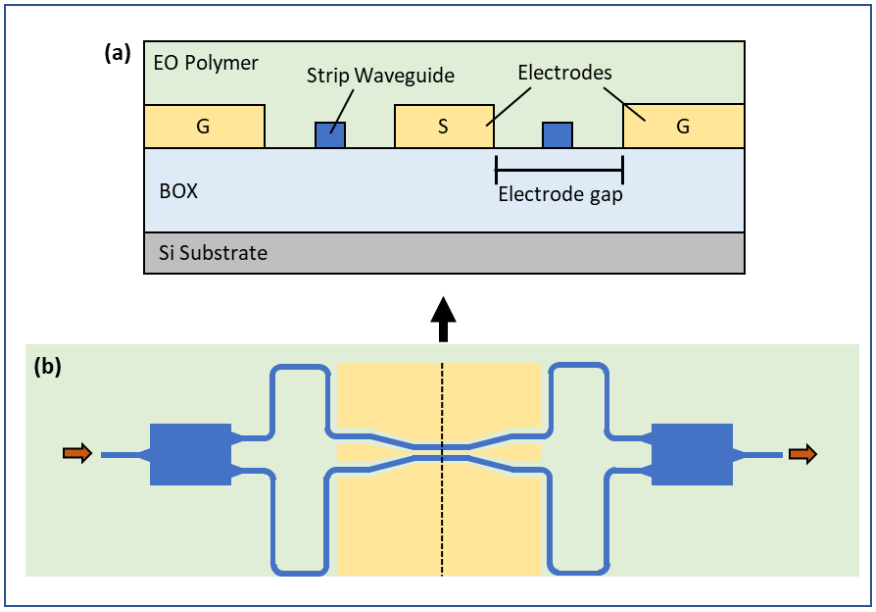

Figure 3-20 (a) Cross-section of modulation region in the modulator device. (b) Top-view of the schematic of modulator including grating coupler, taper, MMI, and MZI.

According to the use of asymmetric MZI for the main structure of testing devices as presented in section 3.2.4, the metal electrodes are arranged parallel to the arms of MZI as demonstrated in Figure 3-20(b). The layer stack (top-to-bottom) of this device comprises 2µm-thick EO polymer/SiN and electrode/2µm -thick buried oxide (BOX)/Si-substrate. In the cross section of the two arms of the MZI, two strip waveguides are located in the middle of Ground-Signal-Ground (GSG) electrode gaps in which full-filled by EO polymer as illustrated in Figure 3-20(a).

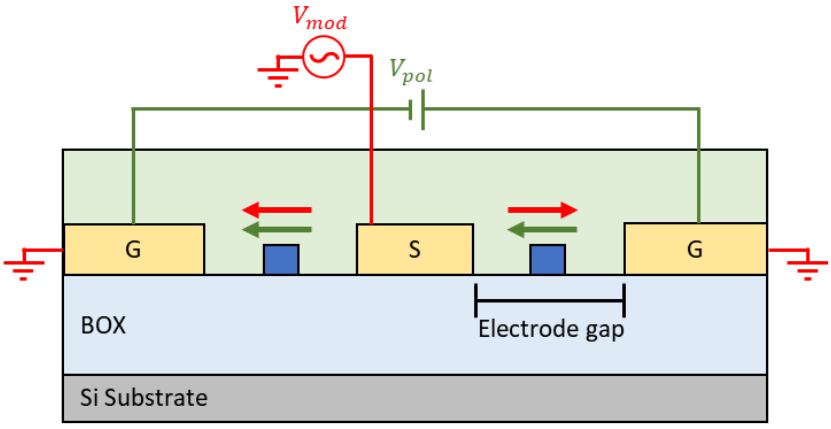

Figure 3-21 Schematic of GSG electrode together with the strip waveguides structure showing that this designed electrode can be used for both poling and modulating the device.

With the advantage of the GSG electrode design in this device, it allows to implement the poling process as well as the modulation by using the same electrode with different electrical connection as shown in Figure 3-21. The poling voltage (V_{pol}) is applied between the ground conductors of GSG while the signal (middle) conductor is left as a floating metal. This generates an electrical poling field in the electrode gaps (green arrows), thereby aligning chromophore molecules in EO polymer. For modulation, the GSG design also enables a capability of push-pull modulation which helps to shorten the modulator length by a factor of 2 comparing to a single-phase modulator. When the modulation signal voltage is applied to the signal conductor and others are held to the electrical ground, it generates an electric field across the electrode gap (red arrows) that are parallel (antiparallel) to the orientation of chromophore molecules in the gap. As a result of the Pockel's effect in EO polymer cladding, the optical phase in one of the MZI arms will be pushed forwards while the other will be pulled backwords, therefore the push-pull operation is achieved.

3.3.1 Simple Strategy for Optimisation of Electrode Design

In term of high-speed optical modulator, the electrical modulation signal can be considered as a RF-signal in the range of tens gigahertz or microwave frequency. To design the GSG electrode for operating at the speed of tens gigahertz, the principle of coplanar waveguide (CPW) must be considered. The target of CPW design is to have 50Ω-impedance and low transmission loss. Thus, three geometric parameters of the CPW need to be optimised in this purpose including electrode thickness, electrode gap and width of the signal (middle) conductor.

To simplify the steps of design optimisation, some parameter can be defined by using a fabrication limit. For example, the electrode thickness was specified by 500nm which was the thickest metal pattern fabricated by our typical lift-off process at that time. As described in section 2.4.2, a thicker electrode is preferred as providing a lower transmission loss in CPW, thereby the thickest value of metal electrode is chosen. On the other hand, the electrode gap is optimised by

considering a perturbation effect on the effective index of the optical mode. The FDE simulation in *Lumerical MODE solution* is used to calculate the propagation loss in only one of the MZI arm at the centre of electrode gap which is depicted in Figure 3-22(a). The waveguide width is set to be the same width as a single mode condition defined in section 3.2.2. As a result of sweeping the electrode gap, Figure 3-22(b) shows that the effective index is stable when the electrode gap is larger than 4µm. However, the electrode gap of 6µm was chosen for the device fabrication when considering the possibility of 1µm-misalignment between the waveguide and metal electrode during a photo-lithography process.

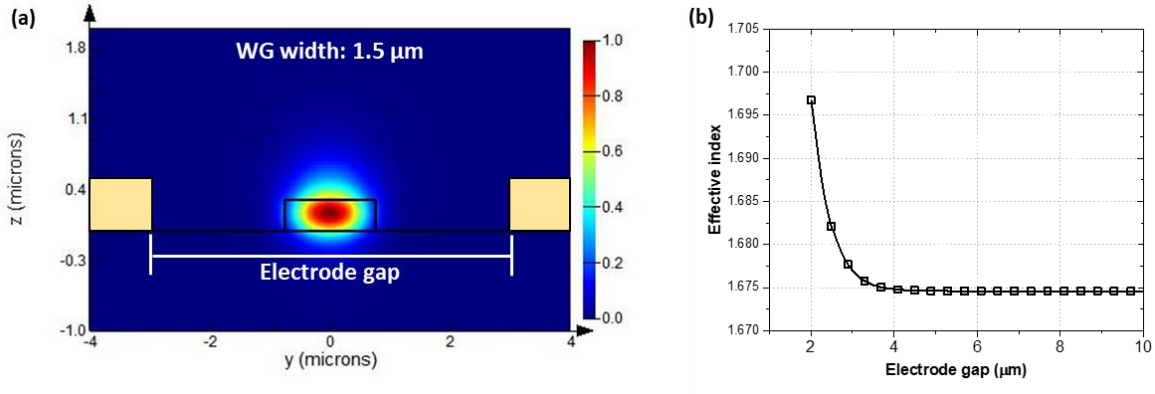

Figure 3-22 (a) Optical simulation of guided mode in the waveguide in the electrode gap to observe the effect of electrode to the loss. (b) Variation of effective index of guided mode in the waveguide to the changing of electrode gap.

The *TX-Line 2003* software was used to optimise the width of signal conductor. Due to the limit of structure configuration in this software, the device model was simplified by ignoring the existence of waveguides, EO polymer and BOX layer as shown in Figure 3-23(a). The target frequency for calculating an impedance and loss was 40 GHz as a typical modulation speed of our testing equipment. The conductive material of electrodes is defined as aluminium with a conductivity of 3.53×10^7 S/m. The 725µm-thick Si-substrate has a dielectric constant of 11.9 and a loss tangent of 0.001.

In order to investigate the effect of a signal conductor width to the characteristics of CPW, the width is scanned with the range of 1 to 20µm. Figure 3-23(b) shows the decrement of electrode impedance and transmission loss against the increment of signal conductor width. The optimum impedance of 50Ω can be obtained at the width of 10µm, and the transmission loss is 6.2dB/cm. When the width of signal conductor is fixed at 10µm and the frequency is swept from 1GHz to 80GHz, Figure 3-23(b) shows the saturation of impedance about 50Ω in the frequency range of 15-80GHz. The transmission loss is lower than 5dB/cm at the frequency lower than 25GHz while it linearly increases at a higher frequency. Due to a skin effect in the conductor, the skin depth starts to be thinner than the conductor thickness at frequency of 27GHz. This leads to the increment of loss at a higher frequency. The impedance value represents the transferable ability of AC signal between

the CPW electrode and its attached device in the experimental setup e.g. GSG-probe, RF cable, signal and pattern generator. The CPW design aims to come up with a 50Ω-impedance in order to be matched with the standard 50Ω-impedance of those attached devices. As a result of matching impedance, the CPW-to-device connection provides the highest signal coupling power as well as the lowest signal reflection.

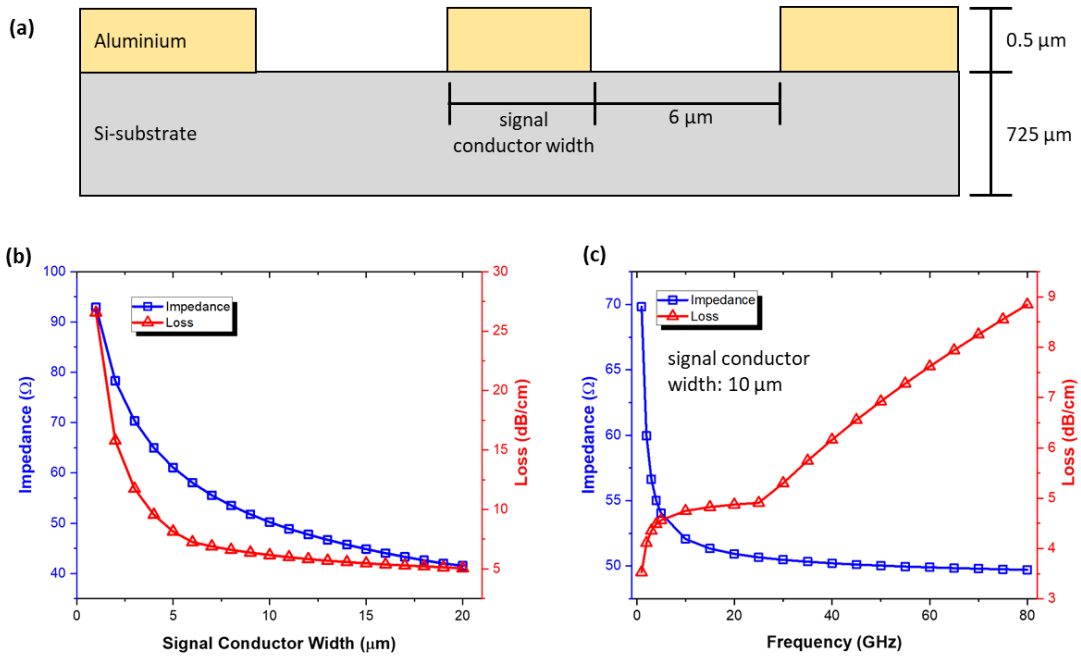

Figure 3-23 (a) Schematic of the cross-section of electrode design. The relation between the electric impedance and loss with the changing of (b) signal conductor width and (c) frequency.

Other than the design of GSG electrode in the modulation region (called "modulating electrode"), the design of electrode in the probing regions (called "probing pads") is also required for the optimisation process. The probing pads are for being contacted with a GSG type of RF-probe during the experiment. The boundaries of probing region are defined on both ends of GSG electrode as shown in Figure 3-24. Based on the standard configuration of the RF-probe existing in our laboratory, there are three common size of probes with pitch of 100, 150, 200µm. Accordingly, the design of probing pads is constrained by these probe pitch. In this case, the gap and the width in probing pads are designed to support the smallest pitch 100µm, and it is also compatible with the larger pitches as an inflated width of the ground pad. Therefore, the sum of width and gap must be equal to the chosen pitch (100µm).

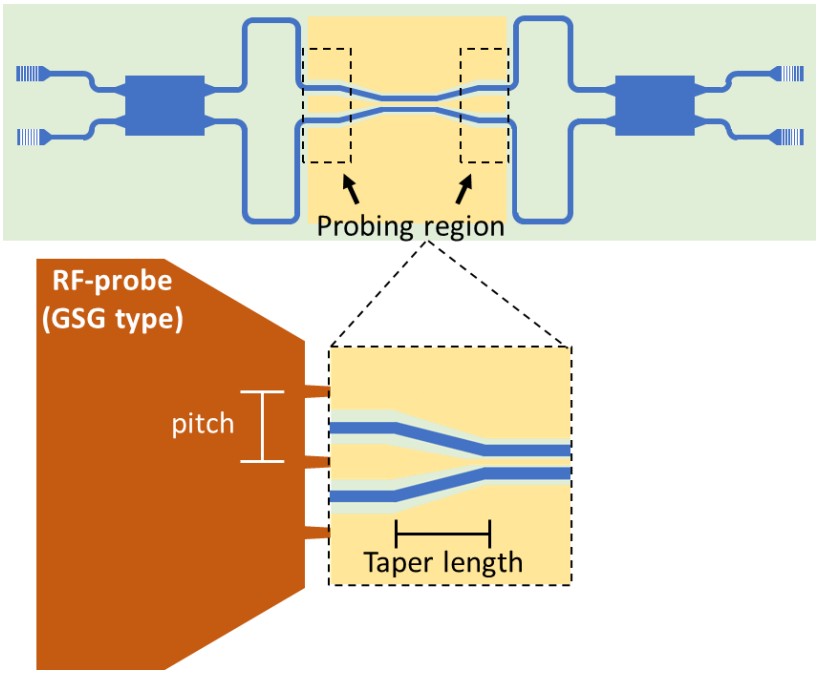

Figure 3-24 Top-view of the modulating device showing the probing region for the signal modulation.

By following the optimisation steps for the modulating electrode, the investigation of optical perturbation by metals is not necessary for the design of probing pad as the electrode gap is several times larger. Figure 3-25 shows the impedance optimised width around 64µm (with the gap of 36µm) and operating frequency range above 10 GHz with roughly linear increment of transmission loss. As a result, the optimal width and gap of probing pads are much larger than those of modulating region. To link these pads to the modulating electrode, a tapering structure is required to act as a RF-mode converter, and the taper length is initially specified with 300µm.

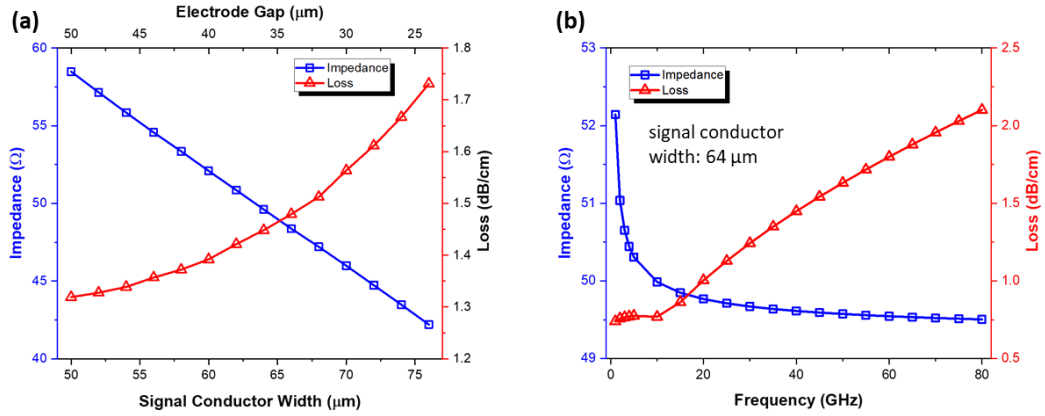

Figure 3-25 The relation between the electric impedance and loss with the changing of (b) signal conductor width and electrode gap and (c) frequency.

3.3.2 Widths of Modulation Waveguide

To improve the interaction between the optical mode and the modulating electric field in the electrode gap, the evanescent field of the optical mode in EO polymer needs to be enhanced. One of simple methods to improve this interaction is to narrow the width of waveguide. There are four different widths have been demonstrated in the early phase of this work including 0.6, 0.9, 1.2 and 1.5µm. The optical simulation result showing that the optical mode will be horizontally squeezed and expanded to EO polymer region as revealed in Figure 3-26.

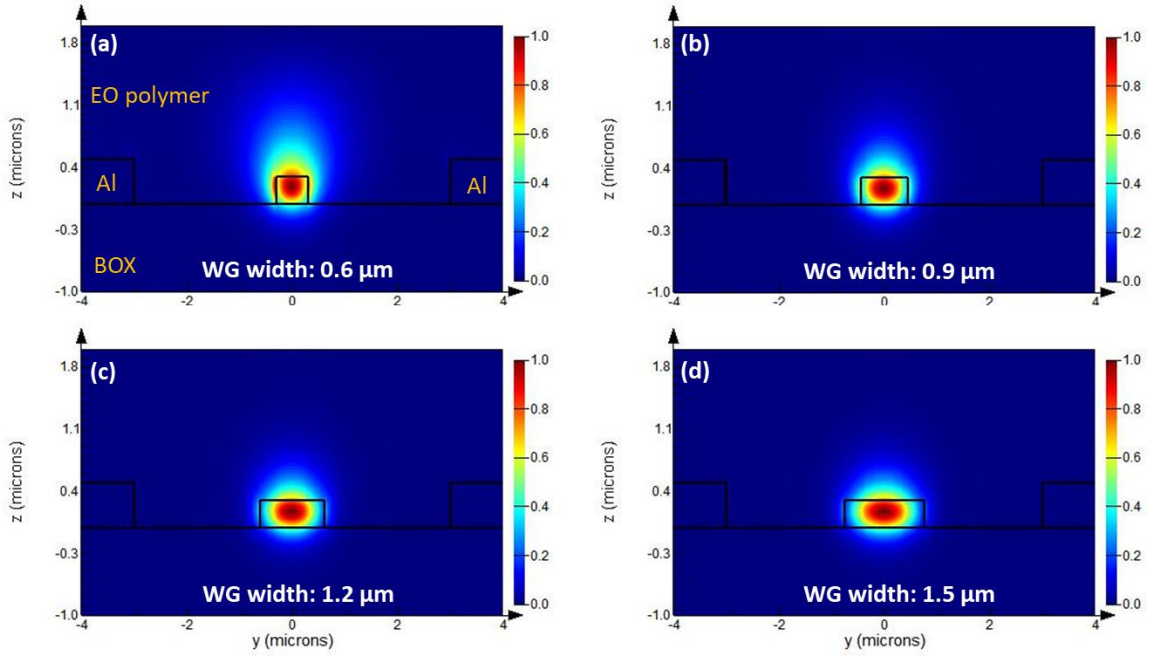

Figure 3-26 Modal profile of the guided mode in the waveguide with different waveguide width of (a) 0.6µm, (b) 0.9µm, (c) 1.2µm, and (d) 1.5µm.

3.4 Slot Waveguide Modulator

In the second phase of this work, the optical slot-waveguide structure has been utilised with the design of optical modulator in order to improve the interaction factor of electric fields between optical mode and electrical modulation signal. The main advantage of slot waveguides compared to strip waveguides is the guiding mechanism where the optical guided mode in the slot waveguide is partially confined in a slot (void structure) between two SiN strips. The slot can be filled with the EO polymer which is an interaction region between the fields to produce a modulation outcome. Therefore, the interaction factor can be improved without an expansion of the mode field distribution around the core material. This eases to provide a small electrode gap with low metal absorption loss.

Firstly, the optimisation method of the modulation waveguide design beginning with the scanning of the slot parameters to obtain the maximum optical power confined in a slot region. Secondary, the simulation model was revised by adding the metal electrode and implemented to

optimise the metal absorption loss. Then, the integral overlapping power is calculated, and the modulation efficiency is predicted. Finally, the structure of strip-to-slot coupler will be simulated.

3.4.1 Slot Design and Optimization Method

In this simulation model, a pair of SiN strip waveguides is presented as a main structure of the slot waveguide design. As indicated in Figure 3-27, three geometric parameters are involved to the optimisation of this structure including a strip thickness, slot width and strip width. BOX thickness of 3µm is thicker than the thickness defined in the former model (of strip waveguide modulator) to reduce an optical mode leakage by a Si-substrate. The upper cladding is defined with 2µm-thick PMMA based EO polymer. More than the use of stoichiometric SiN (n=2.0) for a core material, another waveguide material with Si-rich SiN (n=2.5) is also presented as an alternative platform for the slot design. The higher refractive index of Si-rich SiN aims to increase the index contrast and thereby improve the power confinement in the slot region while the lower index contrast in the stoichiometric SiN platform provides a tolerance for fluctuations from fabrication process and surface roughness.

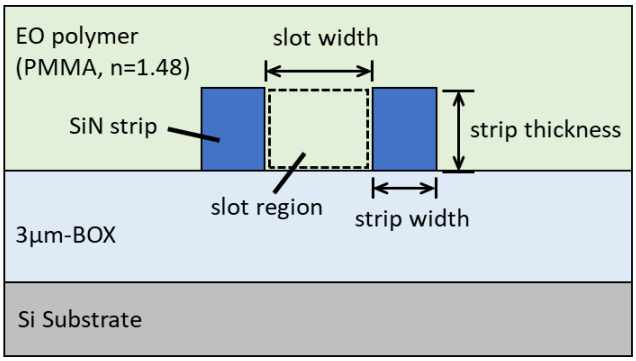

Figure 3-27 Schematic cross section of SiN slot waveguide showing two SiN ridges with slot spacing in between them which are cladded by EO-polymer.

For the first step of the optimisation method, the power confinement in between SiN strips (slot region) was considered as a key factor which indicates the performance of slot waveguide used for the modulator design. At a higher confinement power in the slot region, the optical power distributed outside the core was expected to be lowered which potentially means a possibility of smaller electrode gap. The slot waveguide was modelled and simulated to search for optical modes by using the FDE in *Lumerical MODE solution*, and three parameters including a strip thickness, slot width and strip width, were varied to find the maximum power confinement. In the simulation, only TE modes were chosen for calculating the power confinement, and one with the highest value was selected.

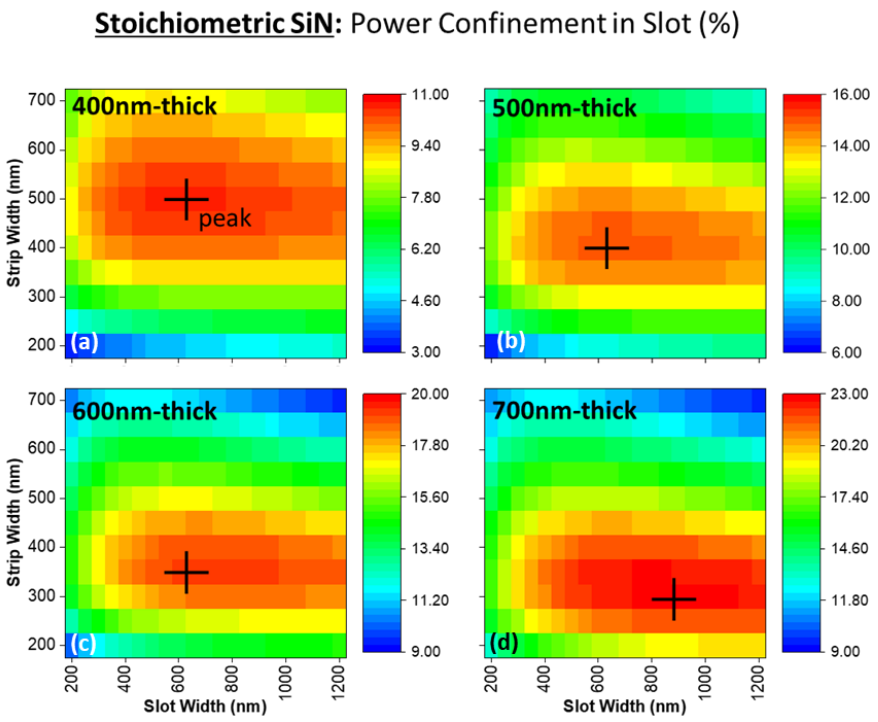

SiN thickness (nm)	Slot width (nm)	Strip width (nm)	Power Confinement in slot (%)
400	600	500	10.61
500	650	400	15.01
600	700	350	19.18
700	900	300	22.74

Figure 3-28 The intensity plotted of power confinement in the stoichiometric SiN slot wavguides with the variation of strip width and slot width with the waveguide thickness of (a) 400nm, (b) 500nm, (c) 600nm, and (d) 700nm. The table reported the percent of power confinement in the slot for different waveguide designs.

For stoichiometric SiN platform, the variation of strip thickness was defined with a set of four different values including 400, 500, 600 and 700nm. The slot width and strip width were swept by a step of 50nm in the ranges of 200-1200nm and 200-700nm, respectively. The simulations were performed to obtain the power confinement of a slot design with parameters in the defined range, and the results are presented as the intensity plots in Figure 3-28. The maximum point from each plot is marked with cross sign, and the parameters at maxima are presented in the table in Figure 3-28. By considering the optimisation results in this table, the increment of the thickness has an effect to improve the power confinement from 10.61% for 400nm to 22.74% for 700nm. It also implies that a thicker SiN strip allows to handle a larger slot width and smaller strip width which means to a larger slot region. It can be concluded that the power confining capability of slot waveguide is potentially improved by increasing a strip thickness.

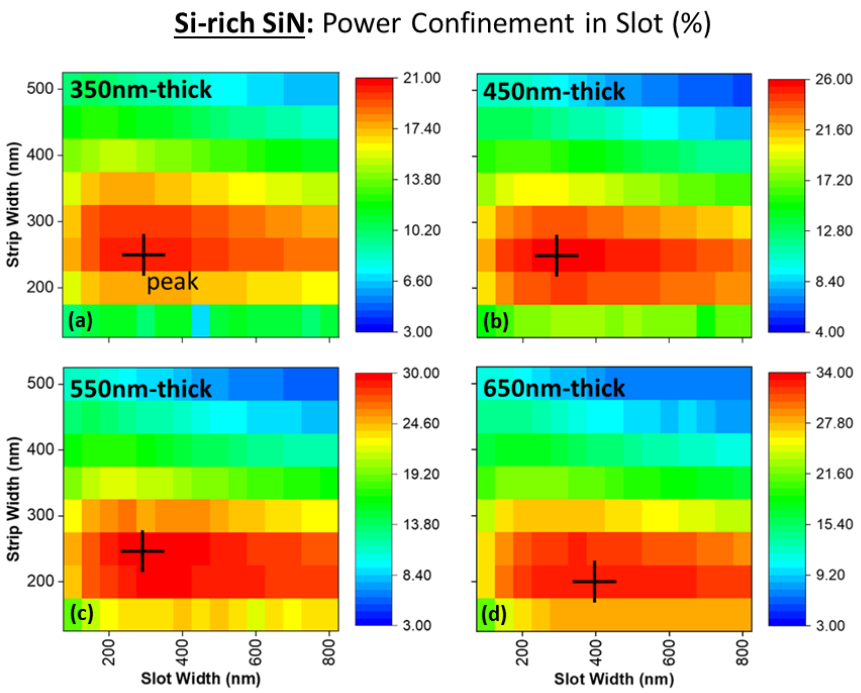

SiN thickness (nm)	Slot width (nm)	Strip width (nm)	Power Confinement in slot (%)
350	300	250	20.24
450	300	250	25.69
550	300	250	29.62
650	400	200	33.11

Figure 3-29 The intensity plotted of power confinement in the Si-rich SiN slot wavguides with the variation of strip width and slot width with the waveguide thickness of (a) 350nm, (b) 450nm, (c) 550nm, and (d) 650nm. The table reported the percent of power confinement in the slot for different waveguide designs.

For Si-rich SiN platform, the variation of strip thicknesses consists of 350, 450, 550 and 650nm. The slot width and strip width were swept by the step of 50nm in the ranges of 100-800nm and 100-500nm, respectively. The intensity plots in Figure 3-29 presents the power confinements from the simulations, and the maximum points from each plot are presented in the table. As for the optimisation results of the stoichiometric SiN platform, the power confinement is improved from 20.24% to 33.11% when the strip thickness is increased from 350 to 650nm.

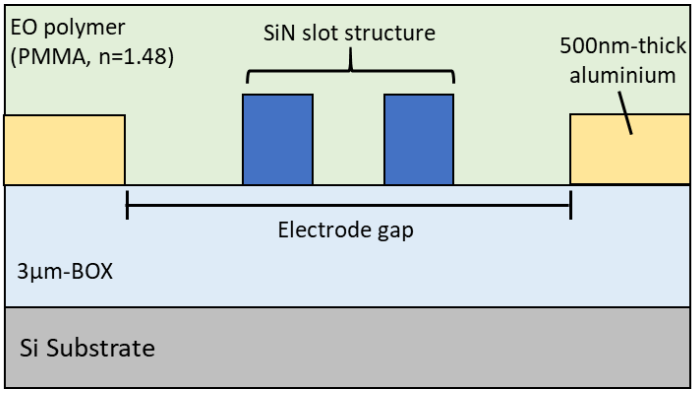

Figure 3-30 Schematic cross section of SiN slot waveguide for the second step of optimisation method showing SiN slot structure and electrode gap of the metal electrode with the thickness of 500nm.

In the second step of this optimisation method, the effect of electrode gap to a propagation loss of optical mode was studied. The metal electrode has been introduced into the simulation model from the previous optimisation step by setting the slot waveguide in the middle between two conductors as shown in Figure 3-30. A layer of aluminium with the thickness of 500nm is used for the conductors in this model. Using the optimal slot parameters from the first step, the simulation was performed to capture the propagation loss of the target TE mode along with a scan of electrode gap. Due to a definition of lossless SiN in this model, the captured loss was only established by the absorption loss of the metal electrode. In order to consider a minimum gap of electrode, the acceptable level of propagation loss was set to 1dB.

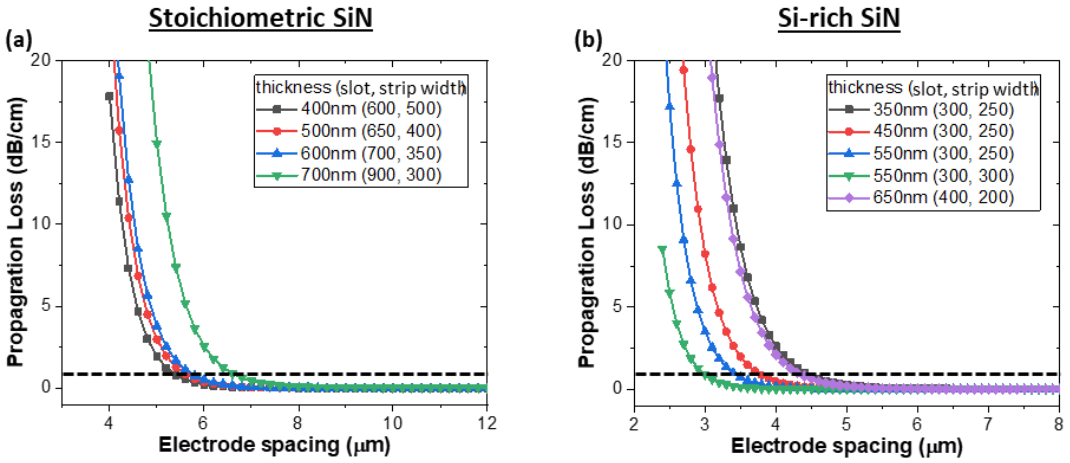

Figure 3-31 The relationship between propagation loss and electrode spacing of (a) stoichiometric SiN waveguide and (b) Si0rich SiN waveguide for different waveguide thicknesses, strip width, and slot width.

The electrode gap was varied from 4 to 12µm for the stoichiometric SiN platform while it was varied from 2.5 to 8µm for the Si-rich SiN platform. The propagation losses are exponentially decreased with the increasing of electrode gap as shown in Figure 3-31 (a-b). For the stoichiometric SiN platform, the electrode gaps at 1dB-loss for thickness of 400-600nm are clustered in a small

range of 5.1-5.4µm the electrode gap for the thickness of 700nm is about 6.7µm. Although the slot design with 600nm-thick strip requires a slightly larger electrode gap compared to the 400nm-thick design, the optical power confine in the slot is 2 times better. Therefore, the slot waveguide with 600nm-thick SiN was selected to be the optimal dimension for this platform.

For the Si-rich SiN platform, the electrode gap at 1dB-loss is varied from 3.4 to 4.4µm by the increment of strip thickness. Although the slot design with 650nm-thick strip can provide the smallest gap, this thickness was not applicable in our fabrication protocol due to a limit of etching selectivity of photoresist to Si-rich SiN. The slot waveguide with 550nm-thick SiN is therefore the most practical and optimal design for this platform. However, the aspect ratio of width-to-height of SiN strip is less than 0.5 (250nm:550nm) which will possibly introduce further difficulty in the fabrication process, where the waveguide may not withstand the ultrasonic cleaning. Therefore, the width of strips was considerably enlarged to 300nm to overcome the aspect ratio limit and has been chosen as the optimal design for this platform.

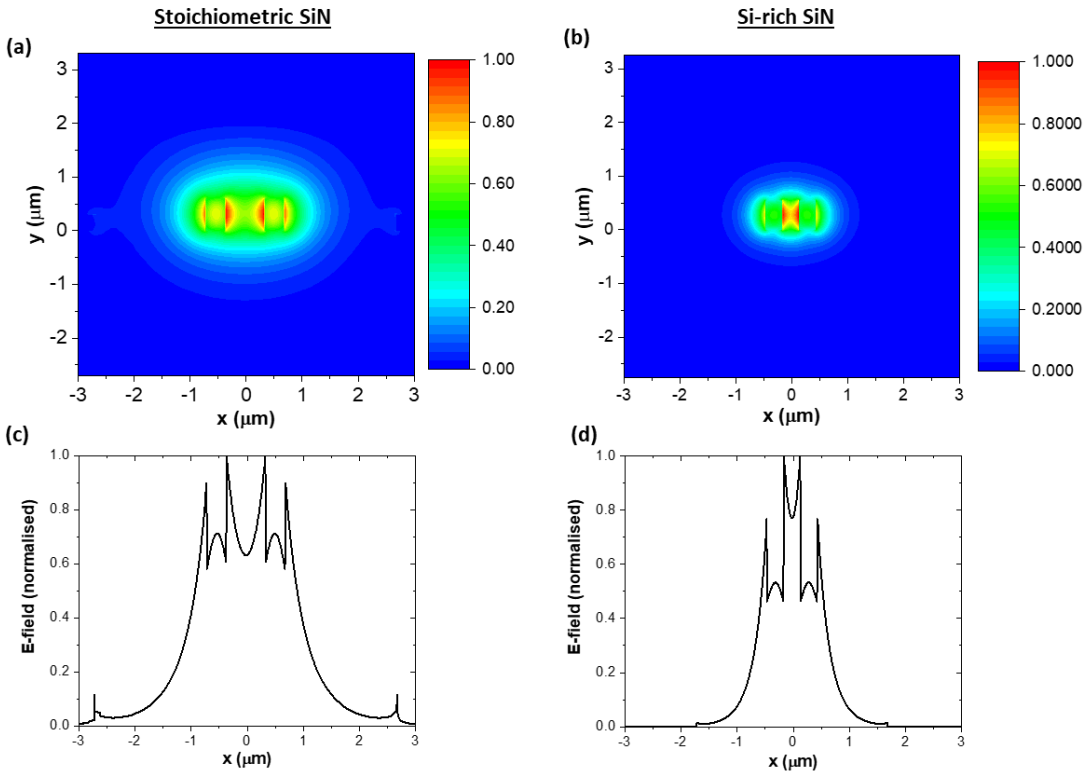

Figure 3-32 Optical mode guided in the optical design slot waveguide in (a) stoichiometric SiN and (b) Si-rich SiN. Electric field profile of guided mode in (c) stoichiometric SiN slot waveguide and (d) Si-rich SiN slot waveguide.

To present the optical mode guided in these optimal designs, the electric field profiles are plotted as a contour map in Figure 3-32(a) and (b), and the colour scale is already in a normalised unit. Due to a higher index contrast in the Si-rich platform, the optical mode is noticeably smaller than the mode in the other platform. Figure 3-32(c) and (d) show the electric fields (horizontally)

across the middle of the slot waveguide. By considering the electric field within a slot region (around x=0), the Si-rich slot waveguide exhibits an obvious difference of strength between the electric field in a SiN strip and a slot region. This is due to the higher index contrast and smaller slot width. Both smaller mode profile and higher confinement in slot is well supported the possibility to have a narrower electrode gap in this Si-rich SiN platform.

Table 3-8 Summary of the design parameters for stoichometric SiN slot waveguide and Si-rich slot waveguide and their optical properties.

Design Parameters					Fundamental TE-mode		
Core material	**SiN thickness (nm)**	**Slot width (nm)**	**Strip width (nm)**	**Electrode gap (µm)**	**Effective index | Group index**	**Power confinement in slot (%)**	**Power overlap integral in polymer (%)**
Stoic. SiN	600	700	350	5.4	1.536 | 1.737	22.14	57.54
Si-rich SiN	550	300	250	3.4	1.632 | 2.075	29.66	59.05
	550	300	300	3.4	1.704 | 2.265	26.34	49.45

Based on the Pockels effect, the electro-optic interaction possibly happens everywhere in EO polymer which is not only in a waveguide slot region. Therefore, the overlap integral of optical power over the polymer should be also calculated as one of the performance factors. The summary of optimal design parameters and TE-mode indices are presented in Table 3-8 including the power confinements and the power overlap integrals. By comparing the power overlap integrals between the designs, the Si-rich SiN design with 250nm strip width has nearly the same value as the stoichiometric SiN design while the 50nm-wider strip has ~10% reduction of this factor. However, the power overlap integral does not solely interpret a modulation efficiency of the design. There are several factors involving to explain the efficiency of EO polymer modulators such as the overlap between electric modulation field and optical field, and the poling efficiency. To precisely estimate the modulation efficiency, a dedicated simulation and calculation method is needed which will be presented in the next section.

3.4.2 Estimation of Voltage-length Product

To estimate the voltage-length product ($V_\pi L$) of the modulators, the Eq. (35) ($V_\pi \cdot L = \frac{\lambda d}{2n^3 \Gamma r_{33,in-device}}$) is considered. The overlap integral factor (Γ) will be obtained by the combination of the results from an electrical and an optical simulation while the in-device electro-optic coefficient ($r_{33,in-device}$) is assumed as equal to 100 pm/V

Firstly, the simulations of electric modulation field in the modulator were modelled by using the optimal parameters from the selected design in Table 3-8 and then performed by employing the TCAD software from *Silvaco.* In Figure 3-24, the 2D model of modulator includes two parallel slot waveguides placing incorporated with a GSG-electrode which is equivalent to a cross-section of

MZM. Without further optimisation on the electrode design, the inter-distance between MZI arm waveguides is obtained from the optimal value of 16µm from the strip waveguide design in section 3.3.1. Thus, the width of signal conductor is varied by the electrode gap which is equal to 12.6µm for stoichiometric SiN design and 10.6µm for Si-rich SiN design. For the material properties, the dielectric constants are defined as 7.5, 3.0 and 3.9 for SiN, EO polymer and buried oxide (BOX).

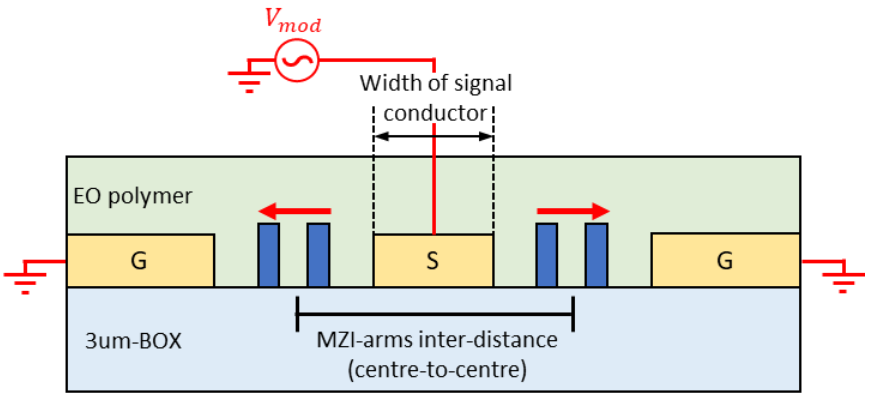

Figure 3-33 The cross-section of the modulating region of slot waveguide modulator including the two slot waveguides which are placed between the GSG electrode gap.

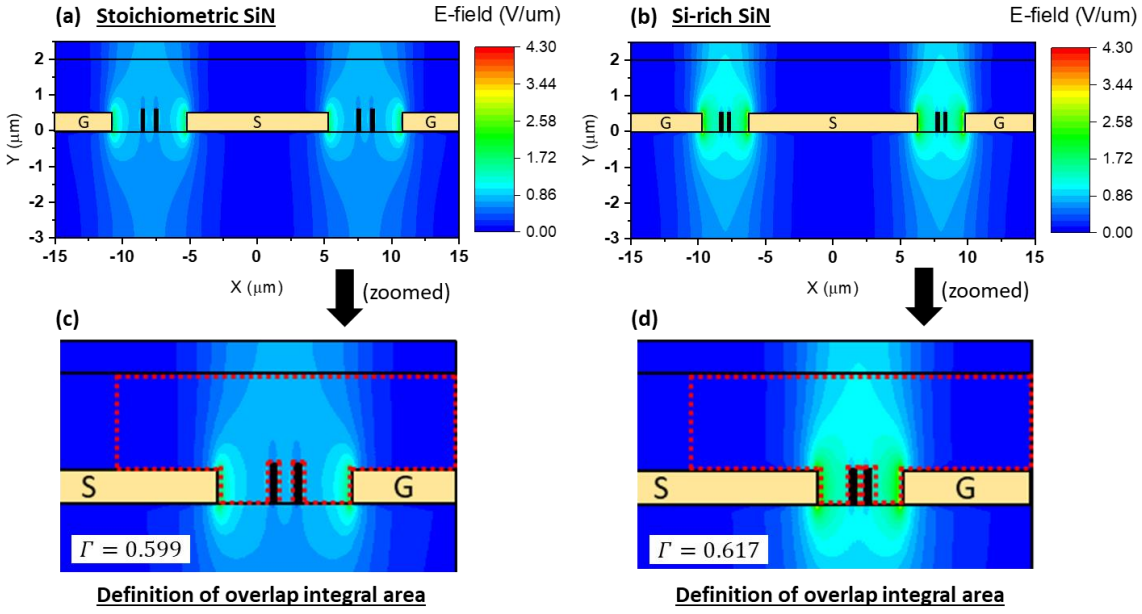

Figure 3-34 The simulated modulating electric fields for (a) stoichiometric and (b) Si-rich SiN.

The simulation aims to generate the distribution of electric field when the signal conductor is applied by D.C. voltage of 5V. Figure 3-34 (a) and (b) present the simulated electric fields for stoichiometric and Si-rich SiN, respectively. Comparing the field profiles between the left- and right-electrode gap, they are symmetrical to each other. Due to a smaller gap size between the electrodes in Si-rich SiN, the field magnitude is obviously more intense inside the electrode gap. To calculate

the overlap integral factor (Γ) between the electric modulation field and the optical field, the integrating area is defined over the EO polymer region around one of the electrode gaps as shown in Figure 3-34 (c) and (d). The data of optical fields were taken from the simulation result of fundamental TE-mode in the previous session. By using Eq.(30) ($\Gamma = \frac{d}{V}\frac{\iint_{EO} E_{mod}(x,y)\cdot|E_{opt}(x,y)|^2 dxdy}{\iint_{-\infty}^{\infty}|E_{opt}(x,y)|^2 dxdy}$), the overlap integral factors are equal to 0.599 and 0.617.

Next, the last parameter which is required for estimating the value of $V_\pi \cdot L$, is an in-device electro-optic coefficient ($r_{33,in-device}$). By considering the practical range of $r_{33,in-device}$ reported in several publications[56, 117, 164-167], the values are reported to be between 78 to 142 pm/V. In this case, we have sensibly utilised the average of those reported values as 100 pm/V. The estimated values of $V_\pi \cdot L$ are presented in Table 3-9 along to the calculated overlap integral factors and all optimal design parameters. While the overlap integral factors for both designs are slightly different, $V_\pi \cdot L$ of Si-rich SiN is ~39% smaller than that of stoichiometric SiN. This is consistent to the difference of ~37% in their electrode gaps.

Table 3-9 Summary of the optimal dimension for the fabrication of the modulator based on stoichiometric SiN and Si-rich SiN slot waveguide and the estimation of modulating properties of each device platform.

Optimal Design Parameters (also adopted for fabrication)							**Simulation/Estimation Parameters**		
Core material	**SiN thickness (nm)**	**Slot width (nm)**	**Strip width (nm)**	**Electrode gap (μm)**	**Electrode thickness (nm)**	**MZI-arms inter-distance (μm)**	**In-device EO coefficient (pm/V)**	**Overlap integral factor**	**$V_\pi \cdot L$ (V-cm)**
Stoic. SiN	600	700	350	5.4	500	16	100	0.599	2.591
Si-rich SiN	550	300	300	3.4				0.617	1.588

3.4.3 Strip-Slot Mode Converter

The design of strip-slot mode converter presented in this work is based on the self-imaging principle with a multimode interference (MMI) which has been already reported [168]. The schematic of mode converter is depicted in Figure 3-35(a) including its definition of dimension parameters. The working concept of this type of mode converter is the use of an MMI cavity for converting a single mode in strip waveguide to be a self-imaging optical profile, and vice versa. The self-imaging profile is mainly generated by a combination of MMI-TE0 and MMI-TE2, and it must be as close as possible to the desire output mode in the slot waveguide (Slot-taper-TE0) as shown in Figure 3-35(b). In order to optimise the dimension parameters, the optical simulations were performed using FDE solver and EME solver in *Lumerical MODE solution*.

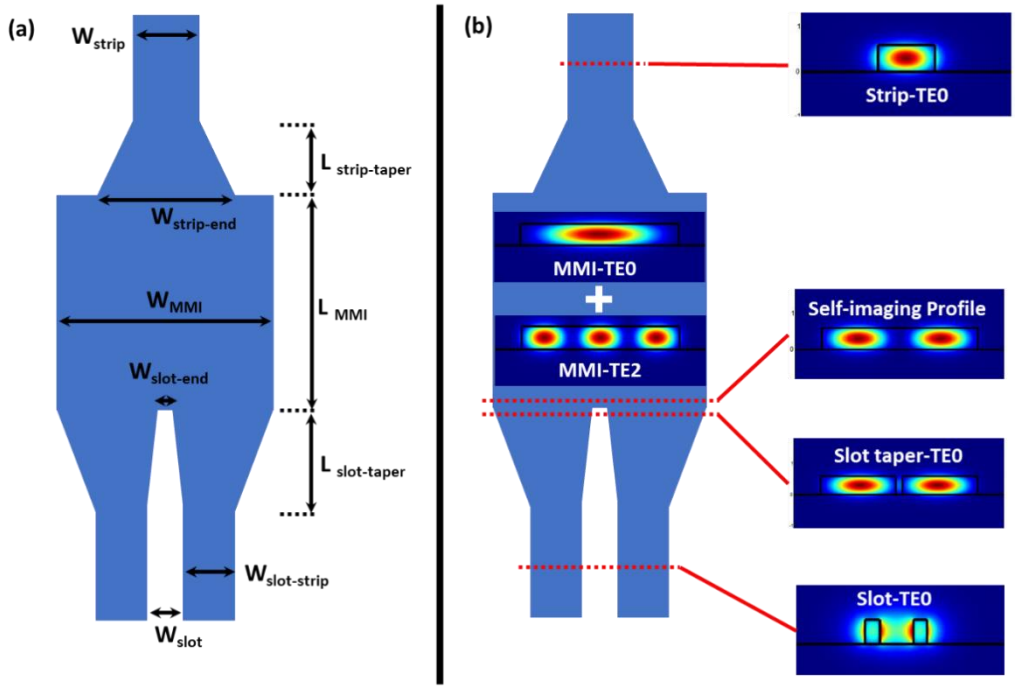

Figure 3-35 (a) The design of strip-slot mode converter including the strip waveguide, MMI, and slot waveguide. (b) Modal profile of guided mode propagate at different position in the strip-slot mode converter.

3.4.3.1 Input/Output slot and strip waveguides

The thicknesses of core material and slot waveguide parameters have been formerly determined during the optimisation of slot design (session3.4.1). They are equal to (thickness | W_{slot} | $W_{slot\text{-}strip}$): (600 | 700 | 300 nm) for stoichiometric SiN and (550 | 300 | 300 nm) for Si-rich SiN. The width of common strip waveguide has been given by the largest width for single mode condition which is 800nm for stoichiometric SiN and 600 for Si-rich SiN as demonstrated in session 3.2.2.

3.4.3.2 Width of slot-end in taper ($W_{slot\text{-}end}$)

To smoothly transfer the optical power between self-image in MMI and slot taper-TE0 mode, $W_{slot\text{-}end}$ should be ideally equal to zero. However, this is practically limited by the critical dimension of lithography technique which is 200nm in our current fabrication tool with deep UV. This value is applied for both stoichiometric SiN and Si-rich SiN designs.

3.4.3.3 Width of MMI cavity (W_{MMI})

With the appropriate width, MMI can provide high coupling efficiency of optical power between the MMI cavity and the slot-taper. MMI-TE1 mode is chosen here as a representative of the MMI self-image in order to achieve the index matching. FDE solver was employed to calculate the effective index of MMI-TE1 mode and slot taper-TE0 mode as a function of width. The calculated effective indices are presented in Figure 3-35(a) and (b). For both designs, a larger width can provide a good index matching, however, it will result to an increase of the minimum slot-taper length ($L_{slot\text{-}}$

$_{taper}$). Therefore, the appropriate widths are determined with the smallest width that can provide an approximate index matching condition and is located in a small slope region of the index curves. The matched effective index for stoichiometric SiN and for Si-rich SiN are at the MMI width of 4500nm and 2500nm, respectively. By choosing the width within a small slope region, the design of mode the converter allows for more fabrication tolerance.

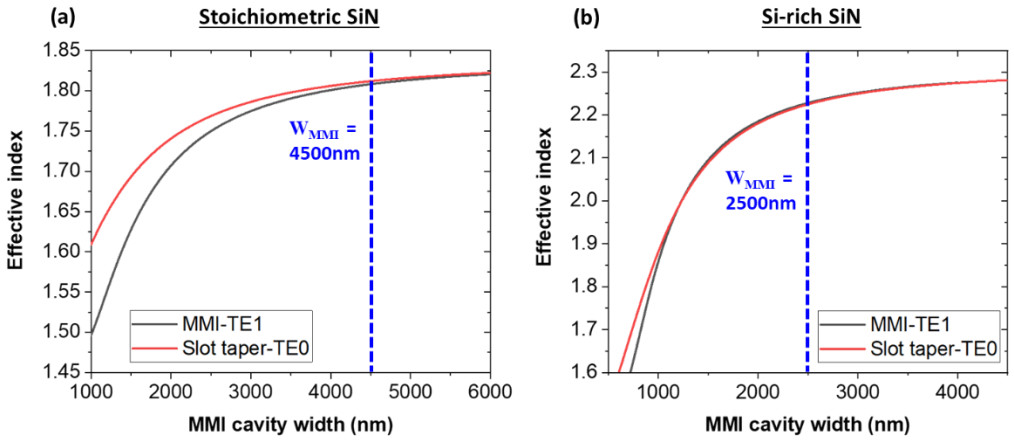

Figure 3-36 Variation of modal effective index in the MMI(TE1) and slot taper (TE0) with the changing of MMI cavity width of (a) stoichiometric SiN and (b) Si-rich SiN.

3.4.3.4 Width of strip-end in taper ($W_{strip\text{-}end}$)

To enhance the coupling efficiency of TE0-mode from the strip-taper to the MMI cavity, the effective index was calculated and plotted to determine the appropriate width. By considering the index curves in Figure 3-36, the effective index of TE0-mode is increased with an increasing of strip-taper width. The appropriate strip-taper width in this work is where the effective index of guided mode in strip-taper is close to the effective index of mode guided in MMI. As presented in Figure 3-37, the change of effective index become stable and close to the index of MMI after the strip-taper width of 2000 nm and 1200 nm for (a) stoichiometric SiN and (b) Si-rich SiN, respectively. By choosing the same strip-taper width as the MMI width, the effective index of guided mode will be exactly the same, but the length of taper will be too long as the length of taper will be increased with and increasing of strip-taper width. Therefore, the chosen strip- taper widths should be the smallest width in which the saturation of effective index is very small in order to provide a close index to MMI-TE0 and to keep a taper as short as possible. The widths have been determined with 2500nm and 1500nm for the stoichiometric SiN and Si-rich SiN, respectively. The indices at the chosen widths are not completely equal to those of the MMI-TE0 modes, but there is still less than 2% difference and should be able to effectively transfer the mode.

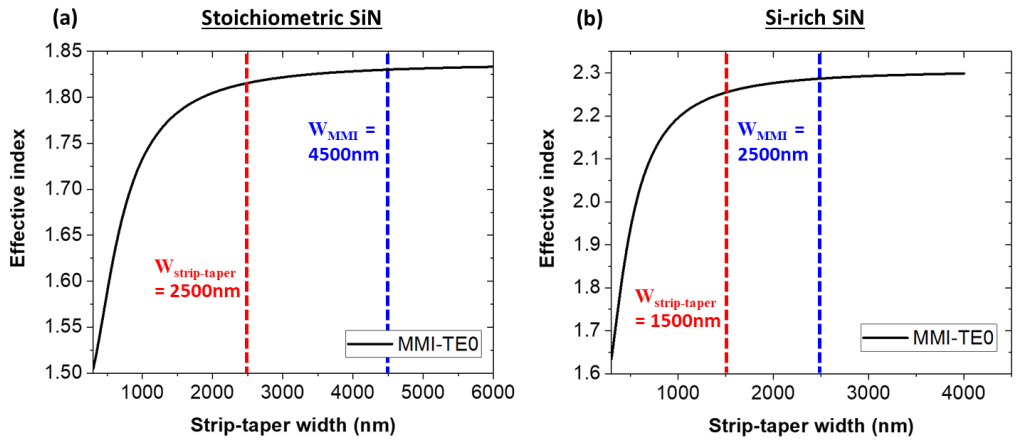

Figure 3-37 Variation of modal effective index in the MMI(TE0) with the changing of strip-taper width of (a) stoichiometric SiN and (b) Si-rich SiN.

3.4.3.5 Length of strip-taper ($L_{strip\text{-}taper}$) and slot-taper ($L_{slot\text{-}taper}$)

For scanning the taper lengths to optimise the mode transmission, the EME solver was employed to calculate the optical transmittance from the strip or slot waveguide to the MMI cavity. As explained before, the major propagating modes in this case are MMI-TE0 and MMI-TE2. The following transmittance curves are calculated from a combination of those modes. Figure 3-38(a) shows the transmittances as a function of strip-taper length ($L_{strip\text{-}taper}$) and indicates the optimal taper length at 20 and 30µm for the stoichiometric SiN and Si-rich SiN, respectively; while Figure 3-38(b) shows those of slot-taper ($L_{slot\text{-}taper}$) and indicates the optimal taper length at 40 and 60µm for the stoichiometric SiN and Si-rich SiN, respectively.

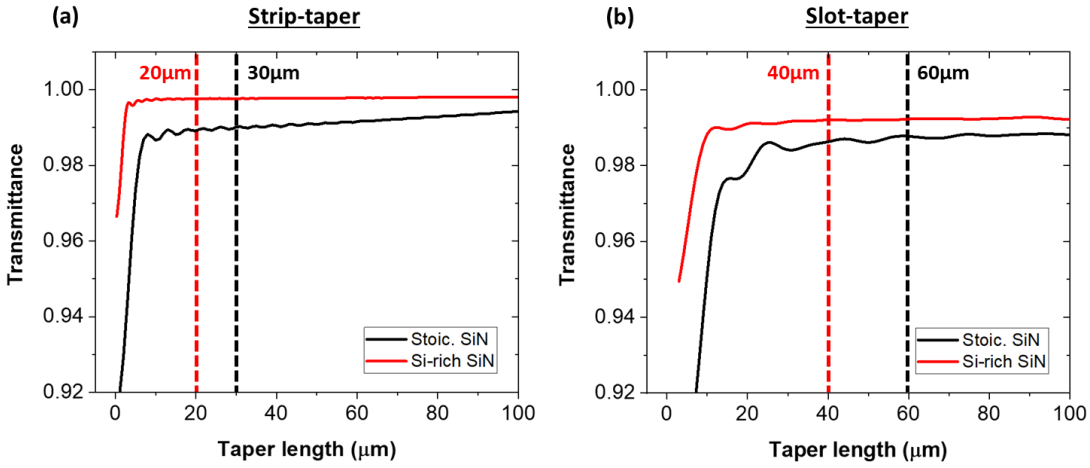

Figure 3-38 The transmittances as a function of strip-taper length for (a) strip-taper and (b) slot-taper.

3.4.3.6 Length of MMI cavity (L_{MMI})

In this step, the simulation of a mode converter was modelled in the EME solver using the optimal design parameters as presented before while the length of MMI cavity was scanned to search

for the occurring position of the desire self-image. Figure 3-39(a) shows the TE0-mode transmittance of strip-slot mode converter as a function of MMI cavity length for the stoichiometric SiN. The transmittance curve is revealed in the periodic pattern because the two-fold self-image are periodically generated along the propagation direction as depicted in the inset. The MMI cavity length at the first maximum transmittance is 13.33µm and this is chosen as the optimal parameter (L_{MMI}). Finally, the mode converter was recreated with all optimal dimension parameters, and its simulated optical filed distribution is presented in Figure 3-39(b) with 99.4% transmittance. Similarly, for the Si-rich SiN, the transmittance is presented in Figure 3-39(c). The first maximum transmittance of 97.0% occurs at the length of 4.82µm, and the optical field distribution is presented in Figure 3-39(d).

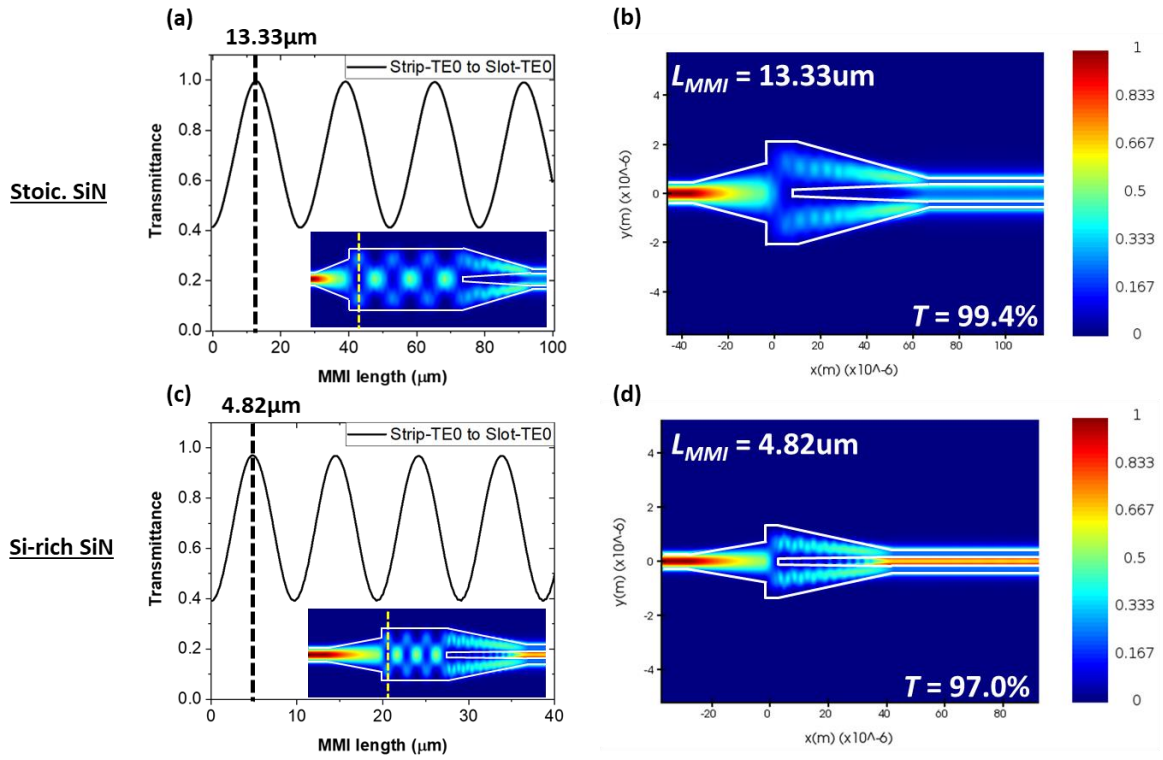

Figure 3-39 Transmittance of the wave propagate in the strip-slot converter at different MMI length of (a) stoichiometric SiN and (c) Si-rich SiN. Simulation of mode propagate along the strip-slot converter at the MMI length of 13.33µm for (b) stoichiometric SiN and 4.82µm for (c) Si-rich SiN.

3.4.3.7 Designs summary

All optimal dimension parameters of the strip-slot mode converters are summarised to Table 3-10. This also includes the transmittances or so called the mode conversion efficiencies.

Table 3-10 Dimension parameters of the strip-slot mode converters.

Optimal Design Parameters										Mode Conversion Efficiency
Core material	**SiN thickness (nm)**	**W_{strip} (nm)**	**W_{slot} | $W_{slot\text{-}strip}$ (nm)**	**$W_{slot\text{-}end}$ (nm)**	**$W_{strip\text{-}end}$ (µm)**	**W_{MMI} (µm)**	**$L_{strip\text{-}taper}$ (µm)**	**$L_{slot\text{-}taper}$ (µm)**	**L_{MMI} (µm)**	
Stoic. SiN	600	800	700 | 300	200	2.5	4.5	30.0	60.0	13.33	99.4%
Si-rich SiN	550	600	300 | 300	200	1.5	2.5	20.0	40.0	4.82	97.0%

3.5 Enhance Design of Slot Waveguide Modulator

In this section, the new optimisation procedure has been proposed in order to improve the designs of slot waveguide modulator for the latter two platforms including 600nm-thick stoichiometric SiN and 550nm-thick Si-rich SiN. The main improvements in this new procedure compared to the previous section are listed as follows:

- Change in the refractive index of polymer cladding from that of PMMA (n=1.475) to the average of EO polymer (n=1.650) from the publications.
- Include silicon-on-insulator (SOI) layer stack as a substrate in order to support the compatibility for BEOL multilayer integration.
- Optimise the CPW electrode using 3D model in *Pathwave ADS* software.
- Calculate the overlap integral factor (Γ) based on the electric field of RF modulation signal.
- Estimate the voltage-length product ($V_\pi \cdot L$) of modulators by using the simulated local r_{33} (generated from the simulation data of high-voltage poling field)
- Evaluate the modulation bandwidth and in-device half-wave voltage by taking into account of RF travelling loss in electrode and RF-optical velocity mismatch (signal walk-off).

3.5.1 Improved Optimization Method

For the enhanced design of phase modulator-based SiN slot waveguide, the thicknesses of the SiN layer in both platforms are the same as previous designs which are 600nm and 550nm for the stoichiometric SiN and Si-rich SiN, respectively. To ensure the maximum optical power confined in the slot of the slot waveguide, the waveguide design is accomplished by optimizing two important parameters of slot waveguide including slot width (W_{slot}) and SiN strip width (W_{ridge}). The commercial software *Lumerical MODE solution* is employed to simulate the waveguide 2D-eigenmode and calculate the optical power in slot (P_{slot}). The refractive index of EO-polymer of 1.65 has been chosen for the simulation as it is the average index of most EO-polymers in other reports (1.6-1.7)[55]. The simulation is focused only on the optical wavelength of 1550nm (C-band

in NIR) and the SiN and EO-polymer are assumed to have no material optical loss at this wavelength. To find the optimal dimension of the SiN, W_{slot} and W_{ridge} are swept in the ranges of 200-1200 nm and 200-600 nm for stoichiometric SiN and in the range of 100-500 nm and 150-400 nm for Si-rich SiN.

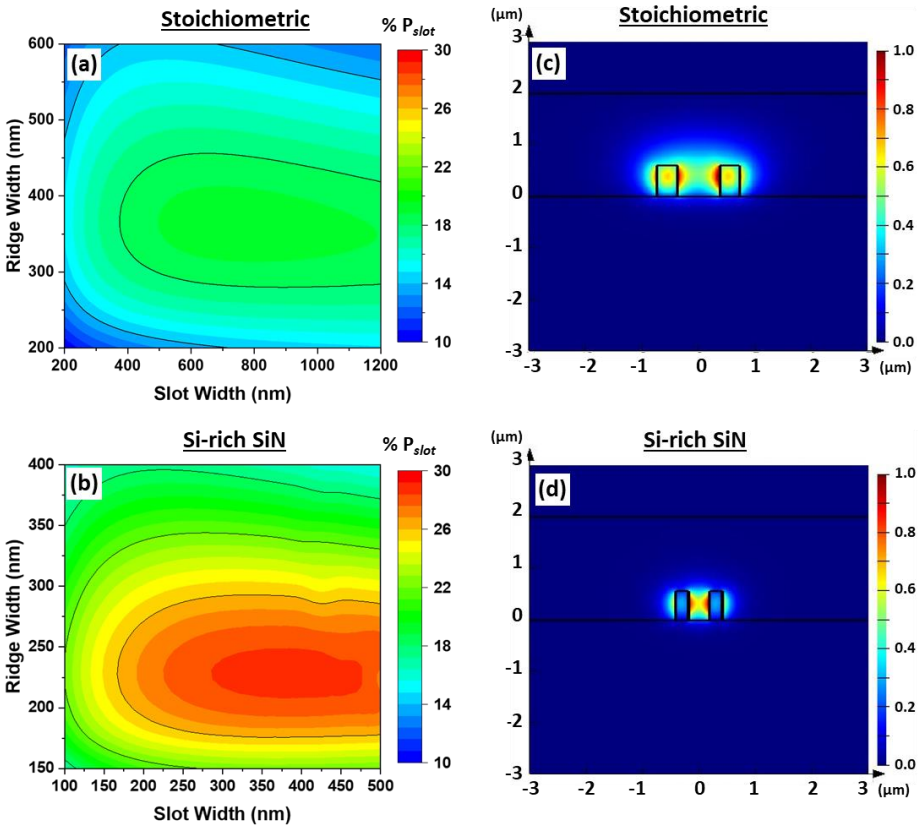

Figure 3-40 (a)-(b) 2D-plot Percentage of optical power confinement (PC) within a slot space versus slot width and strip width for the 600nm-thick stoichiometric and 550nm-thick Si-rich SiN slot waveguides, respectively. (c)-(d) Their electric intensity of TE0 mode profile with the optimal waveguide dimensions.

The contour plot in Figure 3-40(a) reveals the percentage of optical power confined in slot space (P_{slot}) as a function of slot width (W_{slot}) and SiN strip width (W_{ridge}) for the stoichiometric SiN. The maximum value of P_{slot} obtained from the graph is ~19% at W_{slot} = 750 nm and W_{ridge} = 360 nm. By considering the island-like shape of the power distribution in the contour plot, a wider uniformity region of high power confinement along the x-axis (W_{slot}) implies that the slot waveguide can have higher dimension variation for the W_{slot} rather than the W_{ridge}. The simulated optical field profiles of fundamental TE mode in the slot waveguide with optimal dimensions is presented in Figure 3-40(c). For Si-rich SiN waveguide, the contour plot of P_{slot} is depicted in Figure 3-40(b), and the obtained maximum value of P_{slot} is ~29% when W_{slot}= 380 nm and W_{ridge} = 230 nm. Due to the higher refractive index in Si-rich SiN, the P_{slot} is ~10% higher than that of stoichiometric SiN waveguide. Therefore, the optical mode confined in the Si-rich SiN slot reveals a smaller radiation area as shown in Figure 3-40(d). Figure 3-40(c-d) showing that the optical mode is not fully confined

in the slot space as there is a distribution of the mode concentrated around the waveguide structure which can induced higher losses if the waveguide is close to the electrode. Thus, the increase in confinement of the optical field in the slot space could develop the possibility to reduce electrode spacing compared to a simple strip waveguide.

Another key parameter in the design of optical phase modulator based on SiN slot waveguide is the electrode spacing (*d*) which is the distance between two metal electrodes. As the strength of electric field is inversely proportional with the electrode spacing, the closer the two electrodes, the higher and more uniform the electric field. Therefore, the optimization of the electrode spacing in the design requires to position the metal electrodes as close as possible to the waveguide while keeping the absorption loss at acceptable levels (< 1dB/cm). Based on a cross-section of the Mach-Zehnder modulator, the coplanar ground-signal-ground (GSG) transmission line is configured as a push-pull electrode. The GSG electrode structure is formed with a 300 nm-thick aluminium layer deposited on the BOX layer as shown in Figure 3-41(a). This 300nm-thick layer of metal is chosen in order to ease a limitation of a lift-off process for electrode fabrication.

Propagation losses in the waveguide due to metal electrodes and power overlap of guided optical mode with the polymer will be examined to determine the dimension of electrode gap in the design. In the simulations, the electrode spacing (*d*) is swept while the propagation loss and optical power overlap in the active polymer for each electrode spacing were then calculated. The plotted between propagation loss and optical power overlap with different electrode spacing are presented in Figure 3-41(b) for stoichiometric SiN and Figure 3-41(c) for Si-rich SiN waveguides.

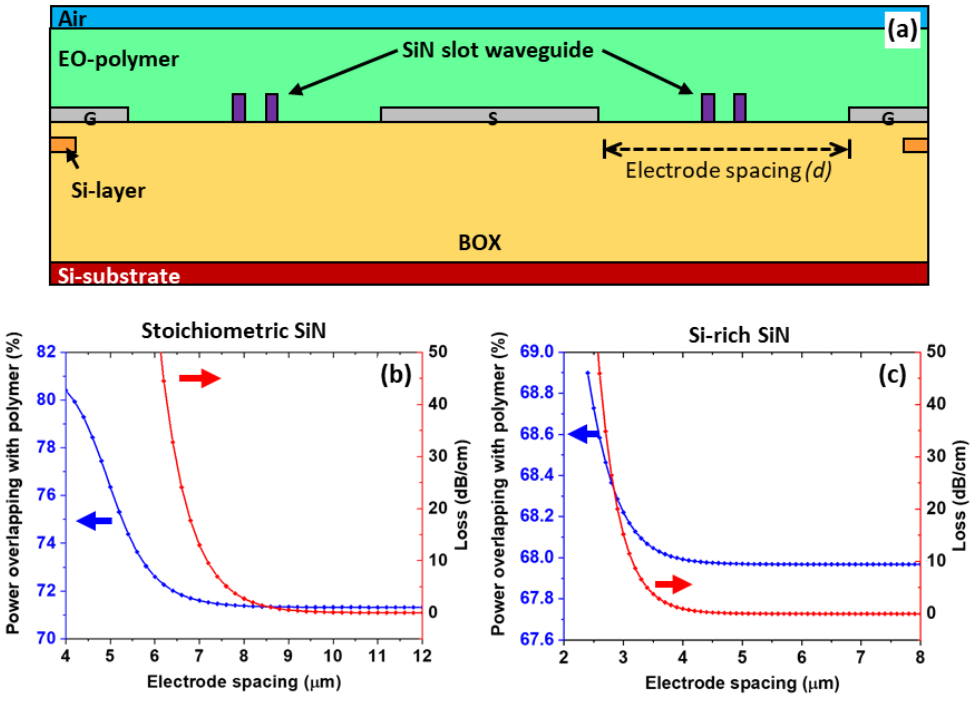

Figure 3-41 (a) Cross-sectional view of Mach-Zehnder modulator with two identical slot waveguides and GSG electrodes. Simulated optical power overlapping with polymer and

propagation loss versus electrode spacing of phase-shifters with a (b) stoichiometric and (c) Si-rich SiN slot waveguide, respectively.

To define the optimal dimension of electrode gap in the design, propagation losses due to metal electrodes is limited to less than 1 dB/cm. Therefore, the optimal electrode spacing of stoichiometric SiN and Si-rich SiN waveguides are 8.6 µm and 4.0 µm (Figure 3-41 (b-c)) which is related to the percentages of integral optical powers overlapping in polymer of ~71% and ~68% respectively. To be in line with a standard multilayer SOI based PIC fabrication process, the SiN waveguide deposited on a silicon-on-insulator wafer. The Si on insulator and Sin layers are shown (Figure 3-41 (a)) where the silicon has been etched under the SiN waveguiding areas leaving a width of 1 µm on each side of the simulation area. The silicon thickness is 300 nm and is positioned 2 µm above the Si-substrate.

Table 3-11 Optimal dimensions of the slot waveguide modulator and their optical properties of fundamental TE-mode.

Optimal Parameters					Fundamental TE-mode		
Core material	**SiN thickness (nm)**	**Slot width (nm)**	**Strip width (nm)**	**Electrode gap (µm)**	**Effective index | Group index**	**Power confinement in slot (%)**	**Power overlap integral in polymer (%)**
Stoic. SiN	600	750	360	8.6	1.6596| 1.7836	19.19	71.34
Si-rich SiN	550	380	230	4.0	1.7293 | 2.0541	28.73	67.99

The optimal parameters and the optical properties of fundamental TE-mode of the slot waveguide modulator are sorted into the Table 3-11 including effective indices and group indices. These calculated effective indices will be used for calculating the modulation bandwidth in the later section.

3.5.2 Fully 3D Simulation for Electrode Design

To complete the modulator design, the width of signal conductor was also optimized in order to minimize the reflection of the RF signal in CPW transmission line (GSG electrode). *Pathwave ADS* software was utilised to optimise the widths by aiming to meet the CPW impedance (Z_0) of 50 Ω. The simulation model is based on the same CPW schematic as presented in Figure 3-24. It consists of three parts of GSG electrode including the modulating electrode in the middle, the probing pads on both ends and the electrode taper connecting between them. As shown in Figure 3-42(a), the layer stack in the model has been defined in the following: (top-to-bottom) 2µm-polymer cladding/2.5µm-SiO_2/725µm-Si substrate. The 300nm-thick electrode (aluminium) layer is positioned onto the top of SiO_2 layer. The values of material dielectric constant are indicated in the parentheses. The design layout (top view) of (half) electrode conductor layer was drawn in a separate tool window (same software) as presented in Figure 3-42(b), and the GSG probing connection is necessary to be defined in this tool. The total width of electrode is 750µm.

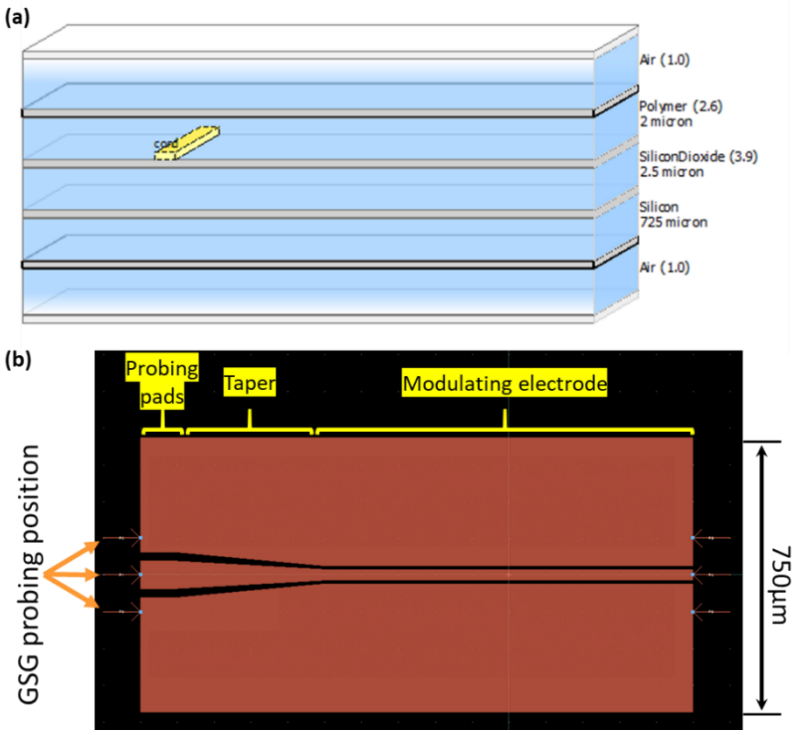

Figure 3-42 (a) Layer stack of electrode for the CPW transmission line. (b) Real design of GSG electrode used in the Pathway ADS software.

Firstly, the probing pads and the modulating electrode were separately optimised by using the individual model. The width of signal conductor was varied to observe the change of electrode impedance and RF travelling loss while the electrode gap (spacing) was set to the optimal value obtained in the previous section (4.0 and 8.6 μm). The monitoring frequency is set to 40GHz in the simulator. For the modulating electrode, the simulated impedances and RF losses as a function of signal conductor width for stoichiometric SiN and Si-rich SiN platform are presented in Figure 3-43(a-b). The optimal widths for 50Ω-impedance of stoichiometric SiN and Si-rich SiN platform are 27.20 and 16.15 μm, respectively. In addition, the corresponding losses at these optimal widths are equal to 0.694 and 1.101 dB/mm, respectively. For the probing pad, the width of signal conductor was varied under the same constraint of RF probe pitch (100μm) as described in the section 3.3.1 (signal conductor width + electrode gap = RF probe pitch). Figure 3-43(c) shows the impedances and losses in the probing pads, and the optimal width of a signal conductor is 71.50 μm (corresponding to the electrode gap of 28.50 μm). The optimal parameters of electrode in the probing pads can be applied for both platforms as no condition of fixed gap size for this electrode.

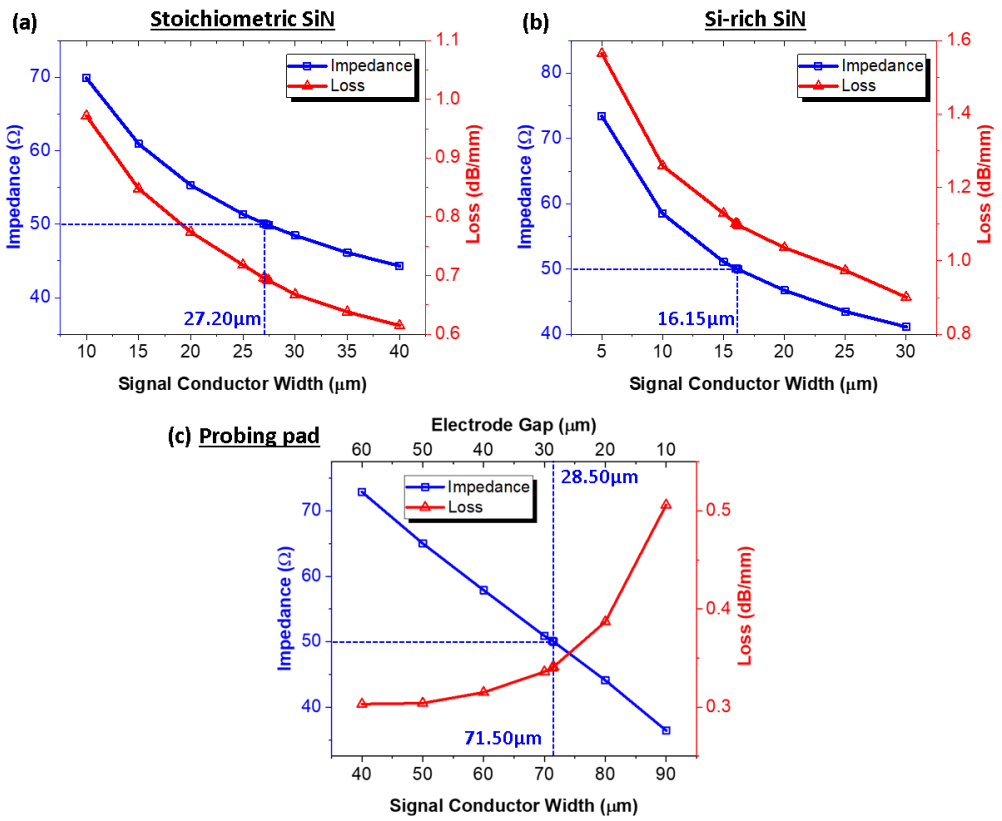

Figure 3-43 The impedances and RF losses as a function of signal conductor width for (a) stoichiometric SiN and (b) Si-rich SiN platform. (c) Impedances and losses in the probing pads with the variation of the width of a signal conductor and electrode gap.

Next, the models of modulating electrode by using the optimal width were re-simulated with a scanning RF frequency over the range of 1-100 GHz. The simulation results as a function of frequency are presented in Figure 3-44 including an impedance, a travelling loss, and an effective index of stoichiometric SiN and Si-rich SiN platform. The stoichiometric SiN platform has a stable impedance value around 48-52Ω in between the frequency range of 10 to 60 GHz (so called "working frequency band"), and the travelling loss is from 0.526 to 0.768 dB/mm. On the other hand, the Si-rich SiN platform has the 20GHz-smaller working frequency band in the range of 20 to 50 GHz, and the travelling loss is from 0.953 to 1.182 dB/mm. Additionally, the curves of effective index and travelling loss will be utilised for calculating the modulation bandwidth in the later section.

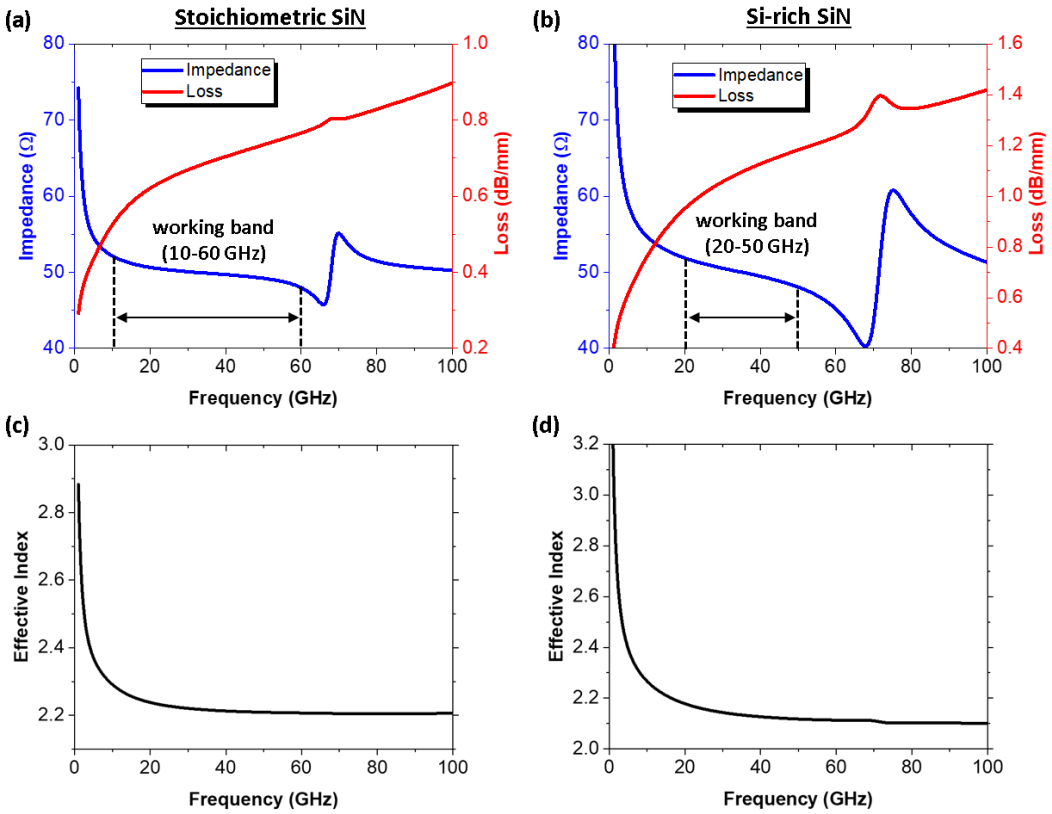

Figure 3-44 Simulation results of an impedance and a travelling loss as a function of frequency for (a)stoichiometric SiN and (b) Si-rich SiN platform. Effective index variation as a function of frequency in (c) stoichiometric SiN and (d) Si-rich SiN platform.

Finally, the lengths of electrode taper were optimised by using the full model of CPW transmission line (probing pads + taper + modulating electrode) as shown in Figure 3-44(b). The signal electrode widths in the probing pads and a modulating region are set to the optimal values. The lengths of probing pads and a modulating electrode are fixed to 100 and 1000 µm, respectively. Then the taper length was swept from 10 to 1000 µm in order to search for the optimal length providing a net impedance of 50Ω. Figure 3-45 presents the simulated impedances as a function of taper length for (a)stoichiometric SiN and (b)Si-rich SiN platform. The optimal taper lengths are indicated at 210 and 450 µm, respectively. The total loss curves represent the RF losses generated by the whole electrode structure.

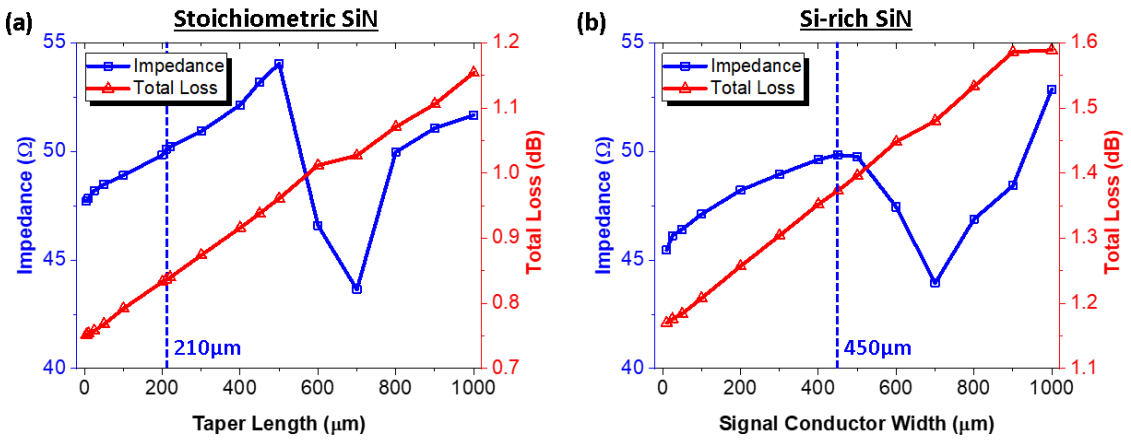

Figure 3-45 Simulation result of impedance and total loss with the variation of taper length for (a) stoichiometric SiN and (b) Si-rich SiN platform.

Table 3-12 Summary of the optimal parameters and RF properties of electrode designs.

Photonics Platform	Conductor thickness (nm)	Optimal Parameters					RF Properties in modulating electrode @ 40 GHz		
		Modulating electrode		Probing pads		Taper length(µm)	Attenuation loss (dB/mm)	Effective index	Working frequency within 48-52Ω
		Gap (µm)	Signal conductor width (µm)	Gap (µm)	Signal conductor width (µm)				
Stoic. SiN	300	8.6	27.20	28.50	71.50	210	0.694	2.2128	10-60 GHz
Si-rich SiN		4.0	16.15			450	1.101	2.1267	20-50 GHz

3.5.3 In-plane Poling and Modulation Field

A schematic of electrical poling connection which are used in this modulator simulations is demonstrated in Figure 3-46. The GSG electrodes are designed for dually used for both in-plane poling and modulation purposes. For the modulation, a modulating signal is connected to the signal electrode (S) while the two sides electrodes (G) are grounded. For the EO-polymer poling, an applied poling voltage (V_{poling}) is applied only between two ground electrodes (right-to-left on Figure 3-46), whilst the signal electrode (centre on Figure 3-46) is left as a floating contact. This poling connection works by the principle of method of image in the electrostatic theory [169]. Once the poling voltage is applied between the two ground electrodes, the E-field induces a movement of charges in the floating electrode following the field direction. Additional fields caused by the induced charges cancels all applied field inside the floating electrode, resulting in a net-zero field with a constant electrical potential. By ignoring all the perturbation from surrounding materials, a uniform gradient of potential as shown in Figure 3-46(a) will be achieved while half of the applied voltage is automatically dropped across each electrical spacing. This uniform gradient implies a good

uniformity of the generated electric field ($E = V_{poling}/2d$) leading to a high uniformity poling profile in the EO-polymer.

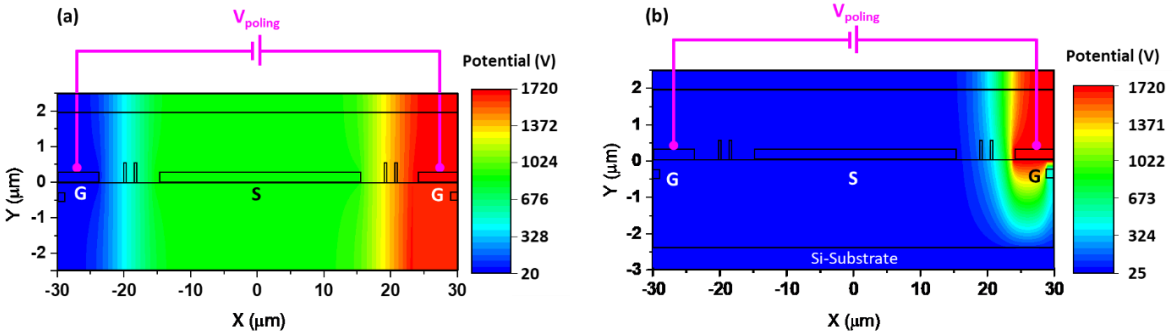

Figure 3-46 Simulated electrical potential distribution of in-plane poling process with ground-signal-ground (GSG) electrodes (a) excluding an effect of a Si-substrate (b) including an effect of Si-substrate.

During the "in-device" poling process, the poling field can however be distorted by a difference in electrical properties of surrounding materials. The first disturbance considered is a contrast of dielectric constant between the EO-polymer, waveguide material and buried oxide. Particularly, within the slot waveguide structure, a moderate part of the optical mode power is confined in the slot, where the higher dielectric constant of the SiN ridges can distort the applied field during the poling process or during modulation. Another major distortion is due to an induced charge effect generated in the Si-substrate, as well as high substrate temperature which is necessary to the poling process will increase charge effect due to the excess of free carriers. Induced charge effect in Si-substrate resulting in the higher electron concentration on the right because the applied poling voltage (V_{poling}) is applied between the positive electrodes (right) and ground electrode (left). The peak of concentration is dependent on the strength of applied voltage. Therefore, nonuniformity of potential distributions during the poling is occurred when considering the induced charge effect in Si-substrate (Figure 3-46(b)).

In order to accurately simulate the distribution of electric field, our simulation setup accounts for dielectric constants of all involving materials. The dielectric constants of SiN, EO-polymer and buried oxide are defined as 7.5, 3.0 and 3.9, respectively. The carrier charge distribution in the Si-substrate is also considered to include the effect of induced charges. The Si-substrate is specified as a p-doped (Boron, $1x10^{15}$ cm^{-3}) silicon wafer. The 2D distributions of electric field and charges are simulated by using the Atlas module in *Silvaco™ TCAD* software. For the poling configuration, the excess temperature induces an increase of the carrier concentration in the Si-substrate. Therefore, the expected poling temperature of 180°C at a Si-substrate boundary is set at by adding a thermal contact in the simulation. The applied poling voltage is designated by referring to the average electric field (100V/µm) required for poling EO-polymer as reported in several publications[55, 170, 171]. By assuming that the applied voltage is equal across two identical electrode spacings as formerly

explained, the applied voltage can be calculated by taking the required electric field and the optimal electrode distance. Thus, the applied poling voltages will be designated as 1,720V for the case of the stoichiometric SiN waveguide and 800V for the case of the Si-rich SiN waveguide. For the simulation of optical

Following the description and definitions of the device parameters, the electrical simulation results of stoichiometric SiN and Si-rich SiN devices are presented in Figure 3-47 and Figure 3-48, respectively. The distributions of electron concentration reveal an influence of the applied voltage to the accumulation of carrier charges in the underlying Si-substrate when poling (Figure 3-47 (a)). These electrons are attracted and build up a layer as near as possible to the positive potential source at the BOX/Si interface. As demonstrated in Figure 3-47 (a), electron concentration is higher on the right because the applied poling voltage (V_{poling}) is applied between the positive electrodes (right) and ground electrode (left). For the poling configuration, the potential distribution can be perturbated by the built-up charges and will be mostly confined to the positive electrode. As presented in Figure 3-47 (b), the voltage dropped across the central floating electrode and ground electrode on the left is less than one-sixth of the total applied voltage while most of the applied voltage is dropped across the space between the central floating electrode and positive electrode. For the simulated electric field during poling, an asymmetric poling field in Figure 3-47 (b) can be clearly observed. On the weaker field side(left), the strength of poling field inside a slot space is about 1.4 V/μm which is two order of magnitude lower than the expected average field. However, the field on the other side is elevated to ~134 V/μm which is more than 100 times stronger and ~30% higher than the expected field.

As the modulation efficiencies of EO-polymer based optical modulators can be significantly affected by the distribution of poling field. In order to enhance the field distribution, the application of an additional bias voltage onto the Si-substrate or the central electrode of the coplanar microwave electrode can play a role in improving the poling process. As presented in Figure 3-47(c) when the bias voltage is applied at the central electrode, the gradient of electron concentration of the induced charge in the Si-substrate is changed. The electron concentration will not only concentrate on the right of substrate but distributed more to the central part. When considering the electric field during poling, the strength of poling field between central electrode and substrate is increased as demonstrated in Figure 3-47(d) resulting in the higher strength of poling field inside a slot space on the left which is about 64.7 V/μm. Thus, the field on the right side is decreased to ~106 V/μm.

In case of an Si-substrate biasing, this will enable a reduction of the induced charge effect, where applying half of the poling voltage will enable the Ground-Ground poling E-field distribution to be equivalent to the ideal case in Figure 3-46(a). The electron concentration in Figure 3-47(e) showing a high concentration of electron in Si-substrate on both sides. This causes the more symmetry of the gradient of poling field inside the slot space as presented Figure 3-47(f). The

strength of E-field during poling when biasing the Si-substrate are ~66.4 and ~66 V/μm for the left and right slot space, respectively.

For the modulation process, the signal is connected to the central electrode which is signal electrode when the two sides electrodes are grounded. In the case of the DC-modulation, the built-up of carrier charges whilst operating the signal electrode is mostly confine at the centre. Thus, the modulating field will be more intense at the centre (the signal electrode). However, at high frequency modulation (RF-modulation) without bias voltage, the carrier effect from substrate can be ignored due to the non-polarity of average E-field. Therefore, modulated E-field at the modulation frequency of 40 GHz will behave like the ideal case as presented in Figure 3-47(g-h).

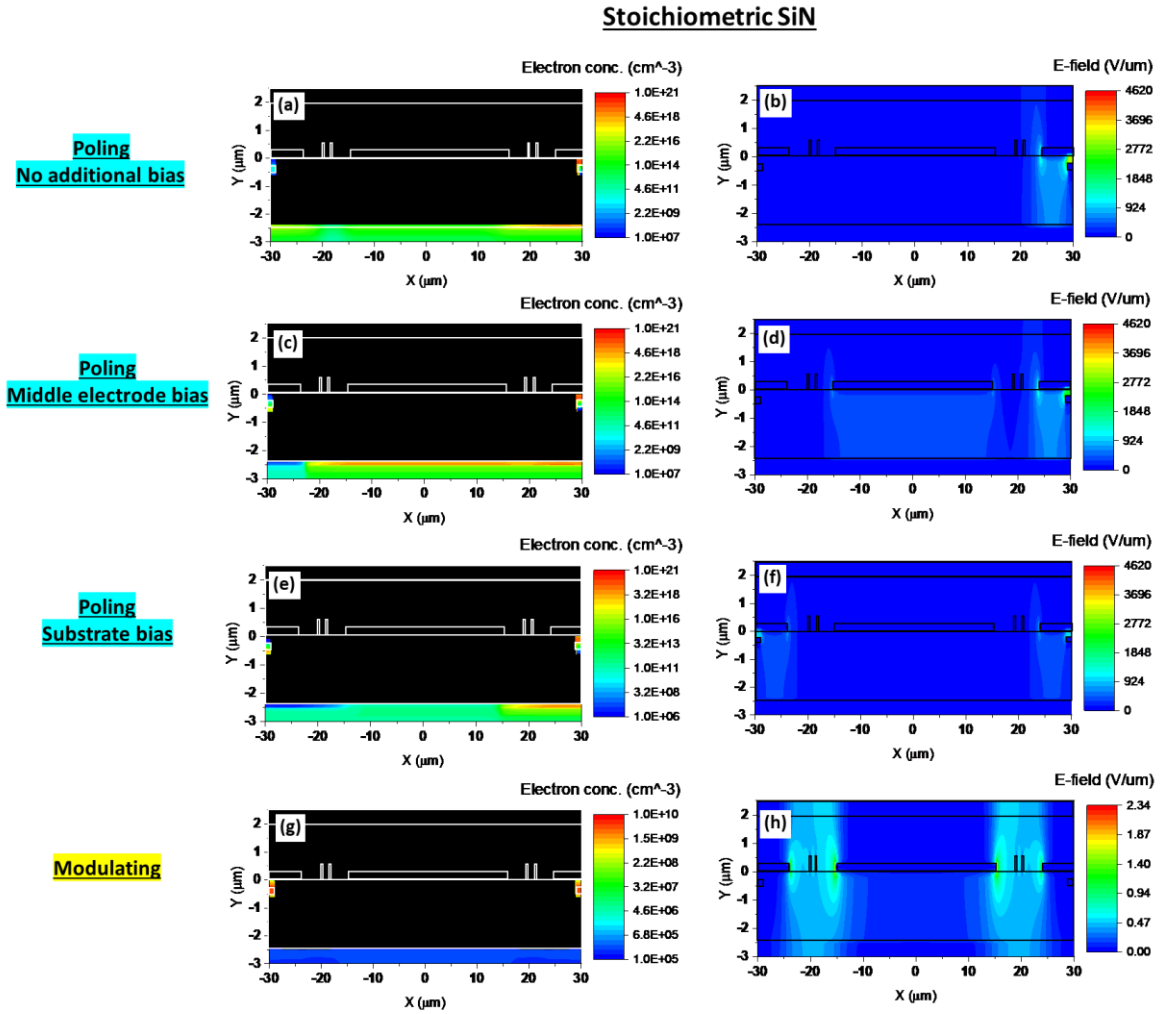

Figure 3-47 Electrical simulation results of the poling process at 1720V and RF-modulation in the stoichiometric SiN design: the electron concentrations presented in Si-substrate (a) Poling with no additional bias, (c) Poling with middle electrode bias, (e) Poling with substrate bias, (g) AC-modulation. The electric field distributions when (b) Poling with no additional bias, (d) Poling with middle electrode bias, (f) Poling with substrate bias, (h) RF-modulation.

The effect of carrier charges in the underlying Si-substrate to the poling field for Si-rich SiN are also the same as stoichiometric SiN which is demonstrated in Figure 3-48. The influence of the

applied voltage to the distributions of electron concentration when poling with no additional bias, biasing of the middle electrode and biasing of the Si-substrate are presented in Figure 3-48(a, c, e), respectively. These electrons are attracted and build up a layer as near as possible to the positive potential source at the BOX/Si interface resulting in the variation of poling electric field. The asymmetric poling field can be clearly observed in Figure 3-48(b) for no additional bias, while more symmetric of poling field are revealed in Figure 3-48(d) for biasing middle electrode, and Figure 3-48(f) for biasing Si-substrate. The strength of poling field inside a slot space for no additional bias is about 7.2 V/μm when the field on the other side is elevated to ~160.3 V/μm. When considering the poling electric field when biasing middle electrode, the strength of poling field between central electrode and substrate is increased leading to the increasing of poling field inside a slot space on the left which is about 88.7 V/μm where the field on the right side is decreased to ~93.2 V/μm. For the poling field of Si-substrate biasing device, the strength of E-field is ~84.5 and ~85.5 V/μm for the left and right slot space, respectively. The modulating E-field in Si-rich SiN is also behaving like the ideal case when modulating with the high frequency of 40 GHz as presented in Figure 3-48(g-h).

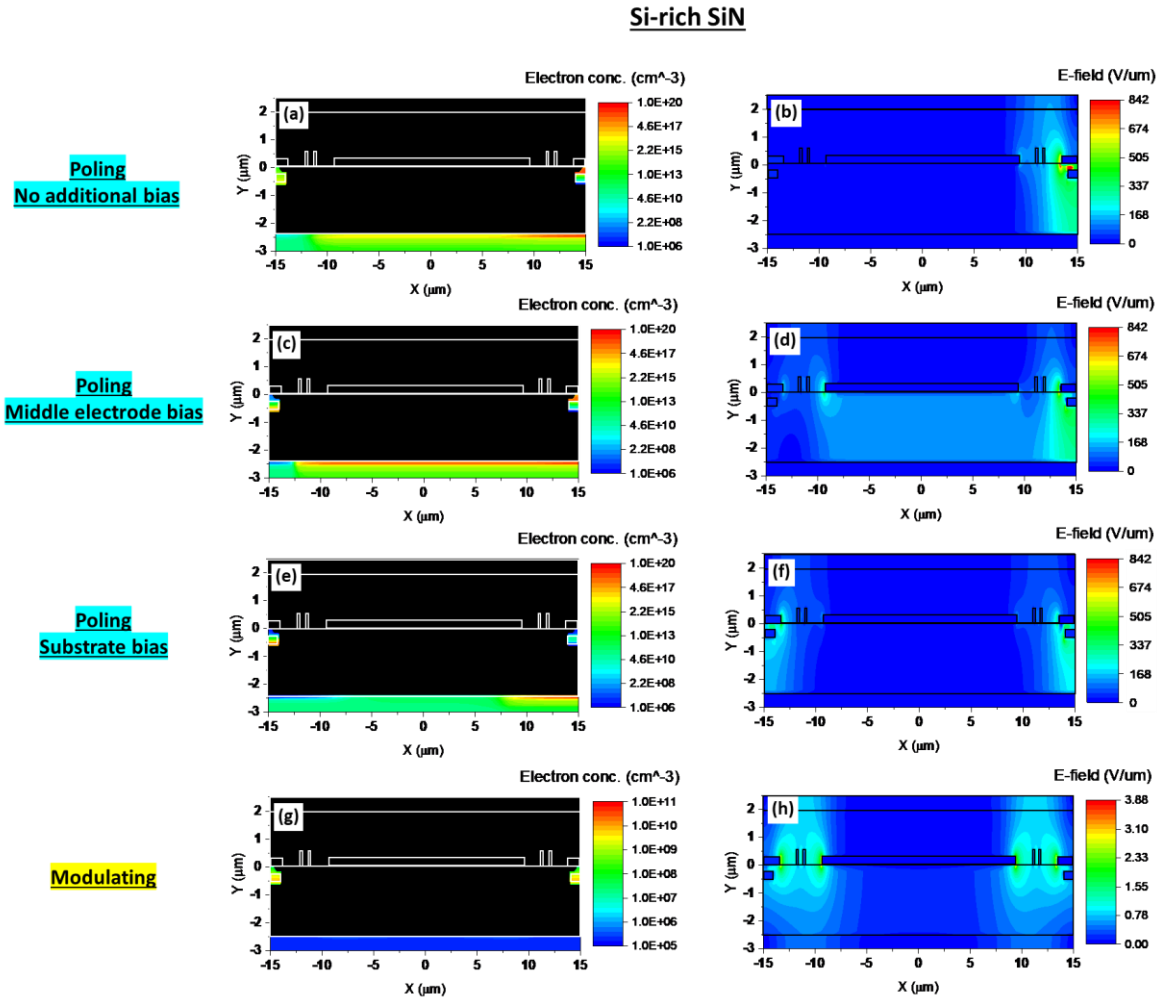

Figure 3-48 Electrical simulation results of the poling process at 800V and RF-modulation in the Si-rich SiN design: the electron concentrations presented in Si-substrate (a) Poling with no

additional bias, (c) Poling with middle electrode bias, (e) Poling with substrate bias, (g) AC-modulation. The electric field distributions when (b) Poling with no additional bias, (d) Poling with middle electrode bias, (f) Poling with substrate bias, (h) RF-modulation.

3.5.4 New Estimation Technique for Voltage-length Product

To monitor the performance of a Mach-Zehnder modulator (MZM) with two identical phase-shifters, the voltage-length product ($V_\pi L$) will be considered where a low $V_\pi L$ represents higher efficiency. The $V_\pi L$ of this type of modulator can be defined as the voltage (V_π) required to achieve a phase different of π between two arms of MZM for the length L [172-174]. By considering the equation Eq.(35) ($V_\pi \cdot L = \frac{\lambda d}{2n^3 \Gamma r_{33,in-device}}$), it can be noticed that two parameters related to the design of the modulator structure are an electrode spacing (d) and an overlap integral factor (Γ). The latter parameter Γ is already well-defined in Eq.(30). The voltage-length product ($V_\pi L$) can be decreased when an optimized waveguide leading to optimum electrode spacing has been designed to have the largest Γ and smallest d whilst optical absorption losses due to the metal electrodes remains negligible.

In EO-polymers, chromophore molecules align preferentially to the applied electric field during the poling process. As shown in Figure 3-47 and Figure 3-48, the poling E-field is not entirely uniform across the electrode spacing, although a biasing has been applied to improve the distribution of poling electrical field. This nonuniformity leads to a difference of local poling efficiency in the EO-polymer. Therefore, to calculate the optical mode accurately, the value of poling field distribution must be transferred to a grid system in the optical simulation instead of assuming an ideally uniform poling profile across the EO-polymer.

As the poling efficiency is linearly related to the strength of poling field [55] and saturated at some certain level, the calculation of Pockels coefficient (r_{33}) is such that the spatial distribution of Pockels coefficients in poled EO-polymer can be defined by Eq.

(52)

.

$$r_{33}(x,y) = \begin{cases} \frac{r_{33,bulk} \cdot E_{poling}(x,y)}{E_{sat}} & ; \left|E_{poling}\right| \le E_{sat} \\ r_{33,bulk} & ; \left|E_{poling}\right| > E_{sat} \end{cases} \quad (52)$$

where $r_{33}(x,y)$ is a local Pockels coefficient in each simulating grid after poling, $E_{poling}(x,y)$ is a local poling electric field and E_{sat} is a minimum electric field strength required for obtaining the saturated Pockels coefficient. In case of $\left|E_{poling}\right| > E_{sat}$, the term $E_{poling}(x,y)/E_{sat}$ is limited to be equal to 1.

To calculate the change of local refractive index in the EO-polymer when modulating, the result of simulated RF-modulation field is also required. The EO-polymer is considered as a diagonal anisotropic material, and the refractive index associated to a diagonal component in material permittivity is defined by n_i. The distribution of refractive index changes ($\Delta n_i(x,y)$) can be calculated by using the following Eq. (19).

$$\Delta n_i(x,y) = -\frac{1}{2}\, n^3 r_{33}(x,y) \left[\hat{\imath} \cdot \frac{\vec{E}_{poling}(x,y)}{\left|\vec{E}_{poling}(x,y)\right|} \cdot \vec{E}_{mod,EO}\right] \tag{53}$$

where n is a refractive index of EO-polymer in the neutral state and $\vec{E}_{mod,EO}$ is a RF-modulating electric field while $\frac{\vec{E}_{poling}(x,y)}{\left|\vec{E}_{poling}(x,y)\right|}$ represents a unit vector pointing in the direction of the orientation of local chromophore which is defined by the direction of local poling electrical field. This equation is adopted from the general definition of refractive index change in Pockels effect $\left(\Delta n = -\frac{1}{2}\, n^3 r_{33} E\right)$.

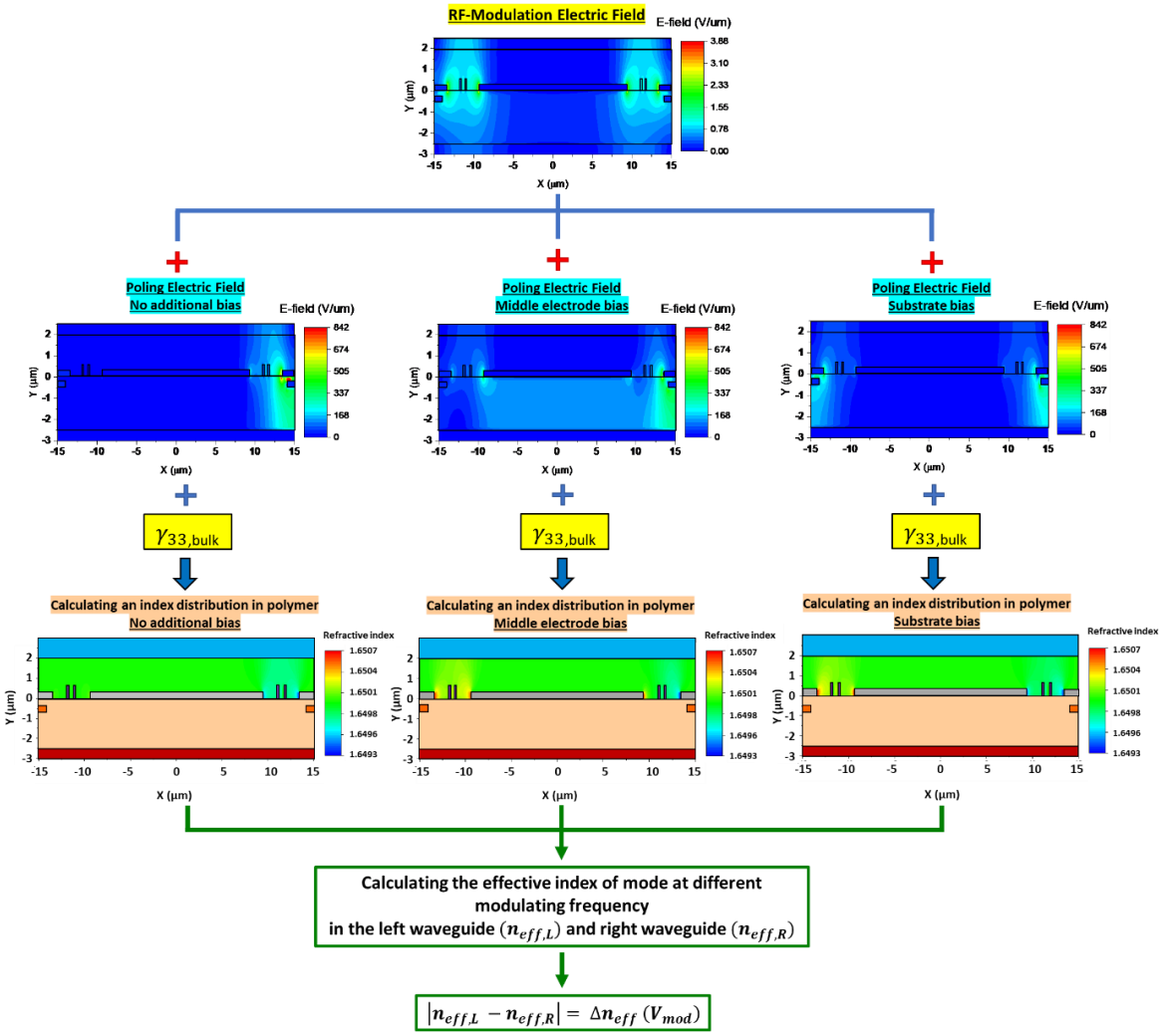

Figure 3-49 Diagram of simulation process for accurately predicting the performance of the proposed SiN slot waveguide modulators.

The performance of slot waveguide modulator ($V_\pi L$) in this work can be estimated by following the procedure presented in Figure 3-49. Firstly, 2D distributions of applied electric field for the stoichiometric SiN and Si-rich SiN designs are simulated by assigning one setup for a poling configuration and another for RF-modulation as reported in Figure 3-47 and Figure 3-48. Then, the 2D distribution of poling electric field was combined with the Pockels coefficient of bulk polymer ($r_{33,bulk}$) to find the local Pockels coefficient ($r_{33}(x,y)$) at each mesh in EO-polymer region. After that, the simulated distributions of $r_{33}(x,y)$ and RF-modulation electric field at each modulating voltage are used together to create a profile of refractive index change in EO-polymer region. Next, this profile will be imported to the optical simulator for calculating a modulated effective index of TE_0 mode between the waveguide on the left ($n_{eff,L}$) and on the right ($n_{eff,R}$) (phase-shifters) of modulator. In general, the length of a modulator is considerably longer than its cross-sectional dimensions, thus the electric field component along the length-side can be ignored. Then, the 2D-spatial refractive indices of modulated polymer are all calculated and transferred to the grid system of the optical simulation setup. Finally, the difference of effective index of TE_0 mode ($\Delta n_{eff}(v_{mod})$)

between the phase-shifters is calculated as a function of the applied modulation voltages (V_{mod}). In this simulation, the Pockels coefficient of bulk polymer ($\gamma_{33,bulk}$) is ranged from 2 to 100 pm/V, and the saturated field (E_{sat}) is defined as 100V/μm which is averaged from a common poling field for determining an Pockels coefficient in polymer [52, 55, 56, 175]. Then, this are used to calculate a voltage-length product of this designed modulator by using Eq.(

(53)

).

$$V_\pi L = \frac{\lambda}{2} \cdot \frac{V_{mod}}{\Delta n_{eff}(V_{mod})} \tag{54}$$

The inhomogeneity of the electric poling field that dictates the local orientation of the chromophore dipoles resulting in the non-uniformity of $r_{33}(x, y)$. Due to this nonuniformity, we consider here the value of the Pockels coefficient in-device $r_{33,in-device}$ which is depending on the poling coefficient (α) of this design device. A linear dependence of the Pockels coefficient of bulk polymer ($r_{33,bulk}$) and Pockels coefficient in-device ($r_{33,in-device}$) is furthermore assumed to be $r_{33,in-device} = \alpha \cdot r_{33,bulk}$ as defined in Eq.(24).

The plot between voltage-length products ($V_\pi L$) against different $r_{33,bulk}$ for stoichiometric SiN and Si-rich SiN are presented in Figure 3-50(a) and Figure 3-50(b). The curve of plotted data is corresponded to the inverse relation of $V_\pi L \; \alpha \; \frac{1}{r_{33,bulk}}$. The electrical-optical field interaction factor or overlap integral factor (Γ_{eff}) of the designed device in this work can be calculated from the simulation. At this point, the poling coefficient (α) can be obtained by using a curve fitting technique, and this factor exhibits efficiency in poling of this design device.

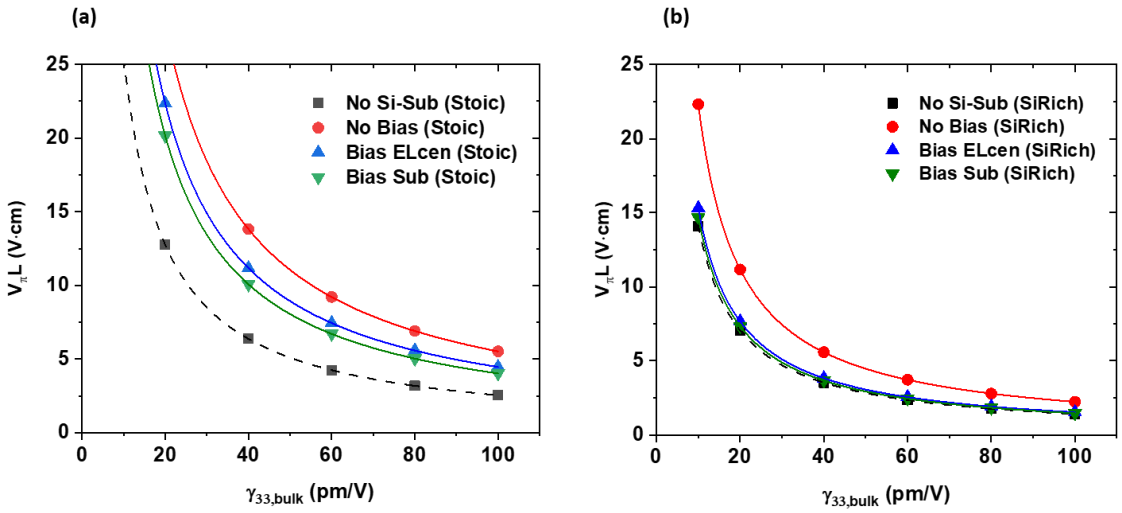

Figure 3-50 The simulation results for calculating the Mach-Zehnder modulator performance. Voltage-length products versus Pockels coefficient bulk polymer, $r_{33,bulk}$ for (a) stoichiometric SiN and (b) Si-rich SiN design.

By implementing the method discussed above with designs based on slot waveguides modulator, the characteristic factors of the design device are obtained and presented in Table 3-13.

The results from the electro-optic simulations show that the poling efficiency (α) of slot waveguide modulators without the Si-substrate are highest for both stoichiometric SiN (α ~ 0.88) and Si-rich SiN (α ~ 0.75). For the slot waveguide modulators with Si-substrate, the insertion of carrier charge effect in Si-substrate significantly reduces the poling efficiency (α). The result of the device with Si-substrate with no applied bias voltage shows the lowest α of 0.43 and 0.49 for stoichiometric SiN and Si-rich SiN, respectively. This is a significant reduction due to induced carrier charges in the Si-substrate leading to nonuniformity of the poling electric field. These results are consistent with the electrical simulation results in Figure 3-47(a-f) and Figure 3-48(a-f). An introduction of bias voltage to the central electrode or the Si-substrate during the poling process dramatically increases the poling efficiency up to ~ 27% for stoichiometric SiN and ~ 34% for Si-rich SiN. The results also show that the poling efficiency for both devices is higher when biasing the Si-substrate rather than the central electrode. This is due to more uniformity of poling electric field when the bias voltage has been applied to the Si-substrate as revealed in Figure 3-47(f) and Figure 3-48(f). Finally, the poling efficiency of Si-rich SiN when biasing the central electrode and Si-substrate is the highest and the values are closer to the device without Si-substrate.

To exhibit the performance of the slot waveguide modulators, the voltage length product ($V_\pi L$) are presented in Table 3-13. The $V_\pi L$ of the stoichiometric SiN and Si-rich SiN show the lowest value with an efficiency of 2.55 V·cm and 1.41 V·cm, respectively, without Si-substrate. By including the effect of carrier charge in the Si-substrate, the $V_\pi L$ of the devices (with no additional biasing voltage) is increased for ~50%. A reduction of $V_\pi L$ can be observed when the biasing voltage has been applied

to central electrode or Si-substrate. It is also shown that the $V_\pi L$ of slot waveguide modulator based on Si-rich SiN waveguide has the lowest $V_\pi L$ of ~ 1.47 V·cm which is only 4% higher than a device simulated without the Si-substrate.

Table 3-13 Parameters of Simulated SiN slot waveguide modulators in this work.

Parameters	600nm Stoichiometric SiN				550nm Si-rich SiN			
	Simulation without Si-substrate	Simulation with Si-substrate			Simulation without Si-substrate	Simulation with Si-substrate		
		No addition bias	Bias on the centre electrode	Bias on the substrate		No addition bias	Bias on the centre electrode	Bias on the substrate
Pockels coefficient bulk polymer, $\gamma_{33,bulk}$	100 pm·V^{-1}							
Widths: [strip | slot | strip] (nm)	[360 | 750 | 360]				[380 | 230 | 380]			
Optimal electrode spacing, d (µm)	8.6				4.0			
Overlap integral factor, Γ_{EO}	0.661	0.632	0.632	0.632	0.650	0.632	0.632	0.632
Poling coefficient, α	0.880	0.425	0.525	0.582	0.754	0.489	0.713	0.744
Voltage-length product, $V_\pi \cdot L$ (V·cm)	2.55	5.55	4.49	4.05	1.41	2.24	1.54	1.47
Electrode absorption loss	< 1 dB/cm							

It can be confirmed that carefully controlled biasing voltages applied to the device during the poling process can significantly improve the performance by almost 50%. However, through the study of devices proposed in this work, it is clear that more complex substrates such as single layer or multilayer SOI or with a high number of semiconductor or metallization levels could result in further distortion of the poling field distribution leading to a non-negligible impact on device efficiency. Finally, it should also be noted that the modulation efficiencies also strongly depends on the polymer and can be significantly improved by more than 2 times (compared to the efficiency reported in this work) if an EO-polymer with r_{33} of 230 pm/V [176, 177] is applied to the modulators.

Although our simulation method which includes the Si-substrate without supplementary biasing process reveals the reduction in 50% performance compared to the device without Si-substrate, the modulator designs with Si-rich SiN can still show the voltage-length product in a comparable range (2.7 – 4.0V·cm for single phase-shifter) compared state-of-the-art silicon pn-junction modulators [11, 178, 179].

3.5.5 Evaluation of 3dB-Bandwidth and Half-wave Voltage

Referring to the derived expression in Eq.(46), the modulation frequency response are calculated by using the RF effective index and travelling loss data from Figure 3-44, the optical effective indices from Table 3-11, and the overlap integral factors from Table 3-13. The overlap integral factor of DC modulation is assumed to be same as that of RF modulation. Figure 3-51(a-b) present the frequency responses normalised by DC modulation for (a) stoichiometric SiN, and (b)

Si-rich SiN platform, respectively. The frequency responses are calculated for three different modulator lengths including 2, 3, 5, and 10 mm (length of modulating electrode). When taking a consideration of the RF-optical velocity mismatch and the RF travelling loss in electrode, these curves imply the degeneration of modulator efficiency against an increment of modulation frequency and modulator length. Every curve gives a negative slope on the modulation frequency domain, and the frequency response at 3dB-level decreases when the modulator length increases. For the stoichiometric SiN, the 3dB-bandwidths are indicated at 77, 49, 26, and 9 GHz for the modulator length of 2, 3, 5, and 10mm, respectively. For the Si-rich SiN, the 3dB-bandwidths are indicated at ~100, 60, 26, and 5 GHz. Furthermore, these bandwidth data are transferred to plotted in another aspect of relation as shown Figure 3-51(c-d). These plots will help to evaluate the modulator length require to obtain the 3dB-bandwidth at some expected frequency. If the target bandwidth is at least 40GHz, the modulator length of stoichiometric SiN modulator must be shorter than 3.5 mm and 3.8 mm for Si-rich SiN.

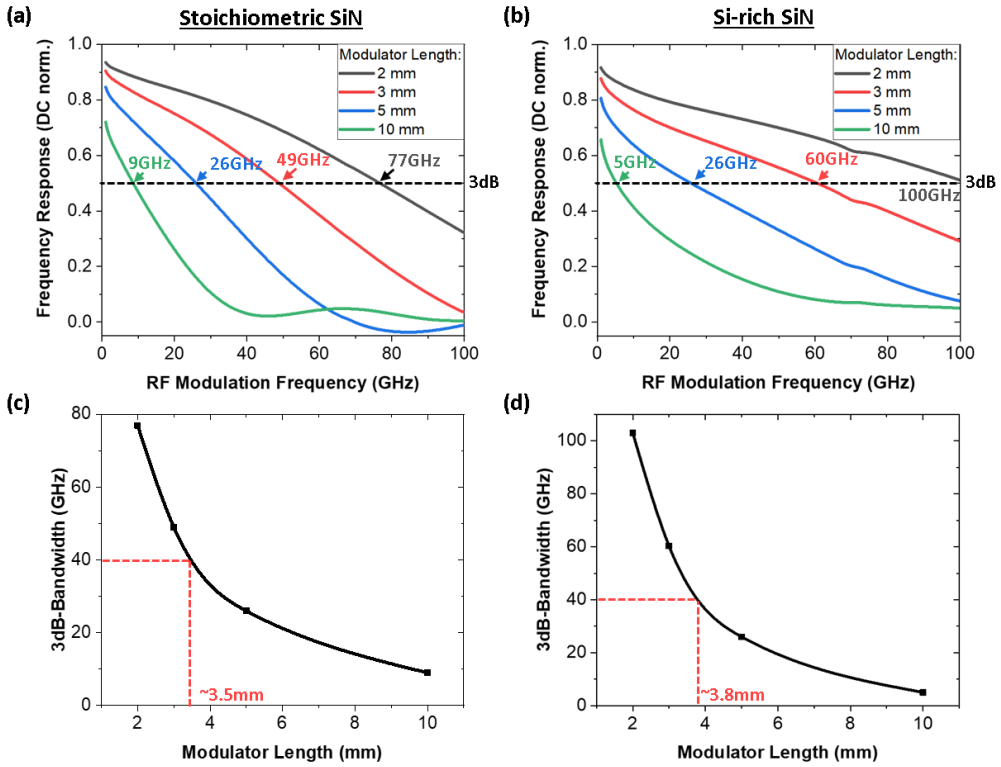

Figure 3-51 Frequency response as a function of RF modulation frequency with different modulator length for (a) stoichiometric SiN and (b) Si-rich SiN. Plotted of 3dB-bandwidth with different modulator length for (c) stoichiometric SiN and (d) Si-rich SiN.

To study the impact of RF traveling phenomena onto the increase of V_π, the frequency responses are considered in another aspect over the domain of modulator length. Using the same expression in Eq. (46), the calculations were implemented by varying the length L and using the fixed RF effective indices and losses at 1, 5, 10, 20, 40, and 60 GHz. In principle, the frequency response is calculated by normalising to the half-wave voltage (V_π) at DC modulation because V_π at DC

modulation represents the ideal efficiency without any effect of velocity mismatch and the RF travelling loss in electrode. By taking the ideal $V_\pi L$ from Table 3-13 in case of poling with bias on substrate, V_π in term of modulation length can be calculated by using the equation $[V_\pi(L) = (ideal\ V_\pi L) \div L \div frequency\ response(L)]$.

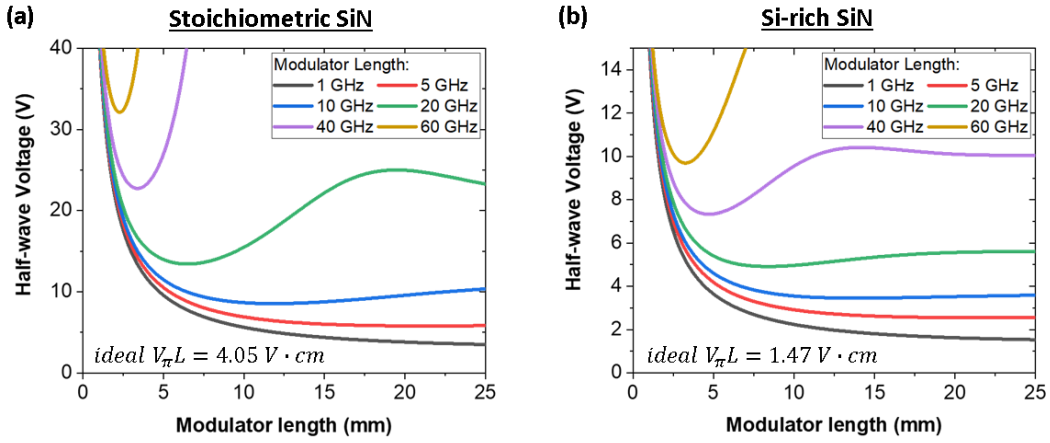

Figure 3-52 Plotted of V_π of RF modulation with the modulator length for (a) stoichiometric SiN and (b) Si-rich SiN.

Based on the theory, V_π should be ideally decreased with an inverse relation ($V_\pi = \frac{constant}{L}$) to the modulator length (L). However, the curves in Figure 3-52(a-b) confirm that the V_π-L relation has been modified when the RF travelling-wave phenomena in electrode are considered. This effect becomes stronger in curves of higher RF frequency because of a larger RF loss and an easier signal walk-off in the shorter RF wavelength. Nevertheless, the inverse relation remains in the 1 and 5GHz curves within the modulation length range of 0.1 - 25 mm. For higher frequencies, the minimum point of V_π has been presented in the curve. At these minimum V_π point, L indicates an optimal length (L_π) to obtain the smallest V_π for that certain frequency. That means the modulator should not be designed with a longer length than L_π, otherwise the modulator will require a larger V_π.

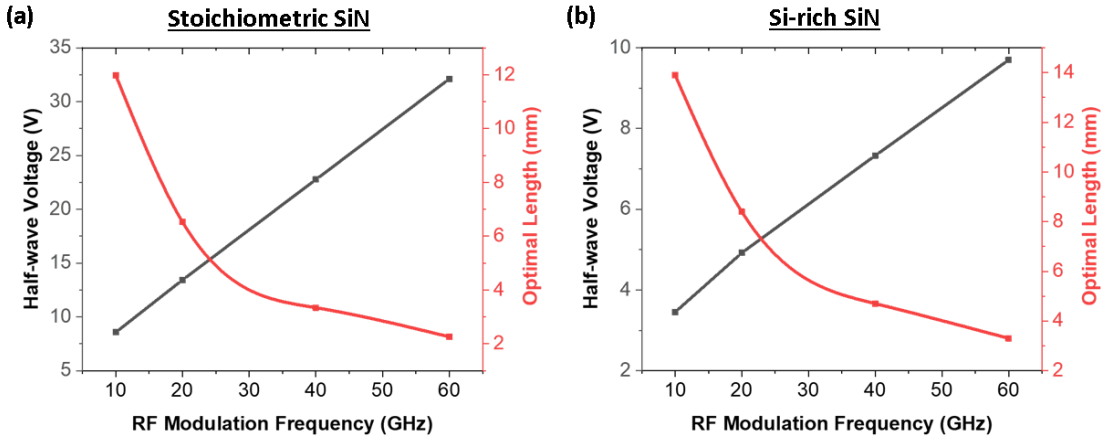

Figure 3-53 The simulation result of half wave voltage (V_π) and optimal length (L_π) as a function of frequency in (a) stoichiometric SiN and (b) Si-rich SiN.

Furthermore, the values of V_π and its L_π at minimum point of each frequency curve were transferred from Figure 3-52 to plot in Figure 3-53(a) for stoichiometric SiN and (b) for Si-rich SiN. In both figures, the V_π data show a linear trend. Within the frequency range of 10 - 60 GHz, V_π increases from 8.6V to 32.1V for stoichiometric SiN while it increases from 3.5V to 9.7V for Si-rich SiN. It seems the slot waveguide modulator in stoichiometric SiN platform might not operate well with 5V-CMOS modulation signal at high frequency. On the other hand, the modulator in Si-rich SiN platform can appropriately function up to 20 GHz with the 5V modulation signal and L_π of ~8.4mm. If we aim to operate this Si-rich SiN modulator at 40 GHz, it will require a signal amplitude of 7.3V and L_π of ~4.7mm. This V_π can be improved by factor of two or greater if the device is fabricated with a higher r_{33} in EO polymer such as 200 pm/V or larger.

Table 3-14 Summary of the condition for the modulator to have a V_π of 5Vand modulator length for 3dB-bandwidth at 40 GHz.

Photonics Platform	**Modulator length (mm) for 3dB-bandwidth of 40 GHz**	**Condition for modulator with In-device r_{33} = 100 pm/V to have V_π = 5V**		**Condition for modulator to have V_π = 5V at 40 GHz**	
		Max. modulation frequency (GHz)	**Optimal length L_π (mm)**	**Min. Required r_{33} (pm/V)**	**Optimal length L_π (mm)**
Stoichiometric SiN	3.5	<5	>12	455	3.3
Si-rich SiN	3.8	20	8.4	147	4.7

In conclusion, the evaluation results of 3dB-bandwidth, V_π, and L_π are presented in Table 3-14. It also includes the proposed values of r_{33} and optimal length L_π which are required to support a modulation with V_π of 5V at 40GHz in each SiN platform. These L_π values have been directly obtained from data points at 40GHz in Figure 3-53(a-b), and the proposed values of r_{33} are calculated by using the relationship of $V_\pi \propto \frac{1}{r_{33}}$ in Eq.(34) when the modulator length is fixed.

3.6 Mask Layout

The mask layout is essentially required for a lithography process in the fabrication of silicon photonic devices. The mask drawing process in this work had been done in the *Tanner L-edit* software. By programming a GDS drawing code in *C++* language, the photonic components were generated and automatically integrated to the MZM structure. The dimensions of component were defined by following the optimal values from simulations, and the components were accurately assembled to build up the modulator structure with the drawing precision of 1 nm. In this section, more details about the process used for preparing the mask will be explained. The designation of

GDS layers is firstly declared, and the waveguide drawing procedure is presented step by step. The associated drawing steps are also given for generating the electrode relevant layers. Lastly, the supplementary layer of central poling circuit is introduced to support the poling process.

3.6.1 Drawing Procedure for The Passive Components

Firstly, we are focusing on the procedure for drawing the GDS layers of passive/waveguide-based components e.g. grating coupler, taper, bend etc. To build the mask layout of these components, only three major GDS layers are required. The GDS layer numbers must be clearly declared at the beginning of the drawing process in order to prevent any possible conflict of layer definition in the future. The declaration of GDS layer in this work has been listed in Table 3-15.

Table 3-15 Details of GDS layer used to draw the mask layout of the passive component.

Layer name	GDS no.	Designator	Description
Grating etched groove	23	GEP	for drawing a region of periodic etched grooves in the grating coupler component
Waveguide	24	WEN	for drawing a waveguide-core structure
Waveguide sleeve	25	WEP	for drawing a region to be etched around the waveguide-core (WEN layer), so-called a waveguide sleeve. The width of this sleeve is given by a biasing size (= 5µm in this work).

Every passive component has been initially drawn from a region to be a SiN core which is normally the main part of the passive component, then followed by the grating etched groove layer (in case of grating coupler) and the waveguide sleeve. An example of drawing steps of grating coupler is shown in Figure 3-54(a) the waveguide and taper of grating coupler are drawn in WEN layer, (b) the grating grooves are drawn in GEP layer across the waveguide part, (c) the etched region is generated in WEP layer around every object of WEN layer with the biasing size of 5µm, and (d) only GEP and WEP layers have been maintained for producing the lithography mask of SiN etching process.

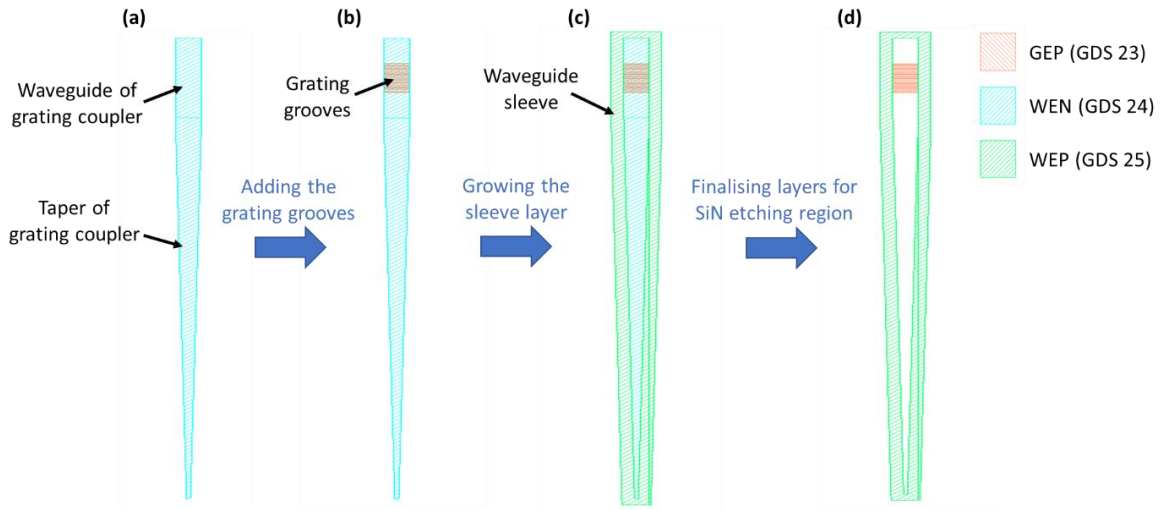

Figure 3-54 The design of grating coupler in three layers including (a) the waveguide and taper of grating coupler in WEN layer, (b) the grating grooves in GEP layer (c) the etched region in WEP layer around every object of WEN layer and (d) the GEP and WEP layers for producing the lithography mask of SiN etching process.

3.6.2 Mach-Zehnder Modulator

To create the mask layers for MZM structure, there are two more layers that need to be additionally defined along with the existing passive layers. They are all related to the drawing of modulating electrode. ELP layer is used to defined the electrode region, and ENP layer is for a clearing region of SiN in which the electrode can be positioned in the same level with a modulation waveguide (corresponding to the expected modulator design shown in Figure 3-20 and Figure 3-27). These layer definitions are presented in Table 3-16.

Table 3-16 Details of mask design layer for electrode and electrode niche.

Layer name	GDS no.	Designator	Description
Electrode	13	ELP	for drawing a metal electrode for the modulating purpose
Electrode niche	16	ENP	for drawing a region to be etched, extending to the WEP layer. This is for creating a clearing window to receive a full/part of ELP layer.

In accordance with the top-view schematic presented in Figure 3-20, the mask of MZM have been initially created from the MZI structure by using the drawing procedure for passive components as shown in Figure 3-55(a). The grating couplers are also integrated onto the input and output waveguide of the MZI where a waveguide bend is inserted in between the grating coupler. Figure 3-55(b) shows the defined region of electrode niche (ENP layer) along to the waveguide in modulating zone. The niche region acts as an additional etching area of SiN material which is to be etched together with structures in GEP and WEP layer. This is to ensure that the part of electrode, which is close to the waveguide, is in the same level with waveguide in order to support the TE-

mode modulation. Finally, the GSG electrode is generated in the ELP layer as shown in Figure 3-55(c), and the WEN layer is also converted to WEP layer.

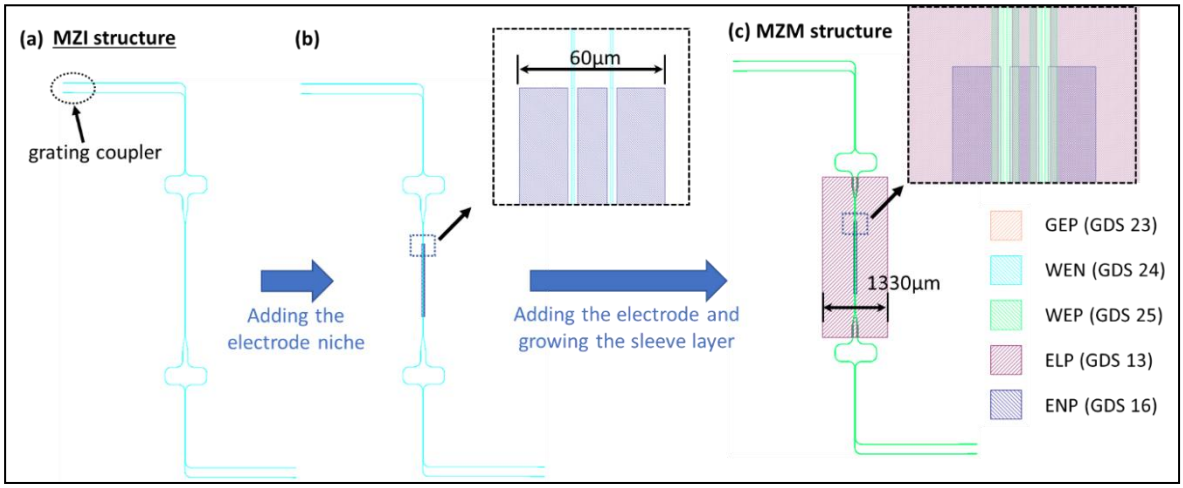

Figure 3-55 WEN layer of (a) MZI structure and (b) MZI structure when the electrode niche is added to the structure. The electrode and the sleeve layer is added to (c) MZM structure.

In addition, there is a major difference in electrode drawing procedure between the masks of the early fabricated devices (for 300nm stoichiometric SiN platform) and the later fabricated devices (for 600nm stoichiometric SiN + 550nm Si-rich SiN platforms). Due to the utilisation of E-beam lithography, the SiN etching area in the early fabricated devices needed to be as small as possible in order to minimise the E-beam patterning time. Its electrode niche region is defined to overlap only a part of electrode region (width of 60µm in total). On the other hand, the electrode niche region in the later fabricated devices is defined with the entirely same structure to the electrode because the photolithography is used for these devices.

To prepare the mask designs for the lithography process, more than a single mask of MZM device can be incorporated into the same fabrication cell layout. All the devices in the same cell layout are intended to be fabricated onto the same physical chip. The different layers in the same cell layout can be separately utilised for different fabrication purposes, for example, [GEP+WEP+ENP] layers are corporately used for the SiN etching process while [ELP] layer is individually used for the metal lift-off process of electrode.

3.6.2.1 Strip waveguide modulators over 300nm stoichiometric SiN platform

Following the design parameters of the strip waveguide modulator reported in section 3.3, the mask layouts of this platform are split into four different cell layouts with the modulation waveguide width of 0.6, 0.9, 1.2, and 1.5µm. All the cell layouts are prepared to use a sharable photolithography mask of ELP layer. Each cell layout consists of four MZMs with the different length of the modulation waveguide including 1.5, 3.0, 4.5, and 6.0 mm. Therefore, there are five lithography masks generated for this platform as shown in Figure 3-56. Four of them are used in E-beam

lithography for etching the passive MZI structure. Another mask is design for fabricating the metal electrode.

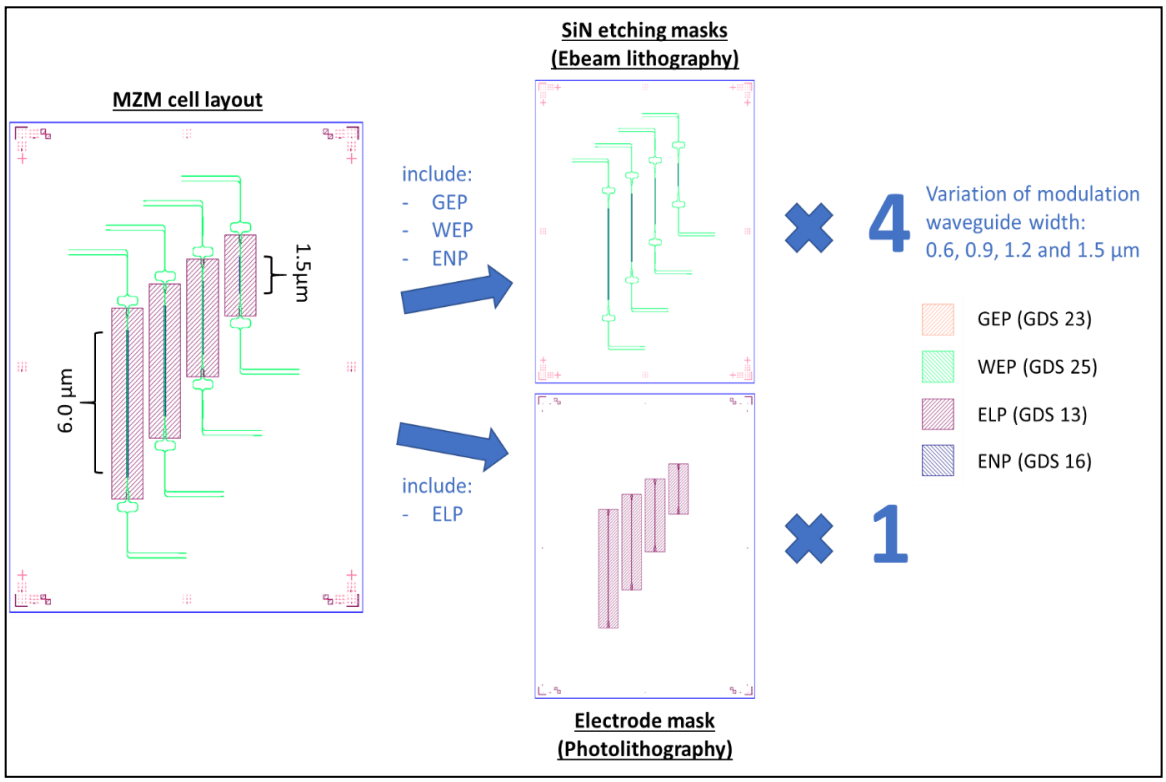

Figure 3-56 Layout of SiN etching mask for E-beam lithography and electrode mask for photolithography.

3.6.2.2 Slot waveguide modulators over 600nm stoichiometric SiN and 550nm Si-rich SiN platforms

Following the design parameters of the slot waveguide modulators revealed in the section 3.4, the mask layouts of both platforms are combined into the same cell layout. The devices of 600nm stoichiometric SiN are in the upper half of the cell layout while the 550nm Si-rich SiN are in the lower half as shown in Figure 3-57. The arrangements of devices between the platforms are mirrored to each other. There are five devices per platform including one MZI passive device and 4 MZM devices. The MZI passive device is designed to provide a reference spectrum in the optical measurement. One of the MZM devices is constructed by using strip waveguides in the modulation region with the optimal single mode width (0.8µm-wide for stoichiometric SiN or 0.6µm-wide for Si-rich SiN) and the modulation length of 4.0mm. The other three MZM devices are constructed by using slot waveguides with the optimal slot waveguide parameters and the modulation length of 0.5, 2.0, and 4.0µm.

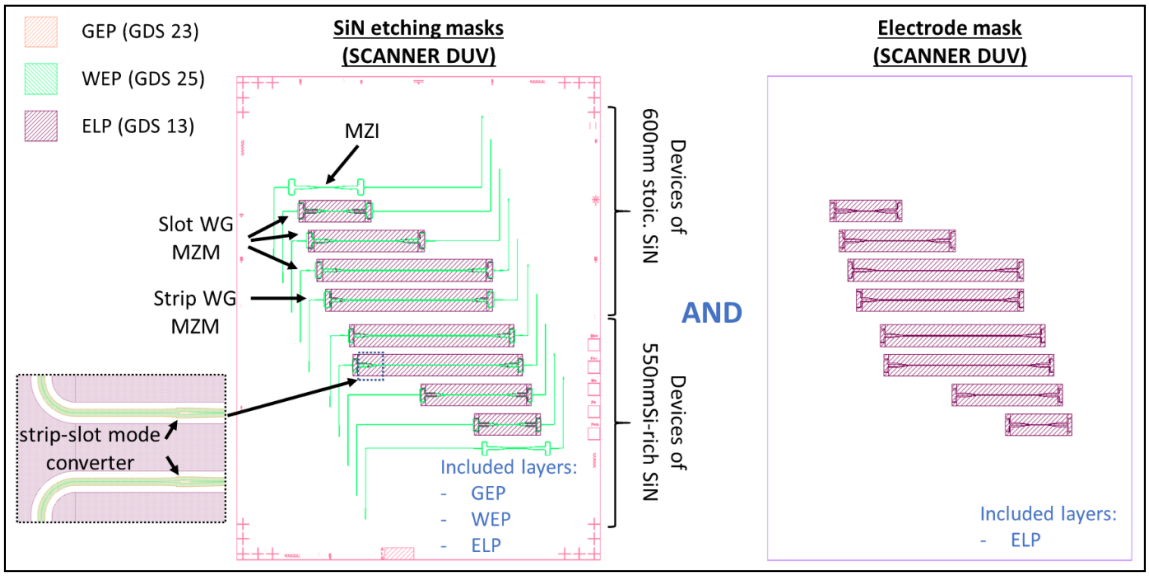

Figure 3-57 Mask design layout of MZI passive device and 4 MZM devices.

In this version of cell layout, an electrode niche layer [ENP] is not required due to the use of scanner photolithography for both of SiN etching and metal life-off processes. Therefore, the mask for SiN etching can directly include the electrode layer [ELP] for using as an electrode niche, then the GSG electrode will be entirely levelled to the same plane of waveguide in the fabricated devices. For the electrode mask, it has been generated with the electrode gap of 5.4 and 3.4µm for 600nm stoichiometric SiN and 550nm Si-rich SiN, respectively. Additionally, a strip-slot mode converter is required for the slot waveguide MZM device. In order to have the length of slot waveguide as short as possible, the mode converters are allocated into the probing region of GSG electrode which is closest to the modulation region. Moreover, the electrode spacing in the probing region is large enough to be occupied by the mode converter.

3.6.3 Circuitry for Poling Process

Regarding the poling process in EO polymer modulator, the fabricated devices require the application of heat and high voltage to activate the modulation ability. These stimuli should simultaneously apply to every device on the same chip or same platform. To heat up all devices in the same chip, this can be performed by applying the heat to the chip substrate. In order to apply the high voltage to all devices at the same time, their electrodes need to be correctly linked together. As shown in the schematic of electrical poling connection in Figure 3-21, both of ground planes in the GSG electrode are employed for this purpose. The additional mask layer is introduced for drawing the circuit to link the device electrodes, so-called a poling circuit layer [PCP] as provided in Table 3-17. Because this PCP layer aims to be fabricated by using the same metal lift-off process with the electrode layer, it is specified by the same GDS number.

Table 3-17 Details of the GDS number and designer for the mask design of poling circuit.

Layer name	GDS no.	Designator	Description
Poling circuit	13	PCP	for drawing a metal electrode for the polymer poling purpose

Figure 3-58(a) shows the added poling circuit for the mask layout of 300nm stoichiometric SiN platform that provides two parallel set of metal pads for the poling probes. One set of pads is near the top edge of cell, and another is near the bottom edge. On the other hand, the poling circuits in Figure 3-58(b) are split to two individual sets of circuit. The poling circuit on the upper half of cell layout is only for the 600nm stoichiometric SiN platform while another circuit in the lower half is for the 550nm Si-rich SiN platform. They need to be completely separated from each other because they require the different poling voltages according to its electrode gap. Only the devices in one of platforms will be appropriately working for each fabricated chip depending on the waveguide-core material of that chip. This means the mask layout is sharable between these two platforms, but they must be fabricated on the separate chip.

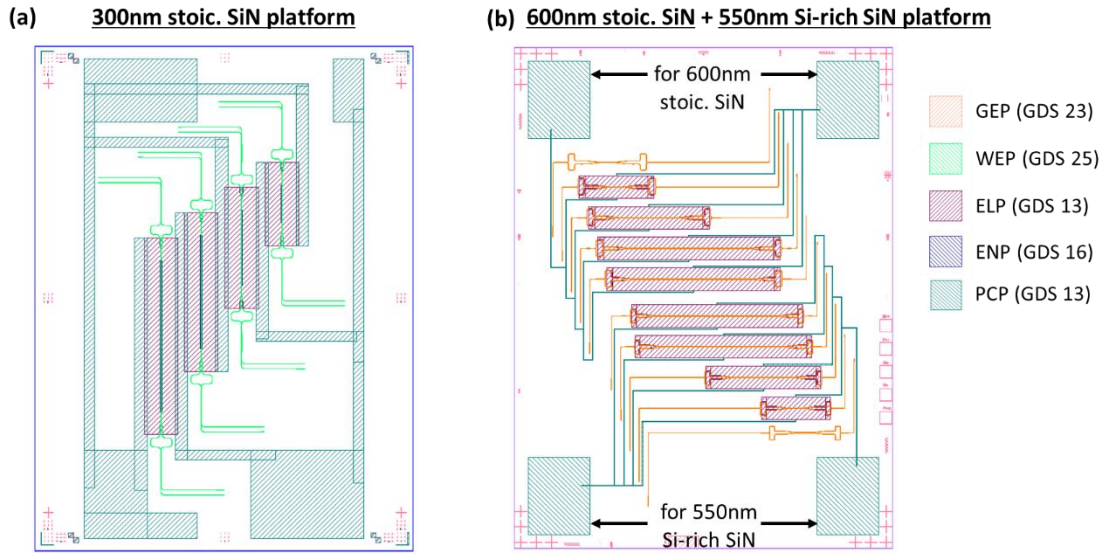

Figure 3-58 Full design of the mask for fabricating the modulator based on (a) 300nm-thick stoichiometric SiN platform and (b) 600nm stoichiometric SiN + 500nm-thick Si-rich SiN platform.

Table 3-18 The complete design parameters of the lithography masks using in this work.

Waveguide core Platform	Mask name	Lithography type	Fixed parameter	Varied parameter	GDS layers included
300nm stoic. SiN	Passive MZI #1	E-beam	Mod. WG width = 0.6 µm	Mod. WG length = 1.5, 3.0, 4.5, 6.0 mm	GEP (GDS 23) WEP (GDS 25) ENP (GDS 16)
	Passive MZI #2	E-beam	Mod. WG width = 0.9 µm		
	Passive MZI #3	E-beam	Mod. WG width = 1.2 µm		
	Passive MZI #4	E-beam	Mod. WG width = 1.5 µm		
	Metal lift-off	Photolithography	Electrode gap = 6 µm		ELP (GDS 13) PCP (GDS 13)
600nm stoic. SiN + 550nm Si-rich SiN	Passive MZI	SCANNER (DUV)	[stoic.] Mod. strip WG width = 0.8 µm [stoic.] Mod. slot WG = 350|700|350 nm [Si-rich] Mod. strip WG width = 0.6 µm [Si-rich] Mod. slot WG = 300|300|300 nm	Mod. strip WG length = 4.0 mm Mod. slot WG length = 0.5, 2.0, 4.0 mm	GEP (GDS 23) WEP (GDS 25) ELP (GDS 13) PCP (GDS 13)
	Metal lift-off	SCANNER (DUV)	[stoic.] Electrode gap = 5.4 µm [Si-rich] Electrode gap = 3.4 µm		ELP (GDS 13) PCP (GDS 13)

3.7 Chapter Conclusion

The design and simulation of photonic component on SiN platform, starting from the introduction of important tools used to design and simulate all components in the EO-polymer modulator in this research were presented. The important parameters and optimisation of passive components including grating coupler, waveguide, MMI, and Mach-Zehnder interferometer structure were also reported. The design and fabrication parameters of two designs of waveguide including strip waveguide and slot waveguide were optimised and all optimal dimension for the device fabrication to achieve the high efficiency modulator are achieved. The drawing procedure of mask layout for fabricating all components in the device were explained. The optimal design of all components in the device for fabrication process are concluded in Table 3-18 The complete design parameters of the lithography masks using in this work..

Chapter 4.
FABRICATION PROCESSES

4.1 Preparation of Electro-Optic Polymer

In this work, there are three kinds of EO polymers categorised by the phase of device development in which polymer has been applied to. To avoid the complication of chemical process for preparing the chromophore in the beginning phase, the earliest version of EO polymer was prepared in the form of side-chain chemical structure by polymerising the commercial chromophore with methyl methacrylate (MMA) monomers. Using this commercial chromophore, the EO polymer could only provide a measurable EO activity. However, it is initially used to fabricate the first workable device and develop the dependent processes such as polymer coating, high-voltage poling, modulator characterisation. For the intermediate phase of this work, the highly efficient chromophore was developed by our internal collaborator (School of Chemistry, University of Southampton). With this synthesised chromophore, the EO polymer was prepared in form of host-guest chemical mixture by only blending the chromophore and host polymer without any polymerisation process. In the latest phase, the outstanding EO polymer has been developed and provided by our external collaborator at Kyushu University, Japan. This EO polymer requires only a solvent mixing step to prepare the chemical solution.

4.1.1 Side-Chain EO Polymer with Commercial Chromophore

The earliest version of EO polymer in this work is a side-chain copolymer PMMA-*co*-DR1MA which was synthesised from two main chemical precursors including methyl methacrylate (MMA) and commercially available chromophore Disperse Red 1 (DR1). For preparing the chemical precursors to obtaining the EO polymer powder, the chemical processes were entirely carried out by our internal collaborator leading by Associate Professor Ramon Rios Torres in School of Chemistry at University of Southampton. The copolymerisation process was started from functionalising the DR1 molecules with a methacryloyl chloride to obtain the DR1MA molecules. This functionalisation step is to modify the DR1 molecules for co-polymerising with the MMA monomers. The DR1MA was co-polymerised with MMA monomer with a weight ratio of 50:50 (MMA:DR1MA), and then they formed the poly(methyl methacrylate) (PMMA) polymer chain with DR1 side-branched molecules, so called PMMA-*co*-DR1MA side-chain copolymer. The chemical process flow is briefly illustrated in Figure 4-1 and described in detail in the MPhil thesis by Matthew Owen Jenner (pp.16-17, 34-36) [180] with the codename as compound 26. Finally, the chemical solution of EO polymer was prepared by dissolving PMMA-*co*-DR1MA copolymer into anisole solvent with a concentration

of 5% by weight and stirring overnight (~14 hours). From this point, the EO polymer is ready for coating onto the SiN waveguide sample which is detailed in the section 4.2.3.

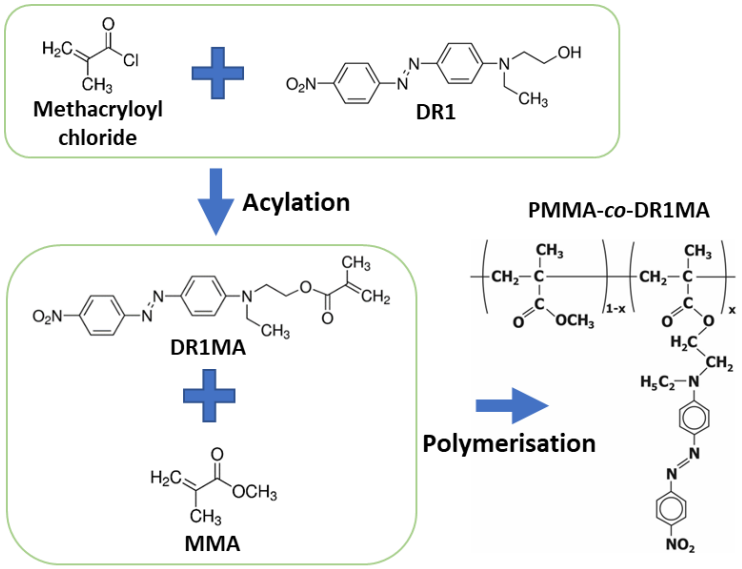

Figure 4-1 – Chemical process for synthesis of side-chain PMMA-*co*-DR1MA.

4.1.2 Host-Guest EO Polymers with Synthesised Chromophore

In the middle phase of this work, we started an internal collaboration with the School of Chemistry, University of Southampton to develop a chemical process for synthesising the second version of chromophore "Phenyl vinylene thiophene" (also called FTC chromophore, see section 2.2.3.2 for molecular structure). The synthesis process had been initially developed by Matthew Owen Jenner, our collaborating PhD student at that moment, and completed by Dr. Marta Meazza. The detail of this chromophore synthesis has been described in Matthew's MPhil thesis (pp.20-31) the codename as chromophore 31. Due to the difficulty of chromophore synthesis on a larger scale, the quantity of synthesised chromophores was not enough to develop the co-polymerisation process for enabling a practical production scale of side-chain EO polymer. Therefore, the initial test of this chromophore is in the form of host-guest polymer system. With the host-guest system, the EO polymer were simply prepared by dissolving the FTC based chromophore in the commercially available PMMA chemical solution which is a well-known 950K PMMA-A4 photoresist by controlling the weight ratio of 50:50 (chromophore:PMMA). The mixture was blended by using a magnetic stirrer for 2 hours at room temperature. The final polymer solution contains 8% by weight of the solid contents in anisole solvent (4% from chromophore and 4% from PMMA). This EO polymer solution has been defined with the codename of "HG PMMA-FTC" for ease of reference in this work.

4.1.3 CN-TK2 EO Polymer from Kyushu University

In the latest phase of this work, a collaboration with Yokoyama Research Group at Kyushu University in Japan which is led by Professor Shiyoshi Yokoyama was initiated. Another version of EO polymer has been provided to us from this research group. This EO polymer is the side-chain polymer with FTC-based chromophore, and it has a codename of "CN-TK2". The EO polymer was synthesized by using the same synthesis process presented in [181] with a chromophore loading ratio of 35% by weight. For this EO polymer, an in-device EO coefficient ($r_{33,in-device}$) has been demonstrated up to165 pm/V [182] along with the thermal and temporal stability [183] as a result of its high glass transition temperature of 182°C. The EO polymer was delivered in the form of polymer powder, and it was then dissolved at 10% by weight in the solvent Cyclopentanone. The mixture was blended by using a magnetic stirrer for 12 hours at room temperature.

4.1.4 Summary

The chemical specifications and codename of all three EO polymers using in this work are summarised into the Table 4-1 as presented below.

Table 4-1 Chemical informations and codenames of three EO polymers used in this research.

EO polymer codename	Chemical packing type	Chromophore basis	Polymer basis	Chromophore loading ratio in polymer (by weight)	Concentration (solvent)
PMMA-co-DR1MA	Side-Chain	Disperse Red 1 (DR1)	PMMA	50:50	5% (in anisole)
HG PMMA-FTC	Host-Guest	Phenyl vinylene thiophene (FTC)		50:50	8% (in anisole)
CN-TK2	Side-Chain			35:65	10% (in cyclopentanone)

4.2 Device Fabrications

By way of cost- and time-effective processes for fabricating the optical modulator with EO polymer in this work, the modulator fabrication process requires only four main steps to enable optical modulation onto the SiN waveguide platforms. The fabrication steps will be explained in this section starting from the deposition of SiN on a bare wafer and end up with the activation of SiN based modulator by using the high-voltage poling tool.

4.2.1 SiN Layer Deposition and Patterning

In this section, the details about processes, recipes and tools that were used to deposit and pattern a layer of SiN will be presented. The aim of this process is for defining a design layout of photonic structures such as waveguide into the SiN layer as presented in Figure 4-2.

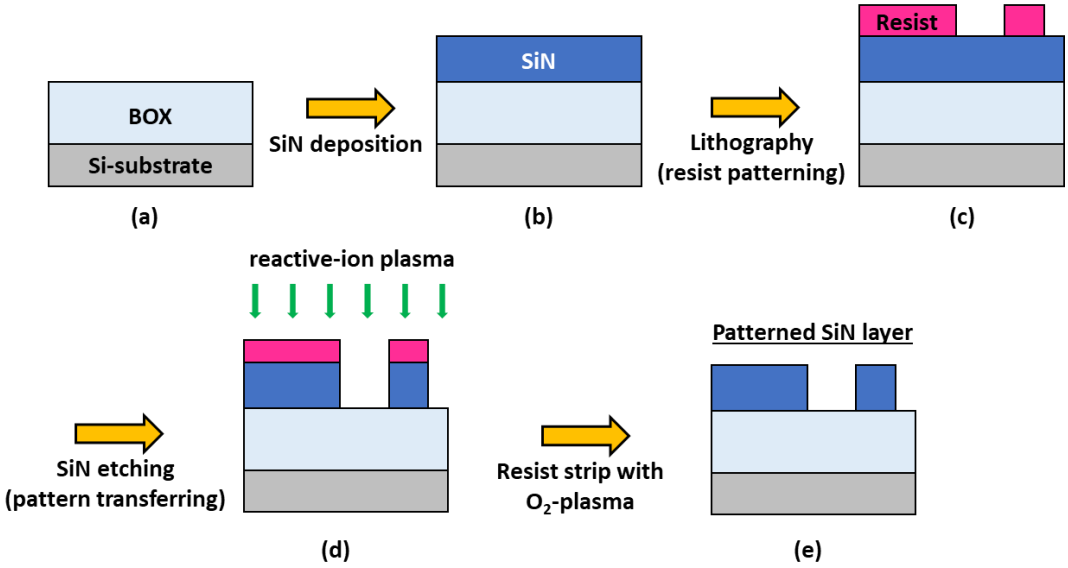

Figure 4-2 Process flow for the fabrication of passive photonic structures in SiN platform: (a) starting from an original wafer with a 2-3µm-thick buried oxide (BOX) on Si-substrate, (b) a layer of SiN layer is deposited on top using PECVD technique, (c) a layer of lithography resist is spin-coated on the top of SiN layer and patterned, (d) the lithography pattern is transferred to the SiN layer using ICP-RIE dry etching technique, and (e) a remained resist is stripped with O_2-plasma.

4.2.1.1 PECVD SiN depositions

The first step of fabrication processes is the deposition of SiN onto a commercially available wafer as illustrated in Figure 4-2(a)-(b). This wafer already had a layer of buried oxide (BOX) on bulk Si substrate. There are two different specifications of wafer used in this work including 6" wafer with 2µm-thick BOX layer and 8" wafer with 3µm-thick BOX layer. The first one was used for the platform of 300nm-thick stoichiometric SiN (aim to the design of stipe waveguide modulator) while the latter one was used for the other two platforms: 600nm-thick stoichiometric SiN and 550nm-thick Si-rich SiN (aim to the designs of slot waveguide modulator) The SiN layer was deposited by using the Plasma-Enhanced Chemical Vapour Deposition (PECVD) technique that was performed with the *Oxford Plasma Technology 100 PECVD* system. This standard PECVD recipe for stoichiometric SiN deposition requires a gas mixture of SiH_4 (at flowrate of 1.8 sccm) and N_2 (at flowrate of 980 sccm), and the reaction chamber is under control at the pressure of 950 mTorr and supplied with RF power of 60W. The temperature of wafer platen in the reaction chamber is fixed at 350°C throughout the process. To deposit the Si-rich SiN layer, only the change of SiH_4 flowrate to be of 3.6 sccm is required. The SiN deposition recipes were developed by Dr. Thalia Dominguez Bucio, thus, deep details of the deposition process are described in her PhD thesis [184].

4.2.1.2 Electron beam (e-beam) lithography

For 300nm-thick stoichiometric SiN platform, the e-beam lithography technique was used to print out the mask layout onto the wafer. Firstly, the wafer was spin-coated with ZEP520A E-beam resist with the target thickness of 450 nm. Next, the mask layout was written down to the layer of resist using the *JEOL JBX-9300FS E-BEAM* tool with the following writing parameters: an exposure dose of 185 μc/cm^2, a beam size of 20nm and a pitch of 20nm. Afterwards, the written pattern on resist was developed using ZED-N50 chemical developer by gently stirring the wafer in a beaker of developer for 2 minutes and 50 seconds. Then, the wafer was immediately cleaned with isopropanol alcohol (IPA) for 30 seconds and with deionised water for 2 minutes, respectively. Finally, the wafer was dried by using a wafer spin dryer and a nitrogen gun to gently blow the wafer surface at the end.

4.2.1.3 Scanner deep-UV lithography

For 600nm-thick stoichiometric SiN and 550nm-thick Si-rich SiN and platforms, the lithography step to print out the layout of waveguide structure was processed by using the *Nikon S240 DUV Scanner* system. This lithography process was entirely performed by the tool operator from the photoresist coating step to the development step. The thickness of *JSR-M91Y* photoresist was chosen at 0.68μm, and the UV exposure dose was set to the optimal value of 20 mJ/cm^2. As explained in the section 3.6, the designs for both SiN platforms are on the same mask layout. Therefore, the wafers for both could be conveniently lithographed in the similar way.

4.2.1.4 Pattern transferring using Inductively Coupled Plasma (ICP) technique

The lithography-defined patterns from the previous steps were transferred to the SiN layer with an Inductively Coupled Plasma Reactive Ion Etch (ICP-RIE) technique. The available ICP-RIE tool used in this work is the Oxford Plasmalab system 100 (ICP380). Principally, the RIE tool aims to perform a dry etching process to remove material deposited on wafers with the chemical reactive-ion plasma. The plasma is generated in a low-pressure chamber of the tool by using a radio frequency (RF) electromagnetic field. In terms of ICP-RIE, a high-powered RF induction coil is integrated to the RIE tool chamber as an ICP source. The ICP source generates a plasma at higher density comparing to a standalone RIE system, therefore, it helps to enhance the etching rate. During the process, the tool chamber must be supplied with an appropriate mixture of chemical precursor gases which is depended upon the target generated plasma and etching material. For the SiN etching recipe used in this work, the ICP-RIE tool was set with the following process parameters: a wafer platen temperature of 15°C, SF_6 gas flowrate of 65 sccm, CHF_3 gas flowrate of 35 sccm, chamber pressure of 15 mTorr, RF power of 50W and ICP source power of 1400W. The SiN layer was intended to be fully etched as shown in Figure 4-2(d). After the etching process, the etch depth was checked using an ellipsometry technique (*J. A. Woollam M2000 Spectroscopic Ellipsometer*). Finally, the remained resist was striped with 800W O_2-plasma recipe over the tool *PVA TePla 300 Microwave Plasma*

System. At this point, the passive photonic structures have been etched in the SiN layer and ready for the integration of a metal electrode and EO polymer cladding.

4.2.2 Metal Electrode Preparations

The metal electrode was fabricated by using the metal lift-off process. This process initially requires a resist patterned with the inverse layout of electrode design (also called a lift-off resist or a negative tone resist). Two kinds of photolithography technique were employed for preparing a lift-off resist layer in this work including a conventional UV lithography with image reversal and a scanner deep-UV lithography. The first technique was used in the first phase of this work for 300nm stoichiometric SiN platform while the other technique was used for the remaining two SiN platforms with a slot waveguide design.

4.2.2.1 Conventional UV lithography with an image reversal technique

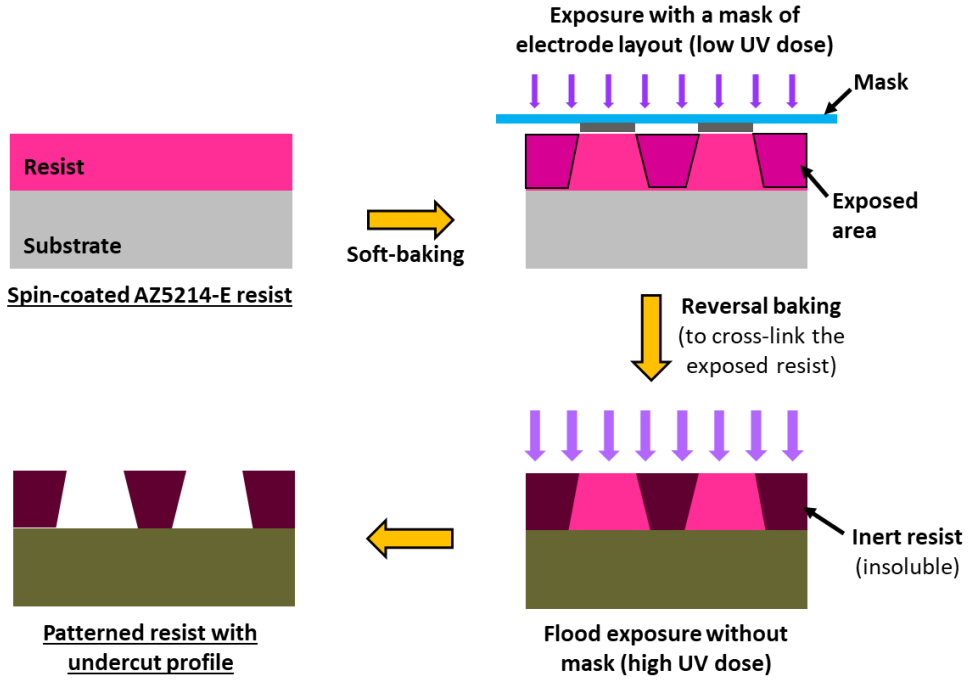

Figure 4-3 Process flow of the photolithography with an image reversal technique.

To prepare a lift-off resist with this technique, the use of specific image reversal photoresist is required, such as an AZ5214-E photoresist which was used in this work. The aim of this technique is to attain an undercut side-wall profile of the resist cross-section for easing the metal lift-off process. Compared with the general protocol for positive tone resists, the image reversal is processed with more steps including the "reversal bake" after first exposure and the subsequent "flood exposure" before development. As shown in Figure 4-3, the process starts from the preparation of a layer of 1.6µm-thick resist on the substrate. The resist was spin-coated at a spinning speed of 3,000 rpm for 40 seconds and soft-baked on a hot plate at 100°C for 3 minutes to get rid of solvent. Next, the sample

with soft-baked resist was exposed at low UV dose for 5 seconds (~17mJ/cm^2) with the mask of electrode layout. After the first UV exposure, the sample was again baked on a hot plate at 125°C for 30 seconds in order to cross-link the resist in an exposed area. The cross-linked resist becomes insoluble in the developer so-called inert resist. Afterwards, the sample was exposed again in a UV flood-exposure mode (without mask) for 45 seconds (~160mJ/cm^2). The second step of UV exposure in the flood mode will make the none-exposed resist in the first step to soluble in the developer. Finally, the resist was developed in a mixture of AZ400K developer and deionised wafer with a mix ratio of 1:3 (developer:water) with a development time of 15 seconds. The UV exposure steps in this process were implemented with the *Karl Suss MA6 Mask Aligner* system.

4.2.2.2 Scanner deep-UV lithography with thick photoresist

For 600nm-thick stoichiometric SiN and 550nm-thick Si-rich SiN platforms, the scanner deep-UV lithography was used again to print out the layout of electrode. That means their lithography steps rely on the use of only the scanner system throughout the fabrication process. For this lift-off process, the thick resist was chosen with the thickness of 1.3µm, and the UV exposure dose was set to 27 mJ/cm^2. All lithography steps with the scanner system were performed by the professional operator.

4.2.2.3 Metal layers deposition

Once the lift-off resist on sample were patterned with the layout of modulator electrode, a stack of metals was deposited onto the top surface of sample and resist. The layer stack is comprised of titanium/aluminium/titanium (Ti/Al/Ti) layers. The bottom Ti-layer acts as an adhesive metal to glue the Al-layer with the dielectric substrate, the thickness of 10 nm was selected for this layer. The top Ti-layer is used for preventing an oxidisation on the Al-layer surface when the sample has been exposed to the air, thus, a Ti-layer with a thickness of 60 nm was chosen. The thickness of the Al-layer depends on the total thickness of the metal electrode and is defined in Chapter 3. For an electrode thickness of 500nm used in the 300nm-thick stoichiometric SiN platform, the thickness of Al-layer was set to be 430nm. To obtain an electrode thickness of 300nm in the two slot waveguide platforms, the thickness of Al-layer was set to be 230nm. This layer stack was deposited by using the *Leybold Optics LAB700 Evaporation* system which is based on an electron beam evaporation technique. The deposition rates were set to 0.05/0.1/0.05 nm per second from bottom to top layer, and the vacuum pressure was set between 10^{-6} and 10^{-5} mbar during the deposition.

4.2.2.4 Metal lift-off process

In the final step of metal electrode preparation, the sample with evaporated metal layers was immersed in a beaker of lift-off solvent for at least 12 hours. For the sample with the AZ5214E lift-off resist, acetone was used as a lift-off solvent, and the sample was cleaned by only rinsing IPA over

the top surface. For the sample with scanner lift-off resist, the suitable lift-off solvent is *Edge-Bead Removal of AZ® Photoresists (AZ®EBR)* solvent, and the sample also requires an additional lift-off step after 12 hours immersion in solvent. The *SSE OPTIWET ST30* lift-off tool was used to complete the additional lift-off processing with scanner resist. With this tool, the pressurised N-Methyl-2-pyrrolidone (NMP) solvent was sprayed onto the sample to remove all residue of metal and resist left over from the first lift-off step. Finally, the sample was dried by using a N_2 gun, and metal electrode was completely patterned onto the device as shown in Figure 4-4.

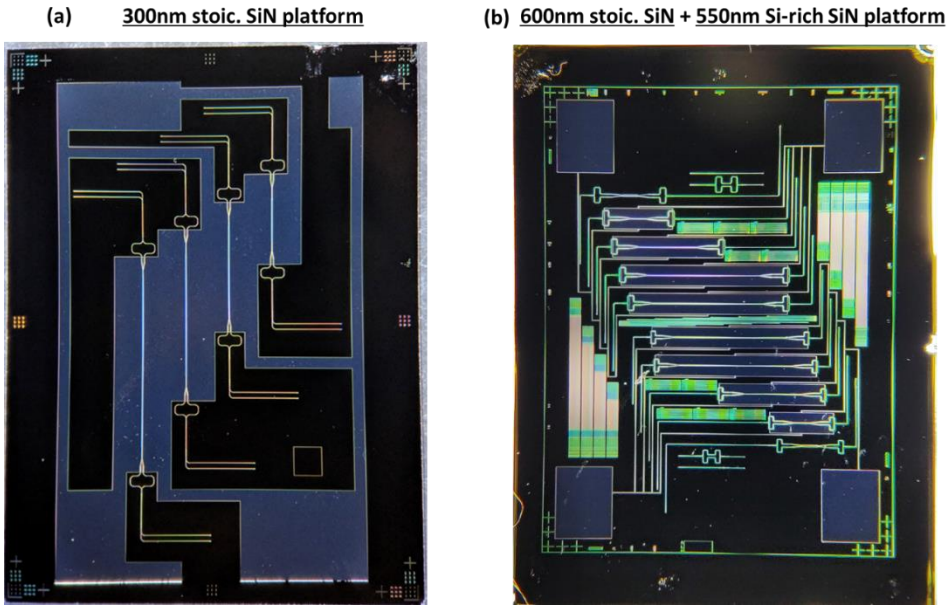

Figure 4-4 Fabricated sample of MZI structures with metal electrode: (a) 300nm-thick stoichiometric SiN platform and (b) 600nm stoichiometric SiN + 550nm-thick Si-rich SiN platform.

The SEM images of the final device after metal lift-off process are presented in Figure 4-5 for the strip waveguide and Figure 4-6 for the slot waveguide.

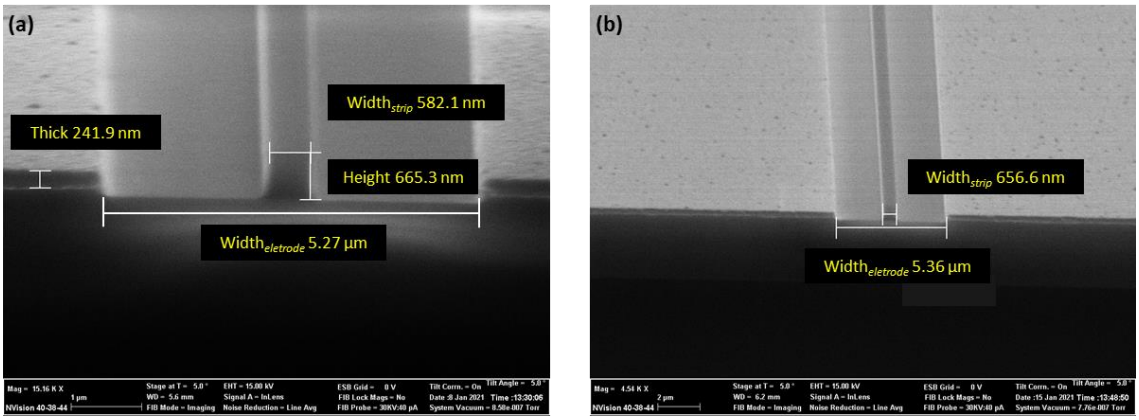

Figure 4-5 Scanning electron microscope (SEM) image of (a) 600nm stoichiometric SiN waveguide and (b) 550nm Si-rich SiN waveguide, taken over the side surface to show the output waveguide.

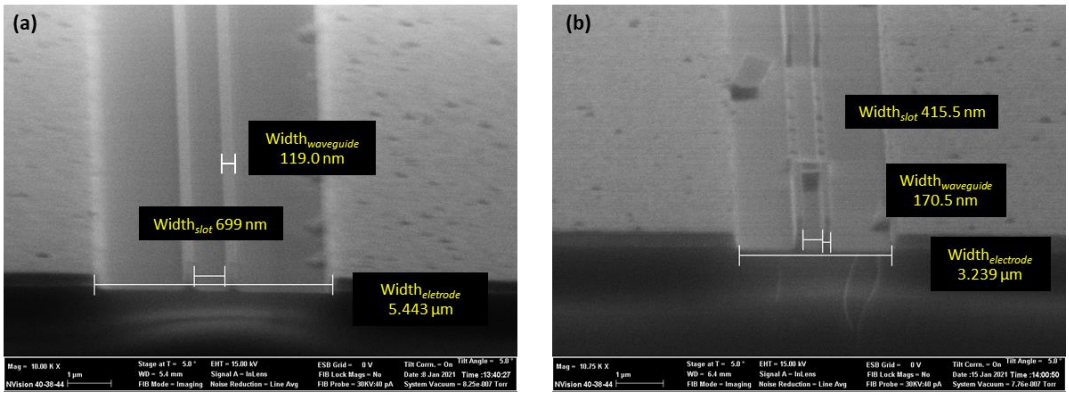

600nm stoic. SiN platform

550nm Si-rich SiN platform

Figure 4-6 Scanning electron microscope (SEM) image of (a) 600nm stoichiometric SiN slot waveguide and (b) 550nm Si-rich SiN slot waveguide, taken over the side surface to show the output waveguide.

As shown in these two figures, there is the dimension error in the fabrication when comparing with the design. These errors can be caused by the deformation of the photoresist (shrink). In the etching process, heat, processing gases, and RF plasma are applied to the chamber environment resulting in the deformation of the photoresist which is the main cause in the error of the fabrication. This error should be able improved by design the mask with oversize dimensions, but the compensation of dimension needs to be accurately optimised or by changing the etching method.

4.2.3 EO Polymer Coating Processes

Once the EO polymer solutions have been prepared and the sample of MZI devices with metal electrode have been fabricated, the integration process was then performed. The EO polymer was incorporated as a layer of top cladding of MZI devices to enable the modulation activity. The spin-coating technique was employed to coat the EO polymer onto the top surface of the sample. To ensure that only EO polymer will be coated on the sample surface, the polymer filtration step is also necessary to be done prior to the polymer spin-coated process. The PTFE-filter with pore size of 0.2µm was use for removing insoluble particles out of the EO polymer solution. In this work, two different coating methods were implemented to deposit EO polymer as the top cladding layers of the modulator devices which will be explained as follows.

4.2.3.1 EO-polymer layer with PMMA top-up cladding (for PMMA-co-DR1MA and HG PMMA-*FTC EO polymers)*

The first method used to coat the EO polymer on the sample is EO-polymer layer with PMMA top-up cladding. With this coating method, the top cladding of the sample consists of two polymer layers including EO polymer and PMMA as illustrated in Figure 4-7. Firstly, a solution of filtered EO polymer was spin-coated at a speed of 1000 rpm on the top surface of sample and baked on a hot

plate at 110°C for 3 minutes. Following the EO polymer coating, the *950K PMMA-A11* photoresist was used to spin on the top of EO polymer layer using the spinning speed of 4000 rpm then baked at 110°C for 10 minutes. This method has been applied for coating the first two types of EO polymer used in this work including a PMMA-*co*-DR1MA and an HG PMMA-FTC. By using the Ellipsometer to check the thickness of the coated polymer layers, the thickness of EO polymer layer was found within the range of 400-650nm while the thickness of *950K PMMA-A11* layer was about 2 µm. Two main reasons to coat a layer of *950K PMMA-A11* photoresist on top of the EO polymer cladding are: (1) to make the total cladding thickness to be in line with the design in simulation that should be thick enough to support the optical field of waveguide mode and (2) to prevent the electrical breakdown which could happens in the high-voltage poling process when the polymer cladding layer is not thick enough.

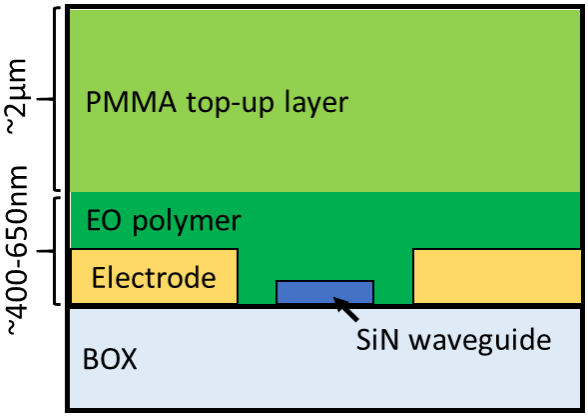

Figure 4-7 Cross-sectional schematic of coated polymer layers as cladding on top of modulator sample.

4.2.3.2 Single thick layer of EO-polymer (for CN-TK2 EO polymer)

Along with the support of CN-TK2 EO polymer from Kyushu University, the suggestions in coating process were provided for depositing a good quality cladding layer of EO polymer. A single 1µm-thick EO polymer layer cladding was deposited by spin-coating at 1000rpm and baking at 80°C on a hot plate for 10 minutes. Due to a high boiling temperature of the solvent used in this EO polymer (cyclopentanone, ~131°C), the sample was then annealed at 95°C in vacuum pressure overnight (~16 hours). The trapped solvent on the sample after the EO polymer coating process can cause an electrical breakdown during the high-voltage poling process. Thus, this vacuum annealing process is to remove all trapped solvent in the polymer cladding layer. The coated thickness of ~1 µm was measured by using an ellipsometry technique.

4.2.4 Polymer Activation with High-Voltage Poling Technique

To activate the EO polymer with the home-build high-voltage poling setup, a pair of copper probes was connected to the electrical poling pads on the sample. By using the home-build high-voltage poling setup, the sample will be placed and fixed on a heating platen as shown in Figure 4-8.

The heat is required to relax the pack of chromophore molecules in EO polymer to be able to change their orientation when the poling electric field is applied. In the poling process, the sample was firstly heated up closely to the glass transition temperature (T_g) of EO polymer (~150°C for PMMA-*co*-DR1MA and HG PMMA-FTC, and ~182°C for CN-TK2). Once the heating temperature was stable near T_g, the high-voltage source was switched on and slowly increased the poling voltage level until the voltage setpoint (V_{poling}). The setpoint value can be calculated by mean of applying a poling electric field (E_{poling}) of 100 V/µm across the modulator electrode gap (d) by using the equation $V_{poling} = E_{poling} \cdot (2d)$. According to this equation, the electrode gap is multiplied by 2 because the poling electric field is simultaneously generating across two gaps according to the electrode configuration presented in Figure 3-21. The applied poling voltage is designated by referring to the average electric field (100V/µm) required for efficiently poling EO-polymer as reported in several publications [117, 170, 185]. By assuming that the applied voltage is equal across two identical electrode spacings as formerly explained, the applied voltage can be calculated by taking the required electric field and the optimal electrode distance. For the electrode designed in this work, the electrode gaps are 6, 5.4, and 3.4 µm for the 300nm stoichiometric SiN, 600nm stoichiometric SiN and 550nm Si-rich SiN platform, respectively. Therefore, the voltage setpoints of the 300nm stoichiometric SiN, 600nm stoichiometric SiN and 550nm Si-rich SiN platform are 1200V, 1080V, and 680V. After steadying the poling voltage at setpoint for 2 minutes, the heating platen was cooled down to the room temperature by retaining the poling voltage at the setpoint. The aim of polymer activation with this high-voltage poling process is to orientate the chromophore molecules in EO polymer as described in the Chapter 2.

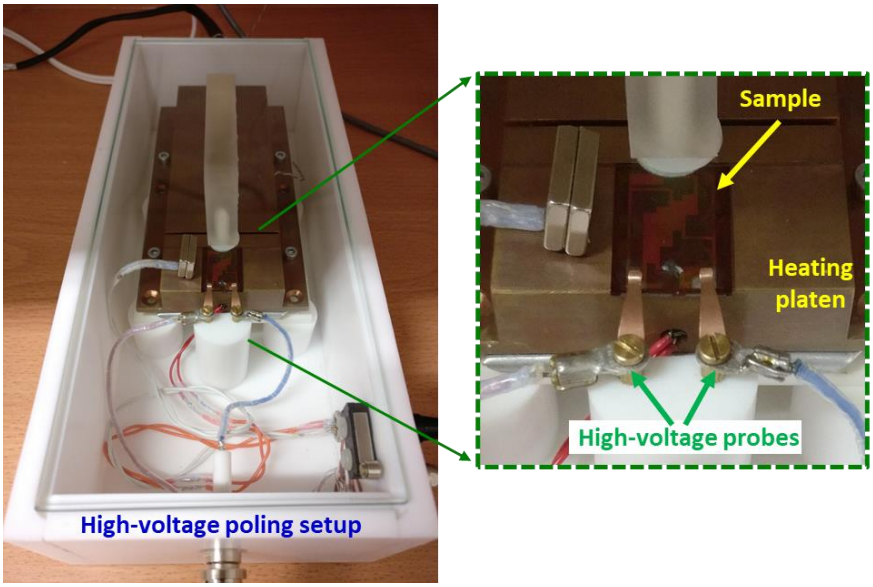

Figure 4-8 High-voltage poling setup for activating an EO effect in the polymer cladding.

In addition to the poling process explained above, a silicone oil (Polydimethylsiloxane, PDMS) was used to prevent the electric breakdown for the samples with CN-TK2 EO polymer

because this sample does not have a top-up PMMA cladding layer. Before the poling process, some silicone oil was dropped on the sample to cover the region of modulator electrode gaps. The silicone oils is a suggested material for this purpose because of its high dielectric breakdown (250 to 635 V/μm [186]). By depositing the top-up PMMA layer on the EO polymer layer, surface roughness between two polymers due to the different matching material can cause the electric break down. Therefore, the use of silicone oil for the poling process is mainly use for preventing the electrical break down during the poling process. Thus, the modulating efficiency the fabricated modulator can be enhanced.

4.2.5 Summary

The lithography techniques, the information of wafer, and the voltage required for EO polymer activation of all three platforms of EO polymers modulator using in this work are summarised into the Table 4-2 as presented below.

Table 4-2 Details of the device fabrication, device information and modulating activation of three 300nm-thick stoichiometric SiN platform, 600nm stoichiometric SiN and 550nm-thick Si-rich SiN platform.

Platform	Lithography technique [Resist type & thickness]		Wafer diameter	BOX thickness (μm)	Electrode thickness (μm)	Poling voltage (V)
	SiN patterning	Metal electrode lift-off				
300nm stoic. SiN	e-beam [ZEP520A – 450nm]	UV image reversal [AZ5214E – 1.6μm]	6”	2	0.5	1200
600nm stoic. SiN	Scanner DUV [JSR-M91Y – 0.68μm]	Scanner DUV [JSR-M91Y – 1.3μm]	8”	3	0.3	1080
550nm Si-rich SiN						680

4.3 Chapter Conclusion

Details of the fabrication processes starting from the preparation of EO- polymer has been reported with three kind of EO polymer including PMMA-*co*-DR1MA, HG PMMA-FTC, and CN-TK2. The fabrication of the components in the device including the deposition and patterning of SiN, the deposition and patterning of metal electrode, the development of polymer coating process, and the activation of EO-polymer were demonstrated. The SEM images result showing that the designed device structures were clearly fabricated. Two polymer coating methods were presented showing the advantage of using CN-TK2 polymer over the others two EO polymer as it is required only single layer of EO polymer.

Chapter 5.

DEVICE CHARACTERISATIONS

Stoichiometric silicon nitride (SiN) has a homogeneous micro-structure, negligible two-photon absorption and a reduced number of N-H and Si-H bonds that allow obtaining low propagation losses in the near-infrared (NIR) wavelength. Thus, NH_3-free stoichiometric SiN with a refractive index close to 2 has proven to be an ideal candidate to develop a platform for the NIR regime. A low-temperature NH_3-free nitrogen rich (Si-rich) SiN platform was developed to improve the device in O-band regime at the centre wavelength of 1310 nm. As a result, the EO polymer modulator based on SiN waveguide in this work have been designed and fabricated by using these two material platforms as reported in the previous two chapters.

In this chapter, the characterisation results of a variety EO polymer modulators fabricated from the stoichiometric SiN and Si-rich SiN platform will be demonstrated. Results of passive device including grating coupler and phase modulator waveguides will be revealed in section 5.2. Then, the modulation result of the modulator fabricated in this research including the DC modulation and the High-frequency modulation will be reported in section 5.3 and 5.4, respectively.

5.1 Designation Codename of Modulator Device

Due to a variety of modulator designs and EO polymer cladding to be characterised in this chapter, each modulator device has been defined with a specific codename which is representative of the specifications. Based on the declarations of modulator designs in Table 3-18 and EO polymer types in Table 4-1, the codenames will consist of the “waveguide platform code”, “modulation waveguide type, width and length”, and “EO polymer type”. For example, the codename “300-Strip900-L6.0/CNTK” stands for the modulator using a 300nm-thick stoichiometric layer. This SiN platform is designed with a 900nm-width strip waveguide, a modulation length of 6.0mm, and CN-TK2 EO polymer as cladding layer. Therefore, the codenames of all available devices have been presented in Table 5-1 along with their design parameters and polymer type utilised.

As shown in Table 5-1, not all device designed and fabricated in this research are workable. For platform 300nm stoichiometric SiN strip waveguide, the non-working modulators are because of the defect in the device during the fabrication process. These are included the broken of waveguides, the contaminated particle in coated polymer, or uncomplete lift-off metal left over in electrode gap. For non-working slot waveguide modulators in 600nm stoichiometric SiN and 550nm Si-rich SiN, the propagation loss of these devices is too high to be measured the output spectrum that will be explained more in the following section.

Table 5-1 Codenames of modulators with associated platform in this work.

Codename (Sample ID)	Platform	Waveguide type	Waveguide parameters	Modulator length (mm)	EO polymer type	Working modulator
300-Strip600-L1.5-4.5/DR1	300nm Stoic. SiN	Strip	width = 600 nm	1.5-4.5	PMMA-co-DR1MA	-
300-Strip600-L6.0/DR1			width = 600 nm	6.0	PMMA-co-DR1MA	Yes
300-Strip600-L1.5-4.5/FTC			width = 600 nm	1.5-4.5	HG PMMA-FTC	-
300-Strip600-L6.0/FTC			width = 600 nm	6.0	HG PMMA-FTC	Yes
300-Strip900-L1.5/CNTK			width = 900 nm	1.5	CN-TK2	Yes
300-Strip900-L3.0-4.5/CNTK			width = 900 nm	3.0-4.5	CN-TK2	-
300-Strip900-L6.0/CNTK			width = 900 nm	6.0	CN-TK2	Yes
300-Strip1200-L1.5/CNTK			width = 1200 nm	1.5	CN-TK2	Yes
300-Strip1200-L3.0/CNTK			width = 1200 nm	3.0	CN-TK2	Yes
300-Strip1200-L4.5/CNTK			width = 1200 nm	4.5	CN-TK2	Yes
300-Strip1200-L6.0/CNTK			width = 1200 nm	6.0	CN-TK2	-
300-Strip1500-all/any			width = 1500 nm	1.5-6.0	any	non-fabricated
600-Strip800-L4.0/CNTK (S1)	600nm Stoic. SiN	Strip	width = 800 nm	4.0	CN-TK2	Yes
600-Strip800-L4.0/CNTK (S2)			width = 800 nm	4.0	CN-TK2	Yes
600-Strip800-L4.0/CNTK (S3)			width = 800 nm	4.0	CN-TK2	Yes
600-Slot-L0.5/CNTK (S1)		Slot	300|700|300 nm	0.5	CN-TK2	Yes
600-Slot-L0.5/CNTK (S2)			300|700|300 nm	0.5	CN-TK2	Yes
600-Slot-L0.5/CNTK (S3)			300|700|300 nm	0.5	CN-TK2	Yes
600-Slot-L2.0-4.0/CNTK (S1-S3)			300|700|300 nm	2.0-4.0	CN-TK2	-
550-Strip800-L4.0/CNTK			width = 600 nm	4.0	CN-TK2	-
550-Slot-L0.5-4.0/CNTK			300|300|300 nm	0.5-4.0	CN-TK2	-

5.2 Characterisations in Passive Mode

5.2.1 Coupling Loss with Grating Coupler

The small features of the designed stoichiometric and Si-rich SiN waveguides used in this work can cause a large mismatch between the optical modes of the input optical fibres and those within the waveguides. Several techniques to couple the light into the waveguide have been demonstrated to solve this problem such as butt-coupling and grating coupler. Amongst them, grating couplers allow achieving high efficiency coupling with advantages such as their flexible placement around photonic circuits and their easier alignment with the input sources. Therefore, grating couplers were chosen as the coupling mechanism for the different SiN platforms discussed in this thesis.

The grating coupler simulations were performed and optimized to achieve high coupling efficiency. As demonstrated in Chapter 3, several grating parameters can potentially affect the performance of grating coupler including their period (Λ), etch dept, filling factor, cladding thickness, and coupling angle (θ). In this work, the simulation of coupling efficiency with the

variation of these parameters were performed and the optimised grating parameters were reported in Table 3-3. Figure 5-1shows an example of the fabricated grating couplers. In this case, a set of grating couplers connected back-to-back with different Λ were included in the fabrication layout to evaluate the response of the designed grating coupler. With this array, it was possible to determine Λ that provided the best coupling efficiency at the wavelength of 1550nm.

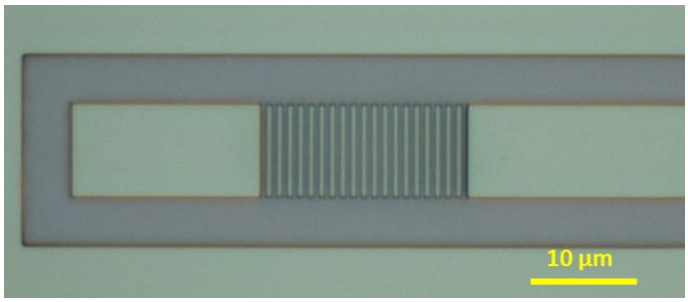

Figure 5-1 Microscopic image of the gratings fabricated on the stoichiometric SiN platform.

As the coupling loss from the grating coupler will be included in the total loss of the modulator device, the overall response of the designed grating coupler in dB versus wavelength was evaluated. Figure 5-2 shows the experimental results of the transmission through the grating coupler in a 600nm-Stoichiometric SiN and 550nm-Si-rich SiN platform. Based on the optimised parameters used to design the grating coupler as reported in Chapter 3, the lowest coupling loss has been designed for the wavelength of 1.55µm. As shown in Figure 5-2, peak of the transmission is located at the wavelength~ 1.565µm for both SiN platforms. The coupling efficiencies obtained are ~13.5dB/grating for 600nm Stoichiometric SiN and ~ 18dB/grating for 550nm Si-rich SiN. The simulated result in Table 3-3 showing that coupling efficiency of grating coupler for 600nm Stoichiometric SiN and 550nm Si-rich SiN are -4.07dB and -3.6dB, respectively.

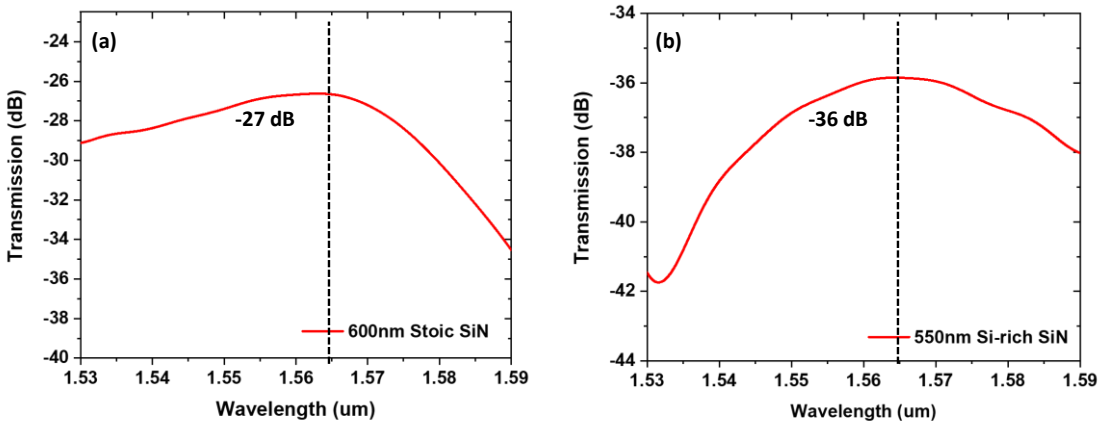

Figure 5-2 Experimental results for grating couplers measured at the wavelength from 1.530–1.590µm for (a) 600nm Stoichiometric SiN and (b) 550nm Si-rich SiN.

The discrepancies between the experimental and simulated coupling loss can be the result of additional losses that were not accounted in the simulations, such as scattering losses due to

imperfections in the etched waveguide profile including side-wall roughness, mismatch losses between the mode of the optical fibre and the grating couplers, losses created by the distance between the fibre and the grating surface, loss due to the reflection from the grating surface, or losses from the connectors in the experimental set-up. The different in the dimension of the fabricated device with the simulated device due to the tolerant in the fabrication and different if the refractive index of polymer use in the simulation and the real experiment are also the main reason for the high coupling loss of the fabricated grating coupler comparing with the simulated grating coupler.

5.2.2 Propagation Loss in Phase Modulator Waveguide

Propagation loss in phase modulator is one of the important parameters of the modulating device. In this work, phase modulator from three different SiN platform were characterised by launching the light through the phase modulator with different length to perform a cut-back measurement. The experimental results from each SiN platform show that, the measurement can be obtained only from the strip waveguide modulator in 300nm Stoichiometric SiN and the slot waveguide modulator in 600nm Stoichiometric SiN. The strip waveguide modulator with 600nm stoichiometric SiN and 550nm Si-rich SiN have not enough conclusive data to derive results from the cut-back measurements. Thus, the loss in phase modulator for these two platforms will be the insertion loss when comparing with the loss from MZI without electrode.

5.2.2.1 300nm stoichiometric SiN platform

For the strip waveguide modulator in 300nm stoichiometric SiN, loss can be calculated from phase modulators with 3 different lengths of 1.5, 3.0 and 4.5mm. Loss in phase modulator with this SiN platform was analysed when it was used together with CNTK polymer. As shown in Figure 5-3(a), transmission of the phase modulator is decreased with an increasing of waveguide length. The propagation loss in phase modulator at the wavelength of 1.550μm can be experimentally calculated by extracting the transmission at this wavelength and plotted together with the waveguide length as presented in Figure 5-3(b). The result from linear fitting showing that the propagation loss of phase modulator for 300nm stoichiometric SiN platform is 1.21 ± 0.23 dB/mm.

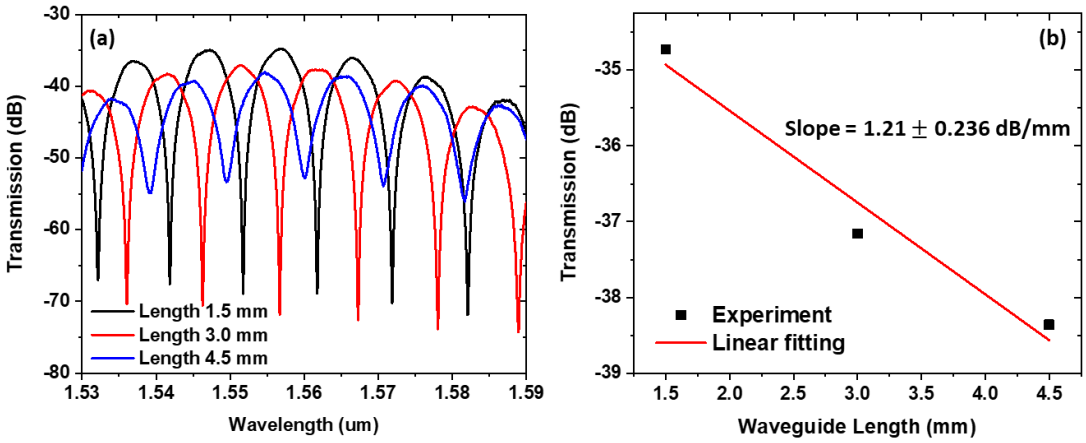

Figure 5-3 (a) Transmission from the phase modulator with 3 different waveguide lengths of 1.5, 3.0, and 4.5 mm. (b) Plotted between transmission as a function waveguide length and its linear fitting to find the loss at the operating wavelength of 1.550µm.

5.2.2.2 Strip 600nm stoichiometric SiN and 550nm Si-rich SiN platform

For the strip waveguide modulator in 600nm stoichiometric SiN and 550nm Si-rich SiN, loss can be estimated by subtracting the modulator insertion loss with the MZI structure without electrode (Figure 5-4).

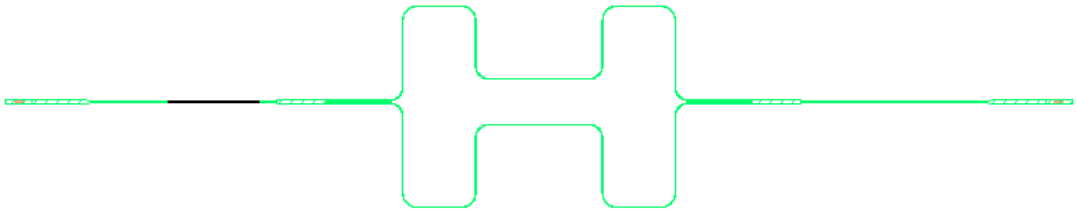

Figure 5-4 Structure of MZI structure without electrode to use as a reference for phase modulator in modulating device.

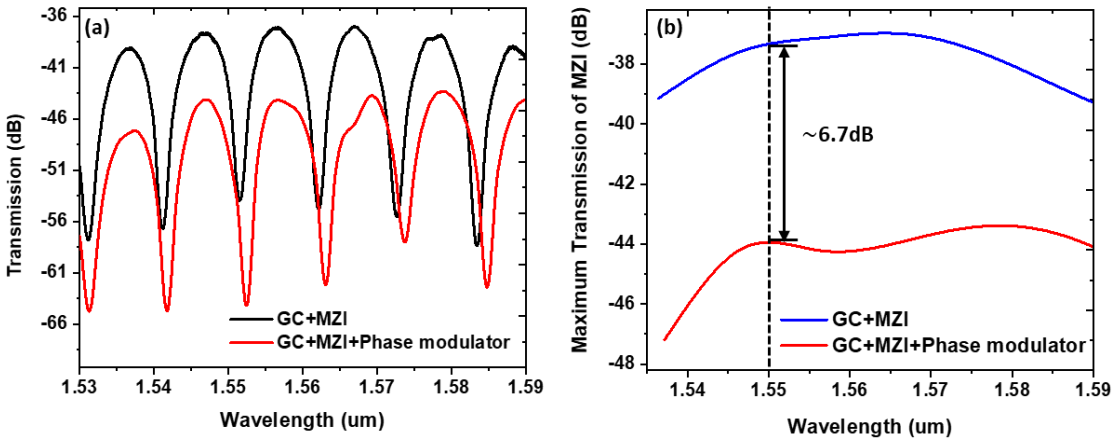

Figure 5-5 (a) MZI interference pattern in wavelength domain of the reference MZI and the modulating device for 550nm strip Si-rich SiN. (b) Comparison between the maximum transmission of the reference MZI and the modulating device for 550nm strip Si-rich SiN.

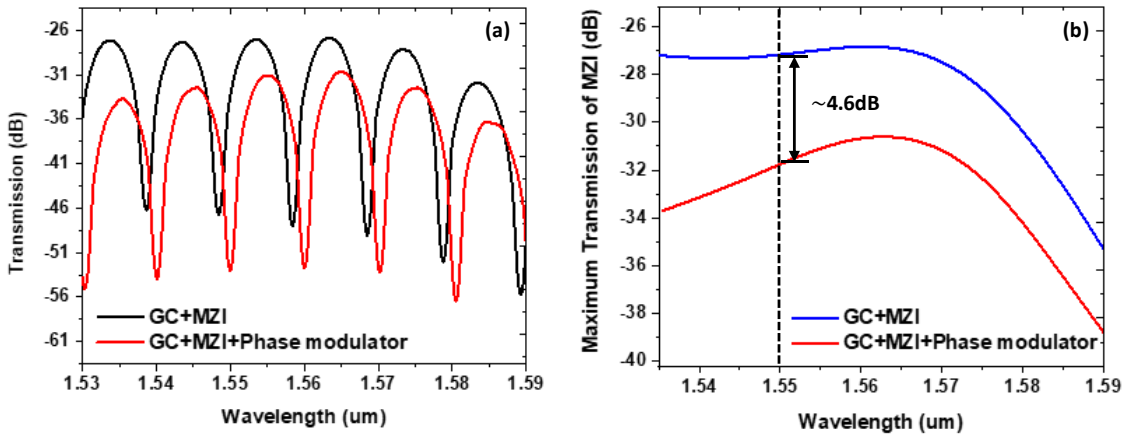

Figure 5-6 (a) MZI interference pattern in wavelength domain of the reference MZI and the modulating device for 600nm strip stoichiometric SiN. (b) Comparison between the maximum transmission of the reference MZI and the modulating device for 600nm strip stoichiometric SiN.

Figure 5-5(a) demonstrates the comparison between transmission of the signal through the reference MZI and the modulating device for 550nm Si-rich SiN platform with the strip waveguide length of 4.0 mm. Same result for 600 nm stoichiometric SiN with the waveguide length of 4.0 mm is presented in Figure 5-6(a). To find the insertion loss of the phase modulator, the transmission of the signal through the reference MZI need to be subtracted with the transmission from the whole modulating device. This can be done by extracting the transmission at the peaks of MZI interference pattern (Figure 5-5(a) and Figure 5-6(a)) for both reference MZI and modulating device. The extracted transmission at the peaks of MZI interference pattern are reported in Figure 5-5(a) and Figure 5-6(b) for 550nm Si-rich SiN and 600 nm stoichiometric SiN, respectively. The insertion loss of the 550nm Si-rich SiN and 600 nm stoichiometric SiN can be estimated to be 16.75 dB/cm and 11.5 dB/cm at the wavelength of 1.550µm, respectively.

5.2.2.3 Slot 600nm stoichiometric SiN platform

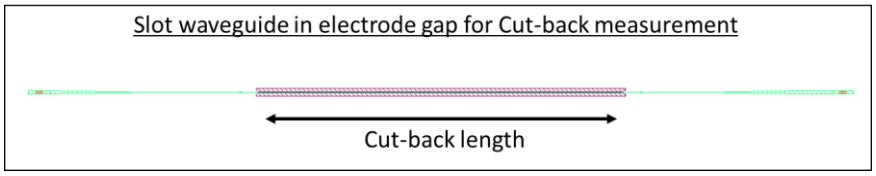

Figure 5-7 Structure of slot waveguide showing the position of waveguide length for cut-back measurement.

For the slot waveguide modulator, a signal can only be measured from the 600nm stoichiometric SiN platform while an output signal from the 550nm Si-rich platform cannot be measured. Propagation losses of the modulating device based on slot 600nm stoichiometric SiN waveguide can be calculated from straight slot waveguide with electrode for 4 different lengths of

1mm, 2mm, 3mm and 4mm. The structure of the slot waveguide in the electrode gap used for cut-back measurement is presented in Figure 5-7.

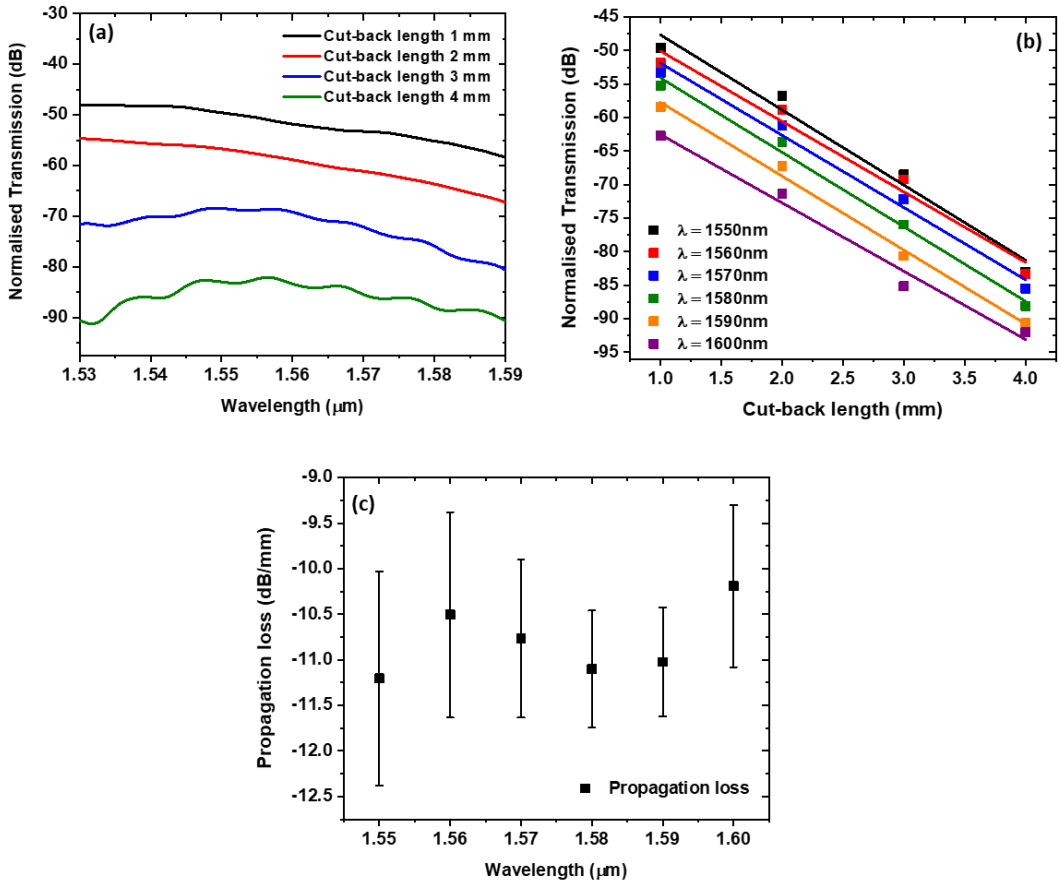

Figure 5-8 (a) Transmission from the modulating device with 4 different cut-back lengths of 1.0, 2.0, 3.0 and 4.0 mm. (b) Plotted between transmission as a function waveguide length and its linear fitting to find the propagation loss. (c) The analysed propagation loss of the modulating device at different operating wavelength.

For the 600nm stoichiometric SiN slot waveguide, the transmission of the modulating device showing that the transmission is deceased with the increasing of the waveguide length. As shown in Figure 5-8(a), the transmission of the phase shifter decreases with wavelength. This is due to the expansion of the guided mode into cladding region, resulting in higher loss at longer wavelength. It can be noticed that the transmission of the device with the cut-back length of 3 and 4 mm are not the same as the length of 1 and 2 mm. For the cut-back length of 3 and 4 mm, the transmission of the device at the shorter wavelength (1.530-1.550μm) are lower than the wavelength of 1.560μm. Then, after the wavelength of 1.560μm, the of transmission are decreased with the increasing of the wavelength. The higher optical loss at shorter wavelengths for the waveguide lengths of 3 and 4 mm is due to high insertion loss of the device at theses lengths. As revealed in the graph that, the insertion loss of the modulating device with the waveguide length of 3 and 4mm is>70dB. At the insertion loss higher than 70dB, the loss affect by the environment is dominant. Therefore, only the transmission results at 1.550-1.600μm were chosen to analyse the propagation loss of 600nm

stoichiometric SiN slot waveguide. Normalised transmission of the modulating device at the wavelength of 1.550-1.600µm with a gap of 10 nm in wavelength were then plotted against the cut-back length to find the propagation loss as presented in Figure 5-8(b). The propagation loss achieved from the linear fitting of the graph in Figure 5-8(b) are presented in Figure 5-8(c). The result shows that the propagation loss of the phase shifter device with a 600nm stoichiometric SiN slot waveguide are in the range of ~10-11dB/mm at in the operating wavelength of 1.550 to 1.600 µm.

The optical loss in phase modulator for all SiN platform in this research is summarised as presented below.

Table 5-2 Summary of optical loss in phase modulator fabricated in this work.

Codename (Sample ID)	Working modulator	Optical loss in modulating waveguide
300-Strip600-L1.5-4.5/DR1	-	-
300-Strip600-L6.0/DR1	Yes	indeterminable
300-Strip600-L1.5-4.5/FTC	-	-
300-Strip600-L6.0/FTC	Yes	indeterminable
300-Strip900-L1.5/CNTK	Yes	indeterminable
300-Strip900-L3.0-4.5/CNTK	-	-
300-Strip900-L6.0/CNTK	Yes	indeterminable
300-Strip1200-L1.5/CNTK	Yes	1.21±0.24 dB/mm
300-Strip1200-L3.0/CNTK	Yes	
300-Strip1200-L4.5/CNTK	Yes	
300-Strip1200-L6.0/CNTK	-	-
300-Strip1500-all/any	non-fabricated	-
600-Strip800-L4.0/CNTK (S1)	Yes	6.7 dB
600-Strip800-L4.0/CNTK (S2)	Yes	
600-Strip800-L4.0/CNTK (S3)	Yes	
600-Slot-L0.5/CNTK (S1)	Yes	10-11 dB/mm
600-Slot-L0.5/CNTK (S2)	Yes	
600-Slot-L0.5/CNTK (S3)	Yes	
600-Slot-L2.0-4.0/CNTK (S1-S3)	-	-
550-Strip800-L4.0/CNTK	-	4.6 dB
550-Slot-L0.5-4.0/CNTK	-	-

5.3 DC Modulation

The experimental setup for DC modulation measurement is present in Figure 5-9. The optical section includes the Agilent 8163B Lightwave Multimeter equipped with Agilent 81950A tunable laser (C-band), a polarisation controller, micrometre positioning stages and 81634B power sensor.

The single mode optical fibres (SMFs) are used to connect all optical components (blue and green lines in the picture).

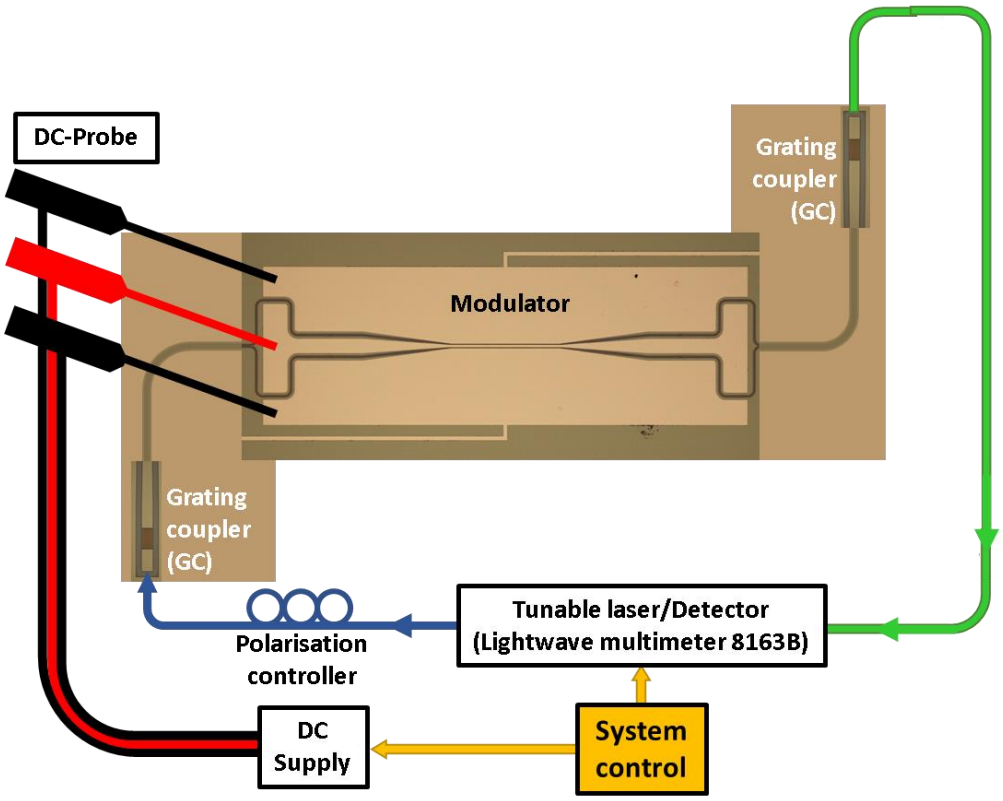

Figure 5-9 Schematic of measurement setup for DC modulation.

In the optical part, light from the tunable laser was launched into to the polarisation controller to allow only TE mode to be coupled into the grating coupler (GC). Output light from the polarisation controller will propagate through a SMF. The SMF fibre tip has been cleaved and inserted into the fibre holder which is held on a micrometre linear stage. At the output side of the modulator, the SMFs is also used to collect the output signal. The SMFs on this side is also cleaved and held using the same arrangement where a fibre holder is held on a micrometre linear stage and connected to the power sensor. The stage with the micrometre controller permits a precise alignment between fibre tip and sample input port and output ports. In this setup, the sample is held on a copper stage (sample holder) using vacuum. This sample holder is also connected with the micrometre linear stage which allow the microstep change in vertical direction to precisely adjust the height between the sample and optical fibres. A Panasonic GP-KR222 camera (alternative camera) on top of the copper stage was used to magnify the device in the sample which is help in the alignment of the fibres on the GC. A photo of the stage section is shown in Figure 5-10(a), showing the sample holder (yellow), the linear stage (blue), the optical fibres (red) and the microscope (green). Figure 5-10(b) presents a close-up of the sample surrounded by the fibre and DC needle holders. In the setup, a titanium needles are connected to DC probes which can be lowered onto the device metal pads.

The electric section is used for electric characterisation (IV curve) and transmission spectra. In this part, the equipment in the setup includes DPP105 Positioner DC probes from Cascade Microtech connected to a Keysight Source Meter SMU 2400.

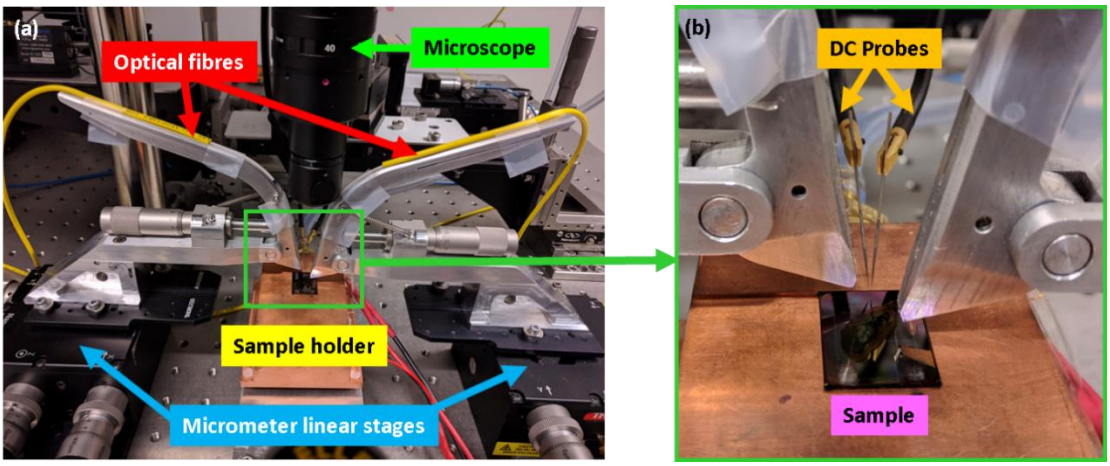

Figure 5-10 (a) Experimental setup for DC modulation measurement. (b) Close-up of a sample on the copper stage which is characterised in DC with optical fibres coming out from the angled fibre holders and titanium needles attached to the Cascade Microtech DC probes.

Tunable laser (Agilent 81950A) and power sensor (Agilent 81634B) are controlled through a controlling software written in Matlab® by Dr. Lorenzo Mastronardi. This software allowing batch measurement and analysis; the graphical user interface is presented in Figure 5-11. By using this software, it is possible to select laser power output, wavelength scan range, photodiode sensitivity, bias and current limit.

Figure 5-11 Graphical user interface of the system control app used for the DC measurement.

For DC measurements, the software drives the laser in wavelength sweep mode and collects the photocurrent amplitude from the power meter. Transmission spectra are retrieved from the Server Engine part of the Keysight N7700A Photonic Application Suite. The DC modulation staring from

the applying of DC biases in the range of -20V to 20V through the system control software. Once both measurements are available, the software analysis measuring the transmission spectra of the SiN modulator by scanning the wavelength from 1530 – 1580 nm at each applying bias voltage.

5.3.1 Investigation of $V_\pi \cdot L$ from Modulation Spectra

Once the DC modulation spectra were measured by using the setup as explained, the spectra present the shifting MZI interference patterns in horizontal direction according to the DC-bias voltage levels (see Figure 5-12). These spectra contain several characteristics of MZI modulator device such as a free spectral range (*FSR*), an extinction ratio (*ER*), and a voltage-length product ($V_\pi \cdot L$). In this work, these characteristics were investigated by using a function fitting method. The fitting function is adopted from the MZI output transmittance formula in the Eq.(20).

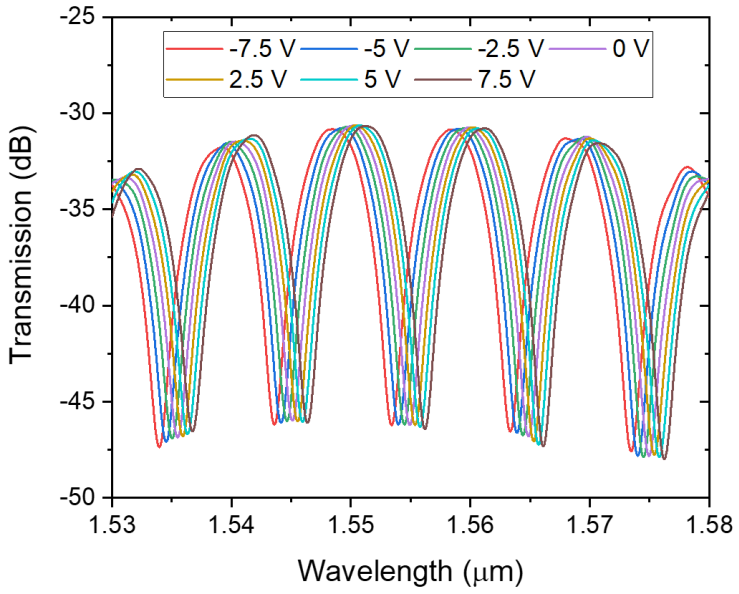

Figure 5-12 Optical transmission spectrum for one arm of the modulator under various bias voltages from -7.5V to 7.5V.

$$T_{MZI} = \left(\frac{1}{ER}\right)^2 + \frac{4\gamma}{(1+\gamma)^2}\cos^2\left(\frac{\Delta\phi}{2}\right) \qquad \text{where } ER = \left(\frac{1+\gamma}{1-\gamma}\right)^2$$

In term of MZI modulator, the total phase difference ($\Delta\phi$) is a combination of three phase resources including an MZI path-difference $\left(\frac{2\pi}{\lambda} n_g L_{path}\right)$, modulating phase($\phi_{mod}$), and MMI output phase($\phi_{MMI}$) as given by:

$$\Delta\phi = \frac{2\pi}{\lambda} n_g L_{path} + \phi_{mod} + \phi_{MMI} \qquad (55)$$

where n_g is a group index of the waveguide in MZI path difference, and L_{path} is a length of path difference. Then the T_{MZI} formula has been converted to compatible with the dB unit in order to fit the measuring MZI spectrum:

$$T_{MZI}(dB) = 10log_{10}\left[\left(\frac{1-\gamma}{1+\gamma}\right)^2 + \frac{4\gamma}{(1+\gamma)^2}\cos^2\left(\frac{\frac{2\pi}{\lambda}n_g L_{path} + \phi_{mod} + \phi_{MMI}}{2}\right)\right] \quad (56)$$

The first step prior to implements the function fitting, the background loss in spectrum needs to be removed because our fitting function is not taken into account of any component loss in the device such as a grating coupler loss, MMI loss, etc. The ideal spectrum to be fitted must have all interference peaks aligned on the zero-dB level. To level all peaks to zero-dB in the modulation spectrum, the peak centres were positioned and used for generating the subtraction line as shown in Figure 5-13(a-b). Once all DC modulation spectra were normalised with the generated subtraction line (see Figure 5-13 (c)), the spectra are ready to be fitted with the function.

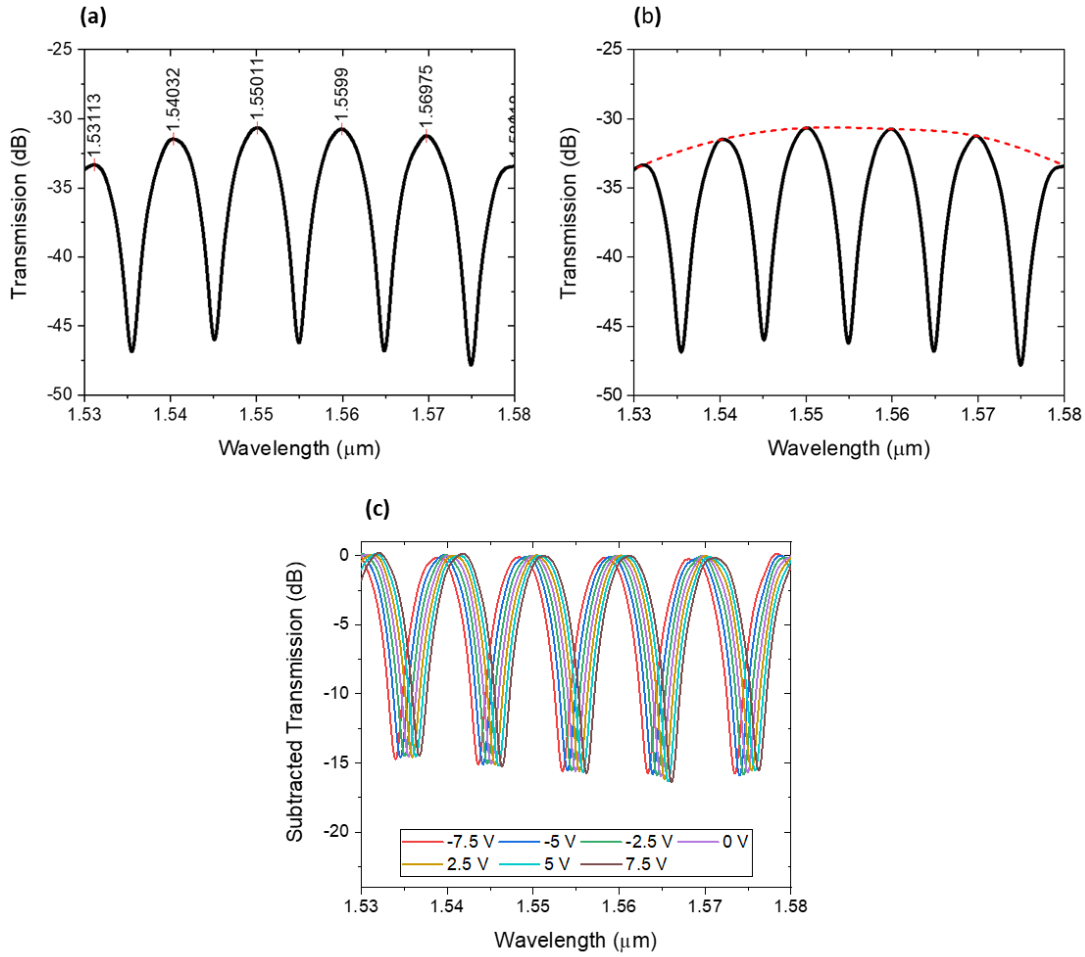

Figure 5-13 (a) Optical transmission spectrum of the modulator with the find peak function. (b) Red dash line showing the peak base line of the transmission spectrum peaks which is used to leveling the peak base line to zero. (c) Optical transmission spectrum of the modulator with various bias voltages when the peaks base line were leveled to be the same level (0dB).

The function fitting method was implemented by using a feature "nonlinear curve fitting" in the *Origin*® software from *OriginLab Corporation*. Firstly, the $T_{MZI}(dB)$ function was fitted onto the spectrum of 0V modulation (see Figure 5-14(a)) in order to extract the common characteristics of MZI including group index (n_g), MMI phase(ϕ_{MMI}), and MMI splitting imbalance factor (γ). These common characteristic parameters were fixed in the fitting process for the spectra with modulation voltage. As a result of function fitting on all spectra, the modulation phase changes (ϕ_{mod}) were obtained as a function of modulation voltage and calculated to the phase change rate as shown in Figure 5-14(b). Then the $V_\pi \cdot L$ were calculated with this equation: $V_\pi L = \frac{180°}{(phase\ change\ rate)} L_{mod}$, and the MZI extinction ratios were calculated by using $ER = \left(\frac{1+\gamma}{1-\gamma}\right)^2$.

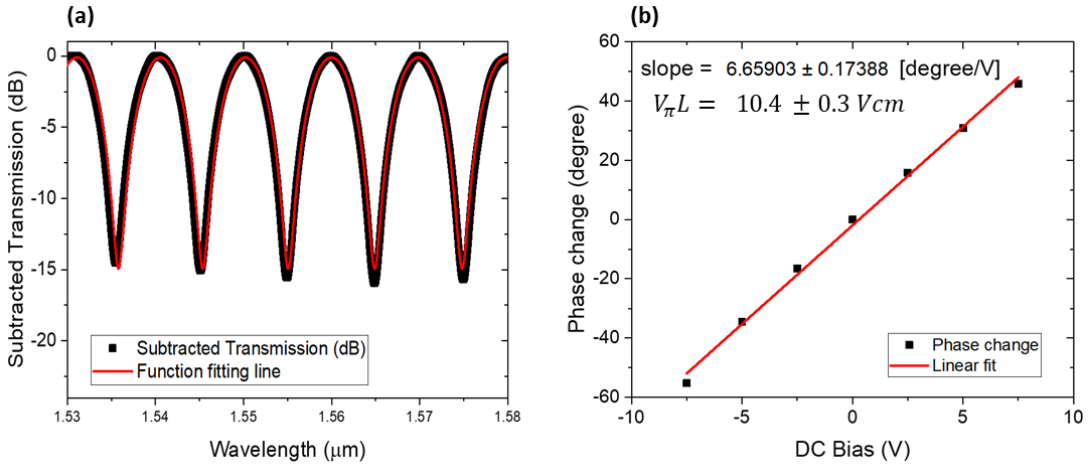

Figure 5-14 (a) Substrated optical transmission spectrum of modulator with the fitting function for analysing the optical phase change in modulator with the applied bias voltage. (b) The plooted of phase change in the modulator which are extracted from the subsrated transmission spectrum with the variation of applied bias voltage.

5.3.1.1 300nm stoichiometric SiN platform

In this platform, the modulator devices have been fabricated and workable with all three types of EO polymer. Since our knowledge of polymer integration method and the quantity of synthesised polymer is seriously limited at the beginning of this work, only few fabricated samples could be measurable with the optical experiment setup. Moreover, not every modulator device was located on the same sample for modulation measurement extraction. For PMMA-*co*-DR1MA and HG PMMA-FTC polymers, there is only one measurable modulator available with each polymer type. Their spectra with DC modulation are shown in Figure 5-15 (codenames: *300-Strip600-L6.0/DR1* and *300-Strip600-L6.0/FTC*). with the new polymer (CN-TK2) the integration method has been greatly improved, and several more samples have been fabricated and measured effectively. Their spectra with DC modulation are shown in Figure 5-15 with codenames ending with "*.../CNTK* ".

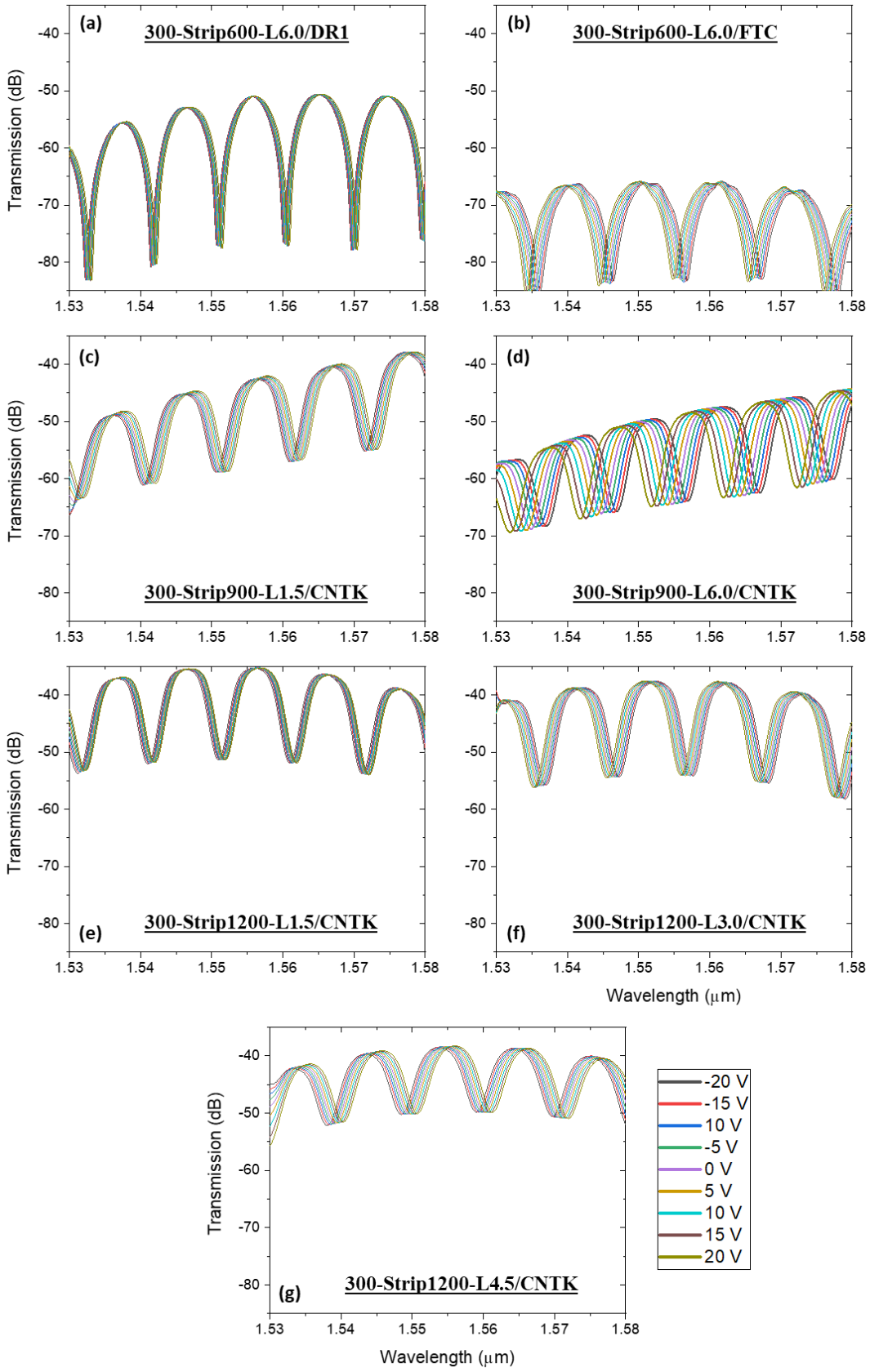

Figure 5-15 Optical transmission spectrum of 300nm strip stoichiometric SiN modulator with the variation of applied bias voltage for a modulator with (a) WG width of 600nm and modulating length of 6.0mm with DR1 polymer, (b) WG width of 600nm and modulating length of 6.0mm with FTC polymer. Modulator with CNTK polymer with (c) WG width of 900nm and

modulating length of 1.5mm and (d) 6.0mm. Modulator with CNTK polymer with (e) WG width of 1200nm and modulating length of 1.5mm, (f) 3.0mm, and (g) 4.5mm.

The presented modulation spectra in Figure 5-15 were analysed with the function fitting method as explained previously. All fitting results of modulator characteristics are summarised into Table 5-3. In this table, we can see that the modulation efficiency $V_\pi \cdot L$ has been significantly improved with the use of EO polymer with higher EO efficiency (r_{33}). Based on literature review in section 2.2.3, PMMA-*co*-DR1MA has been reported with $r_{33,in-device}$ =12 pm/V while FTC-chromophore based polymers have been reported with $r_{33,in-device}$ =36-150 pm/V. Comparing between PMMA-*co*-DR1MA with a reported efficiency of 12 pm/V and HG PMMA-FTC with the lowest reported efficiency of 36 pm/V, the $V_\pi \cdot L$ values exhibited in our fabricated devices with those polymer types display a difference of about 2.6 times which is in line with the literature. In particular, the maximum $r_{33,in-device}$ of CN-TK2 polymer has been found to be up to 165 pm/V in the specific design of a silicon waveguide modulator [182]. A fabricated device demonstrating the highest modulation efficiency (*300-Strip900-L1.5/CNTK*) exhibits a $V_\pi \cdot L$ value of 17.9 V-cm which is about 3.4 times higher than that of the *300-Strip600-L6.0/FTC* device. However, this is insufficient to directly compare the relative values of $r_{33,in-device}$ between the polymers because of the difference in widths of the waveguides.

Table 5-3 $V_\pi \cdot L$ and all modulating properties of the EO polymer modulator for the 300nm stoichiometric strip SiN waveguide.

Device Codename	V_π (V)	$V_\pi L$ (V-cm)	FSR (nm)	MMI phase (°)	ER (dB)	I.L. @1550nm (dB)	$V_\pi L$ after 1 week (V-cm)
300-Strip600-L6.0/DR1	242.7 ± 7.1	145.6 ± 4.3	9.3	81.1	24.8	52.2	145.8 ± 4.5
300-Strip600-L6.0/FTC	101.5 ± 0.6	60.9 ± 0.3	10.4	88.1	17.1	66.0	73.1 ± 0.4
300-Strip900-L1.5/CNTK	119.0 ± 2.9	17.9 ± 0.4	10.3	102.9	16.0	44.3	-
300-Strip900-L6.0/CNTK	39.5 ± 1.2	23.7 ± 0.7	10.0	86.4	15.9	50.2	-
300-Strip1200-L1.5/CNTK	205.2 ± 2.6	30.8 ± 0.4	9.9	102.1	15.8	35.4	-
300-Strip1200-L3.0/CNTK	122.4 ± 1.9	36.7 ± 0.6	10.4	92.2	17.6	37.6	-
300-Strip1200-L4.5/CNTK	94.2 ± 1.3	42.4 ± 0.6	10.5	82.1	12.0	38.8	-

When considering only the devices with CN-TK2 polymer, there are two series of devices for the waveguide widths of 900 and 1200nm with variation of modulator lengths. Ideally, the $V_\pi \cdot L$ of modulator device should not depend on the modulator length. However, the reported values are not in line with that principle for this work. This means that there might be effects linked to the modulator length offset in this modulator design such as the electrode tapering region, which could also provide an EO modulation when applying the DC bias voltage.

In term of FSRs and MMI phases, the devices have been designed to provide the FSR of 10nm and the phase of 2x2MMI of 90°. The fitting results are significantly close to the expected values of

the design. For the extinction ratio (ER), it represents the imbalance of optical power between the MZI arms. In the ideal case, the device with a perfect power balancing can provide an infinite ER value. However, a practical device could have several imperfection factors such as an imbalance of MMI splitting power, or an unidentical loss between the modulating waveguides. Another parameter obtained from the spectrum analysis is the total insertion loss (I.L.) of the device which also includes a grating coupler loss and the losses from MMIs, waveguides, waveguides bent, and tapers in the MZI structure. Due to lack of all modulator length in the same waveguide width series, these losses can only imply that a narrower waveguide provides a higher loss and vice versa. Only series of modulators with waveguide widths of 1200nm can be approximated to determine propagation losses as discussed in 5.2.2.1.

In addition, the experiments of EO polymer degradation were tested on the first two fabricated devices, *300-Strip600-L6.0/DR1* and *300-Strip600-L6.0/FTC*. The devices were firstly measured with the DC modulation on the same day of the polymer integration process and then repeated the measurement in 1 week later. There is no considerable change of $V_{\pi}{\cdot}L$ in *300-Strip600-L6.0/DR1* device, but it was found 20% increment of $V_{\pi}{\cdot}L$ in *300-Strip600-L6.0/FTC*. This degradation testing results is consistent with the principle of having the EO polymer structure with a weak chemical bonding in the host-guest structure of HG PMMA-FTC polymer.

5.3.1.2 600nm stoichiometric SiN platform

In this platform, the modulator devices have been fabricated with only CN-TK2 EO polymer as a cladding layer. Based on the design development in this platform, three modulators with slot waveguide were expected to be key devices with an enhance overlap integral factor while a single modulator with strip waveguide would be used only as a testing reference device. Three different lengths of slot waveguide modulator aimed for optimising a balance between the half-wave voltage (V_{π}) and the insertion loss of modulation waveguide. In the experiments, with three fabricated samples, only the modulator devices with 4mm-long strip waveguide and the shortest 0.5mm-long slot waveguide could be measured to extract DC modulation characteristics. Their DC modulation spectra are presented in Figure 5-16, and the sample ID has been added to the ending of codename for sample identification purpose.

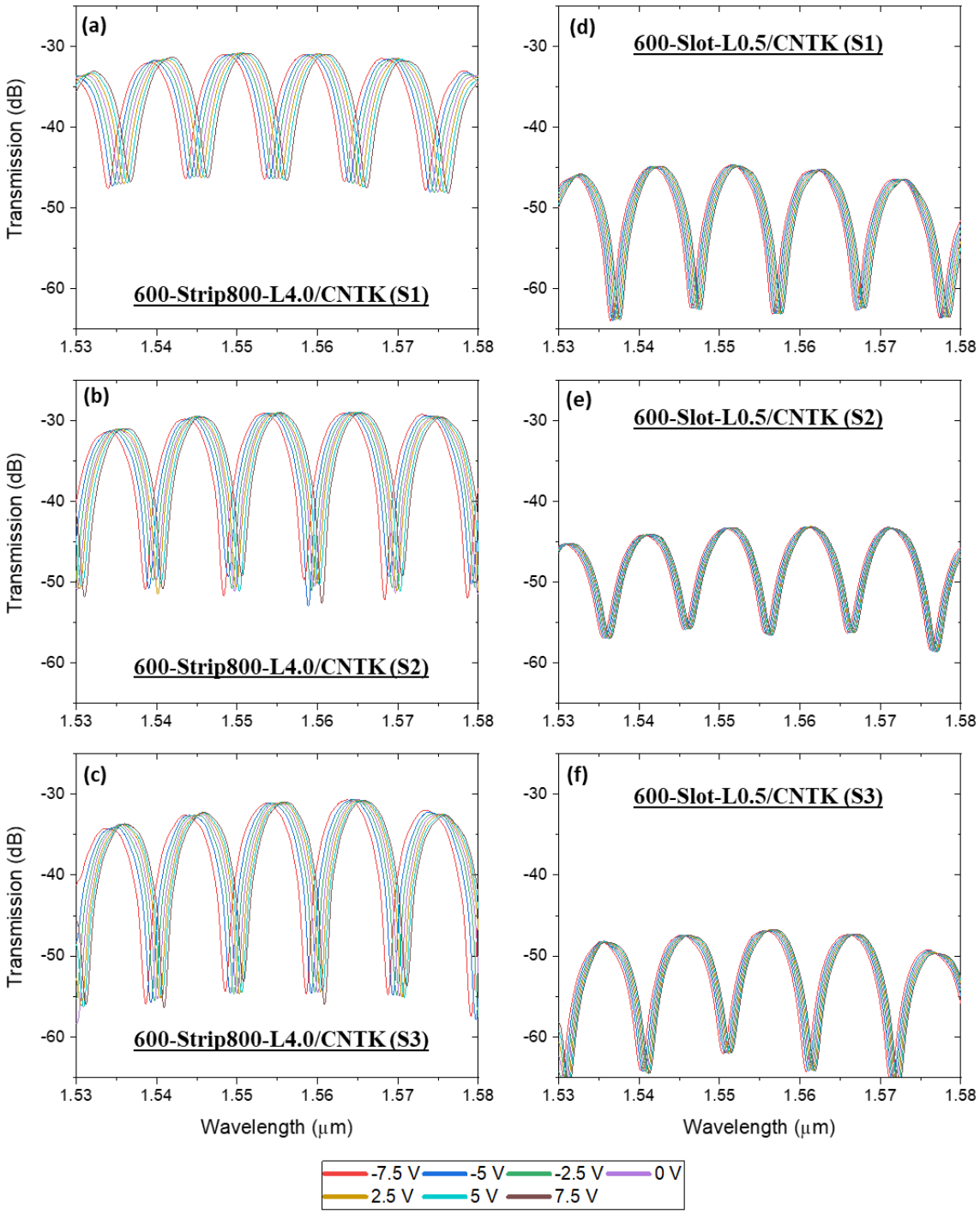

Figure 5-16 Optical transmission spectrum of 600nm strip and slot stoichiometric SiN modulator with the variation of applied bias voltage for a modulator. (a) Modulator with strip WG width of 800nm and modulating length of 4.0mm with (a) CNTK(S1) polymer, (b) CNTK(S2) polymer and (c) CNTK(S3) polymer. Modulator with slot WG with modulating length of 0.5mm with (d) CNTK(S1) polymer, (e) CNTK(S2) polymer and (f) CNTK(S3) polymer.

Once these spectra were analysed by using the function fitting method, the modulator characteristic parameters were extracted and presented in Table 5-4. Considering V_π and $V_\pi \cdot L$ of these devices, they represent a repeatability of device fabrication for either strip or slot waveguide modulators. The *600-Strip800-L4.0/CNTK (S1)* device provides the lowest V_π of 25.9 V, and the *600-*

Slot-L0.5/CNTK (S1) device provides the lowest $V_\pi L$ of 3.1 V·cm if compared to all devices in this work. Based on our best knowledge, the $V_\pi L$ of 3.1 V·cm is the lowest voltage-length product reported to date for EO polymer modulators using a SiN waveguide in C-band. This is backed up by [59] which has currently reported a $V_\pi L$ of 17.6 V·cm.

Table 5-4 $V_\pi \cdot L$ and all modulating properties of the EO polymer modulatoer for the 600nm stoichiometric strip and slot SiN waveguide.

Device Codename	V_π (V)	$V_\pi L$ (V-cm)	FSR (nm)	MMI phase (°)	ER (dB)	I.L. @1550nm (dB)	$r_{33,in-device}$ (pm/V)
600-Strip800-L4.0/CNTK (S1)	25.9 ± 1.0	10.4 ± 0.4	9.7	2.3	14.8	30.7	51.8
600-Strip800-L4.0/CNTK (S2)	31.0 ± 2.9	12.4 ± 1.2	9.9	1.9	21.6	29.0	43.4
600-Strip800-L4.0/CNTK (S3)	31.3 ± 3.1	12.5 ± 1.2	9.9	5.5	24.2	31.5	43.0
600-Slot-L0.5/CNTK (S1)	62.0 ± 2.3	3.1 ± 0.1	10.1	4.5	17.2	44.6	82.4
600-Slot-L0.5/CNTK (S2)	80.0 ± 6.3	4.0 ± 0.3	10.1	7.3	13.4	43.1	64.9
600-Slot-L0.5/CNTK (S3)	68.0 ± 4.7	3.4 ± 0.2	10.1	4.3	15.5	46.8	76.0

Due to the higher refractive index of EO polymer (n=~1.65) in the fabricated devices compared to that presented in simulations (n=1.48), the confinement of optical modes in fabricated slot waveguides is worse than in the simulation. This resulted in a higher propagation loss than the expected value of 1dB. As analysed in section 5.2.2.3, the cut-back structure of slot waveguides with metal electrode exhibits the propagation loss of 11.25 dB/mm. This helps to understand the cause of unmeasurable slot waveguide modulator with the lengths of 2 and 4 mm. Moreover, the imperfection of dimensions in fabricated device (see details in section 4.2.2) is also another cause to the high propagation loss of slot waveguide. On the other hand, the insertion loss of strip waveguide modulator was estimated for ~4.58dB.

In term of FSRs and MMI phases, the fitting results are nicely close to those in the designs. The expected value of FSR is 10nm while the 1x2MMI should provide the output phase of 0°. For the extinction ratio (ER), these devices have an ER in the modulate level that are larger than 10dB. In addition, the $r_{33,in-device}$ were able to calculate by using the eq. (33) and the available overlap integral factors from the simulation. With the same EO polymer cladding, the slot waveguide modulators obviously provide almost two times larger $r_{33,in-device}$ than those values of the strip waveguide, and the highest $r_{33,in-device}$ in this work has been found at 82.4 pm/V That implies more efficient poling activity in the modulator with slot waveguide design.

5.3.1.3 550nm Si-rich SiN platform

Within this platform, no workable or measurable modulator device were found. The low grating coupling efficiency and high propagation losses in the slot waveguide with metal electrode structure (see details in section 5.2.2.2), could be the main reasons causing the modulator with the

slot waveguide structure being undetectable in the optical characterisation. Moreover, the imperfection of waveguide dimensions in the fabricated device has also been measured as shown in the cross-sectional SEM image in Figure 4-6. With a fabrication error size of 38.5% for the slot width and 43.3% for ridge width, this is more than enough to be completely off the expected propagation loss of 1dB from the simulation. There is only one device for the strip waveguide modulator in this platform which can be measured the output spectrum. However, the modulating result from this device cannot be measure due to the damage on the device during the characterisation process. Thus, there were no modulating result from both strip and slot waveguide based on this SiN platform.

5.4 High-Frequency Modulation

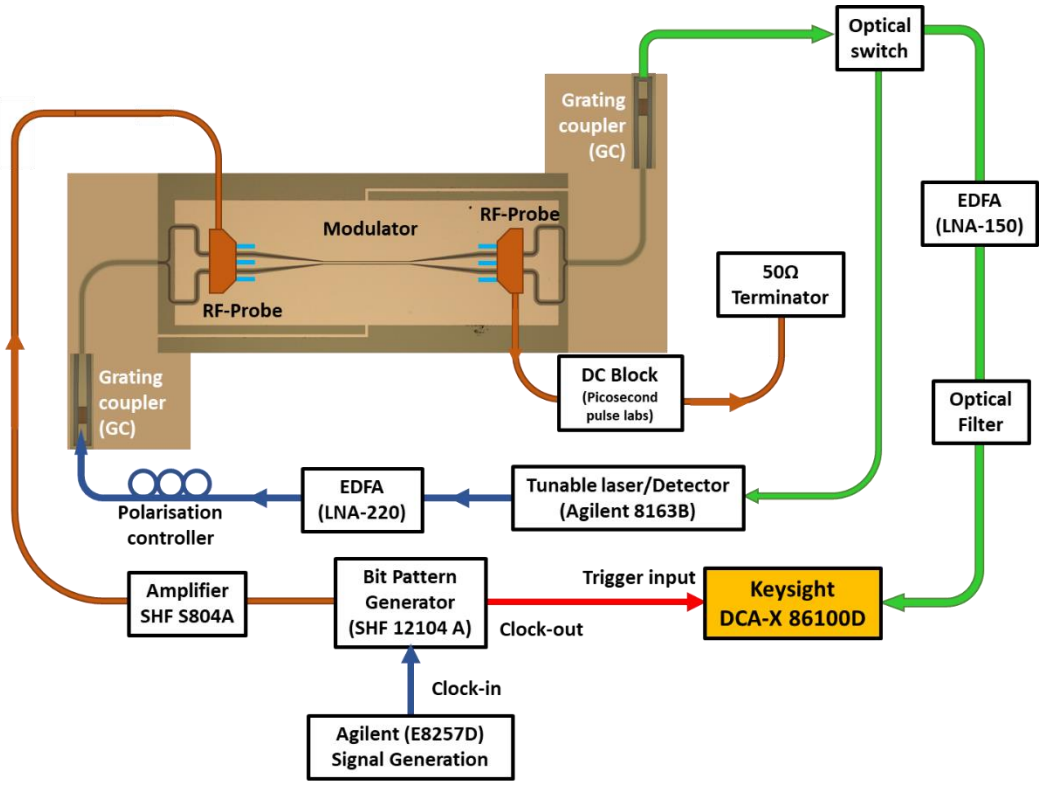

Figure 5-17 Schematic of measurement setup for High-Frequency modulation.

The schematic of high-speed setup for the high-frequency modulation measurement is shown in Figure 5-17. In this measurement, an Agilent (E8257D) Signal generator was used to generate the electrical modulating signal at 20 GHz with the amplitude of 1V peak-to-peak. This electrical modulating signal will be used as a clock-in reference for a bit pattern generator (SHF 12104 A). In this work, 127 bits pseudorandom binary sequence (PRBS) at 40 Gbps will be generated. Then, the output signal from bit pattern generator will be coupled to a RF amplifier (SHF S804A). At the stage, the signal will be amplified to 7.38 V peak-to-peak as shown in Figure 5-18. The amplified signal will be fed to the modulator device by RF GSG probes. At the others end of the modulator device, the DC block is added together with a 50 ohms terminator to avoid all reflected signal.

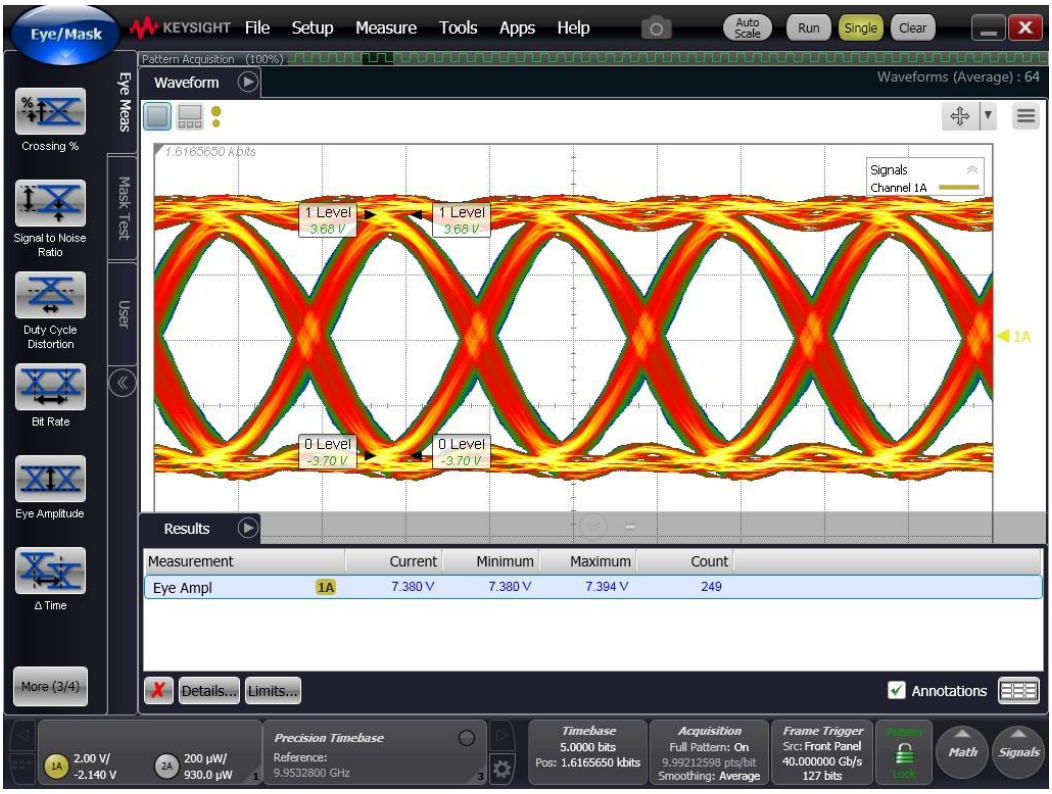

Figure 5-18 Input electrical eye diagram with 7.38 Vpp at 40 Gb/s.

For the optical system, the tunable laser (Agilent 81940 A) is set to the fixed wavelength of 1548.74nm at the output power of 13 dBm. This wavelength is at a -3dB output level from the MZI spectral peak nearby 1550 nm. This -3dB output level is equivalent to quadrature phase difference between MZI-arms. At the output of the modulator device, an optical switch is added to switch the output signal into two paths. One output path is for sending the signal to the power sensor (Agilent 81634 B) for checking the initial spectrum. The other path of signal is for the main RF measurement. For the later path, the signal is sent through the EDFA (LNA-150) for signal amplification. Then, the amplified signal is transmitted through a bandpass filter to allow for noise filtering and the desired modulated wavelength to be received and improve the signal to noise ratio. Finally, the filtered signal will be sent to the optical module (Agilent 86116C) which is plugged in to the DCA oscilloscope (Keysight DCA-X 86100D). In the DCA, the optical signal will be analysed, and the eyes diagram of the modulating signal will be generated and exhibited. Figure 5-19 presents the diagrams of the device at 40 Gb/s with extinction ratios (ER) of 2.629dB. From the eye diagram, ER can be measured by calculating the different in dB unit between the level of logical 0 and logical 1. Eye diagram provides a visual quantitative presentation of the performance of the device.

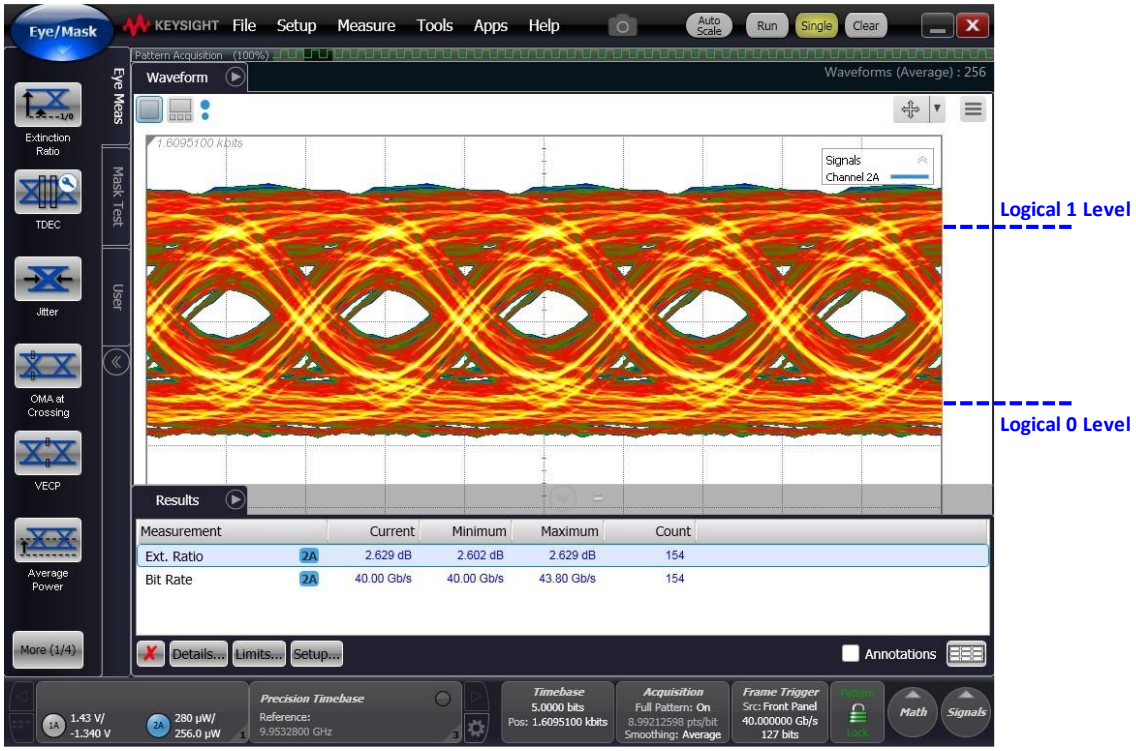

Figure 5-19 Device eye diagram of optical modulation signal with an ER of 2.629 dB at 40.0 Gb/s.

5.4.1 Modulation Speed and Extinction Ratio at 40 Gbps

The *600-Strip800-L4.0/CNTK (S1)* was chosen for testing at high-speed measurement as it has the lowest V_π and the insertion loss of the strip waveguide modulator enables operation on the high-speed setup. To investigate the maximum data rate, the modulation signal frequency was increased step by step to find the maximum speed for which the eye diagram remained opened. Eye diagram provides a visual quantitative presentation of the performance of our modulator device such as modulation speed, extinction ratio, etc. Figure 5-20 presents the eye diagrams of this device modulating at the maximum speed of 40 Gb/s with extinction ratios (ER) of 2.629dB.

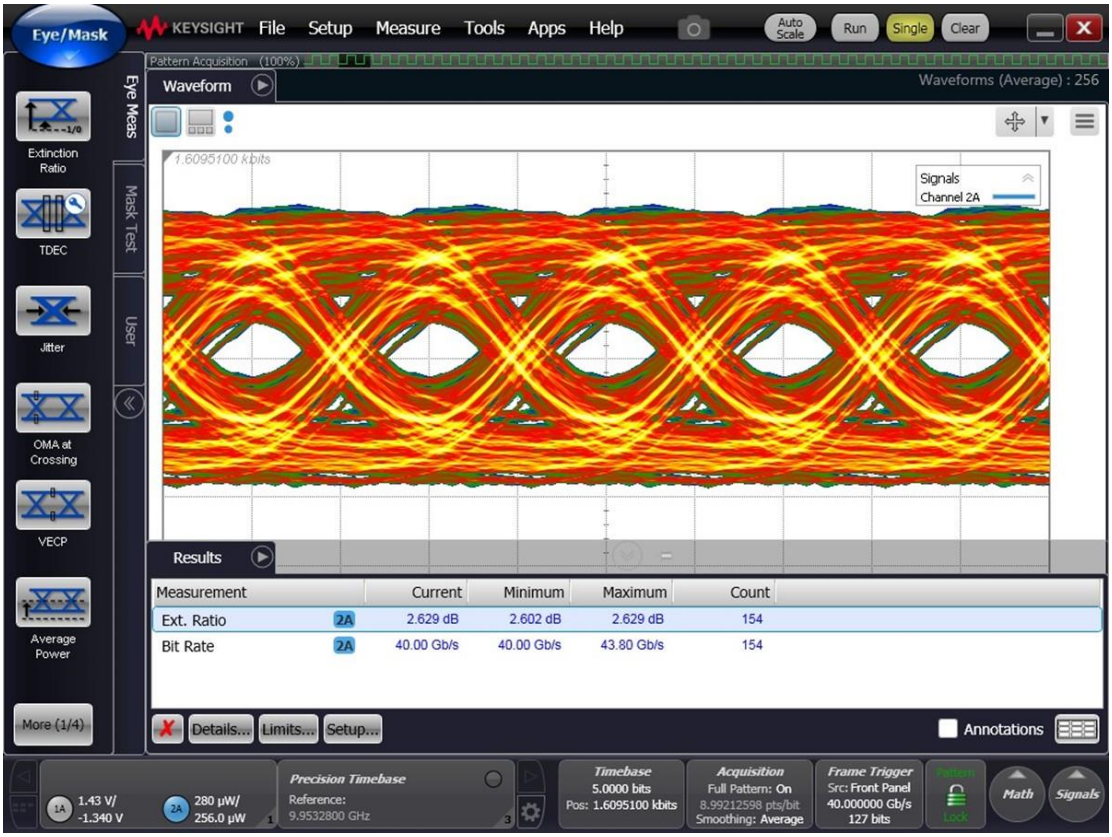

Figure 5-20 Device eye diagram of the device 600-Strip800-L4.0/CNTK (S1) with an ER of 2.629dB at 40.0 Gb/s.

Based on our best knowledge, only two publications reported electro-optic modulators on SiN waveguide operating with speed of tens Gb/s [20, 187]. In the first report[20], the modulator has been demonstrated with a ring resonator structure operating at the maximum modulation speed of 40Gb/s. However, it requires an integration of ferroelectric film of toxic lanthanide-based materials with a high-temperature annealing process beyond 500°C. This is not directly comparable to our work in term of either modulator structures or type of intrinsic material integration. Another report has demonstrated EO polymer MZI modulators on SiN waveguide operating at the maximum speed of 20Gb/s [187]. Therefore, we can confidently declare that the EO polymer MZI modulator on the BEOL SiN waveguide platform which has been developed in this work, is the highest speed MZI polymer modulator reported to date compared to the start-of-the-art of the devices on SiN waveguide technology.

5.4.2 Frequency Dependence of $V_\pi \cdot L$

Apart from the high-speed measurement at 40 Gb/s as explained so far, the modulator device was also examined at other lower speeds including 10, 20 and 28 Gb/s. The amplitude of RF

signal (V_{RF}) and ER of optical modulation signal at those speeds were obtained and presented in Figure 5-21.

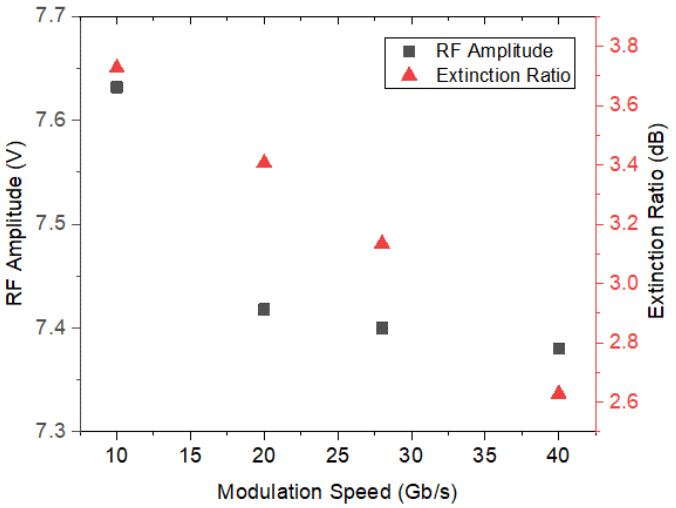

Figure 5-21 The amplitude of RF signal and extinction ratio (ER) of optical modulation signal in 600nm stoichiometric strip SiN as a function of modulation speed.

To estimate the $V_{\pi}{\cdot}L$ by using the RF amplitudes (V_{RF}) and ERs, the equation of MZI-modulator transmission spectrum (eq.(56)) was considered for converting ER value to the corresponding value of modulating phase (ϕ_{mod}). The parameters were obtained from the function fitting process for the calculation of $V_{\pi}{\cdot}L$ in DC modulation including a waveguide group index (n_g), power imbalance factor (γ), and MMI output phase(ϕ_{MMI}), and the wavelength (λ) was fixed at -3dB modulation wavelength (1548.74 nm). The calculated MZI-modulator transmission curve at fixed modulation wavelength was generated as a function of ϕ_{mod} (see Figure 5-22).

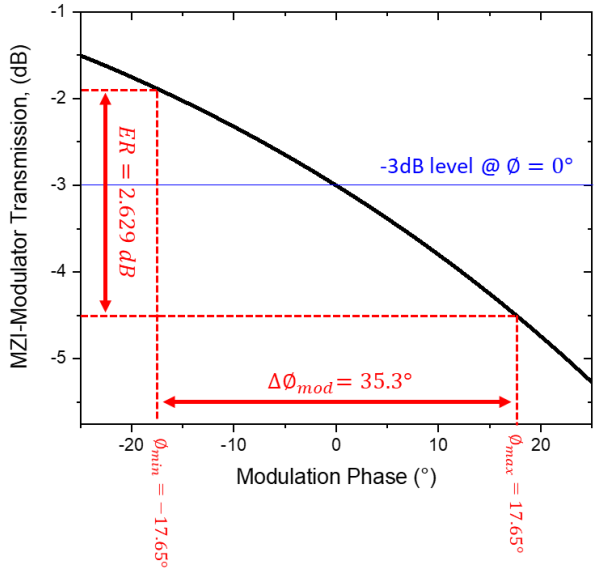

Figure 5-22 Relations between the optical transmission from the MZI modulator with the modulation phase used to analyse the $V\pi{\cdot}L$ of the modulator.

Based on the principle of electro-optic modulation, the modulation phase (ϕ_{mod}) is linearly changed to the modulation voltage as demonstrated in Figure 5-14. Also, the modulation RF signal swing around the centre level at 0 V. Therefore, ϕ_{mod} should also swing within the same magnitude of negative-to-positive range (from $-\Delta\phi_{mod}/2$ to $+\Delta\phi_{mod}/2$). Then, $\Delta\phi_{mod}$ can be extracted from the curve by searching for and appropriated $\Delta\phi_{mod}$ which provides the same ER of eye diagram. For example, the ER at 40Gb/s is 2.629dB. The matching $\Delta\phi_{mod}$ of this ER was found as 35.3° (-17.65° to +17.65°) on the transmission curve. This obtained $\Delta\phi_{mod}$ is according to the RF amplitude at that certain speed, then the half-wave voltage can be calculated by using the equation $V_\pi = \frac{180° \times V_{RF}}{\Delta\phi_{mod}}$. Finally, the $V_\pi \cdot L$ can be calculated using the length of modulator (4 mm) and were presented in Figure 5-23.

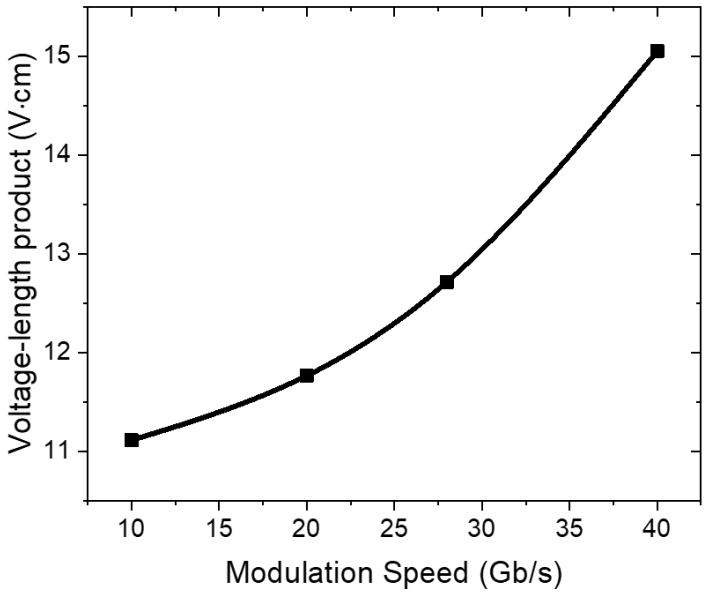

Figure 5-23 Plotted of Vπ·L as a function of modulation speed showing that the Vπ·L is increased with the increasing of speed of modulation.

Comparing to the $V_\pi \cdot L$ of this modulator device in DC modulation at 10.4 V-cm (see Table 5-4), it is slightly increased at 10 and 20 Gb/s. However, it is almost 50% increment at 40 Gb/s. The increasing trend of $V_\pi \cdot L$ showing in this figure could be a result of the RF propagation loss increasing as a function of frequency as shown in Figure 3-23(c). This is a common concern in modulators with travelling wave electrode design.

5.4.3 Investigation on Speed Limit

With a further investigation on speed limit, the device was tested with modulation signal at 60 Gb/s as shown in Figure 5-24(a). In this eye diagram, the input RF signal has an amplitude of 6.204 V peak-to-peak which is about 16% smaller that the amplitude at 40 Gb/s (see Figure 5-18). Moreover, the input signal also obviously contains an intensive level of noise and the RF amplifier

was suspected to be a source of noise. As a result of smaller amplitude and higher noise level in the input RF signal, the eye diagram cannot be detected in the optical modulation signal because of the noise interruption as shown in Figure 5-24(b). By using the signal processing software available in DCA oscilloscope, the signal equalisation technique was applied to improve the signal quality. Linear feed-forward equaliser (FFE) was chosen for suppressing the noise level and extracting the eye diagram of actual modulation signal as shown in Figure 5-24(c). Based on the principle of FFE equaliser, a number of delayed versions (also called "tap" number as indicated in Figure 5-24(c)) of the modulation signal are created and added back to the original signal with the optimal weights. This signal processing aims for improving signal quality at the optical receiver/detector[188]. Figure 5-24(c), presents the diagram with open eye pattern and proves that the transmission data is still available in the optical modulation signal up to the data rate of 60 Gb/s. It also demonstrates that the data rate is not limited at 40 Gb/s because of a frequency response limit of the intrinsic material such as EO polymer. To surpass the measurable speed limit of 40 Gb/s, the quality of optical modulation signal from our device must be improved. For one of the possible solutions, the use of RF amplifier in high-speed experimental setup should be avoided by enhancing the modulator design to obtain a lower V_{π}.

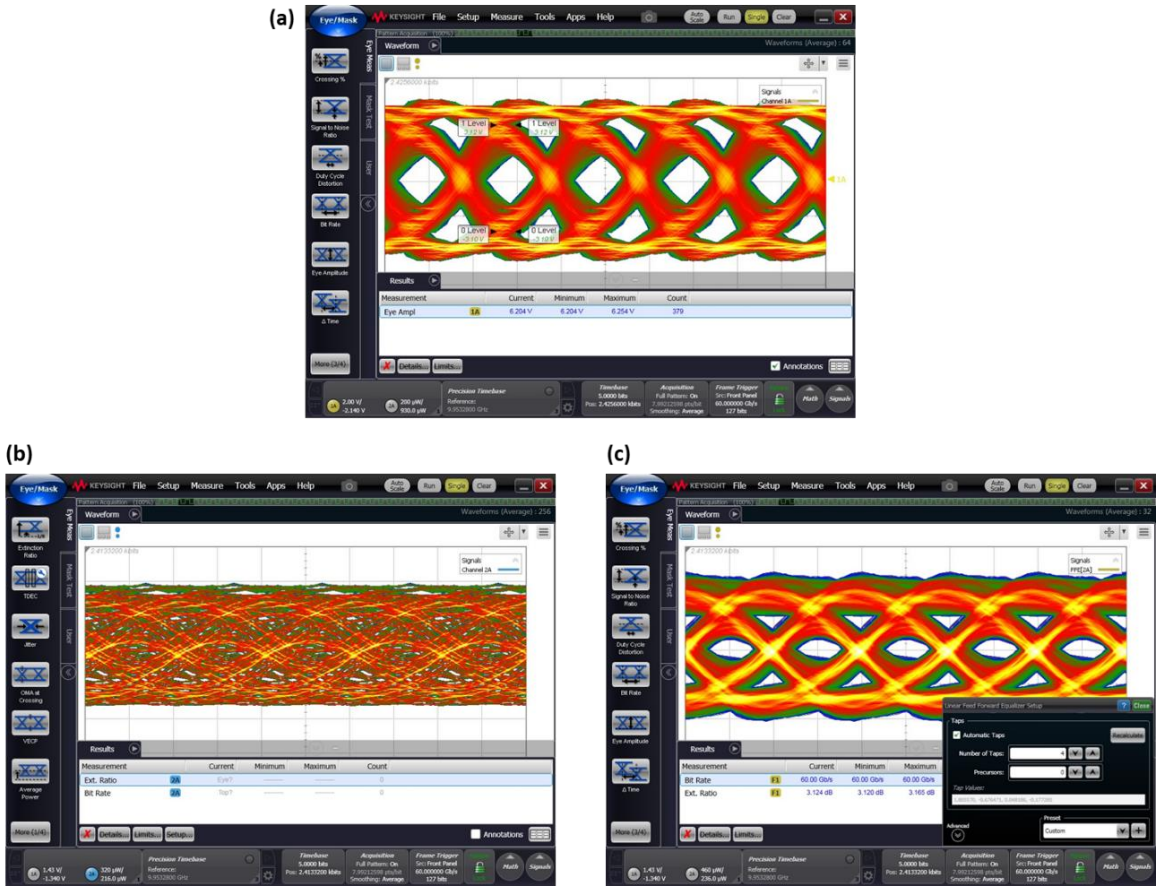

Figure 5-24 Device eye diagram of (a) input RF signal (b) optical modulation signal (c) optical modulation signal when applying the image processing method at 60.0 Gb/s.

5.5 Chapter Conclusion

Table 5-5 Summary of all measured results from all modulating devices fabricated in this research.

Codename (Sample ID)	Working modulator	Optical loss in modulator	$V_\pi L$ (V-cm)	ER of MZI (dB)	I.L. @1550nm (dB)	$r_{33,in-device}$ (pm/V)	High speed modulation
300-Strip600-L1.5-4.5/DR1	-	-	-	-	-	-	-
300-Strip600-L6.0/DR1	Yes	indeterminable	145.6 ± 4.3	24.8	52.2	-	-
300-Strip600-L1.5-4.5/FTC	-	-	-	-	-	-	-
300-Strip600-L6.0/FTC	Yes	indeterminable	60.9 ± 0.3	17.1	66.0	-	-
300-Strip900-L1.5/CNTK	Yes	indeterminable	17.9 ± 0.4	16.0	44.3	-	-
300-Strip900-L3.0-4.5/CNTK	-	-	-	-	-	-	-
300-Strip900-L6.0/CNTK	Yes	indeterminable	23.7 ± 0.7	15.9	50.2	-	-
300-Strip1200-L1.5/CNTK	Yes	1.21±0.24 dB/mm	30.8 ± 0.4	15.8	35.4	-	-
300-Strip1200-L3.0/CNTK	Yes	-	36.7 ± 0.6	17.6	37.6	-	-
300-Strip1200-L4.5/CNTK	Yes	-	42.4 ± 0.6	12.0	38.8	-	-
300-Strip1200-L6.0/CNTK	-	-	-	-	-	-	-
300-Strip1500-all/any	non-fabricated	-	-	-	-	-	-
600-Strip800-L4.0/CNTK (S1)	Yes	6.7 dB	10.4 ± 0.4	14.8	30.7	51.8	ER = 2.629dB @ data rate = 40.0 Gb/s
600-Strip800-L4.0/CNTK (S2)	Yes	-	12.4 ± 1.2	21.6	29.0	43.4	-
600-Strip800-L4.0/CNTK (S3)	Yes	-	12.5 ± 1.2	24.2	31.5	43.0	-
600-Slot-L0.5/CNTK (S1)	Yes	10-11 dB/mm	3.1 ± 0.1	17.2	44.6	82.4	-
600-Slot-L0.5/CNTK (S2)	Yes	-	4.0 ± 0.3	13.4	43.1	64.9	-
600-Slot-L0.5/CNTK (S3)	Yes	-	3.4 ± 0.2	15.5	46.8	76.0	-
600-Slot-L2.0-4.0/CNTK (S1-S3)	-	-	-	-	-	-	-
550-Strip800-L4.0/CNTK	-	4.6 dB	-	-	-	-	-
550-Slot-L0.5-4.0/CNTK	-	-	-	-	-	-	-

The fabricated passive components were optically tested, and it was showing that coupling efficiencies of grating coupler at the peak wavelength of 1.565μm are ~13.5dB/grating for 600nm Stoichiometric SiN and ~ 18dB/grating for 550nm Si-rich SiN. Higher loss in the experimental result compares with the simulated result due to the tolerant in the fabrication and because the simulation was done with the two-dimensional grating while the real grating coupler used in this research are 3D. From the passive component test, the propagation loss of phase modulating device is 1.21 ± 0.23 dB/mm for 300nm stoichiometric SiN strip waveguide and 11.25dB/mm for 600nm stoichiometric SiN slot waveguide. While only insertion loss of 16.75dB/cm and 11.5dB/cm can be estimated for the 550nm Si-rich SiN strip waveguide and 600 nm stoichiometric SiN strip waveguide, respectively.

The characterisation results of the modulating devices with three different SiN platforms have been analysed. The results of the DC modulation showing that the modulator with the CNTK polymer providing the best efficiency with the lowest $V_\pi \cdot L$. By using this polymer, the $V_\pi \cdot L$ of 17.9±0.4 V·cm is achieved from the 300nm strip900-L1.5 while the 600nm strip800-L4.0 provides a $V_\pi \cdot L$ of 12.4±1.2 V·cm. The lowest $V_\pi \cdot L$ in this research of 3.1±0.1 V·cm is achieved from the 600 slot-L0.5 with the highest $r_{33,in-device}$ of 82.4 pm/V. The result from the high-frequency modulations in the modulator with the 600-Strip800-L4.0/CNTK (S1) platform demonstrates a clear eye diagram and shows the possibility to modulate the signal at high speed up to 40.0 Gb/s with an extinction ratio (ER) of 2.629dB.

Chapter 6.
CONCLUSIONS AND FUTURE WORKS

6.1 Conclusions

As the demand for higher bandwidth driven by media and cloud computing applications grows, the need for cost and power efficient, short reach and long-haul optical transceivers becomes more eminent. The current commercial deployment of the 100 Gb/s short reach transmissions in data centres utilizes a 4 × 25 Gb/s, WDM format. However, the next generation transmission systems are envisioned to reach 400 Gb/s transmission rates. The need to generate 100 Gb/s modulation in a single wavelength is one of the main waypoints in realizing 400 Gbps short reach interconnects.

Silicon photonics is emerging as a technology of choice for realising photonic integrated circuits for intensity modulation-direct detection communication systems as well as coherent communication links due to its compatibility with CMOS processes, higher yield, accuracy, and small footprint.

Interferometer modulators is one of the architectures used in photonic platforms. Travelling wave Mach-Zehnder interferometer (MZI) based modulators have been widely used in commercial products in $LiNbO_3$, InP, and especially silicon nitride platform (SiN) platforms. Due to the wavelength and thermal drift insensitivity of MZI, it is an excellent candidate for potential commercial applications. They can reach very high modulation bandwidth, and with careful design can achieve optimal power efficiency.

Silicon Nitride (SiN) is a common material in the electronics industry and is now becoming a choice of materials for the photonics industry as it is a fully compatible platform for photonic integrated circuits. SiN on silicon photonics technology allow an integration of electronic and optical system on the same chip by using the same fabrication techniques. Electro-optic (EO) polymers are recently becoming the new promising material of choice due to 10-times higher EO efficiency compares to $LiNbO_3$. Thus, the integration of EO-polymers with SiN waveguides to form optical modulators provides flexibility and simplicity for BEOL fabrication methods.

This thesis work has addressed the development on the EO polymer modulator based on 3 SiN platforms with Mach-Zehnder (MZ) modulators using a coplanar waveguide (CPW). The design and simulation of photonic component based on SiN platform, starting from the parameters optimisation for fabricating passive components including grating coupler, waveguide, MMI splitters, and Mach-Zehnder interferometer structure have been done.

The estimated coupling efficiency from the simulation showing the loss due to the grating coupler of 11.3, 4.07, and 3.6 dB/grating for a 300nm stoichiometric SiN, 600nm stoichiometric, and 550nm Si-rich SiN, respectively.

The structure for the phase modulator has been designed with aim of investigating the EO phase modulation on the SiN platform. By assembling the optimised passive components together, asymmetric MZIs with a variation of path difference have been designed as an architecture for testing an efficiency of EO polymer, and the metal electrodes were deposited in-levelled with the waveguides layer with various sizes of electrode gap. The phase modulator has been designed with various waveguide width and EO polymer cladding. Three type of EO polymer have been synthesized from our collaborator including a PMMA-*co*-DR1MA, a HG PMMA-FTC, and a CN-TK2 polymer. Different poling efficiency are achieved from these three polymers resulting in the different modulating efficiency of the modulator fabricated from different polymer. The highest efficiency of modulator (lowest $V_\pi \cdot L$.) in this work can be achieved when using the CN-TK2 polymer.

The first platform of EO polymer modulator with 300nm stoichiometric SiN was used together with the strip waveguide. This platform was used as a first design to optimise the fabricating parameters and technique. Therefore, the modulator with 300nm stoichiometric strip SiN waveguide with CN-TK2 polymer providing the lowest $V_\pi \cdot L$ of 17.9±0.4 V·cm compares with the others two platform. The $V_\pi \cdot L$ can be decreased when using a 600nm stoichiometric strip SiN waveguide with a waveguide width of 800nm and modulating length of 4.0mm. This modulating platform provides a $V_\pi \cdot L$ of 12.4±1.2 V·cm. The lowest $V_\pi \cdot L$ in this research is achieved from the 600nm-thick SiN slot waveguide with the modulating length of 0.5mm. It provides the lowest $V_\pi \cdot L$ of 3.1±0.1 V·cm with the highest $r_{33,in-device}$ of 82.4 pm/V. The EO polymer modulator based on this platform giving the propagation loss of ~ 10dB/mm.

Advantage in using the SiN waveguide as the EO polymer modulator are the low number in fabrication step. All designs of modulators in this research can be fabricated using only two lithography steps and a low-cost CMOS compatible BEOL process decreasing substantially fabrication time and design/test turnaround.

High-frequency modulations result of the modulator based on 600nm stoichiometric strip SiN waveguide demonstrates a clear eye diagram and shows the possibility to modulate the signal at high frequency up to 40.0 Gb/s with an extinction ratio (ER) of 2.629dB. To our best knowledge and the literature review, the modulator fabricated in this research is the first EO polymer SiN modulator with interferometer-based structure operating at at 40Gb/s. The modulating rate of modulator in this research can be improved by using an enhance design with correction of EO polymer refractive index.

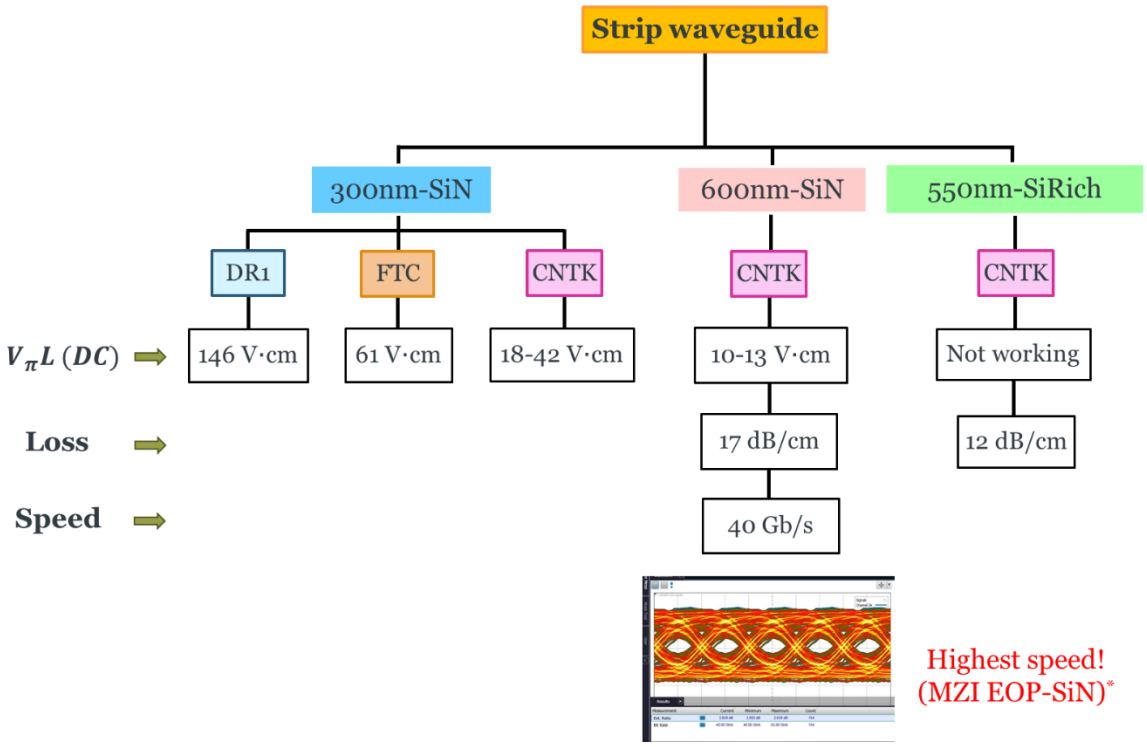

Figure 6-1 Summary diagram showing the $V_\pi L$, loss and speed of EO-polymer modulator based on SiN strip waveguide with 3 waveguide configurations.

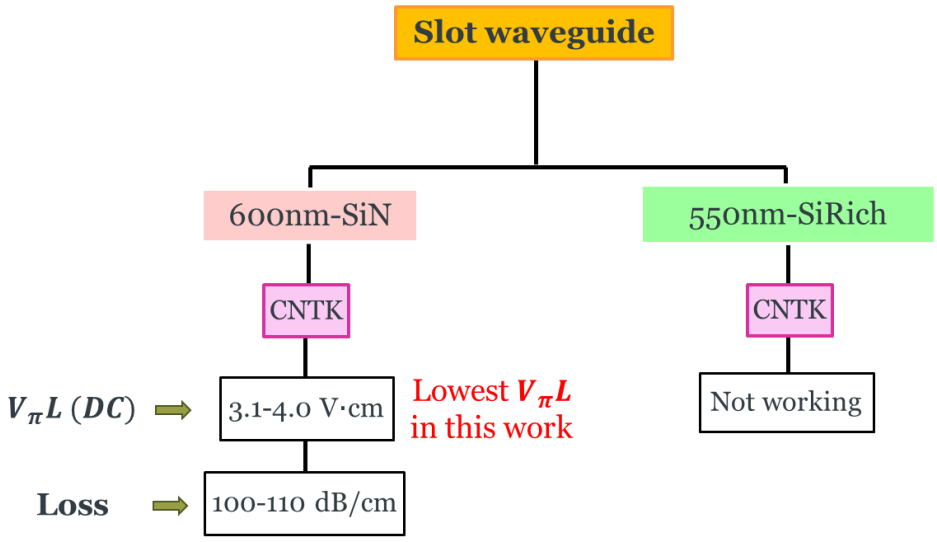

Figure 6-2 Summary diagram showing the $V_\pi L$ and loss of EO-polymer modulator based on SiN slot waveguide with 2 waveguide configurations.

6.2 Future Works

A number of promising projects could explore and extend the currently presented work further.

1) As the enhanced design of the EO polymer modulator based on SiN slot waveguide have been simulated and all fabrications parameters have been optimised as presented in Chapter 3,

section 3.5, the following fabrication parameters need to follow the enhance designs to enable practical slot WG modulator with lower loss.

2) The challenge in the fabrication of the slot waveguide modulator is the small dimension of the device. High accuracy in the fabrication is required to achieve the high efficiency modulator. Therefore, the source of the imperfection of fabricated dimensions in SiN waveguide need to be investigated in the future work.
3) Poling process is one of the important steps of the modulator fabrication process. The work with high voltage (HV) poling can cause the broken of the device due to an electric break down. Thus, the optimal HV poling conditions e.g. increase poling temperature and poling voltage need to be investigated and the poling technique need to be improved. The modification of poling setup to support a poling bias voltage on the centre electrode or Si-substrate as propose in the enhance design need to be done for future work.
4) The device design to support the operating wavelength in visible and O-band will be developed to expand more applications the modulator based on SiN waveguide as SiN has the benefit of allowing the low material absorption for a broadband wavelength from visible to mid-IR.
5) The hybrid design of cladding with a patternable layer of flowable oxide (FOx) or Sol-gel material will be developed in order to ease a polymer integration process and to avoid wasting large amount of expensive polymer with spin-coating technique.
6) Device stability including temporal and thermal degradation test on $V_{\pi}L$ and insertion loss of modulator need to be investigated. Durability of the device also need to be tested with high optical power operation.

Electro-optic (EO) modulators are very useful components to have on a photonics platform. The increasing demand for data, cheap, efficient, and fast optical modulators, the application in telecom and datacom, other application areas are emerging where integrated SiN phase modulators can play an important role. The invention and improvement in stability and modulating speed in EO-polymer modulator based on SiN waveguide in this research will provide the development in the varieties of application such as programmable PICs for microwave photonics and quantum information processing, and optical phased arrays for LIDAR and holographic 3D displays, requiring visible wavelength operation.

Ultimately, with a growing interest in the photonics circuit for many optical applications from institutes and industry around the world, it is envisaged that the research community will continue to offer novel insights into their optical device based on SiN material and develop innovative applications over the coming years.

Appendix A

LIST OF PUBLICATIONS

Journal papers

1. T. Rutirawut, W. Talataisong, F.Y. Gardes, " ***Designs of Silicon Nitride Slot Waveguide Modulators with Electro-Optic Polymer and the Effect of Induced Charges in Si-Substrate on Their Performance***" IEEE Photonics Journal 13(1), (2021)
2. W. Talataisong, R. Ismaeel, S. R. Sandoghchi, T. Rutirawut, G. Topley, M. Beresna, G. Brambilla, "***Novel method for manufacturing optical fiber: extrusion and drawing of microstructured polymer optical fibers from a 3D printer***" Opt. Express 26, 32007-32013 (2018)
3. L. Mastronardi, M. Banakar, A.Z. Khokhar, N. Hattasan, T. Rutirawut, T. Domínguez Bucio, K. M. Grabska, C. Littlejohns, A. Bazin, G. Mashanovich, and F.Y. Gardes, "***High-speed Si/GeSi hetero-structure Electro Absorption Modulator***" Opt. Express 26, 6663-6673 (2018)
4. T. Rutirawut, W. Limphirat, A. Sinsarp, K. Tivakornsasithorn, T. Srikhirin, and T. Osotchan, ***"Composition and Oxidation State of Cobalt and Nickel - Iron Oxide Colloidal Nanoparticles in Liquid Phase"***, Advanced Materials Research, **1103**, 21 (2015).

Conference Papers

1. L. Mastronardi; M. Banakar; A. Z. Khokhar; N. Hattasan; T. Rutirawut; T. Domínguez Bucio; K. M. Grabska; C. Littlejohns; A. Bazin; G. Mashanovich; F. Y. Gardes, **"56 Gbps Si/GeSi integrated EA,"** Proceedings Volume 10823, Nanophotonics and Micro/Nano Optics IV; 108230D (2018)
2. M. Banakar, L. Mastronardi, A.Z. Khokhar, T. Rutirawut, T.D. Bucio, K.M. Grabska, C.G. Littlejohns, A.F.J. Runge, A. Bazin, A.C. Peacock, F.Y. Gardes, ***"Composition Engineering of GeSi Franz–Keldysh Optical Modulator,"*** International Conference on Solid State Devices and Materials (2018)

References

1. Sun, J., et al., *Large-scale nanophotonic phased array.* Nature, 2013. **493**: p. 195.
2. Soref, R., *The Past, Present, and Future of Silicon Photonics.* IEEE Journal of Selected Topics in Quantum Electronics, 2006. **12**(6): p. 1678-1687.
3. Bogaerts, W., M. Fiers, and P. Dumon, *Design Challenges in Silicon Photonics.* IEEE Journal of Selected Topics in Quantum Electronics, 2014. **20**(4): p. 1-8.
4. Soref, R. and B. Bennett, *Electrooptical effects in silicon.* IEEE Journal of Quantum Electronics, 1987. **23**(1): p. 123-129.
5. Li, X., et al., *Highly Efficient Silicon Michelson Interferometer Modulators.* IEEE Photonics Technology Letters, 2013. **25**(5): p. 407-409.
6. Ding, R., et al., *High-Speed Silicon Modulator With Slow-Wave Electrodes and Fully Independent Differential Drive.* Journal of Lightwave Technology, 2014. **32**(12): p. 2240-2247.
7. Samani, A., et al. *OOK and PAM optical modulation using a single drive push pull silicon Mach-Zehnder modulator*. in *11th International Conference on Group IV Photonics (GFP)*. 2014.
8. Zheng, X., et al., *A high-speed, tunable silicon photonic ring modulator integrated with ultra-efficient active wavelength control.* Optics Express, 2014. **22**(10): p. 12628-12633.
9. Dong, P., et al. *High speed silicon microring modulator based on carrier depletion*. in *2010 Conference on Optical Fiber Communication (OFC/NFOEC), collocated National Fiber Optic Engineers Conference*. 2010.
10. Ghione, G., *Semiconductor devices for high-speed optoelectronics*. 2009: Cambridge University Press.
11. Thomson, D.J., et al., *High contrast 40Gbit/s optical modulation in silicon.* Optics express, 2011. **19**: p. 11507-16.
12. Reed, G., et al., *High-speed carrier-depletion silicon Mach-Zehnder optical modulators with lateral PN junctions.* Frontiers in Physics, 2014. **2**.
13. Gardes, F.Y., et al., *A sub-micron depletion-type photonic modulator in Silicon On Insulator.* Optics Express, 2005. **13**(22): p. 8845-8854.
14. Mastronardi, L., et al., *High-speed Si/GeSi hetero-structure Electro Absorption Modulator.* Optics Express, 2018. **26**(6): p. 6663-6673.
15. Mastronardi, L., et al., *High-speed Si/GeSi hetero-structure Electro Absorption Modulator*. Vol. 26 6. 2018. 6663-6673.
16. Chen, L., et al., *Hybrid silicon and lithium niobate electro-optical ring modulator.* Optica, 2014. **1**: p. 112.
17. He, M., et al., *High-performance hybrid silicon and lithium niobate Mach–Zehnder modulators for 100 Gbit s−1 and beyond.* Nature Photonics, 2019. **13**(5): p. 359-364.
18. Eltes, F., et al. *Silicon-Integrated High-Speed Modulators Based on Barium Titanate with Record-Large Pockels Coefficients*. in *2019 Conference on Lasers and Electro-Optics Europe & European Quantum Electronics Conference (CLEO/Europe-EQEC)*. 2019.
19. Li, M. and H.X. Tang, *Strong Pockels materials.* Nature Materials, 2019. **18**(1): p. 9-11.
20. Alexander, K., et al., *Nanophotonic Pockels modulators on a silicon nitride platform.* Nature Communications, 2018. **9**(1): p. 3444.

21. Zhang, X., et al. *Demonstration of effective in-device r_{33} over 1000 pm/V in electro-optic polymer refilled silicon slot photonic crystal waveguide modulator*. in *CLEO: 2013*. 2013.
22. Alloatti, L., et al., *100 GHz silicon–organic hybrid modulator.* Light: Science & Applications, 2014. **3**: p. e173.
23. Bucio, T.D., et al., *Silicon Nitride Photonics for the Near-Infrared.* IEEE Journal of Selected Topics in Quantum Electronics, 2020. **26**(2): p. 1-13.
24. Domínguez Bucio, T., et al., *Low temperature silicon nitride waveguides for multilayer platforms*. SPIE Photonics Europe. Vol. 9891. 2016: SPIE.
25. Riley, F.L., *Silicon Nitride and Related Materials.* Journal of the American Ceramic Society, 2000. **83**(2): p. 245-265.
26. Milek, J.T., *Silicon Nitride for Microelectronic Applications*. 1971, Springer US.
27. Sacher, W.D., et al., *Multilayer Silicon Nitride-on-Silicon Integrated Photonic Platforms and Devices.* Journal of Lightwave Technology, 2015. **33**(4): p. 901-910.
28. Domínguez Bucio, T., et al., *Material and optical properties of low-temperature NH3-free PECVD SiNxlayers for photonic applications.* Journal of Physics D: Applied Physics, 2016. **50**(2): p. 025106.
29. Mashanovich, G., et al., *Silicon and germanium mid-infrared photonics*. SPIE OPTO. Vol. 9755. 2016: SPIE.
30. Romero-García, S., et al., *Visible wavelength silicon nitride focusing grating coupler with AlCu/TiN reflector.* Optics Letters, 2013. **38**(14): p. 2521-2523.
31. Daldosso, N., et al., *Comparison among various Si/sub 3/N/sub 4/ waveguide geometries grown within a CMOS fabrication pilot line.* Journal of Lightwave Technology, 2004. **22**(7): p. 1734-1740.
32. Greta De Paoli, S.L.J., Thalia Dominguez Bucio, Ilias Skandalos, Christopher Holmes, Peter G. R. Smith, Milan M. Milosevic, and Frederic Y. Gardes, *Laser trimming of the operating wavelength of silicon nitride racetrack resonators.* Photon. Res., 2020. **8**.
33. Arbabi, A. and L.L. Goddard, *Measurements of the refractive indices and thermo-optic coefficients of Si3N4 and SiOx using microring resonances.* Optics Letters, 2013. **38**(19): p. 3878-3881.
34. Tu, X., et al., *Thermal independent Silicon-Nitride slot waveguide biosensor with high sensitivity.* Optics Express, 2012. **20**(3): p. 2640-2648.
35. J. B. Khurgin, T.H.S., M. W. Pruessner, and W. S. Rabinovich, *On the origin of the second-order nonlinearity in strained Si–SiN structures.* J. Opt. Soc. Am. B, 2015. **32**.
36. Jen, A., et al. *Exceptional electro-optic properties through molecular design and controlled self-assembly*. 2005.
37. Ding, R., et al., *Demonstration of a low $V_{\pi}L$ modulator with GHz bandwidth based on electro-optic polymer-clad silicon slot waveguides.* Optics Express, 2010. **18**(15): p. 15618-15623.
38. Zhang, X., et al., *Demonstration of Effective In-device r33 over 1000 pmV in Electro-optic Polymer Refilled Silicon Slot Photonic Crystal Waveguide Modulator*. 2013.
39. Sun, S.-S., et al., *Introduction to Organic Electronic and Optoelectronic Materials and Devices (Optical Science and Engineering Series)*. 2008: CRC Press, Inc. 936.
40. Koeber, S., et al., *Femtojoule electro-optic modulation using a silicon-organic hybrid device*. Light Sci Appl, 2015. **4**: p. e255.

41. Ferm, P.M., et al., *Femtosecond response of electro-optic poled polymers.* Applied Physics Letters, 1991. **59**(21): p. 2651-2653.

42. Chen, D., et al., *Demonstration of 110 GHz electro-optic polymer modulators.* Applied Physics Letters, 1997. **70**(25): p. 3335-3337.

43. Bortnik, B., et al., *Electrooptic Polymer Ring Resonator Modulation up to 165 GHz.* IEEE Journal of Selected Topics in Quantum Electronics, 2007. **13**(1): p. 104-110.

44. Gardes, F.Y., et al., *40 Gb/s silicon photonics modulator for TE and TM polarisations.* Optics Express, 2011. **19**(12): p. 11804-11814.

45. Thomson, D.J., et al., *High Performance Mach-Zehnder-Based Silicon Optical Modulators.* IEEE Journal of Selected Topics in Quantum Electronics, 2013. **19**(6): p. 85-94.

46. Baudzus, L. and P. Krummrich, *Low Loss Electro-Optic Polymer Based Fast Adaptive Phase Shifters Realized in Silicon Nitride and Oxynitride Waveguide Technology.* Photonics, 2016. **3**: p. 49.

47. Ishino, M. and S. Yokoyama, *Hybrid thin silicon nitride and electro-optic polymer waveguide modulators*. 2015. 1-2.

48. Palmer, R., et al., *High-Speed, Low Drive-Voltage Silicon-Organic Hybrid Modulator Based on a Binary-Chromophore Electro-Optic Material.* Lightwave Technology, Journal of, 2014. **32**: p. 2726-2734.

49. Alloatti, L., et al., *42.7 Gbit/s electro-optic modulator in silicon technology.* Optics express, 2011. **19**: p. 11841-51.

50. Ding, R., et al., *Demonstration of a low V_πL modulator with GHz bandwidth based on electro-optic polymer-clad silicon slot waveguides.* Optics express, 2010. **18**: p. 15618-23.

51. Wang, X., et al., *Effective in-device r(33) of 735 pm/V on electro-optic polymer infiltrated silicon photonic crystal slot waveguides.* Optics letters, 2011. **36**: p. 882-4.

52. Qiu, F. and S. Yokoyama, *Efficiently poled electro-optic polymer modulators.* Optics express, 2016. **24**: p. 19020-19025.

53. Enami, Y., et al., *Analysis of efficiently poled electro-optic polymer/Tio2 vertical slot waveguide modulators.* Optics Communications, 2015. **362**.

54. Song, R., A. Yick, and W.H. Steier, *Conductivity-dependency-free in-plane poling for Mach-Zehnder modulator with highly conductive electro-optic polymer.* Applied Physics Letters, 2007. **90**(19): p. 191103.

55. Himmelhuber, R., et al., *A Silicon-Polymer Hybrid Modulator—Design, Simulation and Proof of Principle.* Lightwave Technology, Journal of, 2013. **31**: p. 4067-4072.

56. Qiu, F., et al., *A hybrid electro-optic polymer and TiO2 double-slot waveguide modulator.* Scientific Reports, 2015. **5**(1): p. 8561.

57. Witzens, J., T. Baehr-Jones, and M. Hochberg, *Design of transmission line driven slot waveguide Mach-Zehnder interferometers and application to analog optical links.* Optics express, 2010. **18**: p. 16902-28.

58. Ye, C., et al., *A compact plasmonic MOS-based 2×2 electro-optic switch*, in *Nanophotonics*. 2015. p. 261.

59. Ishino, M. and S. Yokoyama. *Hybrid thin silicon nitride and electro-optic polymer waveguide modulators*. in *2015 20th Microoptics Conference (MOC)*. 2015.

60. Baudzus, L. and P. Krummrich, *Low Loss Electro-Optic Polymer Based Fast Adaptive Phase Shifters Realized in Silicon Nitride and Oxynitride Waveguide Technology.* Photonics, 2016. **3**(3): p. 49.

61. Doylend, J.K., et al., *Two-dimensional free-space beam steering with an optical phased array on silicon-on-insulator.* Optics Express, 2011. **19**(22): p. 21595-21604.

62. Stutius, W. and W. Streifer, *Silicon nitride films on silicon for optical waveguides.* Applied Optics, 1977. **16**(12): p. 3218-3222.

63. Gorin, A., et al., *Fabrication of silicon nitride waveguides for visible-light using PECVD: a study of the effect of plasma frequency on optical properties.* Optics Express, 2008. **16**(18): p. 13509-13516.

64. Subramanian, A.Z., et al., *Low-Loss Singlemode PECVD Silicon Nitride Photonic Wire Waveguides for 532-900 nm Wavelength Window Fabricated Within a CMOS Pilot Line.* IEEE Photonics Journal, 2013. **5**(6): p. 2202809-2202809.

65. M. Melchiorri, N.D., F. Sbrana, L. Pavesi, G. Pucker, C. Kompocholis, P. Bellutti, A. Lui, *Propagation losses of silicon nitride waveguides in the near-infrared range.* Applied Physics Letters, 2005. **86**(12).

66. Shaw, M.J., et al. *Fabrication techniques for low-loss silicon nitride waveguides*. in *MOEMS-MEMS Micro and Nanofabrication*. 2005. SPIE.

67. Ikeda, K., et al., *Thermal and Kerr nonlinear properties of plasma-deposited silicon nitride/silicon dioxide waveguides.* Optics Express, 2008. **16**(17): p. 12987-12994.

68. Tan, D.T.H., et al., *Group velocity dispersion and self phase modulation in silicon nitride waveguides.* Applied Physics Letters, 2010. **96**(6): p. 061101.

69. Poulton, C.V., et al., *Large-scale silicon nitride nanophotonic phased arrays at infrared and visible wavelengths.* Optics Letters, 2017. **42**(1): p. 21-24.

70. Boyd, J., et al., *Planar And Channel Optical Waveguides Utilizing Silicon Technology*. 1984 Cambridge Symposium. Vol. 0517. 1985: SPIE.

71. Henry, C.H., et al., *Low loss Si3N4–SiO2 optical waveguides on Si.* Applied Optics, 1987. **26**(13): p. 2621-2624.

72. Heideman, R.G., R.P.H. Kooyman, and J. Greve, *Performance of a highly sensitive optical waveguide Mach-Zehnder interferometer immunosensor*. Sensors and Actuators B: Chemical, 1993. **10**(3): p. 209-217.

73. Woerhoff, K., et al., *Optimization of LPCVD silicon oxynitride growth to large refractive index homogeneity and layer thickness uniformity*. Lasers and Optics in Manufacturing III. Vol. 3099. 1997: SPIE.

74. Wörhoff, K., et al., *Plasma enhanced chemical vapor deposition silicon oxynitride optimized for application in integrated optics.* Sensors and Actuators A: Physical, 1999. **74**(1): p. 9-12.

75. Shaw, M., et al., *Fabrication techniques for low-loss silicon nitride waveguides*. MOEMS-MEMS Micro and Nanofabrication. Vol. 5720. 2005: SPIE.

76. Worhoff, K., et al. *Silicon oxynitride based photonics*. in *2008 10th Anniversary International Conference on Transparent Optical Networks*. 2008.

77. S. C. Mao, et al., *Low propagation loss SiN optical waveguide prepared by optimal low-hydrogen module.* Opt. Express, 2008. **16**: p. 20809-20816.

78. Bauters JF, et al., *Planar waveguides with less than 0.1 dB/m propagation loss fabricated with wafer bonding.* Opt Express., 2011. **19**(24): p. 24090-24101.

79. Bauters JF, et al., *Ultra-low-loss high-aspect-ratio Si3N4 waveguides.* Opt Express, 2011. **19**(4): p. 3163-3174.

80. Kippenberg, T.J., R. Holzwarth, and S.A. Diddams, *Microresonator-Based Optical Frequency Combs.* Science, 2011. **332**(6029): p. 555.

81. Luke K, et al., *Overcoming Si_3N_4 film stress limitations for high quality factor ring resonators.* Opt Express., 2013. **21**(19): p. 22829-22833.

82. Luke K., et al., *Broadband mid-infrared frequency comb generation in a Si_3N_4 microresonator.* Opt. Lett., 2015. **40**: p. 4823-4826.

83. Krückel CJ, et al., *Linear and nonlinear characterization of low-stress high-confinement silicon-rich nitride waveguides: erratum.* Opt Express., 2017. **25**(7): p. 7443-7444.

84. Katarzyna, Ł., et al., *Open access to technology platforms for InP-based photonic integrated circuits.* Advanced Optical Technologies, 2015. **4**(2): p. 157-165.

85. Shang K, et al., *Low-loss compact multilayer silicon nitride platform for 3D photonic integrated circuits.* Opt Express., 2015. **23**(16): p. 21334-21342.

86. Hainberger, R., et al. *Silicon nitride waveguide integration platform for medical diagnostic applications*. in *2016 Progress in Electromagnetic Research Symposium (PIERS)*. 2016.

87. Muñoz, P., et al., *Silicon Nitride Photonic Integration Platforms for Visible, Near-Infrared and Mid-Infrared Applications.* Sensors, 2017. **17**(9): p. 2088.

88. Xu, M., et al., *Design of an Electro-Optic Modulator Based on a Silicon-Plasmonic Hybrid Phase Shifter.* Journal of Lightwave Technology, 2013. **31**(8): p. 1170-1177.

89. Günter, P., *Nonlinear optical effects and materials*. Springer Series in Optical Sciences. 2000: Springer-Verlag Berlin Heidelberg.

90. Bauer, S., *Poled polymers for sensors and photonic applications.* Journal of Applied Physics, 1996. **80**(10): p. 5531-5558.

91. Burland, D.M., R.D. Miller, and C.A. Walsh, *Second-order nonlinearity in poled-polymer systems.* Chemical Reviews, 1994. **94**(1): p. 31-75.

92. Lindsay, G.A. and K.D. Singer, *Polymers for Second-Order Nonlinear Optics, Copyright, 1995 Advisory Board, Foreword*, in *Polymers for Second-Order Nonlinear Optics*. 1995, American Chemical Society. p. i-iv.

93. Bosshard, C., et al., *Organic Materials for Second-Order Nonlinear Optics*, in *Crystal Engineering: From Molecules and Crystals to Materials*, D. Braga, F. Grepioni, and A.G. Orpen, Editors. 1999, Springer Netherlands: Dordrecht. p. 261-278.

94. *Electro-Optics*, in *Fundamentals of Photonics*. 1991. p. 696-736.

95. Kaminow, I.P. and E.H. Turner, *Linear Electrooptical Materials*, in *An Introduction to Electrooptic Devices*, I.P. Kaminow, Editor. 1974, Academic Press. p. 108-120.

96. Norwood, R.A., M.G. Kuzyk, and R.A. Keosian, *Electro-optic tensor ratio determination of side-chain copolymers with electro-optic interferometry.* Journal of Applied Physics, 1994. **75**(4): p. 1869-1874.

97. Dalton, L. and S. Benight, *Theory-Guided Design of Organic Electro-Optic Materials and Devices.* Polymers, 2011. **3**(3): p. 1325-1351.

98. Nagtegaele, P., E. Brasselet, and J. Zyss, *Anisotropy and dispersion of a Pockels tensor: a benchmark for electro-optic organic thin-film assessment.* Journal of the Optical Society of America B, 2003. **20**(9): p. 1932-1936.

99. Boyd, R.W., *Nonlinear Optics*. Third Edition ed. 2008, Oxford, UK: Elsevier, Inc.

100. *Noncentrosymmetric Symmetry Required for Electro-optic Activity*. 2009 [cited 2017; Available from: http://photonicswiki.org/index.php?title=File:Poling_centric.JPG.

101. Park, D.H., *Characterization of Linear Electro-Optic Effect of Poled Organic Thin Films*, in *Department of Electrical and Computer Engineering*. 2008, the University of Maryland, College Park.

102. Kajzar, F., K.-S. Lee, and A.K.-Y. Jen, *Polymeric Materials and their Orientation Techniques for Second-Order Nonlinear Optics*, in *Polymers for Photonics Applications II: Nonlinear Optical, Photorefractive and Two-Photon Absorption Polymers*, K.-S. Lee, Editor. 2003, Springer Berlin Heidelberg: Berlin, Heidelberg. p. 1-85.

103. Nagtegaele, P., E. Brasselet, and J. Zyss, *Anisotropy and dispersion of a Pockels tensor: a benchmark for electro-optic organic thin-film assessment: erratum.* Journal of the Optical Society of America B, 2006. **23**(9): p. 1994-1994.

104. Le Duff, A.-C., et al., *Disperse Red 1-doped solgel planar waveguides for nonlinear optical devices operating at telecommunications wavelengths.* Journal of the Optical Society of America B, 2001. **18**(12): p. 1827-1831.

105. Nahata, A., et al., *Electro-optic determination of the nonlinear-optical properties of a covalently functionalized Disperse Red 1 copolymer.* Journal of the Optical Society of America B, 1993. **10**(9): p. 1553-1564.

106. Shimizu, F.M. and J.A. Giacometti, *Measurement of the electro-optic coefficient during the photoelectric-field assisted poling using a Mach-Zehnder interferometer.* Review of Scientific Instruments, 2016. **87**(12): p. 123102.

107. Xie, S., A. Natansohn, and P. Rochon, *Microstructure of Copolymers Containing Disperse Red 1 and Methyl Methacrylate.* Macromolecules, 1994. **27**(7): p. 1885-1890.

108. Wu, P., et al., *Transient optical modulation with a disperse-red-1–doped polymer film.* Applied Optics, 2000. **39**(5): p. 814-817.

109. Wadell, B.C., *Transmission Line Design Handbook*, in *Transmission Line Design Handbook*. 1991, Artech House Publishers. p. 73.

110. Michel, S., et al. *High-performance electro-optic modulators realized with a commercial side-chain DR1-PMMA electro-optic copolymer*. 2010.

111. Zhang, C., et al., *Progress toward Device-Quality Second-Order Nonlinear Optical Materials. 4. A Trilink High μβ NLO Chromophore in Thermoset Polyurethane: A "Guest−Host" Approach to Larger Electrooptic Coefficients.* Macromolecules, 2001. **34**(2): p. 253-261.

112. Paloczi, G.T., et al., *Replica-molded electro-optic polymer Mach–Zehnder modulator.* Applied Physics Letters, 2004. **85**(10): p. 1662-1664.

113. Harper, A.W., et al., *Translating microscopic optical nonlinearity into macroscopic optical nonlinearity: the role of chromophore–chromophore electrostatic interactions.* Journal of the Optical Society of America B, 1998. **15**(1): p. 329-337.

114. Kim, T.-D., et al., *Binary Chromophore Systems in Nonlinear Optical Dendrimers and Polymers for Large Electrooptic Activities.* The Journal of Physical Chemistry C, 2008. **112**(21): p. 8091-8098.

115. Kim, S.-K., et al., *Electro-optic phase modulator using metal-defined polymer optical waveguide.* Applied Physics Letters, 2005. **87**(1): p. 011107.

116. Yokoyama, S., et al. *Electro-optic polymer modulator with low-driving voltage and high-bandwidth property toward high-refractive index waveguide plateform*. in *2014 IEEE Photonics Conference*. 2014.

117. Qiu, F. and S. Yokoyama, *Efficiently poled electro-optic polymer modulators.* Opt. Express, 2016. **24**: p. 19020-19025.

118. Edgars Nitiss, et al., *All-organic electro-optic waveguide modulator comprising SU-8 and nonlinear optical polymer.* Opt. Express, 2017: p. 31036-31044.

119. Baehr-Jones, T., et al., *Optical modulation and detection in slotted Silicon waveguides.* Opt. Express, 2005. **13**: p. 5216-5226.

120. Baehr-Jones, T., et al., *Nonlinear polymer-clad silicon slot waveguide modulator with a half wave voltage of 0.25V.* Applied Physics Letters, 2008. **92**(16): p. 163303.

121. Alloatti, L., et al. *Silicon high-speed electro-optic modulator*. in *7th IEEE International Conference on Group IV Photonics*. 2010.

122. Qiu, F., et al., *Plate-slot polymer waveguide modulator on silicon-on-insulator*. Opt. Express, 2018(26): p. 11213-11221.

123. Enami, Y., et al., *Analysis of efficiently poled electro-optic polymer/TiO_2 vertical slot waveguide modulators.* Optics Communications, 2016. **362**: p. 77-80.

124. L. Alloatti, et al., *42.7 Gbit/s electro-optic modulator in silicon technology*. Opt. Express, 2011. **19**: p. 11841-11851.

125. Brosi, J.-M., et al., *High-speed low-voltage electro-optic modulator with a polymer-infiltrated silicon photonic crystal waveguide.* Optics Express, 2008. **16**(6): p. 4177-4191.

126. Wang, X., et al., *Effective in-device r_{33} of 735 pm/V on electro-optic polymer infiltrated silicon photonic crystal slot waveguides.* Optics Letters, 2011. **36**(6): p. 882-884.

127. Zhang, X., et al. *Hybrid silicon-electro-optic-polymer integrated high-performance optical modulator*. 2014.

128. Raether, H., *Surface Plasmons on Smooth and Rough Surfaces and on Gratings*, in *Surface Plasmons on Smooth and Rough Surfaces and on Gratings*. 1988, Springer.

129. Brongersma, M.L., J.W. Hartman, and H.A. Atwater, *Electromagnetic energy transfer and switching in nanoparticle chain arrays below the diffraction limit.* Physical Review B, 2000. **62**(24): p. R16356-R16359.

130. Maier, S.A., et al., *Local detection of electromagnetic energy transport below the diffraction limit in metal nanoparticle plasmon waveguides.* Nature Materials, 2003. **2**: p. 229.

131. Weeber, J.-C., et al., *Plasmon polaritons of metallic nanowires for controlling submicron propagation of light.* Physical Review B, 1999. **60**(12): p. 9061-9068.

132. Krenn, J.R., et al., *Non–diffraction-limited light transport by gold nanowires.* EPL (Europhysics Letters), 2002. **60**(5): p. 663.

133. Bozhevolnyi, S.I., et al., *Channel Plasmon-Polariton Guiding by Subwavelength Metal Grooves.* Physical Review Letters, 2005. **95**(4): p. 046802.

134. Zia, R., J.A. Schuller, and M.L. Brongersma, *Near-field characterization of guided polariton propagation and cutoff in surface plasmon waveguides.* Physical Review B, 2006. **74**(16): p. 165415.

135. Melikyan, A., et al., *High-speed plasmonic phase modulators.* Nature Photonics, 2014. **8**: p. 229.

136. Schuller, J.A., et al., *Plasmonics for extreme light concentration and manipulation.* Nature Materials, 2010. **9**: p. 193.

137. Penadés, J.S., et al., *Low-Loss Mid-Infrared SOI Slot Waveguides.* IEEE Photonics Technology Letters, 2015. **27**(11): p. 1197-1199.

138. Almeida, V.R., et al., *Guiding and confining light in void nanostructure.* Optics Letters, 2004. **29**(11): p. 1209-1211.

139. Veronis, G. and S. Fan, *Guided subwavelength plasmonic mode supported by a slot in a thin metal film.* Optics Letters, 2005. **30**(24): p. 3359-3361.

140. Zhang, X., et al., *High Performance Optical Modulator Based on Electro-Optic Polymer Filled Silicon Slot Photonic Crystal Waveguide.* Journal of Lightwave Technology, 2016. **34**(12): p. 2941-2951.

141. Chen, L., J. Shakya, and M. Lipson, *Subwavelength confinement in an integrated metal slot waveguide on silicon.* Optics Letters, 2006. **31**(14): p. 2133-2135.

142. Lauermann, M., et al., *40 GBd 16QAM Signaling at 160 Gb/s in a Silicon-Organic Hybrid Modulator.* Journal of Lightwave Technology, 2015. **33**(6): p. 1210-1216.

143. Inoue, S.-i. and A. Otomo, *Electro-optic polymer/silicon hybrid slow light modulator based on one-dimensional photonic crystal waveguides.* Applied Physics Letters, 2013. **103**(17): p. 171101.

144. Leinse, A., *Polymeric Microring Resonator Based Electro-Optic Modulator*. 2005, University of Twente.

145. Wen, C.P., *Coplanar Waveguide: A Surface Strip Transmission Line Suitable for Nonreciprocal Gyromagnetic Device Applications.* IEEE Transactions on Microwave Theory and Techniques, 1969. **17**(12): p. 1087-1090.

146. M Hein, *High-temperature superconductor thin films at microwave frequencies*. 1999: Springer.

147. Lee, T.H., *Planar Microwave Engineering*. 2004: Cambridge University Press.

148. Breed, G., *There's nothing magic about 50 ohms.* High Frequency Electronics, 2007. **6**: p. 6–7.

149. Kim, C.M. and R.V. Ramaswamy, *Overlap integral factors in integrated optic modulators and switches.* Journal of Lightwave Technology, 1989. **7**(7): p. 1063-1070.

150. Song, R. and W.H. Steier, *Overlap integral factor enhancement using buried electrode structure in polymer Mach-Zehnder modulator.* Applied Physics Letters, 2008. **92**(3): p. 031103.

151. Leuthold, J., et al. *High-speed, low-power optical modulators in silicon*. in *2013 15th International Conference on Transparent Optical Networks (ICTON)*. 2013.

152. Leuthold, J., et al., *Silicon-Organic Hybrid Electro-Optical Devices.* IEEE Journal of Selected Topics in Quantum Electronics, 2013. **19**(6): p. 114-126.

153. Howerton, M.M. and W.K. Burns, *Broadband traveling wave modulators in $LiNbO_3$*, in *RF Photonic Technology in Optical Fiber Links*, W.S.C. Chang, Editor. 2002, Cambridge University Press: Cambridge. p. 133-164.

154. Janner, D., M. Belmonte, and V. Pruneri, *Tailoring the Electrooptic Response and Improving the Performance of Integrated LiNbO3 Modulators by Domain Engineering.* Journal of Lightwave Technology, 2007. **25**(9): p. 2402-2409.

155. Arya, A. and R. Manivasakan. *A compact and high-speed plasmonic slot waveguide coupled with photonic waveguide based 2x2 electro-optic switch*. in *SPIE OPTO*. 2016. SPIE.

156. Block, B.A., et al., *Electro-optic polymer cladding ring resonator modulators.* Optics Express, 2008. **16**(22): p. 18326-18333.

157. *Guide to Using TCAD with Examples (PC version)*. 2009, Silvaco, Inc.

158. *ATLAS User's Manual*. 2010, SILVACO, Inc.

159. *DevEdit User's Manual*. 2014, SILVACO, Inc.

160. *DeckBuild User's Manual*. 2015, Silvaco, Inc.

161. *Optical I/O*, in *Silicon Photonics Design: From Devices to Systems*, L. Chrostowski and M. Hochberg, Editors. 2015, Cambridge University Press: Cambridge. p. 162-214.

162. *Bent waveguide analysis – Lumerical Support*. [cited 2021; Available from: https://support.lumerical.com/hc/en-us/articles/360042799933-Bent-waveguide-analysis.

163. Soldano, L.B. and E.C.M. Pennings, *Optical multi-mode interference devices based on self-imaging: principles and applications.* Journal of Lightwave Technology, 1995. **13**(4): p. 615-627.

164. Enami, Y., et al., *Enhanced conductivity of sol-gel silica cladding for efficient poling in electro-optic polymer/TiO_2 vertical slot waveguide modulators.* Optics Express, 2014. **22**(24): p. 30191-30199.

165. Zhang, X., et al., *Wide optical spectrum range, subvolt, compact modulator based on an electro-optic polymer refilled silicon slot photonic crystal waveguide.* Optics Letters, 2013. **38**(22): p. 4931-4934.

166. Qiu, F., et al., *An electro-optic polymer-cladded TiO_2 waveguide modulator*. Applied Physics Letters, 2016. **109**(17): p. 173301.

167. Enami, Y., et al., *Hybrid cross-linkable polymer/sol-gel waveguide modulators with 0.65V half wave voltage at 1550nm.* Applied Physics Letters, 2007. **91**(9): p. 093505.

168. Deng, Q., et al., *Strip-slot waveguide mode converter based on symmetric multimode interference.* Optics Letters, 2014. **39**(19): p. 5665-5668.

169. Lacava, F., *The Method of Image Charges*, in *Classical Electrodynamics: From Image Charges to the Photon Mass and Magnetic Monopoles*. 2016, Springer International Publishing: Cham. p. 33-53.

170. Zhang, X., et al., *Polymer-Based Hybrid-Integrated Photonic Devices for Silicon On-Chip Modulation and Board-Level Optical Interconnects.* IEEE Journal of Selected Topics in Quantum Electronics, 2013. **19**(6): p. 196-210.

171. Yokoyama, F.Q.a.S., *Efficiently poled electro-optic polymer modulators.* Opt. Express, 2016. **24**.

172. Wolf, S., et al., *Silicon-Organic Hybrid (SOH) Mach-Zehnder Modulators for 100 Gbit/s on-off Keying.* Scientific Reports, 2018. **8**(1): p. 2598.

173. Koeber, S., et al., *Femtojoule electro-optic modulation using a silicon–organic hybrid device.* Light: Science & Applications, 2015. **4**(2): p. e255-e255.

174. Clemens Kieninger, Y.K., Delwin L. Elder, Stefan Wolf, Heiner Zwickel, Matthias Blaicher, Juned N. Kemal, Matthias Lauermann, Sebastian Randel, Wolfgang Freude, Larry R. Dalton, and Christian Koos, *Ultra-high electro-optic activity demonstrated in a silicon-organic hybrid modulator.* Optica, 2018. **5**.

175. Grote, J., et al., *Effect of conductivity and dielectric constant on the modulation voltage for nonlinear optic polymer based opto-electronic devices.* Optical Engineering, 2001. **40**: p. 2464-2473.

176. Zhang, X., et al., *High Performance Optical Modulator Based on Electro-optic Polymer Filled Silicon Slot Photonic Crystal Waveguide*. 2014.

177. Zhang, X., *Hybrid silicon-electro-optic-polymer integrated high-performance optical modulator*. 2014.

178. Reed, G.T., et al., *Silicon optical modulators.* Nature Photonics, 2010. **4**(8): p. 518-526.

179. Ansheng Liu, L.L., Doron Rubin, Hat Nguyen, Berkehan Ciftcioglu, Yoel Chetrit, Nahum Izhaky, and Mario Paniccia, *High-speed optical modulation based on carrier depletion in a silicon waveguide.* Opt. Express, 2007. **15**.

180. Jenner, M.O., *Synthesis of Organic Chromophores for use in Electro-Optic Polymers*, in *School of Chemistry*. 2018, University of Southampton.

181. Piao, X., et al., *Nonlinear optical side-chain polymers post-functionalized with high-β chromophores exhibiting large electro-optic property.* Journal of Polymer Science Part A: Polymer Chemistry, 2011. **49**(1): p. 47-54.

182. Sato, H., et al., *Low driving voltage Mach-Zehnder interference modulator constructed from an electro-optic polymer on ultra-thin silicon with a broadband operation.* Optics Express, 2017. **25**(2): p. 768-775.

183. Miura, H., et al., *High thermal stability 40 GHz electro-optic polymer modulators.* Optics Express, 2017. **25**(23): p. 28643-28649.

184. Bucio, T.D., *NH_3-free PECVD Silicon Nitride for Photonic Applications*, in *Optoelectronics Reseach Centre*. 2018, University of Southampton. p. 288.

185. Himmelhuber, R., et al., *A Silicon-Polymer Hybrid Modulator—Design, Simulation and Proof of Principle.* Journal of Lightwave Technology, 2013. **31**(24): p. 4067-4072.

186. Gerratt, A.P. and S. Bergbreiter, *Dielectric breakdown of PDMS thin films.* Journal of Micromechanics and Microengineering, 2013. **23**(6): p. 067001.

187. Bruce, B., et al. *A low power electro-optic polymer clad Mach-Zehnder modulator for high speed optical interconnects*. in *Proc.SPIE*. 2013.

188. LeCroy, T. *Feed-Forward Equalization*. 2018 23 July 2018 1 March 2021]; Available from: https://blog.teledynelecroy.com/2018/07/feed-forward-equalization.html.